## METHOD OF FUNDAMENTAL SOLUTIONS FOR RAREFIED GAS FLOWS

Ph.D. Thesis

By **HIMANSHI** 



# DEPARTMENT OF MATHEMATICS INDIAN INSTITUTE OF TECHNOLOGY INDORE ${\small \rm JULY~2025}$

## METHOD OF FUNDAMENTAL SOLUTIONS FOR RAREFIED GAS FLOWS

#### A THESIS

Submitted in partial fulfillment of the requirements for the award of the degree

 $\begin{array}{c} \textit{of} \\ \textbf{DOCTOR OF PHILOSOPHY} \end{array}$ 

by **HIMANSHI** 



DEPARTMENT OF MATHEMATICS INDIAN INSTITUTE OF TECHNOLOGY INDORE  ${\rm JULY~2025}$ 



#### INDIAN INSTITUTE OF TECHNOLOGY INDORE

I hereby certify that the work which is being presented in the thesis entitled METHOD OF FUNDAMENTAL SOLUTIONS FOR RAREFIED GAS FLOWS in the partial fulfillment of the requirements for the award of the degree of DOCTOR OF PHILOSOPHY and submitted in the DEPARTMENT OF MATHEMATICS, Indian Institute of Technology Indore, is an authentic record of my own work carried out during the time period from August 2020 to July 2025 under the supervision of Dr. Vinay Kumar Gupta, Associate Professor, Department of Mathematics, Indian Institute of Technology Indore.

The matter presented in this thesis has not been submitted by me for the award of any other degree of this or any other institute.

O1-08-2025
Signature of the student with date
(Himanshi)

This is to certify that the above statement made by the candidate is correct to the best of my knowledge.

01 August 2025

Signature of Thesis Supervisor with date

(Dr. Vinay Kumar Gupta)

-----

Himanshi has successfully given her Ph.D. Oral Examination held on July 30, 2025

01 August 2025

Signature of Thesis Supervisor with date

(Dr. Vinay Kumar Gupta)

\_\_\_\_\_

#### ACKNOWLEDGEMENTS

I would like to express my deepest gratitude to all those who have supported and contributed to the completion of this thesis.

First and foremost, I am immensely grateful to *Dr. Vinay Kumar Gupta*, my Ph.D. supervisor, for his constant guidance, invaluable support, and encouragement throughout my research journey. His mentorship has been instrumental in shaping this work.

I sincerely thank *Dr. Anirudh Singh Rana*, my collaborator and second mentor, for his unwavering support, insightful discussions, and guidance, which were crucial throughout my Ph.D.

I am also thankful to *Prof. Dr. Manuel Torrilhon* for his thoughtful insights and for giving me the opportunity to visit RWTH Aachen University. I extend my gratitude to *Dr. Lambert Theisen* for his generous help during our collaborative project at RWTH Aachen University. The work carried out under the guidance of Prof. Torrilhon and with Dr. Theisen's assistance has significantly contributed to Chapter 7 of my thesis.

I appreciate the valuable feedback and constructive suggestions from the PSPC members, *Dr. Santanu Manna* and *Dr. Harekrishna Yadav*, which have greatly improved the quality of my research.

A heartfelt thanks to *Dr. Sartyvir Singh* and his wife, who made me feel like a part of their family during my stay at Aachen.

I am grateful to all my teachers from graduation and post-graduation, especially *Akashdeep Sir*, whose belief in me has always been a source of inspiration.

I would like to thank my friend Ankit Farkya for many fruitful discussions that enriched my understanding and perspective.

A very special thanks to *Sahil Kalra*, my colleague and best friend, for being a constant source of motivation, encouragement, and support through all the highs and lows of this journey.

My sincere thanks to *Kanupriya*, who has always stood by me like a true friend, uplifting me with her positivity and enthusiasm.

I also extend my thanks to *Aman* and *Shreyas* for their engaging discussions and support, and to my friends and colleagues *Navneet*, *Neha*, *Aditya*, *Prabhu*, *Pinki* and *Harpriya* for their companionship.

I owe my deepest gratitude to my *parents* for their unconditional love, support, and blessings. I am equally thankful to my *brother*, *sister*, *grandmother*, and all other family members for always being there for me.

I also acknowledge the financial support from the Council of Scientific and Industrial Research (CSIR) and the Advanced Research Opportunities Program (AROP) at RWTH Aachen University, Germany. I am also grateful to the Department of Mathematics, IIT Indore and IIT Indore for providing essential infrastructure and funding to attend international conferences.

#### **DEDICATION**

#### То

#### Lord Hanuman,

the revered giver of strength, intellect and knowledge—whose divine blessings guided every step of this journey.

#### Abstract

Rarefied gas flows arise in a variety of physical situations where the molecular mean free path becomes comparable to a characteristic length scale in the system. Such flows occur in high-altitude atmospheric phenomena, vacuum technologies, and micro- and nanoscale devices, where non-equilibrium effects become prominent and classical continuum models, like the Euler or Navier–Stokes–Fourier equations, lose their validity. While the Boltzmann equation offers a complete description of rarefied gas flows, its high dimensional complexity makes it computationally prohibitive in many practical scenarios. An efficient alternative is provided by extended hydrodynamic models that give a macroscopic description of gas flows.

This thesis develops a meshfree numerical framework based on the method of fundamental solutions (MFS) for modeling rarefied gas flows in quasi-two dimensions. An extended hydrodynamic model, which consists of the conservation laws closed with the recently propounded coupled constitutive relations (CCR), is utilized. This model is referred to as the CCR model and is adequate for describing moderately rarefied gas flows. This thesis primarily uses the CCR model for its simplicity and later extends the framework to the regularized 13-moment (R13) model, which is more accurate but more complex than the CCR model.

The core of the work involves deriving the fundamental solutions of the linearized CCR model using the Fourier transformation and implementing the obtained fundamental solutions in the MFS framework. Some internal flow problems, including (monatomic) vapor flows, temperature-induced flows and flow inside a lid-driven cavity, are investigated using the developed CCR-MFS framework. The results obtained from the CCR-MFS framework are validated against existing analytical or numerical benchmarks, demonstrating the accuracy and robustness of the method. External flow of a monatomic rarefied gas past circular and semicircular cylinders is also studied using the CCR model—with artificial boundary introduced to bypass Stokes' paradox. Analytic solution is determined for the circular case and is used to validate the results obtained from the MFS, followed by a numerical investigation of the semi-circular case using the MFS. Additionally, the CCR-MFS framework is employed to analyze evaporation/condensation from/on liquid

jets with circular and non-circular cross-sections. The study explores the effects of geometric deformation—represented using spherical harmonics—on the mass-flux and heat-flux coefficients.

A generic methodology is proposed to derive the fundamental solutions for any linear moment system, including the R13 equations, without predefined Dirac-delta source terms. The generic MFS approach is illustrated for the Stokes equations and extended to the R13 model in two dimensions. The results are compared against an analytical solution to confirm accuracy. The framework is further applied to thermally induced flow between noncoaxial cylinders, where no analytical solution exists. The results obtained from the generic MFS are compared against those from the finite element method, showing comparable accuracy along with faster convergence and lower computational cost.

The thesis also investigates various parameters—such as the numbers of source and collocation points, optimal placement of source points and the effective condition number—that influence the performance of the MFS. The work paves the way for a unified and efficient solver for extended hydrodynamic models applicable to a broad range of rarefied gas flow problems.

#### LIST OF PUBLICATIONS

#### List of Published/Communicated Research Papers from the Thesis

#### Journal publications:

- 1. **Himanshi**, Rana, A. S. and Gupta, V. K., 2023 Fundamental solutions of an extended hydrodynamic model in two dimensions: Derivation, theory, and applications. *Physical Review E* (American Physical Society (APS)), **108**, 015306 . DOI: 10.1103/PhysRevE.108.015306.
- Himanshi, Rana, A. S. and Gupta, V. K., 2024 A viewpoint on thermally-induced transport in rarefied gases through the method of fundamental solutions. *Journal of Computational and Theoretical Transport* (Taylor & Francis), 53, 279–301. DOI: 10.1080/23324309.2024.2336050.
- 3. **Himanshi**, Rana, A. S. and Gupta, V. K., 2025 Exploring external rarefied gas flows through the method of fundamental solutions. *Physical Review E* (American Physical Society (APS)), **111**, 015101. DOI: 10.1103/PhysRevE.111.015101.
- Himanshi, Farkya, A., Rana, A. S. and Gupta, V. K., 2025 Evaporating jets and phase transition in rarefied conditions. *Physics of fluids* (AIP Publishing), 37, 052008. DOI: 10.1063/5.0268832.
- 5. **Himanshi**, Theisen, L., Rana, A. S., Torrilhon, M. and Gupta, V. K. 2025 A generalized fundamental solution technique for the regularized 13-moment system in rarefied gas flows. (arXiv Preprint: https://arxiv.org/abs/2504.18261).

#### Publications in conference proceedings:

- 1. **Himanshi**, Rana, A. S. and Gupta, V. K., 2023 Thermally-induced rarefied gas flows: An approach through the method of fundamental solutions. In the proceedings of *International Conference on Applied Mathematics and Mechanics (ICAMM 2023)* (Accepted).
- 2. **Himanshi**, Rana, A. S. and Gupta, V. K., 2024 A meshless approach to study rarefied gas flows in lid-driven square cavities. In the proceedings of 33rd International Symposium on Rarefied Gas Dynamics (RGD33) (Accepted).

#### List of Published/Communicated Research Papers Apart from the Thesis

1. Farkya, A., **Himanshi**, Dwivedi, G. and Rana, A. S. 2025 A computational framework for nonlinear multiphase flow in porous media using meshfree method: Numerical experiments and applications. (Under Review).

## TABLE OF CONTENTS

LIST	OF FI	GURES	xix
LIST	OF TA	ABLES	XXX
Chap	ter 1	Introduction	1
1.1	Flow	regimes and kinetic description of rarefied gases	1
1.2	Nume	erical methodology and challenges	7
1.3	Prese	nt work and organization of the thesis	10
	1.3.1	Present work	10
	1.3.2	Organization of the thesis	10
Chap	ter 2	Extended hydrodynamic models	13
2.1	Class	ic models	13
2.2	Exter	nded hydrodynamic models	15
	2.2.1	The CCR model	15
	2.2.2	The R13 model	17
	2.2.3	Boundary conditions	20
Chap	ter 3	Method of fundamental solutions	23
3.1	Class	ical MFS	23
	3.1.1	Factors affecting accuracy of the MFS	25
3.2	Funda	amental solutions of the 2D NSF equations	27
3.3	Deriv	ation of the fundamental solutions of the CCR model	32
	3.3.1	Example implementation	36
Chap	ter 4	Application of the CCR-MFS framework for internal flow	
		problems	39

4.1	Vapoi	flow confined between two coaxial cylinders	39
	4.1.1	Problem description	39
	4.1.2	Analytic solution of Onishi [77]	40
	4.1.3	Boundary conditions and implementation of the MFS	41
	4.1.4	Results and discussion	43
	4.1.5	Location of singularities	49
4.2	Temp	erature-induced flow between two non-coaxial cylinders	52
	4.2.1	Problem description	52
	4.2.2	Boundary conditions and implementation of the MFS	53
	4.2.3	Results and discussion	54
	4.2.4	Choice of singularity points	59
4.3	Flows	between coaxial circular and elliptic cylinders	60
	4.3.1	Problem statement	60
	4.3.2	Boundary conditions	62
	4.3.3	Results and discussion	62
4.4	Raref	ded gas flow inside a lid-driven square cavity	72
	4.4.1	Problem statement	72
	4.4.2	Results for a single-sided lid-driven cavity	74
	4.4.3	Results for the two-sided lid-driven cavity with top and bottom walls	
		moving in the same direction	77
	4.4.4	Results for the two-sided lid-driven cavity with top and bottom walls	
		moving in opposite directions	78
4.5	Sumn	nary	<b>7</b> 9
Chap	ter 5	Application of the CCR-MFS framework for external flow	
		problems	81
5.1	Stoke	s' paradox	81
5.2	Flow	past circular cylinder	86
	5.2.1	Problem description	86
	5.2.2	Boundary conditions	87
	5.2.3	Analytic solution	87

	5.2.4	Implementing the MFS	90
	5.2.5	Results and discussion	92
	5.2.6	Sensitivity of the results towards the location of singularities	102
5.3	Flow	past semi-circular cylinder	105
	5.3.1	Results in the case of horizontal flow	108
	5.3.2	Results in the case of the vertical flow	109
	5.3.3	Drag force in the horizontal and vertical cases	110
5.4	Sumn	nary	112
Chapt	ter 6	Phase transition around liquid jets	113
6.1	Proble	em description	114
	6.1.1	Boundary conditions	114
	6.1.2	Numerical implementation	115
6.2	Analy	rtic solution	116
6.3	Valida	ation and discussion	119
6.4	Evapo	oration/condensation on noncircular cross-sections	121
6.5	Sensit	civity analysis	126
6.6	Sumn	nary	132
Chapt	ter 7	Generalizing the MFS to higher-order moment systems	133
7.1	The t	echnique	133
7.2	Imple	menting generic MFS for Stokes' equations	136
	7.2.1	Fundamental solutions	137
	7.2.2	An example setup	139
	7.2.3	Choice of the matrix ${m M}$	140
7.3	Gener	ric MFS for R13 equations	142
7.4	Resul	ts and discussion	144
	7.4.1	Problem description	144
	7.4.2	Validation with analytic solution	145
	7.4.3	Choice of parameters	146
	7.4.4	Choice of the matrix $M$	148

7.5	Comp	arison with the FEM	. 150
	7.5.1	Problem description	. 150
	7.5.2	FEM for the R13 model	. 150
	7.5.3	Results and discussion	. 152
7.6	Summ	ary	. 156
Chapt	ter 8	Summary and future directions	157
8.1	Summ	nary and conclusions	. 157
8.2	Future	e scopes	. 159
Apper	ndices.		
Appei	ndix A	Inverse Fourier transforms	163
Appei	ndix B	Fundamental solutions of the CCR model	165
Appei	ndix C	Interplay between thermal stress and thermal creep	171
C.1	Proble	em statement	. 171
C.2	Result	s demonstrating thermal creep and thermal stress effects	. 172
Appei	ndix D	Analytic solution to the R13 equations	179
REFF	RENC	ES	181

## LIST OF FIGURES

3.1	Schematic of an arbitrarily shaped domain $\Omega$ having boundary $\Gamma$ discretized with boundary nodes, represented by blue symbols. The red symbols denote the singularities or the source points kept on a fictitious boundary $\tilde{\Gamma}$ outside of the domain
3.2	Schematic of a flow past an object of an arbitrary shape depicting the boundary discretization and the placement of singularities outside the flow domain. The red and blue arrows at each boundary node depict the normal (pointing toward the flow domain) and tangential directions at that node, respectively
4.1	Cross-sectional view of a rarefied vapor flow confined between two coaxial cylinders
4.2	Schematic of the boundary nodes on the boundaries and singularity points outside the flow domain for the problem illustrated in Fig. 4.1.  The red and blue arrows at each boundary node depict the normal (pointing toward the flow domain) and tangential directions, respectively at that node.  42
4.3	Variation of the (scaled) temperature in the gap between the two cylinders for different values of $\gamma$ . The solid red, dashed blue, dotted green and dot-dashed magenta lines denote the results obtained from the MFS applied on the CCR model for $\gamma = 0, 3, 7$ and 11, respectively, and the corresponding symbols (disks) indicate the analytic solution from Eq. (4.5), which was obtained analytically for Kn $\approx 0$ through an asymptotic theory [100] performed on the linearized BGK model in

	Ref. [77]. The other parameters are $n_b = 100$ , $n_s = 100$ , $r_1 = 1$ , $r_2 = 2$ , $s_1 = 0.5$ , $s_2 = 4$
4.4	Same as Fig. 4.3 but for $Kn = 0.1$ and the symbols denoting the data from Ref. [77] obtained using the linearized BGK model 4
4.5	Variation of the (scaled) temperature in the gap between the two cylinders for $\gamma=3$ and $\gamma=7$ at Kn = 0.1. Solid lines represent results obtained from the MFS applied to the CCR model. Corresponding symbols (disks) show data from Ref. [77] based on the linearized BGK model. The dashed and dotted lines correspond to MFS solutions of the NSF model with second-order and first-order slip and jump boundary conditions, respectively.
4.6	Variation of the (scaled) radial heat flux with $\gamma$ . The solid blue and dashed red lines denote the results obtained from the MFS applied on the CCR model for Kn = 0.1 and 0.2, respectively, and the corresponding symbols (disks) indicate the data taken directly from Ref. [77], which were obtained using the linearized BGK model. The other parameters are the same as those for Fig. 4.3 4
4.7	Variation of the (scaled) radial velocity with $\gamma$ . The dotted green and solid blue lines denote the results obtained from the MFS applied on the CCR model for Kn $\approx 0$ and Kn = 0.1, respectively, and the corresponding symbols (disks) indicate those from the linearized BGK model (from Eq. (4.4) in the case of Kn $\approx 0$ and directly from Ref. [77] in the case of Kn = 0.1). The other parameters are the same as those for Fig. 4.3.
4.8	The maximum absolute error $\epsilon_{\rm max}$ in the temperature and the effective condition number $\kappa_{\rm eff}$ for the problem of flow between coaxial cylinders plotted over the dilation parameter $\alpha$ for Kn $\approx 0$ and $n_b = n_s = 100$ . 5
4.9	The effective condition number $\kappa_{\text{eff}}$ (left) and the maximum absolute error $\epsilon_{\text{max}}$ in the temperature (right) varying with the dilation parameter $\alpha$ for Kn $\approx 0$ and different values of $n_b$ or $n_s$

4.10	Variation of the effective condition number $\kappa_{\text{eff}}$ with respect to the dilation parameter $\alpha$ for $n_b = n_s = 100$	51
4.11	Cross-sectional view of the flow of a rarefied gas confined between two non-coaxial cylinders having different wall temperatures	52
4.12	Schematic of the boundary nodes on the boundaries and singularity points outside the flow domain for the problem illustrated in Fig. 4.11. The red and blue arrows at each boundary node depict the normal (pointing toward the flow domain) and tangential directions at that node, respectively	53
4.13	Tangential velocity on the right halves of the inner and outer circles associated with the respective cylinders plotted against the angle $\theta$ for different values of the Knudsen number and for $\Delta \tau = 1$ . The dashed red, solid blue and dotted green lines denote the results obtained from the MFS applied on the CCR model for Kn = 0.2, 0.1 and 0.04, respectively, and the corresponding symbols (disks) indicate the data from the linearized BGK model [5]. The other parameters are the same as those for Fig. 4.3.	55
4.14	Velocity streamlines and temperature contours obtained from the MFS applied on the CCR model at Kn = 0.1 and $\Delta \tau$ = 1. The other parameters are the same as those for Fig. 4.3	56
4.15	Velocity streamlines and temperature contours obtained from the MFS applied on the NSF equations with the second-order slip and jump boundary conditions at Kn = 0.1 and $\Delta \tau$ = 1. The other parameters are the same as those for Fig. 4.3.	57
4.16	Drag force on the inner cylinder plotted against the Knudsen number for $\Delta \tau = 1$ . The solid and dashed lines denote the results obtained from the MFS applied on the CCR and NSF models, respectively, while the symbols indicate the data for the drag force obtained from the linearized BGK model [5]. The other parameters are the same as those for Fig. 4.3	58

4.17	Variation of the effective condition number $\kappa_{\text{eff}}$ with respect to the dilation parameter $\alpha$ . The number of boundary nodes at either of the actual boundaries and the number of singularity points at either of the fictitious boundaries are 100 (i.e. $n_b = n_s = 100$ )	59
4.18	Cross-sectional view of the geometry of the problem. The shaded region depicts the flow domain. The cylinders are concentric and coaxial with the radius of the circular cylinder being smaller than both semi axes of the elliptic cylinder	60
4.19	Schematic of the distribution of collocation points (or boundary nodes) on the boundaries and source points outside the flow region for the problem illustrated in Fig. 4.18. The blue and red arrows respectively delineate the tangential and normal directions at each boundary node.	63
4.20	Tangential velocity of the gas on the inner (left panel) and outer (right panel) cylinders with $\beta=1/5$ . The other parameters are $r=0.6$ , $a=1.5, b=1, r_s=0.3, a_s=3, b_s=2, n_b=n_s=70, T_i=0$ and $T_o=1$	64
4.21	Velocity streamlines and temperature contours obtained with the MFS applied on the CCR model for Knudsen numbers (a) Kn = 0.02, (b) Kn = 0.1 and (c) Kn = 0.2 and for $\beta = 1/5$ . The other parameters are the same as those in Fig. 4.20.	65
4.22	Same as Fig. 4.21 but for $\beta = 0.3197$	66
4.23	Same as Fig. 4.21 but with the MFS applied on the NSF model	67
4.24	Variation of the (scaled) temperature of the vapor with the radial distance $r$ between the two cylinders at $\theta=0$ —for three different values of the parameter $\gamma$ , namely $\gamma=1$ (red color), $\gamma=4$ (green color) $\gamma=8$ (blue color), and for three different values of the Knudsen number, namely Kn = 0.02 (solid lines), Kn = 0.1 (dashed lines) and Kn = 0.2 (dotted lines). The other parameters are $a=1.5, b=1, r_s=0.3, a_s=3, b_s=2, n_b=n_s=70, T_i=0.$	69
	$n_s = 0.0, \ u_s = 0, \ v_s = 2, \ n_b = n_s = 10, \ n_t = 0. \dots $ xxii	55

4.25	Heat flow lines plotted over (scaled) temperature contours for (a) $\gamma = 1$ and (b) $\gamma = 8$ and Kn = 0.1. The other parameters are the same as those in Fig. 4.24	70
4.26	Variation of the parameter $\gamma$ with the angle $\theta$ for Kn = 0.02, 0.1 and 0.2. The other parameters are the same as those in Fig. 4.24	71
4.27	Schematics of (a) single-sided lid-driven cavity, and two-sided lid-driven cavities with top and bottom walls moving in the (b) same and (c) opposite directions.	72
4.28	Schematic of the distribution of collocation points (or boundary nodes) on the boundaries and source points outside the flow region for the problem described in Sec. 4.4.1. The magenta and blue arrows demonstrate the tangential and normal directions at each boundary node, respectively	73
4.29	Variation of $v_y$ along the horizontal centerline (i.e., for $y = 0.5$ ) of the cavity (left panel) and variation of $v_x$ along the vertical centerline (i.e., for $x = 0.5$ ) of the cavity (right panel) for Kn = 0.08. The solid blue curve represents the results for the MFS applied to the CCR model, the dashed red curve represents the results for the MFS applied to the NSF model, the green (square) and black (circle) symbols denote the data from the DSMC method and R13 model, respectively, taken from Ref. [85]	74
4.30	Variation in $v_y$ along different horizontal lines $y = 0.1, 0.4$ and 0.8 inside the cavity (left panel) and the variation of $v_x$ along different vertical lines $x = 0.1, 0.4$ and 0.8 inside the cavity (right panel) obtained by the MFS applied to the CCR model.	75
4.31	Velocity streamlines plotted over shear stress contours (left panel) and heat flux lines plotted over temperature contours (right panel) for the case when top wall is moving in the positive x-direction	76
4.32	Velocity streamlines plotted over shear stress contours (left panel) and heat flux lines plotted over temperature contours (right panel) for $\mathrm{Kn}=0.08$ obtained from the MFS applied to the NSF model	77

4.33	Velocity streamlines plotted over shear stress contours (left panel) and heat flux lines plotted over temperature contours (right panel) for the case when top and bottom walls are moving in same directions with the same speeds.	78
4.34	Velocity streamlines plotted over shear stress contours (left panel) and heat flux lines plotted over temperature contours (right panel) for the case when top and bottom walls are moving in opposite directions with the same speeds.	<b>7</b> 9
5.1	Schematic of Stokes flow past an infinite circular cylinder of radius $R$ , where the fluid is moving transversely to the axis of the cylinder 8	82
5.2	Cross-sectional view of the problem of a rarefied gas flow past an infinitely long cylinder. The solid circle represents the periphery of the cylinder while the dashed circle represents an artificial boundary far away from the cylinder	86
5.3	Placement of the collocation points (black dots) on the actual and artificial boundaries and singularities (black stars) outside of these boundaries. The blue and red arrows at each boundary node denote the unit tangent and normal vectors, respectively	91
5.4	Speed of the gas varying with the radial position in different directions for Kn = 0.1, 0.5 and 1. The solid lines represent the results obtained from the MFS applied to the CCR model and the symbols represent the analytic solutions. The other parameters are $N_{b_1} = N_{s_1} = 50$ , $N_{b_2} = N_{s_2} = 100$ , $R_1 = 1$ , $R_2 = 10$ , $R'_1 = 0.5$ and $R'_2 = 20$	93
5.5	Velocity streamlines over speed contours obtained from the MFS applied on the CCR model for the Knudsen numbers $Kn = 0.1, 0.5$ and 1. The other parameters are the same as those for Fig. 5.4	94
5.6	Temperature along the left and right sides of the disk for $Kn = 0.009$ , 0.1 and 0.5. Solid lines represent the results obtained from the MFS applied to the CCR model and the triangles represent the analytic	
	solutions. The other parameters are the same as those for Fig. 5.4	45

5.7	applied to the CCR model for Knudsen numbers Kn = 0.009, 0.1 and 0.5. The other parameters are the same as those for Fig. 5.4 97
5.8	Heat-flux lines over temperature contours obtained from the MFS applied to the NSF model for Knudsen numbers $\mathrm{Kn}=0.009,0.1$ and 0.5. The other parameters are the same as those for Fig. 5.4 97
5.9	Temperature of the gas at $r=1$ and $\vartheta=0$ scaled with $\mathrm{Kn^2}$ plotted against the Knudsen number for different locations of the artificial boundary. The left panel shows the results obtained with the CCR model and the right panel shows the results obtained with the NSF equations and the second-order accurate boundary conditions 98
5.10	Maximum speed of the gas on the disk plotted against the Knudsen number for different locations of the artificial boundary
5.11	Normalized drag on the cylinder plotted against the Knudsen number for different locations of the artificial boundary. The dashed red, blue and magenta lines represent the analytic solution of the CCR model for $R_2 = 10$ , 20 and 30, respectively. The square (red), disk (blue) and diamond (magenta) symbols represent the numerical solution of the CCR model obtained with the MFS for $R_2 = 10$ , 20 and 30, respectively. The solid orange, black and gray lines depict the normalized drag obtained with the analytic expressions given in Refs. [79], [128] and [37]. The green triangle symbol shows the normalized drag computed with the nonlinear R26 equations in Ref. [37]. The other parameters are the same as those for Fig. 5.4
5.12	Effective condition number $\kappa_{\rm eff}$ (left panel) and absolute error $\epsilon$ in speed (right panel) both plotted against the dilation parameter $\alpha$ in the case when the total number of boundary nodes $N_b$ is equal to the total number of singularity points $N_s$ (the case of square collocation matrix) for Kn = 0.1.
5.13	Effective condition number $\kappa_{\text{eff}}$ (left panel) and absolute error $\epsilon$ in speed (right panel) both plotted against the dilation parameter $\alpha$ in

	from the total number of boundary nodes $N_b$ is different from the total number of singularity points $N_s$ (the case of non-square collocation matrix) for Kn = 0.1
5.14	Cross-sectional view of the horizontal and vertical flows past a semicircular cylinder
5.15	Schematic representation for an arrangement of singularities (stars) and boundary nodes (dots). The red and blue arrows represent the normal and tangent vectors at each boundary node
5.16	Velocity streamlines along with contour plots of the speed in the background obtained with the MFS applied on the CCR model for Kn = 0.1, 0.3 and 0.5. The other parameters are $R_1 = 1$ , $R_2 = 10$ , $R'_1 = 0.1$ , $R'_2 = 50$ , $N_{b_1} = N_{s_1} = 200$ and $N_{b_2} = N_{s_2} = 400$
5.17	Heat-flux lines along with density plots of the temperature in the background obtained with the MFS applied on the CCR model for $\mathrm{Kn}=0.1,0.3$ and 0.5. The other parameters are the same as those for Fig. 5.16.
5.18	Velocity streamlines along with contour plots of the speed in the background obtained with the MFS applied on the CCR model for $\mathrm{Kn}=0.1,0.3$ and 0.5. The other parameters are the same as those for Fig. 5.16
5.19	Heat-flux lines along with density plots of the temperature in the background obtained with the MFS applied on the CCR model for $Kn=0.1,0.3$ and 0.5. The other parameters are the same as those for Fig. 5.16.
5.20	Drag force on the semicircular disk plotted against the Knudsen number in the horizontal and vertical cases. The other parameters are the same as those for Fig. 5.16.
6.1	Schematic representation of 2D cross-section of an evaporating liquid jet immersed in its vapor

6.2	Boundary discretization depicting the boundary nodes and singularity			
	points placed outside of the domain along with the normal and tangent			
	vectors shown at each boundary node			
6.3	The mass-flux coefficient $c_1$ in the pressure-driven $(T^I = 0, p_s = 1)$ case (left) and in temperature-driven $(T^I = 1, p_s = 0)$ case (middle); and the heat-flux coefficient $c_2$ for the temperature-driven $(T^I = 1, p_s = 0)$			
	case (right) as a function of Knudsen number with different values of			
	$\Theta$ . The middle panel also represents the heat-flux coefficient $c_2$ in the			
	pressure-driven $(T^I = 0, p_s = 1)$ case. The numerical results obtained			
	from the MFS using expressions $(6.20)$ and $(6.21)$ are represented by			
	symbols while the analytical results calculated using $(6.13)$ and $(6.15)$			
	are shown with solid lines			
6.4	Variation in the radial velocity (left panel) and temperature (right			
	panel) with the radial distance for the pressure-driven case ( $p_s=1$			
	and $T^{I}=0$ ) at Kn = 0.1 for different values of $\Theta$ . Numerical results			
	obtained using the CCR-MFS framework are illustrated using symbols			
	(disks) and analytical solutions are represented by solid lines. $\dots 120$			
6.5	Same as Fig. 6.4 but for the temperature-driven case ( $T^{I}=1$ and			
	$p_s = 0$ )			
6.6	Shapes generated using equation (6.26) for set of parameters $a_0 = 0$ ,			
	$a_1 = 0.01, a_2 = 0.8, a_3 = 0.01, a_4 = 0.01 \text{ (left)} \text{ and } a_0 = 0, a_1 = 0.05,$			
	$a_2 = 0.05, a_3 = 0, a_4 = 0.1 \text{ (right) with } r_0 = 0.5. \text{ The black (disk)}$			
	symbols denote the boundary nodes discretized over the interfacial			
	boundary whereas the red (star) symbols denote the chosen singularity			
	points in both the shapes			
6.7	The mass-flux coefficient $c_1$ in the pressure-driven $(T^I=0,p_s=1)$			
	case (left) and in temperature-driven ( $T^{I} = 1, p_{s} = 0$ ) case (middle);			
	and the heat-flux coefficient $c_2$ for the temperature-driven $(T^I = 1,$			
	$p_s=0$ ) case (right) as a function of Knudsen number for $\Theta=1$ . The			

	middle panel also represents the heat-flux coefficient $c_2$ in the pressure- driven ( $T^I = 0, p_s = 1$ ) case. Results correspond to the circle and two deformed shapes presented in Fig. 6.6
6.8	Velocity streamlines over speed contours (left panel) and heat-flux lines over temperature contours (right panel) in the pressure-driven case ( $T^I = 0$ and $p_s = 1$ ) for shape 1 at Kn = 0.1
6.9	Velocity streamlines over speed contours (left panel) and heat-flux lines over temperature contours (right panel) in the temperature-driven case $(T^I = 1 \text{ and } p_s = 0)$ for shape 1 at Kn = 0.1
6.10	Same as Fig. 6.8 but for shape 2
6.11	Same as Fig. 6.9 but for shape 2
6.12	Absolute errors in the radial velocity and radial heat flux plotted against the dilation parameter in the pressure-driven case for $\mathrm{Kn}=0.1$ and $N_s=45.$
6.13	Same as Fig. 6.12 but in the temperature-driven case
6.14	Absolute errors in the radial velocity and radial heat flux plotted over the number of singularity points in the pressure-driven case for ${\rm Kn}=0.1$ and $\alpha=0.4$ .
6.15	Same as Fig. 6.14 but in the temperature-driven case
6.16	Absolute error $\epsilon$ in the radial velocity at the interface (represented by the blue axis and curves) and the effective condition number $\kappa_{\rm eff}$ (represented by the red axis and curves) varying with the dilation parameter $\alpha$ for different number of boundary nodes and singularity points. The solid, dashed and dot-dashed curves represent the cases with $N_s = 45, N_b = 60; N_s = 60, N_b = 80;$ and $N_s = 90, N_b = 120,$ respectively.
C 17	
6.17	Variation in the effective condition number $\kappa_{\text{eff}}$ with respect to the dilation parameter $\alpha$ for different numbers of boundary and source points in case of shape 1 (left panel) and shape 2 (right panel)131

7.1	Schematic representation for discretization of boundary points (blue disks) on the domain boundary and singularity points (red disks) outside the problem domain
7.2	Stokes' flow between two cylinders (left) and the placement of boundary nodes and singularities in the MFS (right)
7.3	Schematic of the cross-section of rarefied gas confined between two coaxial cylinders where the inner cylinder is rotating anticlockwise $145$
7.4	Variation of the speed (left panel) and temperature (right panel) in the gap between the two cylinders. The solid blue, red and black lines denote the analytic results of the R13 model along $\vartheta=0,\pi/4$ and $\pi/2$ , respectively. The corresponding blue, red and black (triangle) symbols denote the results obtained from the MFS for Kn = 0.5
7.5	Variation in $L^2$ error in velocity $\epsilon_{L^2}$ and effective condition number $\kappa_{\text{eff}}$ with respect to the dilation parameter $\alpha$ for different values of grid spacing $d$ and $\mathbf{M} = \mathbf{B}(\mathbf{x})^{T}$
7.6	Variation in $L^2$ error in velocity $\epsilon_{L^2}$ (left panel) and effective condition number $\kappa_{\text{eff}}$ (right panel) with respect to dilation parameter $\alpha$ for $\mathbf{M} = \begin{bmatrix} 0_{1\times 6} & I_6 & 0_{9\times 6} \end{bmatrix}^T$ for $\mathrm{Kn} = 0.5.\ldots$ 149
7.7	Variation in $L^2$ error in velocity $\epsilon_{L^2}$ (left panel) and effective condition number $\kappa_{\text{eff}}$ (right panel) with respect to dilation parameter $\alpha$ for $\mathbf{M} = \begin{bmatrix} I_9 & 0_{7\times 9} \end{bmatrix}^T$ for Kn = 0.5
7.8	Series of finite element meshes $\mathcal{T}_i$ with decreasing mesh size $h_{\max}$ for increasing $i$
7.9	Velocity streamlines overlaid on temperature contours for different Knudsen numbers $\mathrm{Kn}=0.05,0.1,0.2,0.4$ as predicted by the MFS 153
7.10	Speed of the gas between the two cylinders along $y=x$ in the first quadrant for different Knudsen numbers
C.1	A cross-sectional view illustrating a rarefied gas contained between two coaxial cylinders, the outer of which is circular and the inner of which is elliptic

C.2	remperature contours and velocity streamlines depicted in the first
	quadrant for different values of the Knudsen number (Kn = $0.05, 0.1, 0.15,$
	and 0.2) for fixed $\beta = 1/5$ , $\alpha_0 = 0.3197$ and $Pr = 0.661$
C.3	Temperature comtours and velocity streamlines depicted in the first
	quadrant for different values of the Knudsen number (Kn = $0.05, 0.1, 0.15$
	and 0.2) for fixed $\beta = \alpha_0 = 0.3197$ and $Pr = 0.661$
C.4	Temperature contours and velocity streamlines depicted in the first
	quadrant for different values of the Knudsen number (Kn = $0.05, 0.1, 0.15,$
	and 0.2) for fixed $\beta = \alpha_0 = 2/5$ and $Pr = 2/3$
C.5	Schematic for the depiction of the two type of flows induced due to
	thermal creep and thermal stress effects
C.6	Variation in the normal component of heat flux on the outer (circular)
	cylinder with $\theta$ in the first quadrant for Kn = 0.1. The other parameters
	are $\beta = 1/5$ , $\alpha_0 = 0.3197$ and $Pr = 0.661$

## LIST OF TABLES

6.1	The values of the coefficients $\omega_i$ appearing in the Onsager reciprocity
	coefficients $\eta_{ij}$ in the boundary conditions (6.1) and (6.2) for different
	values of $\Theta$
7.1	Comparison of the heat flow rate through the inner cylinder $Q_{\Gamma_1}$ and
	computation time for FEM (top) and MFS (bottom) for different mesh
	refinements and source distances $d$ using 8 CPU cores
8.1	Summary of problems studied, models used, and validation or model
	limitations

### Chapter 1

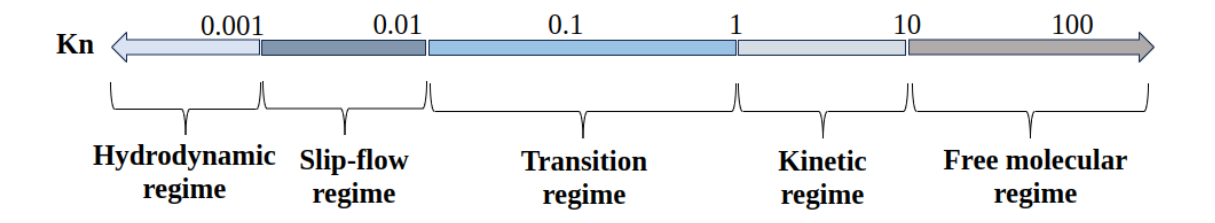
### Introduction

Accurate modeling of rarefied gases in non-equilibrium presents significant challenges. A gas is said to be rarefied when the mean free path of the gas molecules becomes comparable to a characteristic macroscopic length scale associated with the geometry of the problem [1, 18, 59, 105]. The degree of rarefaction is quantified by a dimensionless parameter, known as the Knudsen number Kn, which is the ratio of the mean free path  $\lambda$  of the gas and a characteristic length scale L in the problem. A gas is said to be in equilibrium when the Knudsen number approaches zero, which typically occurs when the mean free path is small compared to the characteristic length scale. In the equilibrium (or very close to equilibrium), the classical fluid dynamic equations—such as the Euler equations or the Navier-Stokes-Fourier (NSF) equations—are quite effective in describing gas flows. However, these classical equations fall short when the Knudsen number becomes significant with the breakdown of the equilibrium assumptions. This breakdown occurs if either the mean free path is large or physical length scale is small. For example, in high-altitude aerospace applications, the mean free path measures in several meters, making the Knudsen number large, as encountered during spacecraft re-entry. On the other hand, in microscale devices like micro-electro-mechanical systems, the small size of the system makes the macroscopic/characteristic length scale comparable to the mean free path, again resulting in a high Knudsen number. In the following section, we classify the gas flows based on the Knudsen number to highlight the different regimes.

#### 1.1 Flow regimes and kinetic description of rarefied gases

Based on the Knudsen number, gas flows can be categorized into different regimes [105, 117, 126]:

Hydrodynamic regime (Kn ≤ 0.01): In this regime, gases are close to the
equilibrium and the classical continuum theories, namely the Euler equation or
Navier-Stokes-Fourier (NSF) equations, are quite effective in describing gas flows.



- Slip flow regime (0.01  $\lesssim$  Kn  $\lesssim$  0.1): For the flows in this regime, the NSF equations still remain valid, but they need to be supplemented with suitable boundary conditions for temperature jump and velocity slip.
- Transition regime  $(0.1 \lesssim \text{Kn} \lesssim 1)$ : Flows in this regime cannot be described by the NSF equations because of strong non-equilibrium. Macroscopic descriptions still remain feasible by employing an extended set of macroscopic equations, while particle-based methods remain computationally very expensive.
- Kinetic regime (1 ≤ Kn ≤ 10): In this regime, non-equilibrium is so pronounced that directly solving the Boltzmann equation or using particle-based methods, such as direct simulation Monte Carlo (DSMC) method [13], becomes essential, despite their computational cost.
- Free molecular flow regime (Kn ≥ 10): In this regime, gas molecules move independently without significant inter-molecular collisions. Consequently, the flow is governed primarily by molecule-wall interactions and molecular dynamics simulations are often employed for describing gas flows in this regime.

A gas outside the hydrodynamic regime is generally classified as rarefied [1, 105]. Rarefied gases exhibit several distinctive non-equilibrium effects, including velocity slip and temperature jump [28, 102], Knudsen layers [102, 109], thermal creep (transpiration) and thermal stress [99–101], non-homogeneity in pressure profile and unusual temperature dip in the Poiseuille flow [75, 84, 110], cross effects where heat flows from a low-temperature region to a high-temperature region [69, 85, 109]. While some of these effects, such as velocity slip and temperature jump, can be described by the NSF equations with appropriate boundary conditions, other rarefaction effects require more refined models for an accurate description.

It is widely recognized that kinetic theory is capable of describing rarefied gas flows based on the statistical description of the gas. The fundamental equation in kinetic theory is the Boltzmann equation, which provides a comprehensive microscopic (or mesoscopic) description of a gas for the entire range of the Knudsen number, from near-equilibrium to strong non-equilibrium [19]. By tracking the evolution of the molecular velocity distribution function in a seven-dimensional phase space (three spatial dimensions, three dimensions for the velocity and one dimension for time), the Boltzmann equation provides a complete statistical description of gas. However, this equation is challenging to solve because of the presence of the Boltzmann collision operator on the right-hand-side of the equation. The Boltzmann collision operator possesses a complex mathematical structure that makes the Boltzmann equation a nonlinear integro-differential equation which is computationally very expensive, particularly in the transition regime. Study of gas flows in the transition regime is critical for wide applications, like microsensors, spacecraft re-entry and high-vacuum systems. In the transition regime, gas molecules are sparse enough to exhibit non-continuum effects, such as velocity slip, thermal creep, etc., yet dense enough for frequent collisions. This makes the particle-based numerical methods to be computationally expensive in the transition regime. To address computational challenges, kinetic models, like the well-known Bhatnagar-Gross-Krook (BGK) model [11] (also referred to as the Boltzmann–Krook–Welander (BKW) kinetic model by some authors [5, 77, 101]), ES-BGK model [46] and S-model [92] have been developed. The BGK model substitutes the Boltzmann collision operator with an integral-free relaxation model and maintains some of the key features of the Boltzmann collision operator, such as conservation laws and the H-theorem. However, the BGK model does not yield the correct Prandtl number value for monatomic gases [20, 105]. Although other kinetic models, such as the ES-BGK model [46] and S-model [92], yield the right Prandtl number for monatomic gases, they exhibit non-realistic behavior in the transition regime [105].

Alternative ways to find approximate solutions of the Boltzmann equation are provided via kinetic theory through macroscopic equations. Macroscopic flow quantities like the mass density, velocity and energy can be obtained by suitable averaging over the velocity distribution function. These macroscopic quantities, obtained from the distribution function, are governed by extended hydrodynamic equations which can be directly obtained from the Boltzmann equation. Two classical approaches in kinetic theory which provide extended hydrodynamic equations from the Boltzmann equation are the Chapman–Enskog expansion method [21, 34] and Grad's moment method [36, 72].

Chapman–Enskog expansion method [21, 34] involves an asymptotic expansion in powers of the Knudsen number. In this approach, the velocity distribution function is expanded around the equilibrium distribution function as a power series in the Knudsen number. The expansion is then substituted into the Boltzmann equation and the coefficients of each power of the Knudsen number are equated on both sides. This process generates constitutive relations of increasing orders for the standard conservation laws of fluid dynamics. At zeroth order, the method produces the Euler equations and at first order, it gives the NSF equations. However, when extended to higher orders, the method leads to the Burnett and super-Burnett equations, which turn out to be unstable for time-dependent problems [14, 15, 120]. Even in steady problems, Burnett equations are difficult to solve because they lack a full set of boundary conditions [105].

In contrast, Grad's moment method extends the space of macroscopic variables by including governing equations for higher-order moments of the distribution function, with the system of the conservation laws. The method truncates the infinite set of coupled moment equations at a specific level and closes them utilizing the Hilbert expansion of the velocity distribution function in Hermite polynomials. The resulting finite set of moment equations is linearly stable and is also capable of describing the Knudsen layers if a relatively high number of moments are considered [91, 106]. Despite its usefulness, Grad's moment method does not offer clear guidance on how many, and which variables are needed to accurately describe flows at a given Knudsen number. Although Grad developed a theory for setting boundary conditions, very few solutions of boundary-value problem have been reported in the literature. Furthermore, because moment equations in Grad's original formulation, known as the Grad 13-moment (G13) equations [36], are hyperbolic in nature, simulations of shock structures often produce unphysical results, like spurious subshocks [72, 123].

To address the limitations of both Chapman–Enskog expansion method and Grad's moment method, Struchtrup and Torrilhon [108] proposed the regularized 13-moment (R13) equations, which are a regularized version of the original G13 equations, obtained by employing a Chapman–Enskog expansion around a pseudo-equilibrium. Another method which does not rely on Grad's closure relations and does not directly utilize the results of asymptotic expansions, was proposed in Refs. [104, 105] to obtain the R13 equations. This approach, referred to as the order-of-magnitude approach, offers a systematic framework

for deriving closed form of moment equations from the infinite system of moment equations resulting from the Boltzmann equation. The method identifies the appropriate equations within a desired order of accuracy in the Knudsen number through three key steps. First, it determines the order of magnitude of the moments by employing a Chapman–Enskog-like expansion on non-equilibrium moments. Second, it constructs an optimized moment set by introducing new variables—formed through linear combinations of the original moments—to minimize their number at each order. Third, it eliminates terms that are of higher-order. The order-of-magnitude approach yields the Euler equations at zeroth order and the NSF equations at first order. At second-order, equations reduce to original G13 system, and at third-order, approximation leads to the R13 equations. This indicates that the R13 system is optimal for describing processes with third-order accuracy in the Knudsen number. The R13 equations avoid unphysical shocks, ensure smooth shock structures, resolve Knudsen layers and are thermodynamically consistent, owing to which they are quite effective in capturing rarefaction effects in the transition regime.

Building on the need for more robust and thermodynamically-consistent models for higher Knudsen numbers, a novel Onsager-consistent approach [1, 95] was introduced a few years back for deriving extended equations similar to the Burnett and Grad systems. In this method, rather than expanding the distribution function in a series based on the Knudsen number (as in the Chapman–Enskog approach) or using Hermite polynomials (as in Grad's method), the distribution function was instead constructed using the thermodynamic forces and fluxes. This Onsager-consistent approach led to the Onsager 13-moment (O13) [95], Onsager-Burnett (OBurnett) [48, 96], extended-OBurnett and super-OBurnett [127] equations, whose derivation is firmly rooted in the principles of nonequilibrium thermodynamics and aims to better capture strong non-equilibrium effects in rarefied gases. While these Onsager-consistent models are promising alternatives to the classical models (e.g. the NSF, G13, Burnett models), they are relatively new, and a detailed investigation of their practical implementation and numerical properties is beyond the scope of the present thesis.

Another pragmatic alternative offered by Rana et al. [88] is a model based on the coupled constitutive relations (CCR), which couple stress and heat flux phenomenologically, based on entropy-flux correction. The consequent model consisting of the mass, momentum and energy balance equations closed with the coupled constitutive relations is referred to as the CCR model. Unlike the approaches in moment methods, which introduce additional moment equations, the CCR model retains the governing equations only for the equilibrium variables (mass, momentum and energy) while incorporating non-equilibrium effects through the coupled constitutive relations. This coupling introduces terms which account for rarefaction effects—including thermal stress, transpiration flows, the Knudsen paradox, and non-Fourier heat transfer—while maintaining a computationally efficient formulation suitable for moderate rarefaction.

The CCR model inherently satisfies two key thermodynamic requirements: they maintain a valid entropy law with non-negative entropy production for all processes and guarantee linear stability. This distinguishes them fundamentally from other rarefied gas models, such as the Burnett equations (which are unstable) or Grad-type moment systems (which produce unphysical subshocks). The CCR model offers a simpler alternative to moment methods that require a large number of variables. In the linearized and steady state, the CCR model reduces to the linearized G13 equations in the steady state as a special case, and on taking the coupling coefficient as zero, the CCR model reduces to the original NSF equations. Owing to its simplicity and viable features, the CCR model has been applied successfully to some problems pertaining to rarefied gas flows [33, 68, 90]. While the CCR model is less accurate than R13 in strongly non-equilibrium flows and does not resolve Knudsen layers, it effectively captures a wide range of rarefaction phenomena in good agreement with kinetic theory and experiments that makes it a versatile and practical choice to capture moderate rarefaction.

In this thesis, we shall primarily focus on exploring rarefied gas flows in the transition regime using the CCR model, due to its practical efficiency and relatively simpler structure. This model effectively captures key non-equilibrium effects while maintaining computational tractability. In the end, we shall extend the study to any general moment system, including the R13 equations, which provides a more accurate representation of rarefied gas flows at moderate Knudsen numbers.

## 1.2 Numerical methodology and challenges

Theoretical advancement of extended hydrodynamic models provide powerful tools for capturing rarefaction phenomena. However, practical application of extended hydrodynamic models demands numerical frameworks capable of handling inherent complexities, like higher-order gradients, nonlinearity, coupling between/among equations, and non-local boundary effects. Traditional mesh-based methods—such as the finite element method (FEM) and the finite volume method (FVM)—face significant challenges in this context. When the geometry includes moving curved boundaries, the mesh needs to be updated frequently, which adds to the computational cost and can reduce accuracy. Moreover, in low-speed external flows, the computational domain often needs to extend far beyond the object to account for long-range molecular effects, making mesh generation even more complex and resource-intensive [64].

These limitations are exacerbated by the coupled nature of extended hydrodynamic models. For example, the R13 equations introduce additional governing equations for stress and heat flux, and the CCR model modifies the constitutive relations for stress and heat flux appearing in the system of the conservation laws. Solving such systems numerically amplifies matrix sizes and risks numerical instability. Furthermore, implementing the boundary conditions derived from kinetic theory (e.g., velocity slip, temperature jump and beyond) often requires significant modifications in the traditional mesh-based solvers, adding complexity to the simulations.

For Stokes flow (or for creeping flow), these numerical difficulties can sometimes be mitigated by leveraging the linearity of the governing equations. In this scenario, the Navier–Stokes equations reduce to the Stokes equations, which describe flow dominated by viscous forces. A particularly effective method for solving Stokes flows relies on fundamental solutions, the so-called Stokeslet, which represents the velocity field due to a point force in a viscous fluid. Originally derived by Lorentz [65] and later named by Hancock [41], the Stokeslet serves as a fundamental solution of the Stokes equations and provides a foundation for developing mesh-free and semi-analytical techniques. By utilizing the fundamental solutions, it becomes possible to construct efficient numerical approaches that avoid some of the key drawbacks of traditional discretization-based methods. The method of fundamental solutions (MFS) introduced by Kupradze and Aleksidze [56] is a

numerical approach, which has been employed widely for solving linear partial differential equations (PDEs). The MFS is a meshfree method that yields remarkably good results with a significantly less computational cost if the *singularity points* (also referred to as the *source points* or *singularities*) are placed at proper locations. The meshfree feature of the MFS is especially useful in the situations wherein changes in the shape of the domain are needed, e.g., in shape optimization and in inverse problems. This is because the MFS does not require creating a mesh over the entire domain, which itself could be a very time-consuming and computationally-expensive task depending on the complexity of the domain. In the MFS, an approximate solution of a (linear) boundary value problem is expressed as a linear combination of Green's functions, referred to as the fundamental solutions, and the boundary conditions are satisfied at several locations on the boundary, referred to as the *boundary nodes* or *collocation points*, aiming to determine the unknown coefficients in the linear combination.

Apart from being time-efficient due to reduced spatial dimension in boundary discretization, the quality of being free from integrals makes the MFS peerless among other meshfree methods (such as the boundary element method [16], finite point method [76], diffuse element method [73], element-free Galerkin method [9]) that involve complex integrals. The MFS has proven to be an efficient executable numerical scheme in various areas, such as thermoelasticity, electromagnetics, electrostatics, wave scattering, inverse problems and fluid flow problems; see, e.g., Refs. [10, 31, 52, 62, 64, 129]. Moreover, the MFS is also suitable for the analysis of problems involving shape optimization, moving boundary and/or unknown boundary [3, 24, 32, 94, 129], since the problems of modeling and satisfying boundary conditions are relatively simpler for them.

Several researchers have employed the MFS to solve the Helmholtz-, harmonic- and biharmonic-type boundary value problems in two dimensions (2D) as well as in three dimensions (3D), see, e.g., Refs. [66, 80]. For more complex boundary value problems, the MFS works as a good numerical strategy if the fundamental solutions of the problem are predefined. In the past few years, there has been a surge of interest in employing the MFS to various models for rarefied gas flows, for instance to the NSF, G13, R13 and CCR models [27, 64, 90], because the predefined fundamental solutions of the well-known equations, such as the Laplace, Helmholtz and biharmonic equations, can be exploited to

determine the fundamental solutions for the NSF, G13, R13 and CCR models. Nevertheless, to the best of the author's knowledge, all the works on the MFS for rarefied gas flows before this thesis have investigated the problems in 3D only. But, for quasi two-dimensional flow problems, it is not really necessary to solve the full three-dimensional problem as the flow profiles obtained in a cross section perpendicular to the transverse direction remain the same in any cross section perpendicular to the transverse direction. Thus, a quasi-two-dimensional study of a full three-dimensional problem (where one dimension in the problem is much larger than the other two) is enough to understand the full three-dimensional problem. Unfortunately, the two-dimensional fundamental solutions, which are the prerequisite of the MFS, for a model cannot be deduced directly from its three-dimensional counterpart due to the fact that the associated Green's functions are entirely different in 2D and 3D.

Traditionally, the MFS relied on evaluating the unknown coefficients in the linear combination of the fundamental solution, by satisfying the given boundary conditions. However, drawing inspiration from the Stokeslet, Lockerby & Collyer [64] introduced physically meaningful point forces and point heat sources in the momentum and energy balance equations, respectively, that represent the strength of individual fundamental solutions. These unknown source strengths are then determined using the underlying boundary conditions. Lockerby & Collyer [64] derived the fundamental solutions for the NSF, G13 and R13 equations (with point force and heat source) in 3D and demonstrated the implementation of the MFS for the G13 equations [36]. As an extension, Claydon et al. [27] introduced an additional (ad hoc) source term in the stress balance equation of the R13 model to obtain the fundamental solutions of the R13 equations in 3D and implemented the MFS for R13 model in spherical geometries. Apart from that, in order to obtain the fundamental solution of the CCR model [88], Rana et al. [90] used a source term in the mass balance equation in addition to the point force and point heat source in momentum and energy balance equations, respectively, for investigating evaporation effects in 3D. All these approaches required deriving fundamental solutions for specific models by prescribing Dirac-delta source terms in some selected equations within the system of governing equations and closure relations. While being effective, this methodology makes it challenging to extend the MFS to new or more complex models, where the fundamental solutions are unknown and the choice of source terms is not straightforward. A general approach to compute the fundamental solutions for a large system without predefined source terms also lacks in the literature.

## 1.3 Present work and organization of the thesis

#### 1.3.1 Present work

The main objective of the thesis is to develop the MFS framework for monatomic rarefied gas flow problems in 2D. Throughout the thesis, 2D refers to quasi-2D. The work relies upon determining the two-dimensional fundamental solutions of the linearized CCR model and to implement them in a numerical framework. A few illustrative internal and external problems have been investigated to gauge the accuracy of the developed framework. The thesis demonstrates the capability of the CCR-MFS framework to capture rarefaction effects, including temperature jump, anti-Fourier effects, thermal stress and thermal transpiration. Evaporation/condensation effects have also been studied for rarefied gas flows using the CCR model. An intriguing problem in 2D that does not arise in 3D is Stokes' paradox [58], which states the non-existence of a steady-state solution to Stokes' equations in 2D. The occurrence of Stokes' paradox in rarefied gases also poses mathematical challenges, which are addressed using the CCR-MFS framework for external flow problems. The final goal is to make the MFS for rarefied gas flows independent of the problem-specific fundamental solutions. For this purpose, a generic approach is presented that systematically computes the fundamental solutions for any linear moment system without predefined source terms. The proposed approach is demonstrated to determine the fundamental solutions of the R13 equations in 2D. The computational efficiency and accuracy of the MFS is also compared with the FEM for the thermally-induced flow between two non-coaxial cylinders to highlight the advantages of the MFS over traditional meshing techniques. The remaining part of the thesis is organized as follows.

## 1.3.2 Organization of the thesis

Chapter 2 introduces the classical hydrodynamic models, namely the Euler and NSF equations, which are effective near the equilibrium. This is followed by presenting two extended hydrodynamic models—the CCR and R13 models—that are capable of capturing non-equilibrium effects in rarefied monatomic gas flows. These models are reduced to

their linear and dimensionless forms and the corresponding thermodynamically-admissible boundary conditions for each model are also discussed in this chapter.

Chapter 3 introduces the MFS approach and presents an idea to extend it for rarefied gas flows. As a preliminary step to develop the MFS framework for flows in quasi 2D, the fundamental solutions of the linearized NSF equations in 2D are derived, followed by a derivation of the fundamental solutions of the CCR model in 2D. The implementation of the MFS for the CCR model is demonstrated with the example of flow past an object of an arbitrary shape.

Chapter 4 investigates some illustrative internal flow problems in rarefied gases using the MFS applied on the CCR model, including the problems of a vapor flow between two coaxial circular cylinders, temperature-driven gas flow between two noncoaxial circular cylinders having different wall temperatures, flow between coaxial circular and elliptic cylinders, and flow inside a lid-driven cavity. The chapter also includes a sensitivity analysis to find an appropriate location of singularities. To examine the impact of geometry, a monatomic rarefied gas flow between an elliptical outer cylinder coaxial with an inner circular cylinder is also studied. The problems with purely temperature-driven gas flows are discussed in detail to demonstrate an intriguing interplay between thermal creep and thermal stress effects.

Chapter 5 presents external flow of a monatomic rarefied gas past circular and semicircular cylinders studied with the CCR model by introducing an artificial boundary to bypass Stokes' paradox. Analytic solution is determined for the circular case and is used to validate the results obtained from the MFS, followed by numerical investigation of the semi-circular cases using the MFS.

Chapter 6 investigates evaporation/condensation from/on a liquid jet having circular and non-circular cross-sections using the CCR model. Analytic results for the circular case are validated against those obtained from the MFS. The mass-flux and heat-flux coefficients for pressure- and temperature-driven flows are analyzed for both partial and complete phase changes. The impact of interface shape deformation on the mass-flux and heat-flux coefficients is investigated using shapes generated via spherical harmonics. A sensitivity analysis highlights the influence of placement of singularities on the accuracy of the MFS.

Chapter 7 presents a methodology to derive the fundamental solutions for a generic linear moment system without predefined Dirac-delta source terms in the governing and/or closure equations. The method is illustrated first for the Stokes equations and then is extended to the R13 equations in 2D.

Chapter 8 presents the final conclusions and outlook.

# Chapter 2

# Extended hydrodynamic models

This chapter first introduces the classical hydrodynamic equations, namely the Euler and NSF equations, which are effective in the equilibrium or near the equilibrium. This is followed by two extended hydrodynamic models—the CCR and R13 models—that are capable of capturing non-equilibrium effects in rarefied monatomic gas flows. Since the goal of the thesis is to employ the MFS to these models, they are subsequently reduced to their linear and dimensionless forms. The corresponding thermodynamically consistent boundary conditions for these models are also discussed.

## 2.1 Classic models

For gases in the hydrodynamic regime, the continuum hypothesis holds and gas flows can be accurately described using classical hydrodynamic models, like the Euler equations or the NSF equations. These models are based on the fundamental conservation laws of the mass, momentum and energy, which govern the macroscopic behavior of gases. Before presenting these equations explicitly, we introduce a notational convention for clarity. All symbols with tilde as an accent will henceforth denote dimensional quantities, while those without any accent will represent dimensionless quantities. The governing conservation equations for a compressible, viscous gas in the dimensional form are given by [55, 105]

$$\frac{\partial \tilde{\rho}}{\partial \tilde{t}} + \tilde{\boldsymbol{v}} \cdot \tilde{\boldsymbol{\nabla}} \tilde{\rho} + \tilde{\rho} \, \tilde{\boldsymbol{\nabla}} \cdot \tilde{\boldsymbol{v}} = 0, \tag{2.1}$$

$$\tilde{\rho} \left( \frac{\partial \tilde{\boldsymbol{v}}}{\partial \tilde{t}} + \tilde{\boldsymbol{v}} \cdot \tilde{\boldsymbol{\nabla}} \tilde{\boldsymbol{v}} \right) + \tilde{\boldsymbol{\nabla}} \tilde{p} + \tilde{\boldsymbol{\nabla}} \cdot \tilde{\boldsymbol{\sigma}} = \tilde{\rho} \tilde{\boldsymbol{F}}, \tag{2.2}$$

$$\tilde{\rho}\tilde{c}_v \left( \frac{\partial \tilde{T}}{\partial \tilde{t}} + \tilde{\boldsymbol{v}} \cdot \tilde{\boldsymbol{\nabla}} \tilde{T} \right) + \tilde{p} \, \tilde{\boldsymbol{\nabla}} \cdot \tilde{\boldsymbol{v}} + \tilde{\boldsymbol{\nabla}} \cdot \tilde{\boldsymbol{q}} + \tilde{\boldsymbol{\sigma}} : \tilde{\boldsymbol{\nabla}} \tilde{\boldsymbol{v}} = 0, \tag{2.3}$$

where  $\tilde{\rho}$ ,  $\tilde{v}$ ,  $\tilde{T}$ ,  $\tilde{\rho}$ ,  $\tilde{\sigma}$ ,  $\tilde{q}$  are the density, velocity, temperature, pressure, stress tensor and heat flux, respectively;  $\tilde{t}$  is the time variable;  $\tilde{F}$  is the external force per unit mass; and the coefficient  $\tilde{c}_v$  is the molar specific heat at constant volume, and for monatomic gases,  $\tilde{c}_v = 3\tilde{R}/2$ , with  $\tilde{R}$  being the ideal gas constant. If the viscous stress and heat flux are neglected, i.e.  $\tilde{\sigma} = \mathbf{0}$  and  $\tilde{q} = \mathbf{0}$ , the NSF equations reduce to the *Euler equations*, which

read

$$\frac{\partial \tilde{\rho}}{\partial \tilde{t}} + \tilde{\boldsymbol{v}} \cdot \tilde{\boldsymbol{\nabla}} \tilde{\rho} + \tilde{\rho} \, \tilde{\boldsymbol{\nabla}} \cdot \tilde{\boldsymbol{v}} = 0, \tag{2.4}$$

$$\tilde{\rho} \left( \frac{\partial \tilde{\boldsymbol{v}}}{\partial \tilde{t}} + \tilde{\boldsymbol{v}} \cdot \tilde{\boldsymbol{\nabla}} \tilde{\boldsymbol{v}} \right) + \tilde{\boldsymbol{\nabla}} \tilde{p} = \tilde{\rho} \tilde{\boldsymbol{F}}, \tag{2.5}$$

$$\tilde{\rho}\tilde{c}_v \left( \frac{\partial \tilde{T}}{\partial \tilde{t}} + \tilde{\boldsymbol{v}} \cdot \tilde{\boldsymbol{\nabla}} \tilde{T} \right) + \tilde{p} \, \tilde{\boldsymbol{\nabla}} \cdot \tilde{\boldsymbol{v}} = 0.$$
(2.6)

The Euler equations (2.4)–(2.6) represent the simplest form of the hydrodynamic equations, capturing compressible, inviscid fluid flow without the influence of viscosity and heat conduction. These equations are particularly useful in high-speed aerodynamics and gas dynamics, where viscous effects are often negligible.

It is important to note that the system of Eqs. (2.1)–(2.3) is not closed as such, owing to the presence of the additional unknowns  $\tilde{\sigma}$  and  $\tilde{q}$ , and requires constitutive relations for these unknowns in order to close the system. In the NSF closure, the constitutive relations for the stress and heat flux are given by

$$\tilde{\boldsymbol{\sigma}} = -2\tilde{\mu} \overline{\tilde{\boldsymbol{\nabla}} \tilde{\boldsymbol{v}}},\tag{2.7}$$

$$\tilde{\mathbf{q}} = -\tilde{\kappa}\tilde{\mathbf{\nabla}}\tilde{\theta},\tag{2.8}$$

where  $\tilde{\mu}$  is the coefficient of the shear viscosity,  $\tilde{\kappa}\tilde{R}$  is the coefficient of the thermal conductivity,  $\tilde{\theta} = \tilde{R}\tilde{T}$  is the temperature in energy units and the overline above a quantity denotes its symmetric and tracefree part of the corresponding tensor. For a d-dimensional vector  $\boldsymbol{\psi}$ , the symmetric-tracefree part of the tensor  $\nabla \boldsymbol{\psi}$  is defined as [40]

$$\overline{\nabla \psi} = \frac{1}{2} \left[ \nabla \psi + (\nabla \psi)^{\mathsf{T}} \right] - \frac{1}{d} (\nabla \cdot \psi) \mathbf{I}, \tag{2.9}$$

where I is the identity tensor in d-dimensions. For three- and quasi-two-dimensional problems, d=3. The validity of the Euler and NSF equations is limited to flows with very small Knudsen numbers. However, as the Knudsen number increases, the continuum assumption underlying both the NSF and Euler equations breaks down. This necessitates the use of more sophisticated extended hydrodynamic models, which are discussed in the following sections.

## 2.2 Extended hydrodynamic models

The inability of the Navier–Stokes–Fourier equations to capture rarefaction effects motivates us to adopt the extended hydrodynamic models. These models go beyond the classical continuum assumptions to account for non-equilibrium phenomena, such as velocity slip, temperature jump and anti-Fourier heat flux, which are significant in the slip and transition regimes. Although several extended hydrodynamic models have been developed over the years, including the Burnett equations, super-Burnett equations, G13 equations, and their regularized forms like the R13 and R26 equations, we present the CCR and R13 models in this section as we shall be using these two models to employ the MFS in the present thesis.

## 2.2.1 The CCR model

An extended hydrodynamic model propounded by Rana *et al.* [88] provides an improved set of closure relations, which are better than the NSF constitutive relations (2.7)–(2.8) in general. This model includes the coupling between the stress and heat flux appearing in the conservation laws (2.1)–(2.3) via a coupling coefficient, and hence the closure relations are known as the coupled constitutive relations (CCR). The constitutive relations for closing the system of Eqs. (2.1)–(2.3) read [88]

$$\tilde{\boldsymbol{\sigma}} = -2\tilde{\mu} \left[ \overline{\tilde{\boldsymbol{\nabla}}} \tilde{\boldsymbol{v}} + \frac{\alpha_0}{\tilde{p}} \left\{ \overline{\tilde{\boldsymbol{\nabla}}} \tilde{\boldsymbol{q}} - \alpha_1 \overline{\tilde{\boldsymbol{q}}} \, \overline{\tilde{\boldsymbol{\nabla}}} (\ln \tilde{\boldsymbol{\theta}}) - \alpha_2 \overline{\tilde{\boldsymbol{q}}} \, \overline{\tilde{\boldsymbol{\nabla}}} (\ln \tilde{p}) \right\} \right], \tag{2.10}$$

$$\tilde{\boldsymbol{q}} = -\tilde{\kappa} \left[ \tilde{\boldsymbol{\nabla}} \tilde{\boldsymbol{\theta}} + \frac{\alpha_0}{\tilde{\rho}} \left\{ \tilde{\boldsymbol{\nabla}} \cdot \tilde{\boldsymbol{\sigma}} - (1 - \alpha_1) \, \tilde{\boldsymbol{\sigma}} \cdot \tilde{\boldsymbol{\nabla}} (\ln \tilde{\boldsymbol{\theta}}) - (1 - \alpha_2) \, \tilde{\boldsymbol{\sigma}} \cdot \tilde{\boldsymbol{\nabla}} (\ln \tilde{\boldsymbol{p}}) \right\} \right], \quad (2.11)$$

where,  $\alpha_0$  is referred to as the coupling coefficient since it induces the coupling between constitutive relations for the stress and heat flux. Setting  $\alpha_0 = 0$  in Eqs. (2.10) and (2.11) removes the coupling between the constitutive relations (2.10) and (2.11) and reduces them simply to the NSF constitutive relations. The coefficients  $\alpha_1$  and  $\alpha_2$  in Eqs. (2.10) and (2.11) are typically determined from experimental or theoretical scenarios; nonetheless, for Maxwell molecules,  $\alpha_1 = \alpha_2 = 0$  [88]. Equations (2.1)–(2.3) along with the constitutive relations (2.10) and (2.11) are referred to as the CCR model [88].

## Linearized CCR model:

As we are interested in employing the MFS, which relies on the linearity of equations, we shall be dealing with the linearized CCR model. For linearization, we choose the

equilibrium state of the gas as the reference state wherein let the density and temperature of the gas be  $\tilde{\rho}_0$  and  $\tilde{T}_0$ , respectively, so that the pressure in the reference state be  $\tilde{p}_0 = \tilde{\rho}_0\tilde{\theta}_0$ , where  $\tilde{\theta}_0 = \tilde{R}\tilde{T}_0$ . The other quantities (velocity, stress tensor and heat flux) in the reference state are zero. For linearization, we introduce small perturbations in the flow variables from their values in the equilibrium state and, for convenience, we also make all quantities dimensionless using the length scale  $\tilde{L}$ , time scale  $\tilde{L}/\sqrt{\tilde{\theta}_0}$  and appropriate combinations of the reference density  $\tilde{\rho}_0$  and reference temperature  $\tilde{T}_0$ . The dimensionless perturbations in the density, temperature, velocity, stress tensor and heat flux from their values in the reference state are given by

$$\rho = \frac{\tilde{\rho} - \tilde{\rho}_0}{\tilde{\rho}_0}, \quad T = \frac{\tilde{T} - \tilde{T}_0}{\tilde{T}_0}, \quad \boldsymbol{v} = \frac{\tilde{\boldsymbol{v}}}{\sqrt{\tilde{\theta}_0}}, \quad \boldsymbol{\sigma} = \frac{\tilde{\boldsymbol{\sigma}}}{\tilde{\rho}_0 \tilde{\theta}_0} \quad \text{and} \quad \boldsymbol{q} = \frac{\tilde{\boldsymbol{q}}}{\tilde{\rho}_0 \tilde{\theta}_0^{3/2}}, \tag{2.12}$$

respectively. Inserting these dimensionless perturbations in the CCR model [Eqs. (2.1)–(2.3) closed with Eqs. (2.10)–(2.11)] and dropping all nonlinear terms in the dimensionless perturbations, we get the linear-dimensionless CCR model, which reads

$$\frac{\partial \rho}{\partial t} + \boldsymbol{\nabla} \cdot \boldsymbol{v} = 0, \tag{2.13}$$

$$\frac{\partial \boldsymbol{v}}{\partial t} + \boldsymbol{\nabla} p + \boldsymbol{\nabla} \cdot \boldsymbol{\sigma} = \boldsymbol{F}, \tag{2.14}$$

$$c_v \frac{\partial T}{\partial t} + \nabla \cdot \boldsymbol{v} + \nabla \cdot \boldsymbol{q} = 0, \qquad (2.15)$$

$$\boldsymbol{\sigma} = -2\operatorname{Kn}\left(\overline{\boldsymbol{\nabla}\boldsymbol{v}} + \alpha_0 \,\overline{\boldsymbol{\nabla}\boldsymbol{q}}\right),\tag{2.16}$$

$$\boldsymbol{q} = -\frac{c_p \operatorname{Kn}}{\operatorname{Pr}} \left( \boldsymbol{\nabla} T + \alpha_0 \, \boldsymbol{\nabla} \cdot \boldsymbol{\sigma} \right), \tag{2.17}$$

where  $t = \tilde{t}\sqrt{\tilde{\theta}_0}/\tilde{L}$ ,  $\nabla \equiv (1/\tilde{L})\tilde{\nabla}$ ,  $p = \rho + T$  is the dimensionless perturbation in the pressure p due to the linearization,  $c_v = \tilde{c}_v/\tilde{R}$ ,

$$Kn = \frac{\tilde{\mu}_0}{\tilde{\rho}_0 \sqrt{\tilde{\theta}_0} \tilde{L}} \quad \text{and} \quad \Pr = c_p \frac{\tilde{\mu}_0}{\tilde{\kappa}_0}$$
 (2.18)

are the Knudsen number and Prandtl number, respectively, with  $\tilde{\mu}_0$  and  $\tilde{\kappa}_0 \tilde{R}$  being the coefficients of the shear viscosity and thermal conductivity, respectively, in the reference state. In Eq. (2.18),  $c_p = \tilde{c}_p/\tilde{R}$  with  $\tilde{c}_p$  being the specific heat at constant pressure. For monatomic gases,  $\tilde{c}_p = 5\tilde{R}/2$ . It may be noted that while performing the linearization, the external force  $\tilde{F}$  has been assumed to be small (of the order of perturbed variables)

and has been scaled with  $\tilde{\theta}_0/L$ , i.e.  $\mathbf{F} = \tilde{\mathbf{F}}L/\tilde{\theta}_0$ . Equations (2.13)–(2.17) are referred to as the linear-dimensionless CCR model.

For all the problems considered in this thesis, there is no external force, i.e.  $\mathbf{F} = \mathbf{0}$  and the steady-state equations are obtained simply by setting all time-derivative terms in Eqs. (2.13)–(2.17) to zero, i.e. by setting  $\partial(\cdot)/\partial t = 0$ . Consequently, the linear-dimensionless CCR model in the steady state reduces to

$$\nabla \cdot \boldsymbol{v} = 0,$$

$$\nabla p + \nabla \cdot \boldsymbol{\sigma} = 0,$$

$$\nabla \cdot \boldsymbol{q} = 0,$$
(2.19)

with the closure (for a monatomic gas)

$$\sigma = -2\operatorname{Kn}\left(\overline{\nabla v} + \alpha_0 \overline{\nabla q}\right),$$

$$q = -\frac{c_p \operatorname{Kn}}{\operatorname{Pr}}\left(\nabla T + \alpha_0 \nabla \cdot \boldsymbol{\sigma}\right).$$
(2.20)

For  $\alpha_0 = 2/5$ , Eqs. (2.19)–(2.20) reduce to the linearized G13 equations in the steady state. Further if coupling coefficient  $\alpha_0 = 0$ , the linear steady-state CCR model reduces to the classical NSF equations, which are Eqs. (2.19) with closure

$$\sigma = -2\operatorname{Kn}\overline{\nabla v},$$

$$q = -\frac{c_p\operatorname{Kn}}{\operatorname{Pr}}\nabla T.$$
(2.21)

#### 2.2.2 The R13 model

Despite the notable improvements offered by the CCR model over the classical NSF equations, its applicability remains limited in gas flows with relatively higher degree of rarefaction or in situations involving strong non-equilibrium effects. A set of extended hydrodynamic equations that can overcome the limitations of the CCR model is the Regularized 13-Moment (R13) equations proposed by Struchtrup and Torrilhon in a series of works [105, 108]. The R13 model incorporates additional higher-order contributions while preserving the structure of the original 13-moment system.

The R13 equations involve gradients of higher-order tensors (than in the CCR model) and therefore we begin by writing the full R13 equations in indicial (component-wise) form for a better understanding. After performing linearization about the equilibrium state and nondimensionalization, we recast the resulting system into vectorial/tensorial

notation. The mass, momentum and energy conservation laws which are the evolution equations for the density, velocity and internal energy, read

$$\frac{\partial \tilde{\rho}}{\partial \tilde{t}} + \tilde{v}_l \frac{\partial \tilde{\rho}}{\partial \tilde{x}_l} + \tilde{\rho} \frac{\partial \tilde{v}_l}{\partial \tilde{x}_l} = 0, \qquad (2.22)$$

$$\tilde{\rho} \left( \frac{\partial \tilde{v}_i}{\partial \tilde{t}} + \tilde{v}_l \frac{\partial \tilde{v}_i}{\partial \tilde{x}_l} \right) + \frac{\partial \tilde{p}}{\partial \tilde{x}_i} + \frac{\partial \tilde{\sigma}_{ij}}{\partial \tilde{x}_i} = \tilde{\rho} \tilde{F}_i, \tag{2.23}$$

$$\frac{3}{2}\tilde{\rho}\left(\frac{\partial\tilde{\theta}}{\partial\tilde{t}} + \tilde{v}_l \frac{\partial\tilde{\theta}}{\partial\tilde{x}_l}\right) + \tilde{p}\frac{\partial\tilde{v}_i}{\partial\tilde{x}_i} + \tilde{\sigma}_{ij}\frac{\partial\tilde{v}_i}{\partial\tilde{x}_j} + \frac{\partial\tilde{q}_i}{\partial\tilde{x}_i} = 0, \tag{2.24}$$

and the evolution equations for the stress tensor and heat flux are given by [105, 117]

$$\frac{\partial \tilde{\sigma}_{ij}}{\partial \tilde{t}} + \frac{\partial \tilde{\sigma}_{ij} \tilde{v}_l}{\partial \tilde{x}_l} + \frac{4}{5} \frac{\partial \tilde{q}_{\langle i}}{\partial \tilde{x}_{j \rangle}} + 2\tilde{p} \frac{\partial \tilde{v}_{\langle i}}{\partial \tilde{x}_{j \rangle}} + 2\tilde{\sigma}_{l \langle i} \frac{\partial \tilde{v}_{j \rangle}}{\partial \tilde{x}_l} + \frac{\partial \tilde{m}_{ijl}}{\partial \tilde{x}_l} = -\tilde{\nu}\tilde{\sigma}_{ij}, \tag{2.25}$$

$$\frac{\partial \tilde{q}_i}{\partial \tilde{t}} + \frac{\partial \tilde{q}_i \tilde{v}_l}{\partial \tilde{x}_l} + \tilde{q}_l \frac{\partial \tilde{v}_i}{\partial \tilde{x}_l} - \left(\frac{5}{2} \tilde{p} \delta_{ij} + \tilde{\sigma}_{ij}\right) \frac{1}{\tilde{\rho}} \frac{\partial \tilde{\sigma}_{jl}}{\partial \tilde{x}_l} - \tilde{\sigma}_{ij} \frac{1}{\tilde{\rho}} \frac{\partial \tilde{p}}{\partial \tilde{x}_i} + \frac{5}{2} \tilde{p} \frac{\partial \tilde{\theta}}{\partial \tilde{x}_i}$$

$$+\left(\frac{6}{5}\delta_{\langle ij}\tilde{q}_{l\rangle}+\tilde{m}_{ijl}\right)\frac{\partial\tilde{v}_{j}}{\partial\tilde{x}_{l}}+\frac{1}{2}\frac{\partial\left(7\tilde{\theta}\tilde{\sigma}_{il}+\tilde{R}_{il}\right)}{\partial\tilde{x}_{l}}+\frac{1}{6}\frac{\partial\tilde{\triangle}}{\partial\tilde{x}_{l}}\delta_{il}=-\frac{2}{3}\tilde{\nu}\tilde{q}_{i},\tag{2.26}$$

where  $\tilde{\nu}$  is the collision frequency and the right-hand sides of Eqs. (2.25) and (2.26) are evaluated from the collision integral in the Boltzmann equation for Maxwell molecules. The angular brackets denote the symmetric trace-free part of the tensor (equivalent to overline notation in tensorial form). For instance, the symmetric trace-free part for a rank-2 tensor  $A_{ij}$  reads

$$A_{\langle ij\rangle} = A_{(ij)} - \frac{1}{3} A_{kk} \delta_{ij} = \frac{1}{2} (A_{ij} + A_{ji}) - \frac{1}{3} A_{kk} \delta_{ij}, \tag{2.27}$$

and the symmetric trace-free part for a rank-2 tensor  $B_{ijk}$  reads

$$B_{\langle ijk\rangle} = B_{(ijk)} - \frac{1}{5} \left( B_{(ill)} \delta_{jk} + B_{(ljl)} \delta_{ik} + B_{(llk)} \delta_{ij} \right), \tag{2.28}$$

where

$$B_{(ijk)} = \frac{1}{6} \left( B_{ijk} + B_{ikj} + B_{jik} + B_{jki} + B_{kij} + B_{kji} \right). \tag{2.29}$$

Furthermore,  $\tilde{m}_{ijl}$ ,  $\tilde{R}_{ij}$  and  $\tilde{\Delta}$  are the higher-order moments which do not have any physical meaning associated and fixing  $\tilde{m}_{ijl} = \tilde{R}_{ij} = \tilde{\Delta} = 0$  reduces the Eqs. (2.25) and (2.26) to the original G13 closure relations. The constitutive relations for  $\tilde{m}_{ijl}$ ,  $\tilde{R}_{ij}$  and  $\tilde{\Delta}$  read [105, 117]

$$\tilde{m}_{ijl} = -2\frac{\tilde{p}}{\tilde{\nu}}\tilde{\theta}\frac{\partial(\tilde{\sigma}_{\langle ij}/\tilde{p})}{\partial\tilde{x}_{l\rangle}} + \frac{20}{15\tilde{p}}\tilde{q}_{\langle i}\tilde{\sigma}_{jl\rangle}, \tag{2.30}$$

$$\tilde{R}_{ij} = -\frac{24}{5} \frac{\tilde{p}}{\tilde{\nu}} \theta \frac{\partial (\tilde{q}_{\langle i}/\tilde{p})}{\partial \tilde{x}_{i\rangle}} + \frac{192}{75\tilde{p}} \tilde{q}_{\langle i} \tilde{q}_{j\rangle} + \frac{20}{7\tilde{\rho}} \tilde{\sigma}_{l\langle i} \tilde{\sigma}_{j\rangle l}, \tag{2.31}$$

$$\tilde{\Delta} = -12\frac{\tilde{p}}{\tilde{\nu}}\theta \frac{\partial(\tilde{q}_l/\tilde{p})}{\partial \tilde{x}_l} + \frac{56}{5\tilde{p}}\tilde{q}_l\tilde{q}_l + \frac{5}{\tilde{\rho}}\tilde{\sigma}_{ij}\tilde{\sigma}_{ij}. \tag{2.32}$$

## Linearized steady-state R13 equations:

To nondimensionalize and linearize the equations, perturbations in flow variables from their respective equilibrium states are considered (similarly to above Sec. 2.2.1). The reference equilibrium density and temperature are  $\tilde{\rho}_0$  and  $\tilde{\theta}_0$ , whereas the velocity, stress and heat flux vanish in the equilibrium state. Considering  $\tilde{L}$  as the physical length scale, the dimensionless position vector  $x_i$ , temperature  $\theta$ , pressure p and velocity  $v_i$  read

$$x_i = \frac{\tilde{x}_i}{\tilde{L}}, \quad \theta = \frac{\tilde{\theta}}{\tilde{\theta}_0}, \quad p = \frac{\tilde{p}}{\tilde{p}_0}, \quad v_i = \frac{\tilde{v}_i}{\sqrt{\tilde{\theta}_0}},$$
 (2.33)

respectively and other dimensionless quantities are

$$\sigma_{ij} = \frac{\tilde{\sigma}_{ij}}{\tilde{p}_0}, \quad q_i = \frac{\tilde{q}_i}{\tilde{p}_0 \sqrt{\tilde{\theta}_0}}, \quad m_{ijk} = \frac{\tilde{m}_{ijk}}{\tilde{p}_0 \sqrt{\tilde{\theta}_0}}, \quad R_{ij} = \frac{\tilde{R}_{ij}}{\tilde{p}_0 \tilde{\theta}_0}, \quad \triangle = \frac{\tilde{\triangle}}{\tilde{p}_0 \tilde{\theta}_0}.$$
 (2.34)

Here,  $\sigma_{ij}$  and  $R_{ij}$  are symmetric trace-free second-order tensors, while  $m_{ijk}$  is a symmetric trace-free third-order tensor. The resulting system of the linear, steady state and dimensionless R13 equations read

$$\frac{\partial v_l}{\partial x_l} = 0, (2.35)$$

$$\frac{\partial p}{\partial x_i} + \frac{\partial \sigma_{ij}}{\partial x_j} = 0, \tag{2.36}$$

$$\frac{\partial q_i}{\partial x_i} = 0, (2.37)$$

$$\frac{4}{5} \frac{\partial q_{\langle i}}{\partial x_{i\rangle}} + 2 \frac{\partial v_{\langle i}}{\partial x_{i\rangle}} + \frac{\partial m_{ijl}}{\partial x_{l}} = -\frac{1}{\mathrm{Kn}} \sigma_{ij}, \tag{2.38}$$

$$\frac{5}{2}\frac{\partial\theta}{\partial x_i} + \frac{\partial\sigma_{il}}{\partial\tilde{x}_l} + \frac{1}{2}\frac{\partial R_{il}}{\partial\tilde{x}_l} + \frac{1}{3}\frac{\partial\Delta}{\partial x_i} = -\frac{2}{3\mathrm{Kn}}q_i, \tag{2.39}$$

closed with

$$m_{ijl} = -2\mathrm{Kn}\frac{\partial \sigma_{\langle ij}}{\partial x_{l\rangle}},\tag{2.40}$$

$$R_{ij} = -\frac{24}{5} \frac{\partial q_{\langle i}}{\partial x_{j\rangle}},\tag{2.41}$$

$$\Delta = -12 \operatorname{Kn} \frac{\partial q_l}{\partial x_l},\tag{2.42}$$

where  $\text{Kn} = \sqrt{\tilde{\theta}_0}/(\tilde{\nu}_0\tilde{L})$  is the Knudsen number. Recasting Eqs. (2.35)–(2.42) in vector notation, we obtain

$$\nabla \cdot \boldsymbol{v} = 0, \tag{2.43}$$

$$\nabla p + \nabla \cdot \boldsymbol{\sigma} = \mathbf{0},\tag{2.44}$$

$$\nabla \cdot \boldsymbol{q} = 0, \tag{2.45}$$

$$\frac{4}{5}\overline{\nabla q} + 2\overline{\nabla v} + \nabla \cdot \boldsymbol{m} = -\frac{1}{\mathrm{Kn}}\boldsymbol{\sigma}, \qquad (2.46)$$

$$\frac{5}{2}\nabla\theta + \nabla \cdot \boldsymbol{\sigma} + \frac{1}{2}\nabla \cdot \boldsymbol{R} + \frac{1}{6}\nabla\triangle = -\frac{1}{\operatorname{Kn}}\frac{2}{3}\boldsymbol{q}, \qquad (2.47)$$

with the closure

$$\mathbf{R} = -\frac{24}{5} \operatorname{Kn} \overline{\nabla q}, \tag{2.48}$$

$$m = -2\operatorname{Kn}\overline{\nabla}\sigma,$$
 (2.49)

$$\triangle = -12 \text{Kn} \nabla \cdot \boldsymbol{q}. \tag{2.50}$$

Utilizing Eq. (2.45) in Eq. (2.50), we obtain  $\triangle = 0$ .

## 2.2.3 Boundary conditions

### 2.2.3.1 Boundary conditions for the CCR model

The thermodynamically-consistent boundary conditions complementing the linear CCR model have been derived in Ref. [90]. For a three-dimensional problem, the boundary conditions complementing the linear CCR model are given in Eqs. (4.2a), (4.2b), (4.3a) and (4.3b) of Ref. [90]. Eqs. (4.2a) and (4.2b) of Ref. [90] are the boundary conditions on the normal components of the mass and heat fluxes, respectively, while Eqs. (4.3a) and (4.3b) of Ref. [90] are the boundary conditions on the shear stress—two conditions due to two tangential directions in 3D. In this thesis, we only consider quasi-two-dimensional problems (where one dimension in the problem is much larger than the other two). Since for a quasi-two-dimensional flow in the  $x_1x_2$ -plane, the wall normal direction and one tangential direction are in the  $x_1x_2$ -plane while the other tangential direction is along the  $x_3$ -direction, boundary condition (4.3b) of Ref. [90] is irrelevant in the present work and the superscript '(1)' can be dropped from the unit tangent vector  $t^{(1)}$  in (4.3a) of Ref. [90]

for simplicity. Consequently, the linear-dimensionless boundary conditions complementing the linearized CCR model for a quasi two-dimensional flow read [90]

$$(\boldsymbol{v} - \boldsymbol{v}^{I}) \cdot \boldsymbol{n} = -\eta_{11}(p - p_{\text{sat}} + \boldsymbol{n} \cdot \boldsymbol{\sigma} \cdot \boldsymbol{n}) + \eta_{12}(T - T^{I} + \alpha_{0}\boldsymbol{n} \cdot \boldsymbol{\sigma} \cdot \boldsymbol{n}), \tag{2.51}$$

$$\mathbf{q} \cdot \mathbf{n} = \eta_{12}(p - p_{\text{sat}} + \mathbf{n} \cdot \boldsymbol{\sigma} \cdot \mathbf{n}) - (\eta_{22} + 2\tau_0)(T - T^I + \alpha_0 \mathbf{n} \cdot \boldsymbol{\sigma} \cdot \mathbf{n}),$$
 (2.52)

$$\boldsymbol{t} \cdot \boldsymbol{\sigma} \cdot \boldsymbol{n} = -\varsigma(\boldsymbol{v} - \boldsymbol{v}^I + \alpha_0 \boldsymbol{q}) \cdot \boldsymbol{t}, \tag{2.53}$$

where n and t are the unit normal and tangent vectors, respectively. Furthermore,  $v^I$ ,  $T^I$  and  $p_{\rm sat}$  in boundary conditions (2.51)–(2.53) represent the velocity, temperature and saturation pressure at the interface. Boundary conditions (2.51) and (2.52) determine the evaporative mass flux and heat flux by the difference between the pressure and saturation pressure, and the temperature difference across the interface, respectively, while Eq. (2.53) governs the velocity slip at the boundary. In boundary conditions (2.51)–(2.53),  $\eta_{ij}$ 's, for  $i, j \in \{1, 2\}$  are the Onsager reciprocity coefficients, which from Sone's asymptotic kinetic theory [101] turn out to be

$$\eta_{11} = 0.9134 \sqrt{\frac{2}{\pi}} \frac{\chi}{2 - \chi} \frac{\Theta}{2 - \Theta}, 
\eta_{12} = 0.3915 \sqrt{\frac{2}{\pi}} \frac{\chi}{2 - \chi} \frac{\Theta}{2 - \Theta}, 
\eta_{22} = 0.1678 \sqrt{\frac{2}{\pi}} \frac{\chi}{2 - \chi} \frac{\Theta}{2 - \Theta},$$
(2.54)

with  $\chi$  being the accommodation coefficient which is unity (which also holds true for the diffuse reflection boundary condition). The parameter  $\Theta$  in the above coefficients is the evaporation/condensation coefficient. For canonical boundaries and phase-change boundaries,  $\Theta = 0$  and 1, respectively, are the largely accepted values of  $\Theta$  in the literature. The coefficients  $\tau_0$  and  $\varsigma$ , appearing in Eqs. (2.52) and (2.53), are the temperature-jump and velocity-slip coefficients, which are given by [90]

$$\tau_0 = 0.8503\sqrt{\frac{2}{\pi}} \quad \text{and} \quad \varsigma = 0.8798\sqrt{\frac{2}{\pi}},$$
(2.55)

respectively. It is important to note that the coefficients  $\alpha_0$  in boundary conditions (2.51)–(2.53) are actually the fitting parameters and could be different from the coupling coefficient  $\alpha_0$ . Moreover, the coefficient  $\alpha_0$  in each of boundary conditions (2.51)–(2.53)

could also be different from each other. The only reason that the coefficients  $\alpha_0$  in boundary conditions (2.51)–(2.53) have been taken as the same as the coupling coefficient in the CCR model because the boundary conditions obtained in this way are thermodynamically consistent [88].

## 2.2.3.2 Boundary conditions for the R13 model

The boundary conditions for the R13 equations were derived in Ref. [38] and later extended and refined in Refs. [83, 119] using the Maxwell's accommodation model. Analogously to Sec. 2.2.3.1, the boundary conditions for R13 equations in (quasi) 2D requires one wall normal direction and one tangential direction. The thermodynamically admissible linearized (dimensionless) boundary conditions for the R13 equations in 2D are [113, 118]

$$(\boldsymbol{v} - \boldsymbol{v}^{w}) \cdot \boldsymbol{n} = \epsilon^{w} \sqrt{\frac{2}{\pi}} \frac{\chi}{2 - \chi} \left( p - p^{w} + \boldsymbol{n} \cdot \boldsymbol{\sigma} \cdot \boldsymbol{n} \right),$$
 (2.56)

$$\boldsymbol{n} \cdot \boldsymbol{\sigma} \cdot \boldsymbol{t} = \sqrt{\frac{2}{\pi}} \frac{\chi}{2 - \chi} \left( \boldsymbol{v} - \boldsymbol{v}^{w} + \frac{1}{5} \boldsymbol{q} + \boldsymbol{n} \cdot \boldsymbol{m} \cdot \boldsymbol{n} \right) \cdot \boldsymbol{t},$$
 (2.57)

$$\boldsymbol{n} \cdot \boldsymbol{R} \cdot \boldsymbol{t} = \sqrt{\frac{2}{\pi}} \frac{\chi}{2 - \chi} \left( -(\boldsymbol{v} - \boldsymbol{v}^{\mathrm{w}}) + \frac{11}{5} \boldsymbol{q} - \boldsymbol{n} \cdot \boldsymbol{m} \cdot \boldsymbol{n} \right) \cdot \boldsymbol{t}, \tag{2.58}$$

$$\boldsymbol{q} \cdot \boldsymbol{n} = \sqrt{\frac{2}{\pi}} \frac{\chi}{2 - \chi} \left( 2(\theta - \theta^{w}) + \frac{1}{2} \boldsymbol{n} \cdot \boldsymbol{\sigma} \cdot \boldsymbol{n} + \frac{2}{5} \boldsymbol{n} \cdot \boldsymbol{R} \cdot \boldsymbol{n} \right), \tag{2.59}$$

$$(\boldsymbol{n} \cdot \boldsymbol{m} \cdot \boldsymbol{n}) \cdot \boldsymbol{n} = \sqrt{\frac{2}{\pi}} \frac{\chi}{2 - \chi} \left( -\frac{2}{5} (\theta - \theta^{w}) + \frac{7}{5} \boldsymbol{n} \cdot \boldsymbol{\sigma} \cdot \boldsymbol{n} - \frac{2}{25} \boldsymbol{n} \cdot \boldsymbol{R} \cdot \boldsymbol{n} \right), \quad (2.60)$$

$$\boldsymbol{n} \cdot \left(\frac{1}{2}\boldsymbol{n} \cdot \boldsymbol{m} \cdot \boldsymbol{n} + \boldsymbol{t} \cdot \boldsymbol{m} \cdot \boldsymbol{t}\right) = \sqrt{\frac{2}{\pi}} \frac{\chi}{2 - \chi} \left(\frac{1}{2}\boldsymbol{n} \cdot \boldsymbol{\sigma} \cdot \boldsymbol{n} + \boldsymbol{t} \cdot \boldsymbol{\sigma} \cdot \boldsymbol{t}\right), \tag{2.61}$$

where  $\boldsymbol{n}$  and  $\boldsymbol{t}$  are the unit normal and tangent vectors. In Eq. (2.56),  $\boldsymbol{\epsilon}^{\mathrm{w}}$  is the velocity prescription coefficient used to implement artificial in- and outflow conditions with interface pressure  $p^{\mathrm{w}}$  and velocity  $\boldsymbol{v}^{\mathrm{w}}$ . This boundary condition (2.56) is reduced to the standard boundary condition  $\boldsymbol{v} \cdot \boldsymbol{n} = 0$  for  $\boldsymbol{v}^{\mathrm{w}} = 0$  and  $\boldsymbol{\epsilon}^{\mathrm{w}} = 0$ .

# Chapter 3

# Method of fundamental solutions

The MFS is a meshless, boundary-type numerical technique widely used for solving linear partial differential equations, particularly in problems involving complex geometries and/or complex boundary conditions. The core idea of the MFS is to represent the solution as a linear combination of fundamental solutions—analytic solutions to the governing differential equation with singularities (or source points) located outside the physical domain. By enforcing the prescribed boundary conditions at discrete collocation points on the boundary of the domain, the method transforms the problem into a system of algebraic linear equations for the unknown source strengths.

In this chapter, we describe the basic procedure of the MFS for a general PDE and factors affecting the accuracy of the MFS. We then derive the fundamental solutions for the NSF equations and the CCR model in 2D in order to extend the MFS approach for rarefied gas flows.

# 3.1 The approach

A brief basic working of the MFS is as follows. Let  $w: \mathbb{R}^n \to \mathbb{R}$  be the solution to the problem

$$\mathcal{L}w(\boldsymbol{x}) = 0, \quad \boldsymbol{x} \in \Omega,$$

$$Bw(\boldsymbol{x}) = h(\boldsymbol{x}), \quad \boldsymbol{x} \in \Gamma,$$
(3.1)

where  $\Omega$  is a connected and bounded domain in  $\mathbb{R}^n$  (see Fig. 3.1),  $\mathcal{L}$  is a linear partial differential operator and  $\mathcal{B}$  is the boundary operator. Let the fundamental solution (or the Green's function) of Eq. (3.1)<sub>1</sub> be given by  $G(\boldsymbol{x}, \boldsymbol{x}^s)$ , which satisfies the equation

$$\mathcal{L}G(\boldsymbol{x}, \boldsymbol{x}^s) = \delta(\boldsymbol{x}, \boldsymbol{x}^s). \tag{3.2}$$

Here  $\delta$  is the Dirac-delta function and  $\boldsymbol{x}^s$  is the position vector of a source point. To apply the MFS for solving the boundary value problem (3.1), a fictitious boundary  $\partial \widetilde{\Omega}$  is chosen on which  $N_s$  number of source points are placed, i.e.  $\boldsymbol{x}_i^s \in \widetilde{\Gamma}$ ,  $1 \leq i \leq N_s$ . Owing

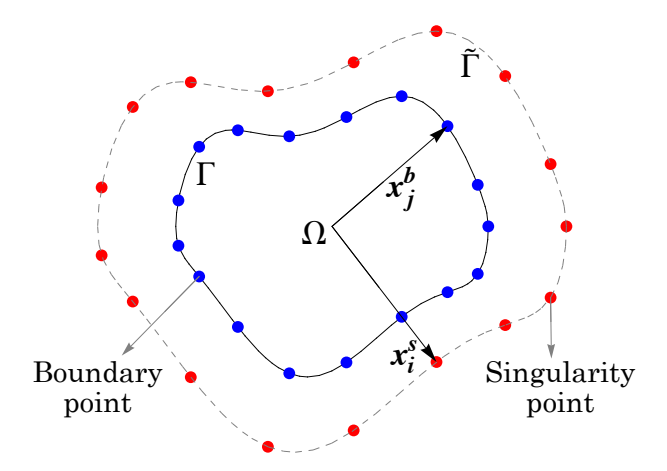


Figure 3.1: Schematic of an arbitrarily shaped domain  $\Omega$  having boundary  $\Gamma$  discretized with boundary nodes, represented by blue symbols. The red symbols denote the singularities or the source points kept on a fictitious boundary  $\tilde{\Gamma}$  outside of the domain.

to the linearity of the problem, the approximated solution at any point  $x \in \Omega$  is given by

$$w(\boldsymbol{x}) = \sum_{i=1}^{N_s} c_i G(\boldsymbol{x}, \boldsymbol{x}_i^s). \tag{3.3}$$

Here,  $c_i$ 's are the constants to be determined by satisfying boundary condition  $(3.1)_2$  at  $N_b$  boundary nodes (or collocation points) discretized over the entire boundary  $\Gamma$ . Therefore for each boundary node  $\boldsymbol{x}_i^b \in \Gamma$ ,

$$\mathcal{B} w(\boldsymbol{x}_j^b) = h(\boldsymbol{x}_j^b), \text{ where } 1 \le j \le N_b.$$
 (3.4)

Plugging Eq. (3.3) in Eq. (3.4), we get a linear system of algebraic equations of order  $N_b \times N_s$ , which is used to determine  $c_i$ 's

$$\sum_{i=1}^{N_s} c_i G(\boldsymbol{x}_j^b, \boldsymbol{x}_i^s) = h(\boldsymbol{x}_j^b), \quad 1 \le j \le N_b,$$
(3.5)

which leads to the following system

$$\begin{bmatrix} G(\boldsymbol{x}_{1}^{b}, \boldsymbol{x}_{1}^{s}) & G(\boldsymbol{x}_{1}^{b}, \boldsymbol{x}_{2}^{s}) & G(\boldsymbol{x}_{1}^{b}, \boldsymbol{x}_{3}^{s}) & \dots & G(\boldsymbol{x}_{1}^{b}, \boldsymbol{x}_{N_{s}}^{s}) \\ G(\boldsymbol{x}_{2}^{b}, \boldsymbol{x}_{1}^{s}) & G(\boldsymbol{x}_{2}^{b}, \boldsymbol{x}_{2}^{s}) & G(\boldsymbol{x}_{2}^{b}, \boldsymbol{x}_{3}^{s}) & \dots & G(\boldsymbol{x}_{2}^{b}, \boldsymbol{x}_{N_{s}}^{s}) \\ \vdots & \vdots & \vdots & \ddots & \vdots \\ G(\boldsymbol{x}_{N_{b}}^{b}, \boldsymbol{x}_{1}^{s}) & G(\boldsymbol{x}_{N_{b}}^{b}, \boldsymbol{x}_{2}^{s}) & G(\boldsymbol{x}_{N_{b}}^{b}, \boldsymbol{x}_{3}^{s}) & \dots & G(\boldsymbol{x}_{N_{b}}^{b}, \boldsymbol{x}_{N_{s}}^{s}) \end{bmatrix} \begin{bmatrix} c_{1} \\ c_{2} \\ \vdots \\ c_{N_{s}} \end{bmatrix} = \begin{bmatrix} h(\boldsymbol{x}_{1}^{b}) \\ h(\boldsymbol{x}_{2}^{b}) \\ \vdots \\ h(\boldsymbol{x}_{N_{b}}^{b}) \end{bmatrix}.$$
(3.6)

System (3.6) is in the form  $\mathcal{MX} = \mathbf{b}$  where the matrix  $\mathcal{M}$  is of the size  $N_b \times N_s$  and is referred to as the collocation matrix. The coefficients  $c_j$ 's can be calculated using a linear

solver if  $\mathcal{M}$  is a square non-singular matrix, and using the method of least squares if  $\mathcal{M}$  is rectangular. Once the coefficients  $c_j$ 's are obtained, the solution at any arbitrary point inside the domain  $\Omega$  can be obtained from Eq. (3.3).

Now, instead of expressing the solution in terms of coefficients  $c_i$ , one may equivalently pose the problem in terms of unknown source strengths embedded in the governing equation. Specifically, consider the modified fundamental solution  $G'(x, x_i^s)$  satisfying

$$\mathcal{L}G'(\boldsymbol{x}, \boldsymbol{x}_i^s) = f_i \,\delta(\boldsymbol{x}, \boldsymbol{x}_i^s),\tag{3.7}$$

where  $f_i$  is the unknown source strength at the source point  $x_i^s$ . By the linearity of the operator  $\mathcal{L}$ , it follows that

$$G'(\boldsymbol{x}, \boldsymbol{x}_i^s) = f_i G(\boldsymbol{x}, \boldsymbol{x}_i^s), \tag{3.8}$$

so that the approximate solution can be written as

$$w(\boldsymbol{x}) = \sum_{i=1}^{N_s} G'(\boldsymbol{x}, \boldsymbol{x}_i^s) = \sum_{i=1}^{N_s} f_i G(\boldsymbol{x}, \boldsymbol{x}_i^s),$$
(3.9)

which is mathematically identical to Eq. (3.3), but interprets the coefficients as strengths of singularities introduced directly into the given equation. This formulation allows for a physical interpretation of the unknowns as source terms and also provides a convenient framework for generalizing the method to moment systems where the fundamental solutions are derived from source-driven equations.

#### 3.1.1 Factors affecting accuracy of the MFS

Accuracy of the MFS depends on several interrelated computational and geometrical parameters. A key consideration is the choice of the number of boundary points and source points. Using more boundary points than source points can improve stability but may reduce accuracy, while using an equal number can increase accuracy but make the system more sensitive to numerical errors. Furthermore, the numerical conditioning of the MFS system matrix plays a pivotal role: exponential growth in the traditional condition number (often exceeding 10<sup>10</sup>) can obscure solutions even with an optimal placement of source points. These factors underscore the need for systematic strategies to balance accuracy and stability of the MFS.

In the MFS, positioning of the singularity points has been a widely-discussed issue in order to achieve accurate results [3, 23, 26, 122] due to the fact that the linear system

resulting from the MFS can have an ill-conditioned coefficient matrix [3], and there is a trade-off between the accuracy and well conditioning. For meshfree methods, including the MFS, Alves [3] states, "In these methods a sort of uncertainty principle occurs—we cannot get both accurate results and good conditioning—one of the two is lost." To address this issue in the MFS, recent studies have introduced the concept of the effective condition number, which provides a more reliable indicator of numerical stability than the traditional condition number [22, 30, 125]. An ill-conditioned matrix has a high condition number. Thus the MFS can yield accurate results even with the collocation matrix having a high condition number. This seems to be implausible intuitively; notwithstanding, it should be noted that the traditional condition number is not adequate for measuring the accuracy and stability of the resulting system since the condition number does not take boundary data into account. For instance, while forming matrix system (3.6), the boundary data  $h(x_k)$  appear in the vector b and not in the collocation matrix  $\mathcal{M}$ . Hence, the (usual) condition number of the matrix  $\mathcal{M}$  is not an adequate parameter to gauge the sensitivity of the MFS toward the location of the source points.

A more accurate estimation of the sensitivity of the MFS toward the location of the source points can be made by the effective condition number, which also takes the boundary data into account (through the right-hand side vector). The concept of the effective condition number has been used by many authors to determine an optimal location of the singularity points by conjecturing a reciprocal relationship between the inaccuracy of the MFS and the effective condition number [22, 30, 125].

Using the singular value decomposition,  $\mathcal{M}$  (having dimensions  $N_b \times N_s$ ) can be decomposed as  $\mathcal{M} = UDV^{\mathsf{T}}$ , where U and V are  $N_b \times N_b$  and  $N_s \times N_s$  orthogonal matrices and D is a  $N_b \times N_s$  diagonal matrix containing the positive singular values in descending order:  $\sigma_1 \geq \sigma_2 \geq \sigma_3 \geq \cdots \geq \sigma_r > 0$ , where  $r \leq \min(N_b, N_s)$ . The traditional condition number for the system is given by

$$\kappa = \frac{\sigma_1}{\sigma_r},\tag{3.10}$$

where  $\sigma_1$  and  $\sigma_r$  represent the largest and smallest (non-zero) singular values of  $\mathcal{M}$ , respectively. Thus, the traditional condition number only depends on the matrix  $\mathcal{M}$  and not the right-hand-side vector  $\boldsymbol{b}$ . On the other hand, the effective condition number is

defined as [22, 125]

$$\kappa_{\text{eff}} = \frac{\|\boldsymbol{b}\|_2}{\sigma_r \|\boldsymbol{\mathcal{X}}\|_2},\tag{3.11}$$

where  $\|.\|_2$  represents the  $\ell^2$ -norm. The effective condition number  $\kappa_{\text{eff}}$  takes into account the right-hand-side vector  $\boldsymbol{b}$  and provides a more accurate measure of stability than the traditional condition number. Thus, we shall utilize  $\kappa_{\text{eff}}$  to justify the location for singularity points in different problems considered in Chapters 4–7.

## 3.2 Fundamental solutions of the NSF equations in 2D

The fundamental solution to the Stokes equations (which are the linearized Navier-Stokes equations in the steady-state) is referred to as the Stokeslet. To account for the effects of energy transfer, which is particularly important in problems involving phase change, one needs to consider the energy balance equation along with the classical Navier-Stokes equations. The Navier–Stokes equations together with the energy balance equation are referred to as the Navier-Stokes-Fourier (NSF) equations. To study the fundamental solutions of the NSF equations, the concept of "thermal Stokeslet" was propounded by Lockerby & Collyer [64]. The Stokeslet and thermal Stokeslet, however, do not incorporate mass exchange in the case of closed boundary due to the Gauss divergence theorem. Therefore, to address processes involving phase change, a new fundamental solution referred to as the "sourcelet"—was obtained in [90] by introducing a point mass source in 3D. It should be noted that the Stokeslet and sourcelet in 2D are different from their counterparts in 3D due to different Green's functions associated with the equations that are used for obtaining the fundamental solutions. To the best of the authors' knowledge, the sourcelet in 2D for phase-change processes does not exist in the literature. Therefore, following the approaches of [64, 90], we derive the fundamental solutions of the NSF equations in 2D in this section. Recall the NSF closure (2.21) [for closing conservation laws (2.19)] in linearized steady state

$$\boldsymbol{\sigma} = -2\mathrm{Kn}\overline{\boldsymbol{\nabla}\boldsymbol{v}},\tag{3.12}$$

$$\boldsymbol{q} = -\frac{c_p \mathrm{Kn}}{\mathrm{Pr}} \boldsymbol{\nabla} T. \tag{3.13}$$

The computation of fundamental solutions to the NSF equations in 2D for processes involving phase change is as follows.

### Case 1: Stokeslet

The Stokeslet is obtained by introducing a point forcing term (given by the Dirac delta function) on the right-hand side of the momentum balance equation and by assuming the process to be isothermal conditions (i.e. by assuming a constant temperature) [64]. Assuming the point force to be of strength f, system (2.19) of the mass, momentum and energy balance equations changes to

$$\nabla \cdot \boldsymbol{v} = 0, \tag{3.14}$$

$$\nabla p + \nabla \cdot \boldsymbol{\sigma} = \boldsymbol{f} \, \delta(\boldsymbol{r}), \tag{3.15}$$

$$\nabla \cdot \mathbf{q} = 0, \tag{3.16}$$

while the NSF closure [Eqs. (3.12) and (3.13)] remains unaltered.

Since the temperature is assumed to be a constant, T being the (dimensionless) perturbation in the temperature from its equilibrium value vanishes and the constitutive relation (3.13) readily yields  $\mathbf{q} = \mathbf{0}$ . Inserting  $\boldsymbol{\sigma}$  from the constitutive relation (3.12) in Eq. (3.15), we obtain

$$\nabla p - \operatorname{Kn} \Delta v = f \, \delta(r). \tag{3.17}$$

On taking the divergence of this equation and exploiting Eq. (3.14), we obtain

$$\Delta p = \boldsymbol{f} \cdot \boldsymbol{\nabla} \delta(\boldsymbol{r}). \tag{3.18}$$

From the fundamental solution of Laplace equation in 2D, it turns out that

$$\delta(\mathbf{r}) = \Delta\left(\frac{\log r}{2\pi}\right),\tag{3.19}$$

which on substituting in Eq. (3.18) yields

$$p(\mathbf{r}) = \frac{\mathbf{f} \cdot \mathbf{r}}{2\pi r^2}.\tag{3.20}$$

Now, inserting the values of  $\delta(\mathbf{r})$  and p from Eqs. (3.19) and (3.20) into Eq. (3.17), we obtain

$$\Delta \boldsymbol{v} = \frac{1}{\mathrm{Kn}} \boldsymbol{f} \cdot (\boldsymbol{\nabla} \boldsymbol{\nabla} - \boldsymbol{I} \Delta) \left( \frac{\log r}{2\pi} \right). \tag{3.21}$$

This leads to

$$\boldsymbol{v} = \frac{1}{\mathrm{Kn}} \boldsymbol{f} \cdot (\boldsymbol{\nabla} \boldsymbol{\nabla} - \boldsymbol{I} \Delta) \gamma(\boldsymbol{r}), \tag{3.22}$$

where  $\gamma(\mathbf{r}) = r^2(\log r)/(8\pi)$  is the fundamental solution of biharmonic equation [98]. On simplification, Eq. (3.22) yields

$$\boldsymbol{v} = \frac{1}{8\pi \text{Kn}} \boldsymbol{f} \cdot \left[ \frac{2\boldsymbol{r}\boldsymbol{r}}{r^2} - (2\log r - 1)\boldsymbol{I} \right]. \tag{3.23}$$

Substituting the expression for v from Eq. (3.23) into constitutive relation (3.12), the stress tensor turns out to be

$$\sigma = -\frac{\mathbf{f} \cdot \mathbf{r}}{2\pi} \left( \frac{\mathbf{I}}{r^2} - \frac{2\mathbf{r}\mathbf{r}}{r^4} \right). \tag{3.24}$$

## Case 2: Thermal Stokeslet

The thermal Stokeslet is obtained when the energy balance equation in the system of the NSF equations is subjected to a point heat source under the stationary and isobaric conditions [64]. Assuming the point heat source to be of strength g, system (2.43)–(2.45) of the mass, momentum and energy balance equations changes to

$$\nabla \cdot \boldsymbol{v} = 0, \tag{3.25}$$

$$\nabla p + \nabla \cdot \boldsymbol{\sigma} = \mathbf{0},\tag{3.26}$$

$$\nabla \cdot \boldsymbol{q} = g \, \delta(\boldsymbol{r}), \tag{3.27}$$

while the NSF closure [Eqs. (3.12) and (3.13)] again remains unchanged. Under the assumption of flow being stationary,

$$v = 0, (3.28)$$

using which the constitutive relation (3.12) gives

$$\sigma = 0. \tag{3.29}$$

Moreover, under isobaric condition,

$$p = 0. (3.30)$$

Inserting q from the constitutive relation (3.13) into Eq. (3.27), we obtain

$$-\frac{c_p \operatorname{Kn}}{\operatorname{Pr}} \Delta T = g \,\delta(\mathbf{r}). \tag{3.31}$$

Again, from the fundamental solution of Laplace equation in 2D,  $\delta(\mathbf{r})$  is given by Eq. (3.19). Therefore, using Eq. (3.19), we obtain

$$T = -\frac{g}{2\pi} \frac{\Pr}{c_p \operatorname{Kn}} \log r. \tag{3.32}$$

Substituting this in constitutive relation (3.13), we obtain

$$q = \frac{g}{2\pi} \frac{\mathbf{r}}{r^2}.\tag{3.33}$$

## Case 3: Sourcelet

The sourcelet is obtained by introducing a point mass source on the right-hand side of the mass balance equation in the system of the NSF equations under the isothermal conditions [90]. The case needs to be considered for the phase change processes because the mass of the vapor is not conserved due to phase change. Assuming the point mass source to be of strength h, system (2.43)–(2.45) of the mass, momentum and energy balance equations changes to

$$\nabla \cdot \boldsymbol{v} = h \, \delta(\boldsymbol{r}), \tag{3.34}$$

$$\nabla p + \nabla \cdot \boldsymbol{\sigma} = \mathbf{0},\tag{3.35}$$

$$\nabla \cdot \mathbf{q} = 0, \tag{3.36}$$

while the NSF closure [Eqs. (3.12) and (3.13)] again remains unchanged.

Following [90], we solve this system with the help of the Fourier transformation. The Fourier transformation of the function  $F(\mathbf{r})$  is defined as

$$\mathcal{F}[F(\mathbf{r})] = \hat{F}(\mathbf{k}) := \int_{\mathbb{R}^2} F(\mathbf{r}) e^{i\mathbf{k}\cdot\mathbf{r}} d\mathbf{r}$$
(3.37)

and the corresponding inverse Fourier transformation defined as

$$\mathcal{F}^{-1}[\hat{F}(\boldsymbol{k})] = F(\boldsymbol{r}) := \frac{1}{(2\pi)^2} \int_{\mathbb{R}^2} \hat{F}(\boldsymbol{k}) e^{-i\boldsymbol{k}\cdot\boldsymbol{r}} d\boldsymbol{k}, \qquad (3.38)$$

where  $\hat{F}$  denotes the Fourier transform of F. Here, i is the imaginary unit and k is the wavevector in the spatial-frequency domain. Taking the Fourier transforms of Eqs. (3.34),

(3.35) and (3.12), we obtain

$$\mathbf{k} \cdot \hat{\mathbf{v}} = i h, \tag{3.39}$$

$$\hat{p}\,\mathbf{k} + \hat{\boldsymbol{\sigma}}\cdot\mathbf{k} = \mathbf{0},\tag{3.40}$$

$$\hat{\boldsymbol{\sigma}} = i \operatorname{Kn} \left[ \hat{\boldsymbol{v}} \boldsymbol{k} + \boldsymbol{k} \hat{\boldsymbol{v}} - (\boldsymbol{k} \cdot \hat{\boldsymbol{v}}) \boldsymbol{I} \right], \tag{3.41}$$

respectively. Solving these equations, we obtain

$$\hat{\boldsymbol{v}} = i h \frac{\boldsymbol{k}}{k^2}, \quad \hat{\boldsymbol{\sigma}} = -2 \operatorname{Kn} h \left( \frac{\boldsymbol{k} \boldsymbol{k}}{k^2} - \frac{1}{2} \boldsymbol{I} \right) \quad \text{and} \quad \hat{p} = \operatorname{Kn} h.$$
 (3.42)

Taking the inverse Fourier transforms of the quantities in Eq. (3.42), we obtain

$$\mathbf{v} = i h \mathcal{F}^{-1} \left( \frac{\mathbf{k}}{k^2} \right) = \frac{h}{2\pi} \frac{\mathbf{r}}{r^2}, \tag{3.43}$$

$$\boldsymbol{\sigma} = -2\operatorname{Kn}h\,\mathcal{F}^{-1}\left(\frac{\boldsymbol{k}\boldsymbol{k}}{k^2} - \frac{1}{2}\boldsymbol{I}\right) = \frac{h}{\pi}\operatorname{Kn}\left(\frac{2\boldsymbol{r}\boldsymbol{r}}{r^4} - \frac{\boldsymbol{I}}{r^2}\right),\tag{3.44}$$

$$p = 0. (3.45)$$

Similarly, taking the Fourier transforms of Eqs. (3.36) and (3.13), we obtain

$$\mathbf{k} \cdot \hat{\mathbf{q}} = 0, \tag{3.46}$$

$$\hat{\boldsymbol{q}} = i \frac{5}{2} \frac{\mathrm{Kn}}{\mathrm{Pr}} \boldsymbol{k} \hat{T}, \tag{3.47}$$

respectively. The inverse Fourier transforms of these equations readily lead to

$$q = 0 \quad \text{and} \quad T = 0. \tag{3.48}$$

Combining the three cases we obtain the fundamental solutions for the NSF equations, which read

$$\boldsymbol{v}(\boldsymbol{r}) = \frac{\boldsymbol{f}}{8\pi \mathrm{Kn}} \cdot \left[ \frac{2\boldsymbol{r}\boldsymbol{r}}{r^2} - (2\ln r - 1)\boldsymbol{I} \right] + \frac{h\,\boldsymbol{r}}{2\pi r^2},\tag{3.49}$$

$$p(\mathbf{r}) = \frac{\mathbf{f} \cdot \mathbf{r}}{2\pi r^2},\tag{3.50}$$

$$\boldsymbol{\sigma}(\boldsymbol{r}) = \frac{\boldsymbol{f} \cdot \boldsymbol{r} + 2\mathrm{Kn}h}{2\pi} \left[ \frac{2\boldsymbol{r}\boldsymbol{r}}{r^4} - \frac{\boldsymbol{I}}{r^2} \right], \tag{3.51}$$

$$T(\mathbf{r}) = -\frac{\Pr}{c_p \operatorname{Kn}} \frac{g \ln r}{2\pi},\tag{3.52}$$

$$q(r) = \frac{g}{2\pi} \frac{r}{r^2}.$$
 (3.53)

## 3.3 Fundamental solutions of the CCR model

In this section, we derive the fundamental solutions of the CCR model in 2D from scratch. The derivation is presented in the indicial notation for a better understanding. For two-dimensional flows, let us say in the  $x_1x_2$ -plane, the field variables do not change in the direction perpendicular to the plane of the flow, i.e. they do not change along the  $x_3$ -direction. As a result, the CCR model [Eqs. (2.19)–(2.20)] for a two-dimensional flow in the  $x_1x_2$ -plane reduces to

$$\frac{\partial v_i}{\partial x_i} = 0, (3.54)$$

$$\frac{\partial p}{\partial x_i} + \frac{\partial \sigma_{ij}}{\partial x_j} = 0, \tag{3.55}$$

$$\frac{\partial q_i}{\partial x_i} = 0, (3.56)$$

$$\sigma_{ij} = -2\operatorname{Kn}\left[\frac{1}{2}\left(\frac{\partial v_i}{\partial x_j} + \frac{\partial v_j}{\partial x_i}\right) - \frac{1}{3}\delta_{ij}\frac{\partial v_\ell}{\partial x_\ell}\right] - 2\alpha_0\operatorname{Kn}\left[\frac{1}{2}\left(\frac{\partial q_i}{\partial x_j} + \frac{\partial q_j}{\partial x_i}\right) - \frac{1}{3}\delta_{ij}\frac{\partial q_\ell}{\partial x_\ell}\right],$$
(3.57)

$$q_i = -\frac{c_p \operatorname{Kn}}{\operatorname{Pr}} \left( \frac{\partial T}{\partial x_i} + \alpha_0 \frac{\partial \sigma_{ij}}{\partial x_j} \right), \tag{3.58}$$

where the indices i, j and  $\ell$  can take the values 1 and 2 only,  $\delta_{ij}$  is the Kronecker delta and the Einstein summation applies over the repeated indices in a term. It may be noted that Eq. (3.55) represents two equations: for i=1 the momentum balance equation in the  $x_1$ -direction and for i=2 the momentum balance equation in the  $x_2$ -direction, and that the momentum balance equation in the  $x_3$ -direction is identically satisfied. It is also worthwhile noting that  $\sigma_{11} + \sigma_{22} = 0$  in view of Eqs. (3.54) and (3.56), which is consistent with the fact that the stress tensor  $\sigma$  is tracefree because  $\sigma_{33} = 0$  for two-dimensional flows in the  $x_1x_2$ -plane. Thus, the CCR model for a two-dimensional flow in the  $x_1x_2$ -plane [Eqs. (3.54) and (3.58)] essentially consists of the unknown field variables  $v_1, v_2, p, T, \sigma_{11}, \sigma_{12}, q_1, q_2$ .

To derive the fundamental solutions, we add a Dirac delta forcing term of strength  $f_i$   $(i \in \{1, 2\})$  on the right-hand side of the momentum balance equation (3.55) to represent a (vector) point force and a point heat source of strength g on the right-hand side of the energy balance equation (3.56). Furthermore, to deal with phase-change effects at the

liquid-vapor interface, a point mass source of strength h is also added on the right-hand side of the mass balance equation (3.54). For determining the fundamental solutions of a system of partial differential equations, it is customary to consider only one point source at a time and then to superimpose the solutions obtained by taking each point source at a time in order to incorporate the effects of all point sources; see, e.g., Refs. [64, 90] and the fundamental solutions for the NSF equations in previous section. Nevertheless, we take all three point sources  $\mathbf{f} \equiv (f_1, f_2)^\mathsf{T}$ , g and h simultaneously and solve the resulting system of equations altogether. We have verified—shown in the Appendix B—that this procedure also yields exactly the same solution as that obtained by superimposing the solutions obtained by solving the systems separately with one point source at a time.

To determine the fundamental solutions of the CCR model in 2D, the mass, momentum and energy balance equations (3.54)–(3.56) are written with the point source terms on their right-hand sides. These equations read

$$\frac{\partial v_i}{\partial x_i} = h \,\delta(\mathbf{r}),\tag{3.59}$$

$$\frac{\partial p}{\partial x_i} + \frac{\partial \sigma_{ij}}{\partial x_j} = f_i \, \delta(\mathbf{r}), \tag{3.60}$$

$$\frac{\partial q_i}{\partial x_i} = g \,\delta(\mathbf{r}),\tag{3.61}$$

where  $\mathbf{r} = (x_1, x_2)^{\mathsf{T}}$ . Equations (3.59)–(3.61) are closed with the CCR (3.57) and (3.58). We solve the system of Eqs. (3.59)–(3.61), (3.57) and (3.58) using the Fourier transformation [defined in Eqs. (3.37)]. Applying the Fourier transformation in Eqs. (3.59)–(3.61), (3.57) and (3.58) and using the fact that  $\mathcal{F}[\delta(\mathbf{r})] = 1$ , we obtain  $(i, j, \ell \in \{1, 2\})$ 

$$k_i \hat{v}_i = i h, \tag{3.62}$$

$$k_i \hat{p} + k_j \hat{\sigma}_{ij} = i f_i, \tag{3.63}$$

$$k_i \hat{q}_i = i g, \tag{3.64}$$

$$\hat{\sigma}_{ij} = i \operatorname{Kn} \left[ k_j (\hat{v}_i + \alpha_0 \hat{q}_i) + k_i (\hat{v}_j + \alpha_0 \hat{q}_j) - \frac{2}{3} \delta_{ij} k_\ell (\hat{v}_\ell + \alpha_0 \hat{q}_\ell) \right], \tag{3.65}$$

$$\hat{q}_i = i \frac{c_p \operatorname{Kn}}{\operatorname{Pr}} \left( k_i \hat{T} + \alpha_0 k_j \hat{\sigma}_{ij} \right), \tag{3.66}$$

where the variables with hat are the Fourier transforms of the corresponding field variables. Using Eqs. (3.62) and (3.64), Eq. (3.65) simplifies to

$$\hat{\sigma}_{ij} = i \operatorname{Kn} \left[ k_j (\hat{v}_i + \alpha_0 \hat{q}_i) + k_i (\hat{v}_j + \alpha_0 \hat{q}_j) \right] + \frac{2}{3} \delta_{ij} \operatorname{Kn}(h + \alpha_0 g). \tag{3.67}$$

Multiplying the above equation with  $k_j$  and  $k_i k_j$ , we obtain

$$k_j \hat{\sigma}_{ij} = i \operatorname{Kn} k^2 (\hat{v}_i + \alpha_0 \hat{q}_i) - \frac{1}{3} \operatorname{Kn} k_i (h + \alpha_0 g), \tag{3.68}$$

$$k_i k_j \hat{\sigma}_{ij} = -\frac{4}{3} \operatorname{Kn} k^2 (h + \alpha_0 g), \tag{3.69}$$

respectively, where  $k_i k_i = |k_i|^2 = k^2$  has been used. Multiplying Eq. (3.66) with  $k_i$  and exploiting Eqs. (3.64) and (3.69), we obtain

$$\hat{T} = \frac{\Pr}{c_p \operatorname{Kn}} \frac{g}{k^2} + \frac{4}{3} \alpha_0 \operatorname{Kn}(h + \alpha_0 g). \tag{3.70}$$

Again, multiplying Eq. (3.63) with  $k_i$  and exploiting Eq. (3.69), we obtain

$$\hat{p} = i \frac{k_i f_i}{k^2} + \frac{4}{3} \text{Kn}(h + \alpha_0 g). \tag{3.71}$$

Now, from Eqs. (3.63) and (3.71), one can easily write

$$k_j \hat{\sigma}_{ij} = i f_i - i \frac{k_i k_j f_j}{k^2} - \frac{4}{3} k_i \text{Kn}(h + \alpha_0 g).$$
 (3.72)

Substituting the value of  $\hat{T}$  from Eq. (3.70) and the value of  $k_j \hat{\sigma}_{ij}$  from Eq. (3.72) into Eq. (3.66), we obtain

$$\hat{q}_i = i \frac{k_i g}{k^2} - \frac{c_p \operatorname{Kn}}{\operatorname{Pr}} \alpha_0 f_j \left( \delta_{ij} - \frac{k_i k_j}{k^2} \right). \tag{3.73}$$

Now, from Eqs. (3.68), (3.72) and (3.73)

$$\hat{v}_i = \frac{f_j}{\operatorname{Kn}} \left( \frac{\delta_{ij}}{k^2} - \frac{k_i k_j}{k^4} \right) + \frac{c_p \operatorname{Kn}}{\operatorname{Pr}} \alpha_0^2 f_j \left( \delta_{ij} - \frac{k_i k_j}{k^2} \right) + i \frac{k_i h}{k^2}. \tag{3.74}$$

Finally, using Eqs. (3.73) and (3.74) in Eq. (3.65), we obtain

$$\hat{\sigma}_{ij} = i f_{\ell} \left( \frac{k_j \delta_{i\ell} + k_i \delta_{j\ell}}{k^2} - 2 \frac{k_i k_j k_{\ell}}{k^4} \right) - 2 \operatorname{Kn} \left( \frac{k_i k_j}{k^2} - \frac{\delta_{ij}}{3} \right) (h + \alpha_0 g). \tag{3.75}$$

Applying the inverse Fourier transformation in Eqs. (3.70), (3.71) and (3.73)–(3.75) with the help of the formulae derived in Appendix A, the field variables turn out to be

$$v_{i} = \frac{f_{j}}{\text{Kn}} \left( \frac{x_{i}x_{j}}{4\pi r^{2}} - \frac{2\ln r - 1}{8\pi} \delta_{ij} \right) + \frac{c_{p}\text{Kn}}{\text{Pr}} \alpha_{0}^{2} \frac{f_{j}}{2\pi} \left( \frac{2x_{i}x_{j}}{r^{4}} - \frac{\delta_{ij}}{r^{2}} \right) + \frac{hx_{i}}{2\pi r^{2}}, \tag{3.76}$$

$$q_{i} = \frac{g}{2\pi} \frac{x_{i}}{r^{2}} - \frac{c_{p} \operatorname{Kn}}{\operatorname{Pr}} \alpha_{0} \frac{f_{j}}{2\pi} \left( \frac{2x_{i} x_{j}}{r^{4}} - \frac{\delta_{ij}}{r^{2}} \right), \tag{3.77}$$

$$p = \frac{f_i x_i}{2\pi r^2},\tag{3.78}$$

$$T = -\frac{\Pr}{c_p \operatorname{Kn}} \frac{g \ln r}{2\pi},\tag{3.79}$$

$$\sigma_{ij} = \frac{f_{\ell}x_{\ell} + 2\operatorname{Kn}(h + \alpha_0 g)}{2\pi} \left(\frac{2x_i x_j}{r^4} - \frac{\delta_{ij}}{r^2}\right), \tag{3.80}$$

where  $r = |x_i|$  and  $i, j, \ell \in \{1, 2\}$ . The field variables in Eqs. (3.76)–(3.80) are the fundamental solutions of the linearized CCR model in 2D. These fundamental solutions in the vectorial/tensorial notation can be written as

$$\boldsymbol{v}(\boldsymbol{r}) = \frac{\boldsymbol{f} \cdot \boldsymbol{A}(\boldsymbol{r})}{8\pi \mathrm{Kn}} + \frac{1}{2\pi} \frac{c_p \mathrm{Kn}}{\mathrm{Pr}} \alpha_0^2 \boldsymbol{f} \cdot \boldsymbol{B}(\boldsymbol{r}) + \frac{h \, \boldsymbol{r}}{2\pi r^2}, \tag{3.81}$$

$$p(\mathbf{r}) = \frac{\mathbf{f} \cdot \mathbf{r}}{2\pi r^2},\tag{3.82}$$

$$\sigma(r) = \frac{f \cdot r + 2Kn(h + g\alpha_0)}{2\pi} B(r), \tag{3.83}$$

$$T(\mathbf{r}) = -\frac{\Pr}{c_p \operatorname{Kn}} \frac{g \ln r}{2\pi},\tag{3.84}$$

$$q(r) = \frac{g}{2\pi} \frac{r}{r^2} - \frac{1}{2\pi} \frac{c_p \text{Kn}}{\text{Pr}} \alpha_0 \mathbf{f} \cdot \mathbf{B}(\mathbf{r}), \qquad (3.85)$$

where  $r = |\mathbf{r}|$  and

$$\boldsymbol{A}(\boldsymbol{r}) = \frac{2\boldsymbol{r}\boldsymbol{r}}{r^2} - (2\ln r - 1)\boldsymbol{I},\tag{3.86}$$

$$\boldsymbol{B}(\boldsymbol{r}) = \frac{2\boldsymbol{r}\boldsymbol{r}}{r^4} - \frac{\boldsymbol{I}}{r^2}.$$
 (3.87)

Note that, in Eqs. (3.81)-(3.87),

$$\mathbf{f} = \begin{bmatrix} f_1 \\ f_2 \end{bmatrix}, \quad \mathbf{v}(\mathbf{r}) = \begin{bmatrix} v_1(\mathbf{r}) \\ v_2(\mathbf{r}) \end{bmatrix}, \quad \mathbf{q}(\mathbf{r}) = \begin{bmatrix} q_1(\mathbf{r}) \\ q_2(\mathbf{r}) \end{bmatrix},$$

$$\mathbf{\sigma}(\mathbf{r}) = \begin{bmatrix} \sigma_{11}(\mathbf{r}) & \sigma_{12}(\mathbf{r}) \\ \sigma_{12}(\mathbf{r}) & -\sigma_{11}(\mathbf{r}) \end{bmatrix}, \quad \mathbf{I} = \begin{bmatrix} 1 & 0 \\ 0 & 1 \end{bmatrix}.$$
(3.88)

It is also worthwhile noticing that the fundamental solutions for the linearized NSF and G13 equations in 2D can be obtained directly from Eqs. (3.81)–(3.85) by taking  $\alpha_0 = 0$  and  $\alpha_0 = 2/5$ , respectively.

### 3.3.1 Example implementation

To implement the fundamental solutions (3.81)–(3.85) in the MFS, we describe the construction of a system of algebraic equations through the problem of a rarefied gas flow past a complex geometry as depicted in Fig. 3.2. As an example, the geometry of the object in Fig. 3.2 is mathematically defined in the parametric form as

$$(x,y) = \left(\frac{5}{4}a\cos\theta, \frac{1}{4}a(5-\cos 5\theta)\sin\theta\right)$$
(3.89)

with  $0 \le \theta \le 2\pi$  and  $a \le 1$  being the scaling factor. As mentioned in Sec. 3.1.1, the location of the singularity points is a major concern as the results obtained from the MFS are highly sensitive toward the location of singularities [3, 23, 26]. There are two most common ways of distributing singularities in the MFS. One way is to place the singularities on a fictitious boundary of a very simple shape—irrespective of the shape of the object—with just one parameter to control; for example, on a circle in the two-dimensional case and on a sphere in the three-dimensional case, and the radius of the circle or sphere would be the controlling parameter. Another way is to recreate a dilated (or shrunk) fictitious boundary, which has the same shape as the boundary of the original object and to place

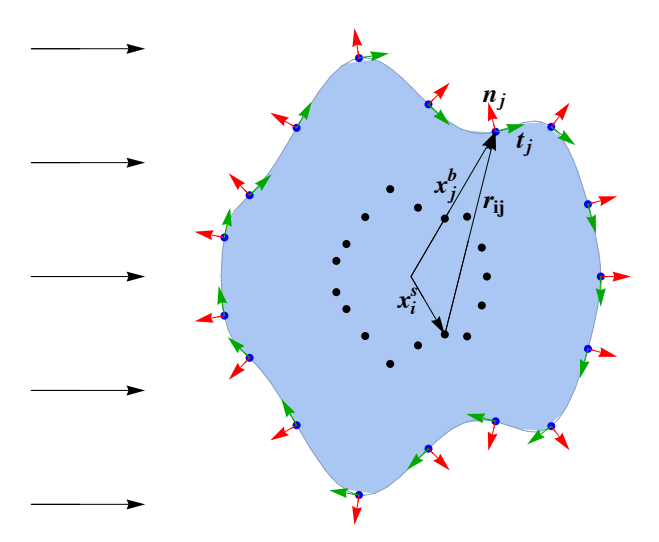


Figure 3.2: Schematic of a flow past an object of an arbitrary shape depicting the boundary discretization and the placement of singularities outside the flow domain. The red and blue arrows at each boundary node depict the normal (pointing toward the flow domain) and tangential directions at that node, respectively.

the singularities on this fictitious boundary [26, 61]—similarly to that shown in Fig. 3.2 as well. The latter is also easy if the original boundary of the object can be described by a set of parametric equations having only a single controlling parameter, the dilation factor. For illustration purposes, we have taken the fictitious boundary to be of the same shape as the original boundary in Fig. 3.2.

Let  $N_b$  be the number of the discretized boundary nodes and  $N_s$  the number of singularity points. The boundary nodes and the singularities are placed at equispaced angles  $\theta$  on the original and the fictitious boundary, respectively, and the distance between both boundaries can be varied by changing the value of the dilation factor a. It may be noted that singularities need not be placed at equispaced angles in principle; nonetheless, we have done so for the sake of simplicity. Let  $x_i^s$  and  $x_i^b$  be the position vectors of the  $i^{
m th}$  singularity site and the  $j^{
m th}$  boundary node, respectively. Then the position vector from the  $i^{\text{th}}$  singularity site to any position  $\boldsymbol{x}$  in the domain is  $\boldsymbol{r}_i = \boldsymbol{x} - \boldsymbol{x}_i^s$  and the position vector from the  $i^{\text{th}}$  singularity site to the  $j^{\text{th}}$  boundary node is  $\boldsymbol{r}_{ij} = \boldsymbol{x}_j^b - \boldsymbol{x}_i^s$ . It is important to note that the subscripts i and j are now being used for denoting the  $i^{\rm th}$  singularity site and  $j^{\rm th}$  boundary node and consequently, the repetition of indices henceforth shall not imply the Einstein summation per se, unless stated otherwise (particularly, in Appendix A, wherein the Einstein summation does hold over the repeated indices). Since the point sources f, g and h are to be put at each singularity site, there are four degrees of freedom corresponding to each singularity point (two scalars q and hfrom the point heat and mass sources, and two components  $f_1$  and  $f_2$  of the point force vector  $\boldsymbol{f} = \begin{bmatrix} f_1 & f_2 \end{bmatrix}^\mathsf{T}$ ). In total, we have  $4 \times N_s$  unknowns, which are determined typically by satisfying the boundary conditions at the boundary points. Once the location of the singularity points is decided, the next step in the implementation of the MFS is superposition of the fundamental solutions associated with each singularity site, which makes sense because of the linearity of equations and gives the value of the field variables at the  $j^{\text{th}}$  boundary node. Superimposing the fundamental solutions (3.81)–(3.85) for each singularity site, the field variables at the  $j^{th}$  boundary node read

$$\boldsymbol{v}_{j} = \sum_{i=1}^{N_{s}} \left[ \frac{\boldsymbol{f}_{i} \cdot \boldsymbol{A}(\boldsymbol{r}_{ij})}{8\pi \operatorname{Kn}} + \frac{1}{2\pi} \frac{c_{p} \operatorname{Kn}}{\operatorname{Pr}} \alpha_{0}^{2} \boldsymbol{f}_{i} \cdot \boldsymbol{B}(\boldsymbol{r}_{ij}) + \frac{h_{i} \boldsymbol{r}_{ij}}{2\pi r_{ij}^{2}} \right],$$
(3.90)

$$p_j = \sum_{i=1}^{N_s} \frac{\boldsymbol{f}_i \cdot \boldsymbol{r}_{ij}}{2\pi r_{ij}^2},\tag{3.91}$$

$$\boldsymbol{\sigma}_{j} = \sum_{i=1}^{N_{s}} \frac{\boldsymbol{f}_{i} \cdot \boldsymbol{r}_{ij} + 2\operatorname{Kn}\left(h_{i} + g_{i} \alpha_{0}\right)}{2\pi} \boldsymbol{B}(\boldsymbol{r}_{ij}), \tag{3.92}$$

$$T_j = -\sum_{i=1}^{N_s} \frac{\Pr}{c_p \text{Kn}} \frac{g_i \ln r_{ij}}{2\pi},$$
 (3.93)

$$\boldsymbol{q}_{j} = \sum_{i=1}^{N_{s}} \left[ \frac{g_{i}}{2\pi} \frac{\boldsymbol{r}_{ij}}{r_{ij}^{2}} - \frac{1}{2\pi} \frac{c_{p} \operatorname{Kn}}{\operatorname{Pr}} \alpha_{0} \boldsymbol{f}_{i} \cdot \boldsymbol{B}(\boldsymbol{r}_{ij}) \right], \tag{3.94}$$

where  $r_{ij} = |\mathbf{r}_{ij}|$ ;  $\mathbf{f}_i = \begin{bmatrix} f_1 & f_2 \end{bmatrix}^\mathsf{T}$ ,  $g_i$  and  $h_i$  are the point force (vector), point heat source and point mass source, respectively, applied on the  $i^{\text{th}}$  singularity site; and

$$\boldsymbol{A}(\boldsymbol{r}_{ij}) = \frac{2\boldsymbol{r}_{ij}\boldsymbol{r}_{ij}}{r_{ij}^2} - (2\ln r_{ij} - 1)\boldsymbol{I}, \qquad (3.95)$$

$$\boldsymbol{B}(\boldsymbol{r}_{ij}) = \frac{2\boldsymbol{r}_{ij}\boldsymbol{r}_{ij}}{r_{ij}^4} - \frac{\boldsymbol{I}}{r_{ij}^2}.$$
 (3.96)

This system is solved for the unknowns  $f_{1i}, f_{2i}, g_i, h_i, i \in \{1, 2, 3, ..., N_s\}$  by employing the boundary conditions at each boundary node. Once the unknowns  $f_{1i}, f_{2i}, g_i, h_i$  for  $i \in \{1, 2, 3, ..., N_s\}$  are found, the flow variables at any position  $\boldsymbol{x}$  in the flow domain can be determined simply by dropping the subscript 'j' everywhere in Eqs. (3.90)–(3.94). Hence, the fundamental solutions of the CCR model in 2D at any point located by the position vector  $\boldsymbol{x}$  in the flow domain are given by

$$\boldsymbol{v} = \sum_{i=1}^{N_s} \left[ \frac{\boldsymbol{f}_i \cdot \boldsymbol{A}(\boldsymbol{r}_i)}{8\pi \text{Kn}} + \frac{1}{2\pi} \frac{c_p \text{Kn}}{\text{Pr}} \alpha_0^2 \boldsymbol{f}_i \cdot \boldsymbol{B}(\boldsymbol{r}_i) + \frac{h_i \, \boldsymbol{r}_i}{2\pi r_i^2} \right], \tag{3.97}$$

$$p = \sum_{i=1}^{N_s} \frac{\mathbf{f}_i \cdot \mathbf{r}_i}{2\pi r_i^2},\tag{3.98}$$

$$\boldsymbol{\sigma} = \sum_{i=1}^{N_s} \frac{\boldsymbol{f}_i \cdot \boldsymbol{r}_i + 2\operatorname{Kn}(h_i + g_i \alpha_0)}{2\pi} \boldsymbol{B}(\boldsymbol{r}_i), \tag{3.99}$$

$$T = -\sum_{i=1}^{N_s} \frac{\Pr}{c_p \operatorname{Kn}} \frac{g_i \ln r_i}{2\pi}, \tag{3.100}$$

$$\boldsymbol{q} = \sum_{i=1}^{N_s} \left[ \frac{g_i}{2\pi} \frac{\boldsymbol{r}_i}{r_i^2} - \frac{1}{2\pi} \frac{c_p \text{Kn}}{\text{Pr}} \alpha_0 \boldsymbol{f}_i \cdot \boldsymbol{B}(\boldsymbol{r}_i) \right]. \tag{3.101}$$

The above procedure to evaluate flow variables works for any geometry and we have implemented this in a numerical framework. We shall elaborate on the placement of boundary nodes and source points, formation and solution of the system separately corresponding to the different problems in the following chapters.

# Chapter 4

# Application of the CCR-MFS framework for internal flow problems

In this chapter, we implement the fundamental solutions of the CCR model derived in Sec. 3.3 by solving some internal flow problems. The CCR-MFS framework developed for these problems is validated against benchmark solutions available in the literature.

## 4.1 Vapor flow confined between two coaxial cylinders

For the validation of the developed numerical framework, we revisit the problem of a rarefied vapor flow confined between two concentric cylinders. The same problem was investigated by Onishi [77] with the linearized BGK model and diffuse-reflection boundary conditions.

## 4.1.1 Problem description

Let us consider a moderately rarefied vapor confined between the condensed phases of two concentric infinitely long circular cylinders of radii  $\tilde{R}_1$  and  $\tilde{R}_2$ , where  $\tilde{R}_1 < \tilde{R}_2$ . Owing to the axial symmetry along the  $\tilde{z}$ -axis, it is sufficient to investigate the problem in 2D. A cross-sectional (two-dimensional) view of the problem is illustrated in Fig. 4.1. For the purpose of non-dimensionalization, we take the inner radius as the characteristic length  $\tilde{L}$ , i.e.  $\tilde{L} = \tilde{R}_1$ . Consequently, the dimensionless radii of the inner and outer cylinders are  $r_1 = \tilde{R}_1/\tilde{L} = 1$  and  $r_2 = \tilde{R}_2/\tilde{L}$ , respectively. The condensed phases of the vapor at the inner and outer cylinders are assumed to be negligibly thin. These interfaces are not treated as impermeable solid walls but rather as surfaces across which phase change can occur. As a result, the standard no-penetration condition does not apply here. Instead, evaporation and condensation boundary conditions (2.51)–(2.53) are imposed on these interfaces. Let the temperatures of the inner and outer condensed phases be maintained at uniform temperatures  $\tilde{T}_0$  and  $\tilde{T}_s$ , respectively; see Fig. 4.1. The parameters  $\tilde{P}_0$  and  $\tilde{P}_s$  denote the saturation pressures corresponding to the temperatures  $\tilde{T}_0$  and  $\tilde{T}_s$ , respectively, of the condensed phases on the inner and outer walls. The difference between the actual

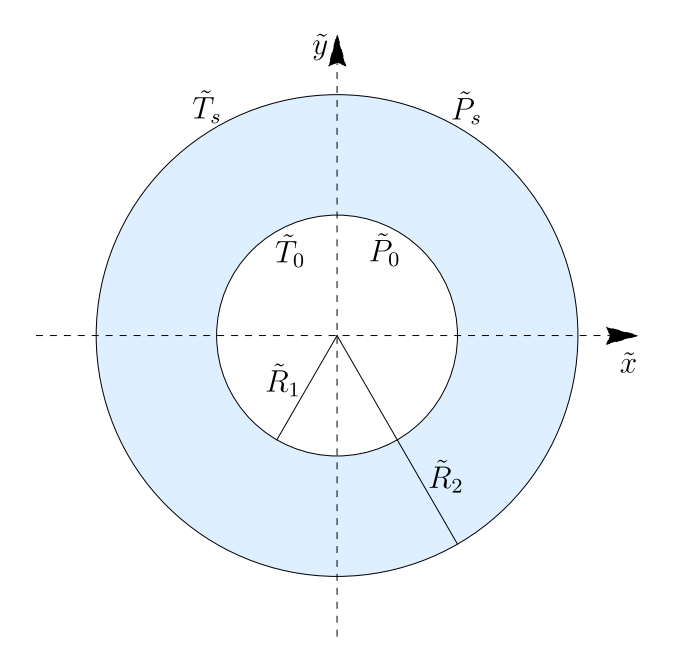


Figure 4.1: Cross-sectional view of a rarefied vapor flow confined between two coaxial cylinders.

gas pressure in the vapor and the local saturation pressure at the wall determines the evaporation/condensation, as specified by the boundary conditions (2.51)–(2.52). Again, for the purpose of linearization and non-dimensionalization, we take the temperature at the inner wall  $\tilde{T}_0$  as the reference temperature and the saturation pressure at the inner wall  $\tilde{P}_0$  as the reference pressure. Thus, the dimensionless perturbations in the temperature and saturation pressure at the inner wall vanish, and the dimensionless perturbations in the temperature and saturation pressure at the outer wall read

$$\tau_s = \frac{\tilde{T}_s - \tilde{T}_0}{\tilde{T}_0} \quad \text{and} \quad p_s = \frac{\tilde{P}_s - \tilde{P}_0}{\tilde{P}_0},$$
(4.1)

respectively.

## 4.1.2 Analytic solution of Onishi [77]

Onishi [77] investigated the problem by employing an asymptotic theory [100]. According to this theory, a field variable  $\tilde{h}$  of the gas can be written as

$$\tilde{h} = \tilde{h}_H + \tilde{h}_K, \tag{4.2}$$

where  $\tilde{h}_H$  is referred to as the hydrodynamic part or the Hilbert part that describes the flow behavior in the bulk of the flow domain and  $\tilde{h}_K$  is referred to as the kinetic boundary layer part or the Knudsen layer part that can be seen as a correction to the Hilbert part

and is significant only in small layers near an interface. Both  $\tilde{h}_H$  and  $\tilde{h}_K$  for all field variables are expanded in power series of the Knudsen number, and the contribution at each power of the Knudsen number is then computed by means of the considered BGK model and the diffuse-reflection boundary conditions.

The linearized CCR model is anyway not able to predict Knudsen layers. Therefore, it makes sense to compare the results obtained from the MFS only with the Hilbert part of the solution given in Ref. [77]. For the problem under consideration and for the linearized BGK model with the diffuse-reflection boundary conditions, the Hilbert part of the solution is indeed straightforward to determine by solving a set of simple ordinary differential equations analytically. Denoting the radius ratio by  $\varrho = r_2/r_1$  and the ratio of  $p_s$  to  $\tau_s$  by  $\gamma = p_s/\tau_s$ , the analytic solution obtained from the linearized BGK model with the diffuse-reflection boundary conditions for Kn  $\approx 0$  is given by

$$p = p_s \left(\frac{1}{r_1} + \frac{1}{r_2}\right)^{-1} \frac{1}{r_1},\tag{4.3}$$

$$v_r = -\frac{p_s}{C_0} \left(\frac{1}{r_1} + \frac{1}{r_2}\right)^{-1} \frac{1}{r},\tag{4.4}$$

$$T = \tau_s \left[ \left( 1 - \frac{D_0}{C_0} \gamma \right) \frac{\ln r}{\ln \varrho} - \left( 1 - \frac{D_0}{C_0} \gamma \right) \frac{\ln r_1}{\ln \varrho} \right] + \frac{D_0}{C_0} \gamma \tau_s \left( \frac{1}{r_1} + \frac{1}{r_2} \right)^{-1} \frac{1}{r_1}, \tag{4.5}$$

$$q_r = 0, (4.6)$$

where  $C_0 = 2.132039$  and  $D_0 = 0.4467494$ .

#### 4.1.3 Boundary conditions and implementation of the MFS

We shall investigate the problem described above by means of the MFS applied on the linearized CCR model. Recall that we have already determined the fundamental solutions of the linearized CCR model and outlined the way to implement them in Sec. 3.3.1 for a general two-dimensional object. The solution for the field variables at the  $j^{\text{th}}$  boundary node can directly be used from Eqs. (3.81)–(3.85) once the boundary nodes and singularity points for the present problem have been decided.

Since the singularity sites are to be placed outside of the computational domain, we assume the source points to be placed on two fictitious circular boundaries, one inside the circle associated with the inner cylinder and the other outside the circle associated with the outer cylinder, as shown in Fig. 4.2. Note that both fictitious boundaries are concentric

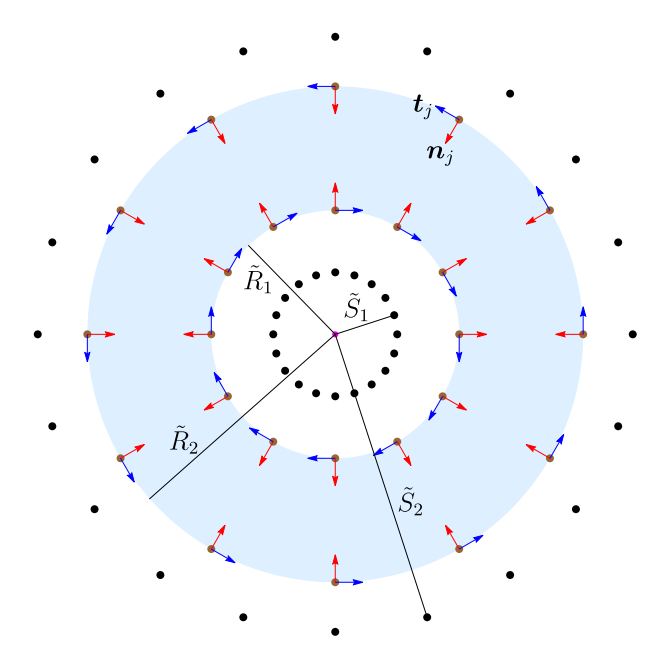


Figure 4.2: Schematic of the boundary nodes on the boundaries and singularity points outside the flow domain for the problem illustrated in Fig. 4.1. The red and blue arrows at each boundary node depict the normal (pointing toward the flow domain) and tangential directions, respectively at that node.

with the circles associated with the cylinders. Let the radii of the inner and outer fictitious boundaries be  $\tilde{S}_1$  and  $\tilde{S}_2$ , respectively. For simplicity, we consider  $n_s$  equispaced source points on each of the two fictitious boundaries and  $n_b$  equispaced boundary nodes on each of the actual boundaries (the boundaries of the inner and outer cylinders). As explained in Sec. 3.3.1, we have four degrees of freedom corresponding to each source point, and the total number of singularity points for the problem under consideration is  $N_s = 2n_s$ . Thus, there will be a total of  $4 \times N_s = 4 \times 2n_s$  unknowns in the problem. Accordingly, the summations in Eqs. (3.81)–(3.85) will run from i = 1 to  $i = 2n_s$ .

Boundary conditions at the  $j^{\text{th}}$  boundary node are obtained from (2.51)–(2.53) by replacing the flow variables and the normal and tangent vectors with their respective values at the  $j^{\text{th}}$  boundary node. Furthermore, since the walls of the cylinders are fixed,  $\mathbf{v}^I = \mathbf{0}$ . Consequently, the boundary conditions at the  $j^{\text{th}}$  boundary node read

$$\boldsymbol{v}_i \cdot \boldsymbol{n}_i = -\eta_{11}(p_i - p_{\text{sat}} + \boldsymbol{n}_i \cdot \boldsymbol{\sigma}_i \cdot \boldsymbol{n}_i) + \eta_{12}(T_i - T^I + \alpha_0 \boldsymbol{n}_i \cdot \boldsymbol{\sigma}_i \cdot \boldsymbol{n}_i), \tag{4.7}$$

$$\mathbf{q}_j \cdot \mathbf{n}_j = \eta_{12}(p_j - p_{\text{sat}} + \mathbf{n}_j \cdot \boldsymbol{\sigma}_j \cdot \mathbf{n}_j) - (\eta_{22} + 2\tau_0)(T_j - T^I + \alpha_0 \mathbf{n}_j \cdot \boldsymbol{\sigma}_j \cdot \mathbf{n}_j),$$
 (4.8)

$$\boldsymbol{t}_{i} \cdot \boldsymbol{\sigma}_{i} \cdot \boldsymbol{n}_{i} = -\varsigma(\boldsymbol{v}_{i} + \alpha_{0}\boldsymbol{q}_{i}) \cdot \boldsymbol{t}_{i}. \tag{4.9}$$

The dimensionless perturbations in the saturation pressures at the inner and outer interfaces are  $p_{\rm sat}=0$  and  $p_{\rm sat}=p_s$ , respectively, and the dimensionless perturbations in the temperatures at the inner and outer interfaces are  $T^I=0$  and  $T^I=\tau_s$ , respectively, which need to be replaced in boundary conditions (4.7)–(4.9) accordingly. Note that boundary conditions (4.7)–(4.9) are to be satisfied at  $N_b=2n_b$  boundary nodes. On substituting the values of the field variables at the  $j^{\rm th}$  boundary node from Eqs. (3.90)–(3.94) into boundary conditions (4.7)–(4.9), the resulting system of equations (associated with the  $j^{\rm th}$  boundary node) can be written in a matrix form as

$$\sum_{i=1}^{N_s} M_{ji} \boldsymbol{u}_i = \boldsymbol{b}_j, \tag{4.10}$$

for the unknown vector associated with the  $i^{\text{th}}$  singularity  $\mathbf{u}_i = (f_{1i}, f_{2i}, g_i, h_i)^{\mathsf{T}}$ . Here,  $M_{ji}$ 's are the coefficient matrices of dimensions  $3 \times 4$  and  $\mathbf{b}_j$  is the  $3 \times 1$  vector containing the interface properties, such as  $p_s$  and  $\tau_s$ . We collect all such systems into a new system

$$\mathcal{M}\mathcal{X} = \mathcal{B},\tag{4.11}$$

where  $\mathcal{X} = \begin{bmatrix} f_{11} & f_{21} & g_1 & h_1 & f_{12} & f_{22} & g_2 & h_2 & \dots & f_{1N_s} & f_{2N_s} & g_{N_s} & h_{N_s} \end{bmatrix}^\mathsf{T}$  is the vector containing all  $4N_s$  unknowns, the matrix  $\mathcal{M}$ —containing all the coefficients—has dimension  $3N_b \times 4N_s$  (or  $6n_b \times 8n_s$ ) and is referred to as the collocation matrix. We have solved system (4.11) in the computer algebra software, Mathematica<sup>®</sup> using the method of least squares. For the identification purpose, the first  $N_s$  singularity points  $(i=1,2,\dots,n_s)$  in our code belong to the inner fictitious boundary and the rest  $N_s$  singularity points  $(i=n_s+1,n_s+2,\dots,2n_s)$  to the outer fictitious boundary. Similarly, the first  $n_b$  boundary nodes  $(j=1,2,\dots,n_b)$  belong to the actual inner boundary and the rest  $n_b$  boundary nodes  $(j=n_b+1,n_b+2,\dots,2n_b)$  to the actual outer boundary.

#### 4.1.4 Results and discussion

For numerical computations, we have taken  $n_b = 100$  boundary nodes on each of the actual boundaries and  $n_s = 100$  singularity points on each of the fictitious boundaries. The dimensionless radii of the original and fictitious boundaries are taken as  $r_1 = 1$ ,  $r_2 = 2$ ,  $s_1 = \tilde{S}_1/\tilde{R}_1 = 0.5$  and  $s_2 = \tilde{S}_2/\tilde{R}_2 = 4$ .

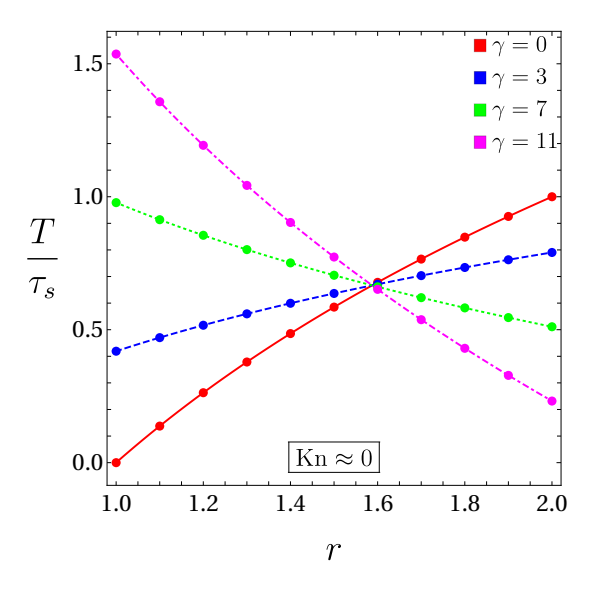


Figure 4.3: Variation of the (scaled) temperature in the gap between the two cylinders for different values of  $\gamma$ . The solid red, dashed blue, dotted green and dot-dashed magenta lines denote the results obtained from the MFS applied on the CCR model for  $\gamma = 0, 3, 7$  and 11, respectively, and the corresponding symbols (disks) indicate the analytic solution from Eq. (4.5), which was obtained analytically for Kn  $\approx 0$  through an asymptotic theory [100] performed on the linearized BGK model in Ref. [77]. The other parameters are  $n_b = 100$ ,  $n_s = 100$ ,  $r_1 = 1$ ,  $r_2 = 2$ ,  $s_1 = 0.5$ ,  $s_2 = 4$ .

Figure 4.3 illustrates the variation of the (scaled) temperature of the vapor in the radial direction for  $Kn \approx 0$  and for different values of the parameter  $\gamma (= p_s/\tau_s)$ , wherein  $\tau_s = 4$  is fixed and  $p_s$  is being varied for varying  $\gamma$ . The (solid red, dashed blue, dotted green and dot-dashed magenta) lines represent the results obtained from our numerical framework based on the MFS while the symbols delineate the results from Eq. (4.5), which was obtained analytically for  $Kn \approx 0$  through an asymptotic theory [100] performed on the linearized BGK model in Ref. [77]. It is evident from the figure that the results obtained with the MFS in the present work are in an excellent agreement with the analytic results from the linearized BGK model for  $Kn \approx 0$ .

Although not shown here for brevity, the results for the pressure and velocity from the MFS are also in excellent agreement with the analytic results from Eqs. (4.3) and (4.4) for  $Kn \approx 0$ .

It is also evident from Fig. 4.3 that the temperature increases on moving away from the inner cylinder toward the outer cylinder for smaller values of  $\gamma$  (solid red and dashed blue lines with corresponding symbols in the figure) and vice versa for larger values of  $\gamma$  (dotted green and dot-dashed magenta lines with corresponding symbols in the figure). This indicates the existence of a reverse temperature gradient after a critical value of  $\gamma$ . Indeed, at this critical value of  $\gamma$ , the (scaled) temperature remains constant along the radial direction. An expression for this critical value of  $\gamma$  from the asymptotic theory [100] is given by [77]

$$\gamma_c = \frac{C_0}{D_0} \left[ 1 - \operatorname{Kn} \frac{C_0}{D_0} (0.124226) \left( \frac{1}{r_1} - \frac{1}{r_2} \right) + \mathcal{O}(\operatorname{Kn}^2) \right]. \tag{4.12}$$

For Kn  $\approx 0$ , the critical value of  $\gamma$  from the above expression is  $\gamma_c = C_0/D_0 \approx 4.772337$ . From the MFS presented here, the critical value of  $\gamma$  for Kn  $\approx 0$  turns out to be  $\gamma_c \approx 4.7723$ , which is also very close to that computed from the above expression. The phenomenon of reverse temperature gradient can be understood from boundary condition (4.8) as follows. There are two factors determining the normal heat flux component in boundary condition (4.8) according to which the evaporation/condensation rate depends on (i) the difference between the pressure and saturation pressure, and (ii) the temperature difference between the temperatures of the gas (or vapor) and the interface. The temperature gradient gets reversed when one dominates the other. To gauge the capabil-

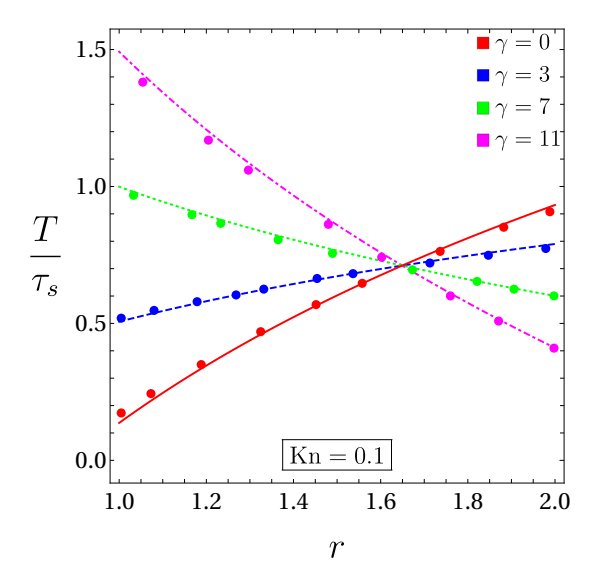


Figure 4.4: Same as Fig. 4.3 but for Kn = 0.1 and the symbols denoting the data from Ref. [77] obtained using the linearized BGK model.

ities of the developed method, we also study the problem for higher Knudsen numbers. Figure 4.4 exhibits the variation of the (scaled) temperature of the vapor in the radial direction for Kn = 0.1 and for different values of the parameter  $\gamma$ . The (solid red, dashed blue, dotted green and dot-dashed magenta) lines again represent the results obtained from our numerical framework based on the MFS but the symbols now denote the data from the linearized BGK model taken directly from Ref. [77]. It is clear from the figure that the results from the MFS are in good agreement with those from the linearized BGK model even for Kn = 0.1; nonetheless, the quantitative differences in the results from both methods are now noticeable.

To better contextualize the performance of the CCR-MFS framework, we now compare it with the NSF model supplemented with velocity-slip and temperature-jump boundary conditions. It is important to note that both approaches yield practically identical results for  $Kn \approx 0$  as rarefaction effects are negligible, and the standard NSF equations remain valid. However, as the Knudsen number increases, the differences between these models become more pronounced. For instance, at Kn = 0.1, a clear distinction emerges. Figure 4.5 illustrates the variation of the (scaled) temperature in the gap between the two cylinders for  $\gamma = 3$  and  $\gamma = 7$  at Kn = 0.1, wherein the temperature profiles predicted by the NSF model with both first-order and higher-order slip and jump conditions are presented alongside the results obtained from the CCR and BGK models. The classical first-order velocity-slip and temperature-jump boundary conditions for the NSF model are obtained by setting  $\alpha_0 = 0$  in the boundary conditions (4.7)–(4.9). To incorporate more refined corrections, we also implement the higher-order velocity slip and temperature jump conditions by setting  $\alpha_0 = 1/2$  in Eq. (4.7),  $\alpha_0 = 1/4$  in Eq. (4.8), and  $\alpha_0 = 1/5$ in Eq. (4.9). It can be observed that although the NSF model with higher-order slip and jump conditions shows improved accuracy over the first-order conditions, noticeable quantitative differences persist when compared to the results obtained from the CCR and BGK models. This demonstrates that even with higher-order corrections, the NSF model is limited in capturing certain rarefaction effects, whereas the CCR model provides better quantitative agreement with kinetic theory across the parameter range considered.

In addition, Figs. 4.4 and 4.5 also show the existence of a reverse temperature gradient. For Kn = 0.1, the critical value of  $\gamma$ , at which the phenomenon of reverse temperature

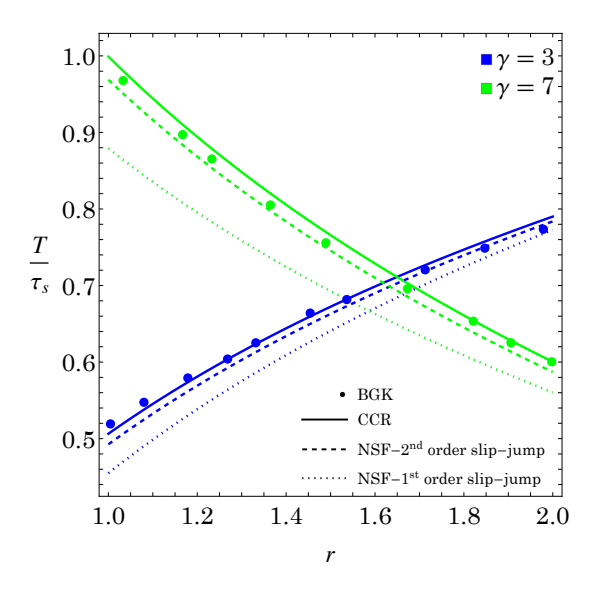


Figure 4.5: Variation of the (scaled) temperature in the gap between the two cylinders for  $\gamma=3$  and  $\gamma=7$  at Kn = 0.1. Solid lines represent results obtained from the MFS applied to the CCR model. Corresponding symbols (disks) show data from Ref. [77] based on the linearized BGK model. The dashed and dotted lines correspond to MFS solutions of the NSF model with second-order and first-order slip and jump boundary conditions, respectively.

gradient occurs, is  $\gamma_c = 4.66247$  from the MFS whereas its reported value from the linearized BGK model in Ref. [77] is  $\gamma_c = 4.63087$ .

To have further insight on the reverse temperature gradient, the (scaled) radial heat flux at the actual inner boundary (i.e. at r=1) is plotted against  $\gamma$  in Fig. 4.6. The (solid blue and dashed red) lines and symbols denote the results from the MFS in the present work and the data from the linearized BGK model given in Ref. [77], respectively. It is apparent from the figure that our results for the radial heat flux are also in good agreement with the data from the linearized BGK model for a smaller value of the Knudsen number (Kn = 0.1 in the figure); however, for a higher value of the Knudsen number (Kn = 0.2 in the figure), there is a noticeable mismatch between the results obtained from the MFS and the data from the linearized BGK model given in Ref. [77]. The exact source of this discrepancy is not entirely clear as per our current understanding. One possible reason could be the truncation of the power series at first order in Ref. [77], where neglected higher-order terms might contribute significantly at larger Knudsen numbers. Another

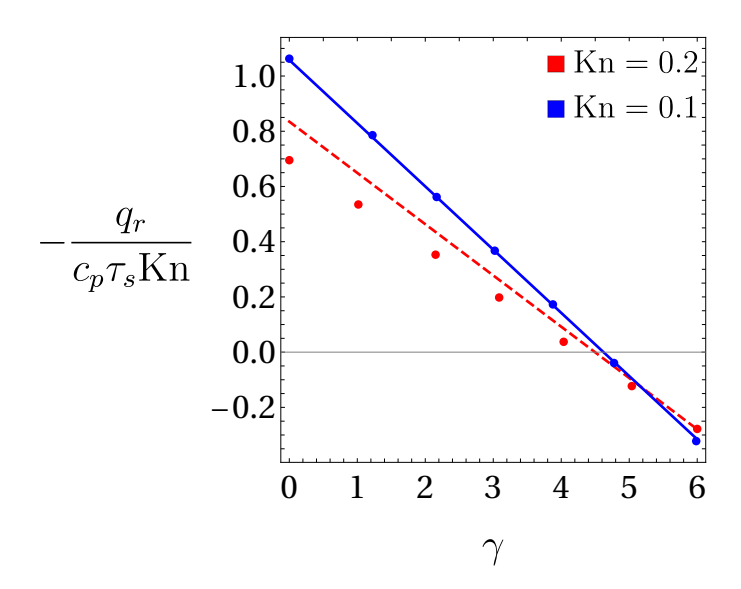


Figure 4.6: Variation of the (scaled) radial heat flux with  $\gamma$ . The solid blue and dashed red lines denote the results obtained from the MFS applied on the CCR model for Kn = 0.1 and 0.2, respectively, and the corresponding symbols (disks) indicate the data taken directly from Ref. [77], which were obtained using the linearized BGK model. The other parameters are the same as those for Fig. 4.3.

plausible explanation is the limitation of the CCR model itself, particularly its inability to capture Knudsen layers that become increasingly prominent near boundaries at higher Knudsen numbers. Figure 4.6 also shows that for each value of the Knudsen number, there is a  $\gamma$  at which the radial heat flux changes its sign. This  $\gamma$  is indeed the same as the  $\gamma_c$  described above, at which reversal of the temperature gradient takes place.

Through the plots of heat flux lines, although not shown here, it has been found that, in the case of  $\tau_s > 0$ , heat flows from the outer cylinder toward the inner cylinder for  $\gamma < \gamma_c$  and vice versa for  $\gamma > \gamma_c$ . This makes sense in view of Figs. 4.3 and 4.4. The direction of heat flow reverses in both cases when  $\tau_s$  is taken to be negative or, in other words, when the initial temperature of the inner cylinder is taken higher than that of the outer cylinder.

Figure 4.7 displays the (scaled) radial velocity at r = 1, plotted against  $\gamma$  for Kn  $\approx 0$  and Kn = 0.1. The solid blue and dotted green lines are again the results from the MFS in the present work while the symbols in the case of Kn  $\approx 0$  denote the results from Eq. (4.4) and those in the case of Kn = 0.1 denote the data taken from Ref. [77]; nevertheless, in

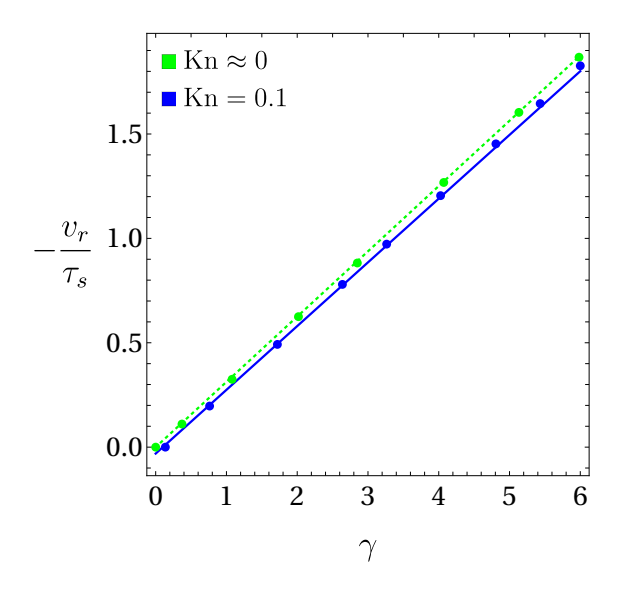


Figure 4.7: Variation of the (scaled) radial velocity with  $\gamma$ . The dotted green and solid blue lines denote the results obtained from the MFS applied on the CCR model for Kn  $\approx 0$  and Kn = 0.1, respectively, and the corresponding symbols (disks) indicate those from the linearized BGK model (from Eq. (4.4) in the case of Kn  $\approx 0$  and directly from Ref. [77] in the case of Kn = 0.1). The other parameters are the same as those for Fig. 4.3.

both cases symbols denote the results from the linearized BGK model. The figure also demonstrates a good agreement between the results from the method developed in the present work and those from the linearized BGK model.

### 4.1.5 Location of singularities

As mentioned in Sec. 3.1.1, the collocation matrix associated with the linear system resulting from the MFS could be ill-conditioned and there is a trade-off between the accuracy and good conditioning. Therefore, it is important to determine an appropriate location for the fictitious boundary in order to obtain the solutions with a desired accuracy.

Using the definition of the effective condition number, we first verify the inverse relationship between the maximum error and the effective condition number. Let  $\alpha > 1$  be the dilation parameter that determines the separation between the actual boundary (containing boundary nodes) and the fictitious boundary (containing singularities) such that  $s_1 = r_1/\alpha$  and  $s_2 = \alpha r_2$ . A larger value of  $\alpha$  corresponds to a larger gap between the actual and fictitious boundaries.

For the current problem, the maximum absolute error  $\epsilon_{\text{max}}$  in the temperature computed with the MFS and with the analytic solution for  $Kn \approx 0$  along with the effective condition number is plotted against the dilation parameter  $\alpha$  in Fig. 4.8. The figure shows that the inaccuracy of the MFS is roughly inversely proportional to the effective condition number. It is also evident from the figure that the maximum value of the effective condition number is attained for  $\alpha$  around 1.6, where the effective condition number is of order 10<sup>8</sup> and the absolute error is minimum. It is worthwhile noting that the order of the effective condition number remains  $10^8$  for higher values of  $\alpha$  beyond  $\alpha \approx 1.6$ ; similarly, the order of the maximum absolute error remains  $10^{-5}$  for higher values of  $\alpha$ beyond  $\alpha \approx 1.6$ . To further investigate the effect of the number of boundary nodes and singularity points, Fig. 4.9 illustrates the variation in the effective condition number (left) and the maximum absolute error in the temperature (right) with the dilation parameter  $\alpha$ . As depicted in the left panel of Fig. 4.9, it turns out that the value of  $\alpha$  at which the highest effective condition number is attained increases (decreases) with decrease (increase) in the number of boundary nodes and singularities. Analogously, from the right panel it is evident that the value of  $\alpha$  at which the minimum error is attained increases (decreases) with decrease (increase) in the number of boundary nodes and singularities. Therefore, to save computational time, one can use smaller number of boundary nodes

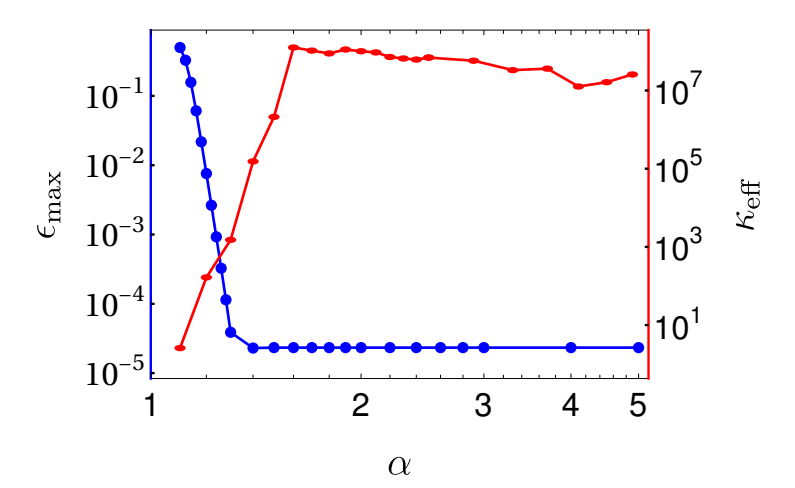


Figure 4.8: The maximum absolute error  $\epsilon_{\text{max}}$  in the temperature and the effective condition number  $\kappa_{\text{eff}}$  for the problem of flow between coaxial cylinders plotted over the dilation parameter  $\alpha$  for Kn  $\approx 0$  and  $n_b = n_s = 100$ .

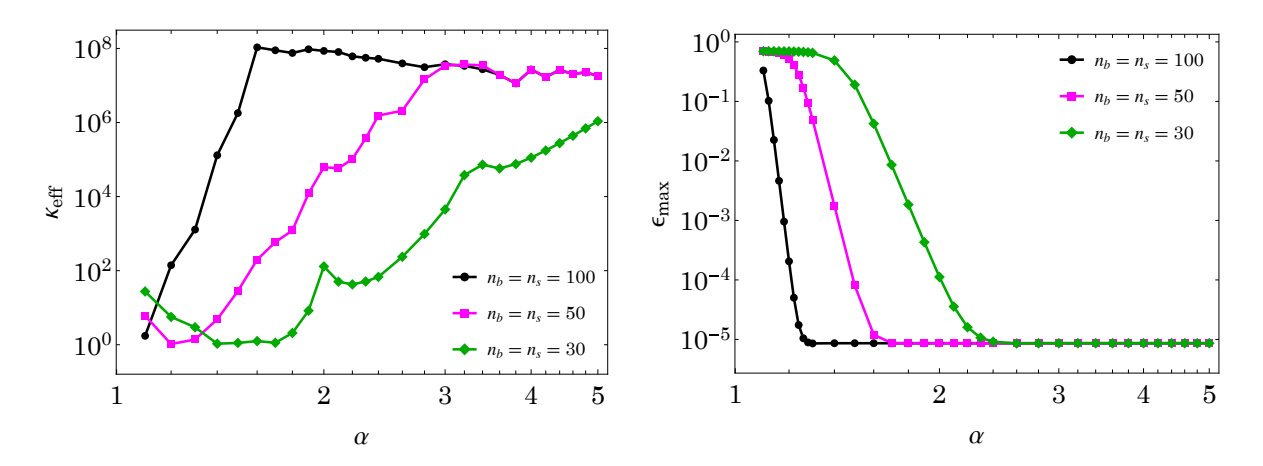


Figure 4.9: The effective condition number  $\kappa_{\rm eff}$  (left) and the maximum absolute error  $\epsilon_{\rm max}$  in the temperature (right) varying with the dilation parameter  $\alpha$  for Kn  $\approx 0$  and different values of  $n_b$  or  $n_s$ .

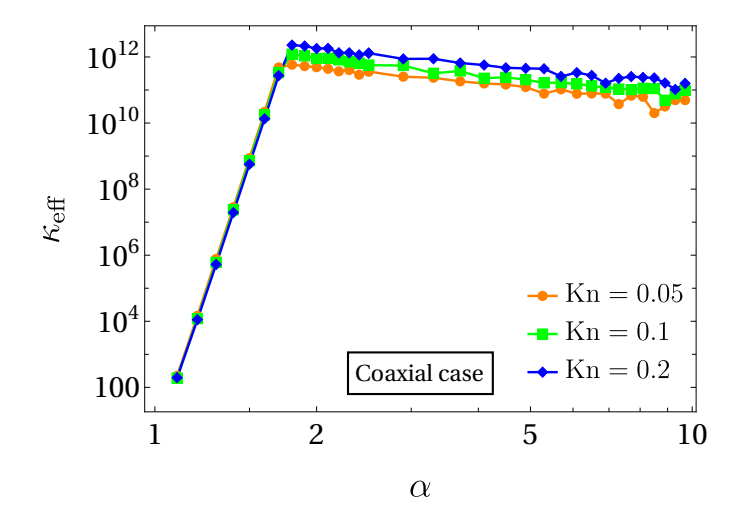


Figure 4.10: Variation of the effective condition number  $\kappa_{\text{eff}}$  with respect to the dilation parameter  $\alpha$  for  $n_b = n_s = 100$ .

and source points along with a bigger value of  $\alpha$ . Choosing  $\alpha \geq 2$  appears sufficient to achieve optimal accuracy for  $n_b = n_s = 100$ .

For higher Knudsen numbers, the variation in the effective condition number with respect to the dilation parameter is illustrated in Fig. 4.10. It can be noticed from the figure that the highest value of the effective condition number for a given Knudsen number is attained at a value of  $\alpha$  somewhere in between 1.8 and 2. Accordingly, the fictitious boundaries have been safely placed at locations corresponding to  $\alpha = 2$ .

# 4.2 Temperature-induced flow between two non-coaxial cylin-

In this section, we investigate the problem of flow induced by a temperature difference in a rarefied gas confined between two non-coaxial cylinders via the CCR-MFS framework developed in Sec. 3.3. The same problem was investigated numerically by Aoki, Sone and Yano [5] with the linearized BGK model and the diffuse-reflection boundary conditions.

# 4.2.1 Problem description

ders

Let us consider a rarefied monatomic gas confined between two infinitely long circular cylinders of radii  $\tilde{R}_1$  and  $\tilde{R}_2$  (with  $\tilde{R}_1 < \tilde{R}_2$ ) that are not coaxial. Again, owing to the axial symmetry, it is sufficient to investigate the problem in 2D. Let the locations of both cylinders be fixed according to the cross-sectional view portrayed in Fig. 4.11 so that the centers of the circles associated with the outer and inner cylinders be at the origin and at  $(0, -\tilde{d})$ , respectively. Furthermore, let the temperatures of the inner and outer cylinders be kept fixed at  $\tilde{T}_i = \tilde{T}_0$  and  $\tilde{T}_o = \tilde{T}_0(1 + \Delta \tau)$ , respectively, with  $\Delta \tau$  being sufficiently small in comparison to  $\tilde{T}_0$  so that the linear theory remains meaningful.

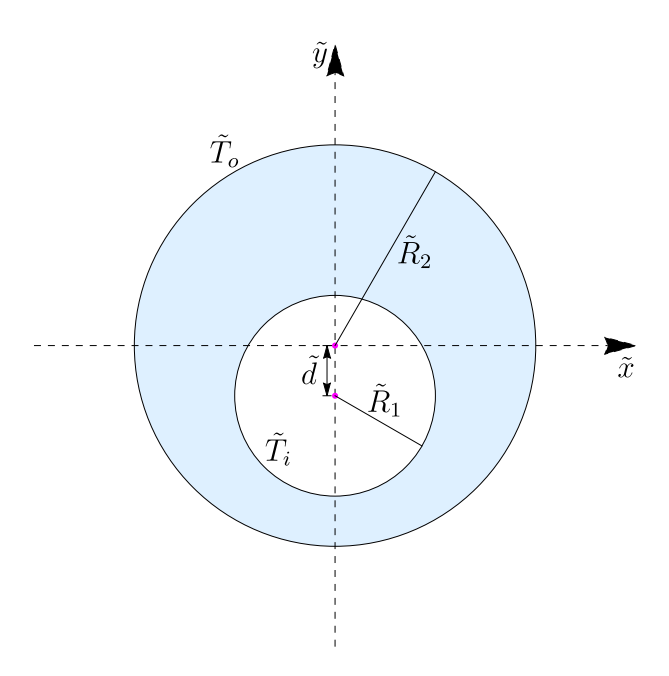


Figure 4.11: Cross-sectional view of the flow of a rarefied gas confined between two non-coaxial cylinders having different wall temperatures.

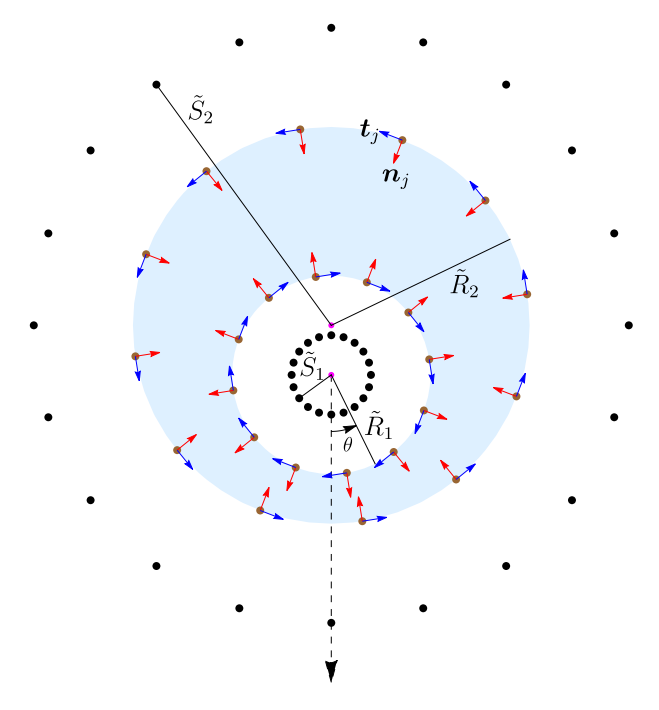


Figure 4.12: Schematic of the boundary nodes on the boundaries and singularity points outside the flow domain for the problem illustrated in Fig. 4.11. The red and blue arrows at each boundary node depict the normal (pointing toward the flow domain) and tangential directions at that node, respectively.

For the purpose of non-dimensionalization, we again take the radius of the inner cylinder as the characteristic length  $\tilde{L}$ , i.e.  $\tilde{L} = \tilde{R}_1$ . Consequently, the dimensionless radii of the inner and outer cylinders are  $r_1 = \tilde{R}_1/\tilde{L} = 1$  and  $r_2 = \tilde{R}_2/\tilde{L}$ , respectively, and the dimensionless distance between the centers of the cylinders is  $d = \tilde{d}/\tilde{L}$ . Furthermore, for the purpose of the linearization and non-dimensionalization, the equilibrium pressure of the gas  $\tilde{p}_0$  is taken as the reference pressure and the temperature of the inner cylinder  $\tilde{T}_i$  as the reference temperature so that the dimensionless perturbations in temperatures on the inner and outer walls are  $T_i = (\tilde{T}_i - \tilde{T}_i)/\tilde{T}_i = 0$  and  $T_o = (\tilde{T}_o - \tilde{T}_i)/\tilde{T}_i = \Delta \tau$ , respectively.

#### 4.2.2 Boundary conditions and implementation of the MFS

In order to place the singularity sites outside the computational domain, we again assume the source points to be placed on two fictitious circular boundaries, one inside the circle associated with the inner cylinder and the other outside the circle associated with the outer cylinder, as shown in Fig. 4.12. The inner (outer) fictitious boundary

is concentric with the circle associated with the inner (outer) cylinder. Let the radii of the inner and outer fictitious boundaries be  $\tilde{S}_1$  and  $\tilde{S}_2$ , respectively. Consequently, the dimensionless radii of the inner and outer fictitious boundaries are  $s_1 = \tilde{S}_1/\tilde{L}$  and  $s_2 = \tilde{S}_2/\tilde{L}$ . Similarly to the Sec. 4.1, we consider  $n_s$  equispaced source points on each of the two fictitious boundaries and  $n_b$  equispaced boundary nodes on each of the actual boundaries (the boundaries of the inner and outer cylinders).

Since the walls of the cylinders are fixed for this problem as well,  $\mathbf{v}^I = \mathbf{0}$ . Hence, the boundary conditions (4.7)–(4.9) at the  $j^{\text{th}}$  boundary node hold true for the present problem as well. However, since the present problem does not involve evaporation and condensation, the evaporation/condensation coefficient  $\Theta$  is zero for this problem. Consequently, boundary conditions (4.7)–(4.9) for the problem under consideration further reduce to

$$\mathbf{v}_j \cdot \mathbf{n}_j = 0, \tag{4.13}$$

$$\boldsymbol{q}_{i} \cdot \boldsymbol{n}_{i} = -2\tau_{0}(T_{i} - T^{I} + \alpha_{0} \, \boldsymbol{n}_{i} \cdot \boldsymbol{\sigma}_{i} \cdot \boldsymbol{n}_{i}), \tag{4.14}$$

$$\boldsymbol{t}_{i} \cdot \boldsymbol{\sigma}_{i} \cdot \boldsymbol{n}_{i} = -\varsigma(\boldsymbol{v}_{i} + \beta \boldsymbol{q}_{i}) \cdot \boldsymbol{t}_{i}. \tag{4.15}$$

Note that the coefficient  $\alpha_0$  in boundary condition (4.15) has been changed to  $\beta = 1/5$  (see, e.g., Refs. [105, 109, 110]) in order to have a fair comparison with the findings of Ref. [5]. The interface temperature  $T^I$  in boundary condition (4.14) is 0 for the inner cylinder and  $\Delta \tau$  for the outer cylinder.

The construction of the collocation matrix and the formation of system (4.11) for the present problem is exactly similar to that demonstrated in Sec. 4.1.3. We have again solved system (4.11) for the present problem analogously in the computer algebra software, Mathematica<sup>®</sup> using the method of least squares to determine the unknowns  $f_{11}, f_{21}, g_1, h_1, f_{12}, f_{22}, g_2, h_2, \ldots, f_{1N_s}, f_{2N_s}, g_{N_s}, h_{N_s}$ .

## 4.2.3 Results and discussion

We have computed the results numerically by taking the parameters as  $\Delta \tau = 1$ ,  $n_b = n_s = 100$ ,  $r_1 = 1$ ,  $r_2 = 2$ ,  $s_1 = 0.5$ , d = 0.5 and  $s_2 = 4$ . Figure 4.13 illustrates the variation of the tangential component of the (dimensionless) velocity on the right halves of the inner (left panel) and outer (right panel) circles associated with the respective cylinders with respect to the angle  $\theta$ , which is the angle measured from the negative

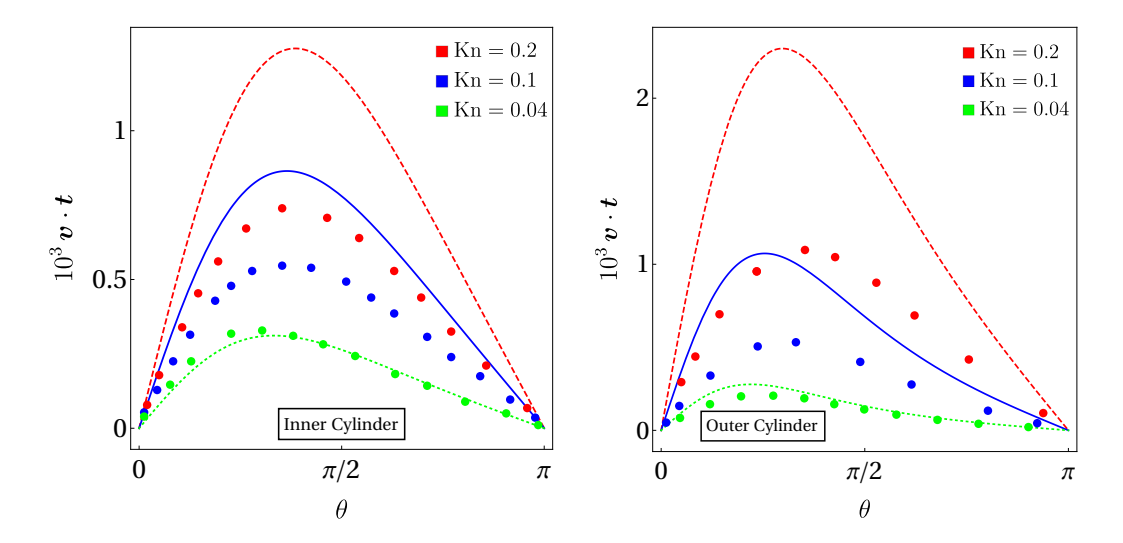


Figure 4.13: Tangential velocity on the right halves of the inner and outer circles associated with the respective cylinders plotted against the angle  $\theta$  for different values of the Knudsen number and for  $\Delta \tau = 1$ . The dashed red, solid blue and dotted green lines denote the results obtained from the MFS applied on the CCR model for Kn = 0.2, 0.1 and 0.04, respectively, and the corresponding symbols (disks) indicate the data from the linearized BGK model [5]. The other parameters are the same as those for Fig. 4.3.

y-axis anticlockwise around the center of the inner circle as shown in Fig 4.12. the (dashed red, solid blue and dotted green) lines represent the results obtained with the MFS applied on the CCR model in the present work and the symbols denote the data taken from Ref. [5], which were obtained using the linearized BGK model. The angle has been taken in this way in order to maintain the geometrical similarity with Ref. [5]. The unit tangential directions on the inner and outer circles are marked in Fig 4.12 with blue arrows. Figure 4.13 shows that the tangential components of the velocity for both inner and outer circles remain zero at  $\theta = 0$  and  $\theta = \pi$  and that they attain the maximum values somewhere in  $(0, \pi/2)$ . Furthermore, the value of  $\theta$  at which the maximum is attained also shifts more toward  $\theta = \pi/2$  on increasing the value of the Knudsen number. Figure 4.13 evinces that the results from the MFS applied on the CCR model (lines) are in reasonably good agreement with those from the linearized BGK model for small Knudsen numbers (dotted green lines and symbols) and that the differences between the results from both methods become more and more prominent with increasing Knudsen numbers (dashed red and solid blue lines with corresponding symbols), where the present method starts

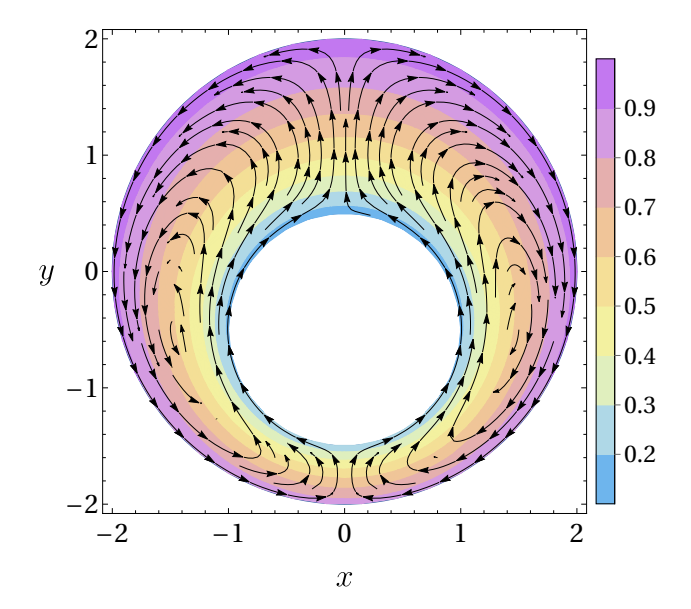


Figure 4.14: Velocity streamlines and temperature contours obtained from the MFS applied on the CCR model at Kn = 0.1 and  $\Delta \tau = 1$ . The other parameters are the same as those for Fig. 4.3.

overpredicting the results, though the trends from both methods remain qualitatively similar to each other even for high Knudsen numbers. The reason for these quantitative mismatches for large Knudsen numbers is attributed to the limitation of the CCR model in capturing the Knudsen layers, which are more conspicuous near the boundaries for large Knudsen numbers. The thickness of the Knudsen layers increases with increasing the Knudsen number [106], which renders larger deviations in the tangential component of the velocity near the inner and outer walls of the cylinders with increasing the Knudsen number.

Figure 4.13, in other words, also reveals that at  $\theta = 0$  and  $\theta = \pi$  the flow can happen only in the normal directions. This prompts us to draw streamlines of the flow in Fig. 4.14. For explanatory purpose, we also display the temperature contours in Fig. 4.14. The streamlines in Fig. 4.14 show that at the narrowest gap (at  $\theta = 0$ ), the gas starts moving from the outer (hotter) cylinder toward the inner (colder) cylinder due to the largest temperature gradient at  $\theta = 0$  and flows along the surface of the inner cylinder on both halves until it reaches  $\theta = \pi$ , at which it can flow only in the normal direction. Therefore, at the widest gap (near  $\theta = \pi$ ), the gas flows from the inner cylinder toward the outer cylinder and returns back from there toward the narrowest gap along the surface of the outer cylinder (but in the opposite directions due to symmetry along the y-axis).

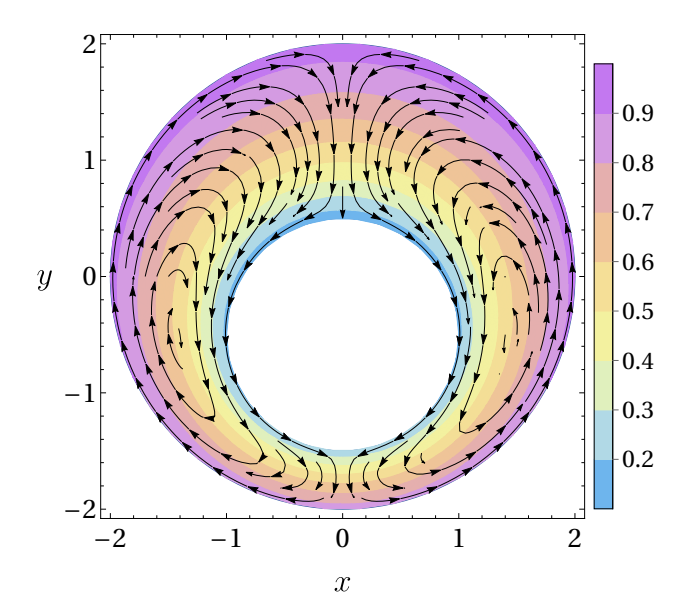


Figure 4.15: Velocity streamlines and temperature contours obtained from the MFS applied on the NSF equations with the second-order slip and jump boundary conditions at Kn = 0.1 and  $\Delta \tau$  = 1. The other parameters are the same as those for Fig. 4.3.

This renders two counter-directional circulating flows, one in the left half of the domain and the other in the right half of the domain. The directions of the circulating flows reverse on taking  $\Delta \tau < 0$ , i.e. when the inner cylinder is at a higher temperature than the outer one. With the considered values of the Knudsen number, the directions of the circulating flows apparently do not depend on the Knudsen number. The direction of the streamlines obtained from the MFS applied on the CCR model in Fig. 4.14 is consistent with that obtained using the linearized BGK model in Ref. [5].

In order to gain more insight into the process, we have also implemented the MFS to the (linearized) NSF equations [by setting  $\alpha_0 = 0$  in Eqs.  $(2.20)_1$  and  $(2.20)_2$ ] with the second-order slip and jump boundary conditions [105, 109, 110] [obtained by setting  $\alpha_0 = 1/4$  in Eq. (4.14) and  $\beta = 1/5$  in Eq. (4.15)], and plotted the streamlines obtained with them in Fig. 4.15. From Figs. 4.14 and 4.15, it is evident that, in contrast to the CCR model, the NSF equations even with the second-order slip and jump boundary conditions predict streamlines in completely opposite and incorrect directions. This affirms the inadequacy of the NSF equations in describing thermal-stress slip flows [101] accurately, which—on the other hand—can be described reasonably well with the CCR model due to the coupling between the stress and heat flux. The superposition of all the point force

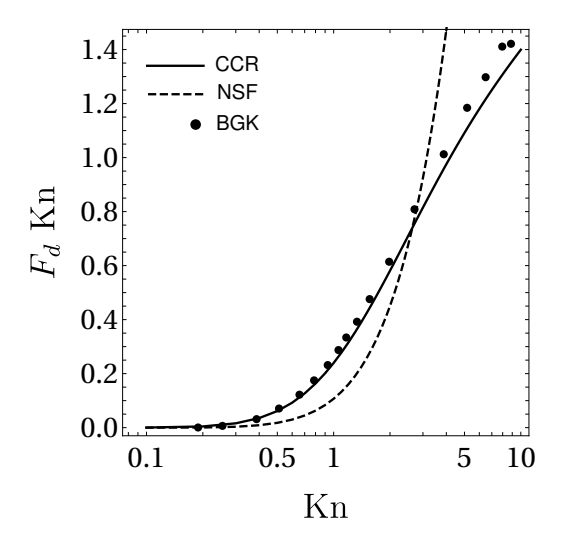


Figure 4.16: Drag force on the inner cylinder plotted against the Knudsen number for  $\Delta \tau = 1$ . The solid and dashed lines denote the results obtained from the MFS applied on the CCR and NSF models, respectively, while the symbols indicate the data for the drag force obtained from the linearized BGK model [5]. The other parameters are the same as those for Fig. 4.3.

vectors at the inner source points yields the total force F acting on the inner cylinder, i.e.

$$\boldsymbol{F} = \sum_{i=1}^{N_s} \boldsymbol{f}_i, \tag{4.16}$$

where  $i = 1, 2, ..., N_s$  refer to the points on the inner fictitious boundary. The projection of the total force in the direction opposite to the streamwise direction is referred to as the drag force (on the inner cylinder), which is given by

$$F_d = \mathbf{F} \cdot (-\hat{\mathbf{y}}) = -\sum_{i=1}^{N_s} \mathbf{f}_i \cdot \hat{\mathbf{y}}, \tag{4.17}$$

where  $\hat{y}$  represents the unit vector in the streamwise direction. Variation of the drag force with the Knudsen number is illustrated in Fig. 4.16, which shows good agreement between the results from the MFS applied on the CCR model (solid lines) and those from the linearized BGK model (symbols) even for high Knudsen numbers (especially, for  $\text{Kn} \lesssim 2$ ).

This was actually not the case for tangential velocity displayed in Fig. 4.13, where the differences between the results from the two models were noticeable for high Knudsen numbers. This shows that the CCR model is capable of predicting the global quantities,

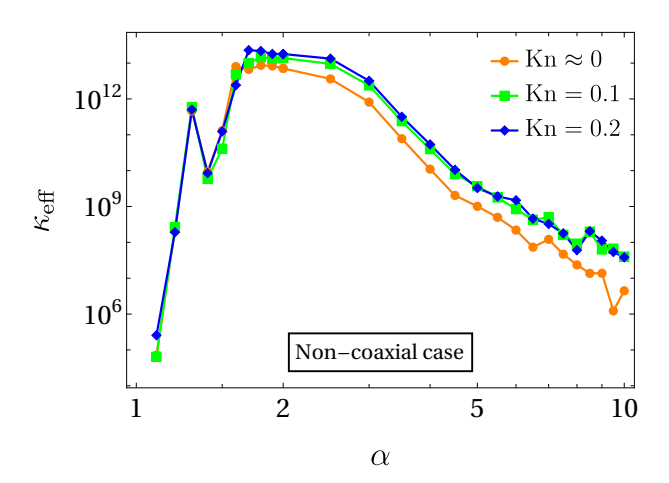


Figure 4.17: Variation of the effective condition number  $\kappa_{\text{eff}}$  with respect to the dilation parameter  $\alpha$ . The number of boundary nodes at either of the actual boundaries and the number of singularity points at either of the fictitious boundaries are 100 (i.e.  $n_b = n_s = 100$ ).

e.g., the drag force, quite accurately but is incapacitated of predicting the local quantities, e.g., the velocity and temperature, for high Knudsen numbers due to its limitation of not being able to predict Knudsen layers. On the contrary, the drag force obtained with the NSF equations (depicted by the dashed line in Fig. 4.16) deviates significantly from the drag force obtained with the linearized BGK model for  $Kn \gtrsim 0.2$ .

## 4.2.4 Choice of singularity points

Following the definition of the effective condition number (3.11) we plot the variation of the effective condition number with respect to dilation parameter (as also done in Sec 4.1.5) for different Knudsen numbers. It can be noticed from the Fig. 4.17 that the highest value of the effective condition number for a given Knudsen number is again attained at a value of  $\alpha$  somewhere in between 1.8 and 2. From Fig. 4.17, although the effective condition number decreases on increasing  $\alpha$  after a certain value of  $\alpha$ , we have not encountered any significant change in the results on keeping the singularities farther (or on taking bigger values of  $\alpha$ ). Therefore, it is apparently sufficient to just ensure  $\alpha \geq 2$  to attain an optimal accuracy in the case of  $n_b = n_s = 100$ . Therefore, the fictitious boundaries for this problem has safely been positioned at locations for which  $\alpha = 2$ .

# 4.3 Rarefied gas flows between coaxial circular and elliptic cylin-

# ders

In this section, we aim to explore the effect of curvature of the geometry by considering two coaxial cylinders with outer cylinder being elliptic and inner cylinder being circular, instead of two circular cylinders as considered in Sec. 4.1.

### 4.3.1 Problem statement

We consider flows of a rarefied gas confined between two coaxial cylinders having different temperatures. The inner cylinder is circular while the outer is elliptic. Let the radius of the circular cylinder be  $\tilde{r}$  and the lengths of the semi-major and semi-minor axes of the elliptic cylinder be  $\tilde{a}$  and  $\tilde{b}$ , respectively, with  $\tilde{r} < \tilde{b} < \tilde{a}$ . The cross-sectional view of the geometry of the problem is exhibited in Fig. 4.18. Both cylinders are assumed to be infinitely long along the  $\tilde{z}$ -axis. Owing to symmetry along the transverse direction (i.e. along the  $\tilde{z}$ -axis), it is again sufficient to study the quasi two-dimensional representation of the problem in the  $\tilde{x}\tilde{y}$ -plane. For the purpose of non-dimensionalization, we choose the length of the semi-minor axis  $\tilde{b}$  as the length scale  $\tilde{L}$  following [4], which has been referred for qualitative comparison. Consequently, the dimensionless lengths

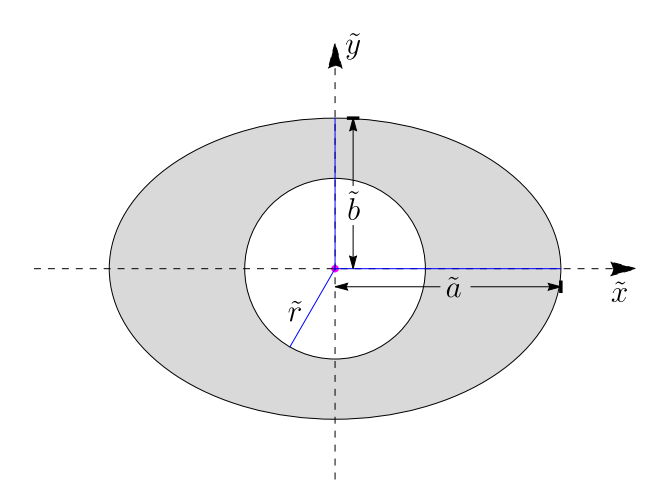


Figure 4.18: Cross-sectional view of the geometry of the problem. The shaded region depicts the flow domain. The cylinders are concentric and coaxial with the radius of the circular cylinder being smaller than both semi axes of the elliptic cylinder.

of the semi-major and semi-minor axes are  $a = \tilde{a}/\tilde{b}$  and  $b = \tilde{b}/\tilde{L} = 1$ , respectively, and the dimensionless radius of the inner cylinder is  $r = \tilde{r}/\tilde{b}$ . Furthermore, let the temperatures of the inner and outer cylinders be  $\tilde{T}_i$  and  $\tilde{T}_o$ , respectively. To make the flow variables dimensionless, we take  $\tilde{T}_i$  as the reference temperature. As also discussed in Secs. 4.1 and 4.2, we shall be dealing with the linearized equations in this work. The wall temperatures of the cylinders are also linearized around the reference temperature  $\tilde{T}_i$ . Consequently, the dimensionless perturbations in the temperatures (from the reference temperature) on the inner and outer walls are  $T_i = (\tilde{T}_i - \tilde{T}_i)/\tilde{T}_i = 0$  and  $T_o = (\tilde{T}_o - \tilde{T}_i)/\tilde{T}_i$ , respectively. The two distinct problems considered in this set-up are as follows.

- 1. **Thermally-induced flow**: In this problem, we investigate the flow of rarefied gas rendered purely due to the temperature difference between the walls of the two cylinders. The problem was also investigated as a special case in Refs. [4] and [82] using the DSMC method.
- 2. Phase-transition flow: We consider a moderately rarefied monatomic vapor confined between negligibly thin condensed phases on the walls of the two cylinders and investigate the phenomenon of evaporation/condensation of the vapor. The condensed phases on the walls are assumed to be so thin that the temperatures of the vapor in these phases are assumed to be the same as those of the respective cylinders. The phenomenon of evaporation/condensation is governed both by the temperature difference between the phases near the walls and by the saturation pressures of the condensed phases. Corresponding to the temperatures  $\tilde{T}_i$  and  $\tilde{T}_o$  of the inner and the outer cylinders, let the saturation pressure at the inner wall  $\tilde{p}_i$  as the reference pressure corresponding to the reference temperature  $\tilde{T}_i$ . Consequently, the dimensionless perturbations in the saturation pressures (from the reference pressure) on the inner and outer condensed phases are  $p_i = (\tilde{p}_i \tilde{p}_i)/\tilde{p}_i = 0$  and  $p_o = (\tilde{p}_o \tilde{p}_i)/\tilde{p}_i$ , respectively. We denote the ratio of  $p_o$  to  $T_o$  by  $\gamma = p_o/T_o$ .

It is important to note that the two problems are completely independent of each other and that the same notations used for the wall temperatures in the two problems should not be confusing.

### 4.3.2 Boundary conditions

The boundary conditions (2.51)–(2.53) in the case of problem 1 (requiring canonical boundaries or  $\Theta = 0$ ) reduce to [42, 90]

$$\boldsymbol{v} \cdot \boldsymbol{n} = 0, \tag{4.18}$$

$$\boldsymbol{q} \cdot \boldsymbol{n} = -2\tau_0 (T - T_w + \alpha_0 \, \boldsymbol{n} \cdot \boldsymbol{\sigma} \cdot \boldsymbol{n}), \tag{4.19}$$

$$\boldsymbol{t} \cdot \boldsymbol{\sigma} \cdot \boldsymbol{n} = -\varsigma(\boldsymbol{v} + \beta \boldsymbol{q}) \cdot \boldsymbol{t}. \tag{4.20}$$

where  $T_w$  represents the (dimensionless) temperature on the wall, having values  $T_i$  and  $T_o$  respectively for the inner and outer cylinders. Note that in boundary condition (4.20), a new parameter  $\beta$  has been introduced in place of  $\alpha_0$ . The parameter  $\beta$  is referred to as the thermal-slip coefficient. The relevant works available in the literature based on the asymptotic analysis as well as on numerical experiments emphasize on the importance of boundary condition (2.53) and of the coefficient  $\beta$ , especially when dealing with temperature-induced flows. For boundary conditions (2.51)–(2.53) to be thermodynamically-consistent, the thermal-slip coefficient  $\beta$  is taken to be the same as the coupling coefficient  $\alpha_0$  [90]. Nevertheless, some other values for the thermal-slip coefficient  $\beta$  also exist in the literature; see, e.g., Refs. [63, 86, 93]. Among the existing values of the thermal-slip coefficient  $\beta$ , the commonly used value is  $\beta = 1/5$  [105, 109, 110]. We shall also demonstrate the effect of the thermal-slip coefficient by considering two values for it, namely  $\beta = 1/5$  and  $\beta = \alpha_0 = 0.3197$ .

For problem 2 (requiring phase-change boundaries), the boundary conditions (2.51)–(2.53) are used directly with  $\Theta = 1$ .

# 4.3.3 Results and discussion

In order to keep the source points outside the flow domain, we consider two fictitious boundaries concentric with the actual boundaries of the cylinders: the first one in a circular shape of radius  $\tilde{r}_s$  shrunk inside the actual circular boundary (i.e.,  $\tilde{r}_s < \tilde{r}$ ) and the second one in an elliptic shape with semi-major axis  $\tilde{a}_s$  and semi-minor axis and  $\tilde{b}_s$ , dilated outside the actual elliptic boundary (i.e.,  $\tilde{a}_s > \tilde{a}$  and  $\tilde{b}_s > \tilde{b}$ ) as illustrated in Fig. 4.19. For numerical computations in both problems, the (dimensionless) radius of the inner cylinder has been fixed to r = 0.6, the (dimensionless) semi-major and semi-minor axes of the outer cylinder to a = 1.5 and b = 1, respectively, the (dimensionless) radius of the

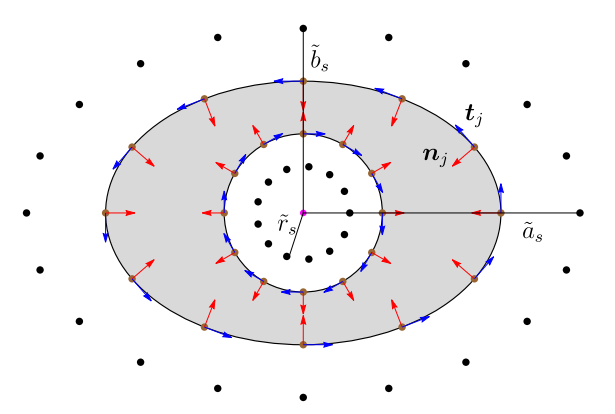


Figure 4.19: Schematic of the distribution of collocation points (or boundary nodes) on the boundaries and source points outside the flow region for the problem illustrated in Fig. 4.18. The blue and red arrows respectively delineate the tangential and normal directions at each boundary node.

inner fictitious boundary to  $r_s = 0.3$ , and the (dimensionless) semi-major and semi-minor axes of the outer fictitious boundary to  $a_s = 3$  and  $b_s = 2$ , respectively. Furthermore,  $n_b = 100$  boundary nodes have been chosen on each of the two actual boundaries of the cylinders and  $n_s = 100$  source points have been placed on each of the two fictitious boundaries. Note that, with the length scale  $\tilde{L} = \tilde{b}$  used in the non-dimensionalization of the equations, the  $\tilde{x}$ - and  $\tilde{y}$ -axes are also scaled to  $x = \tilde{x}/\tilde{L}$  and  $y = \tilde{y}/\tilde{L}$  in order to present the results in the (dimensionless) xy-plane. Owing to the geometrical symmetry in both the problems, we shall present the results only in the first quadrant of the xy-plane, which can be replicated in the other three quadrants in a straightforward way.

# 4.3.3.1 Problem 1: Thermally-induced flow between coaxial circular and elliptic cylinders

As the flow in this problem is driven by temperature difference between the walls of the cylinders, the dimensionless perturbations in temperatures of the inner and outer cylinders are set to  $T_i = 0$  and  $T_o = 1$ , respectively. Furthermore, to study the impact of the thermal-slip coefficient, two values, namely  $\beta = 1/5$  and  $\beta = \alpha_0 = 0.3197$ , of the thermal-slip coefficient are considered.

Figure 4.20 illustrates the tangential component of the velocity on the inner and outer cylinders across the first quadrant for  $\beta = 1/5$ . The figure shows that the tangential velocity at both cylinders remains zero at  $\theta = 0$  (i.e. along the x-axis) as well as at  $\theta = \pi/2$  (i.e. along the y-axis) for all Knudsen numbers and it increases on increasing

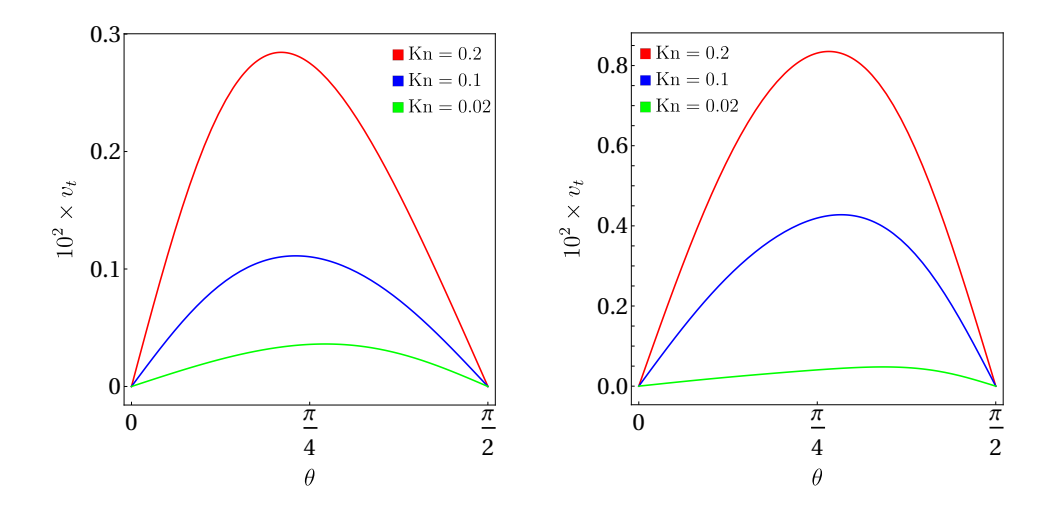


Figure 4.20: Tangential velocity of the gas on the inner (left panel) and outer (right panel) cylinders with  $\beta = 1/5$ . The other parameters are r = 0.6, a = 1.5, b = 1,  $r_s = 0.3$ ,  $a_s = 3$ ,  $b_s = 2$ ,  $n_b = n_s = 70$ ,  $T_i = 0$  and  $T_o = 1$ .

the Knudsen number for all  $0 < \theta < \pi/2$  as non-equilibrium becomes stronger with the increasing Knudsen number. The former observation, in other words, apprises that the flow at  $\theta = 0$  (i.e. along the x-axis) and  $\theta = \pi/2$  (i.e. along the y-axis) can occur only in the normal directions to the cylinders. This actuates us to draw the streamlines in order to have further insights into the flow.

The streamlines along with the temperature contours are exhibited for Kn = 0.02, 0.1 and 0.2 in Fig. 4.21. Evidently, there is no flow in the tangential directions at  $\theta = 0$  and  $\theta = \pi/2$ , which is consistent with the observation made from Fig. 4.20. Owing to the most significant temperature gradient occurring at  $\theta = \pi/2$  (attributed to the narrowest gap between the cylinders), the gas initiates movement from the outer (warmer) cylinder toward the inner (cooler) cylinder along  $\theta = \pi/2$  in the negative y-direction. Subsequently, it follows a path along the inner cylinder till it reaches to  $\theta = 0$ , and from there it again flows in the normal direction at  $\theta = 0$  toward the outer cylinder (due to the widest gap between the cylinders). Once it reaches the outer cylinder at  $\theta = 0$ , it has no other choice but to flow along the outer cylinder from  $\theta = 0$  toward  $\theta = \pi/2$ . This results in a counterclockwise circulating flow in the first quadrant that is symmetrically replicated in the other three quadrants. This phenomenon holds true for all considered Knudsen numbers, i.e. Kn = 0.02, 0.1 and 0.2. Such a circulating flow in this problem is a consequence of thermal stress rendered by the difference in temperature gradients at  $\theta = 0$  and  $\pi/2$ .

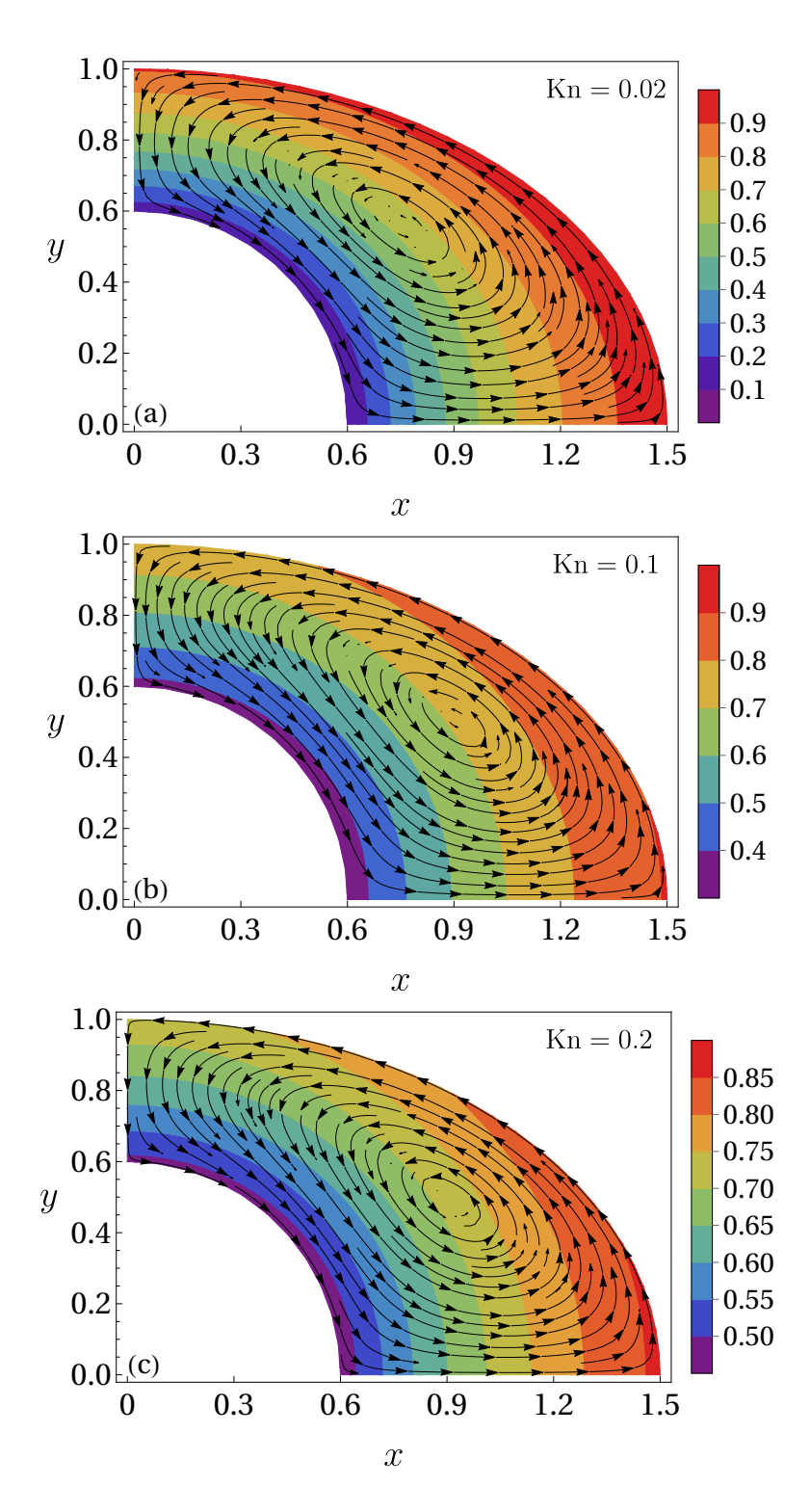


Figure 4.21: Velocity streamlines and temperature contours obtained with the MFS applied on the CCR model for Knudsen numbers (a) Kn = 0.02, (b) Kn = 0.1 and (c) Kn = 0.2 and for  $\beta = 1/5$ . The other parameters are the same as those in Fig. 4.20.

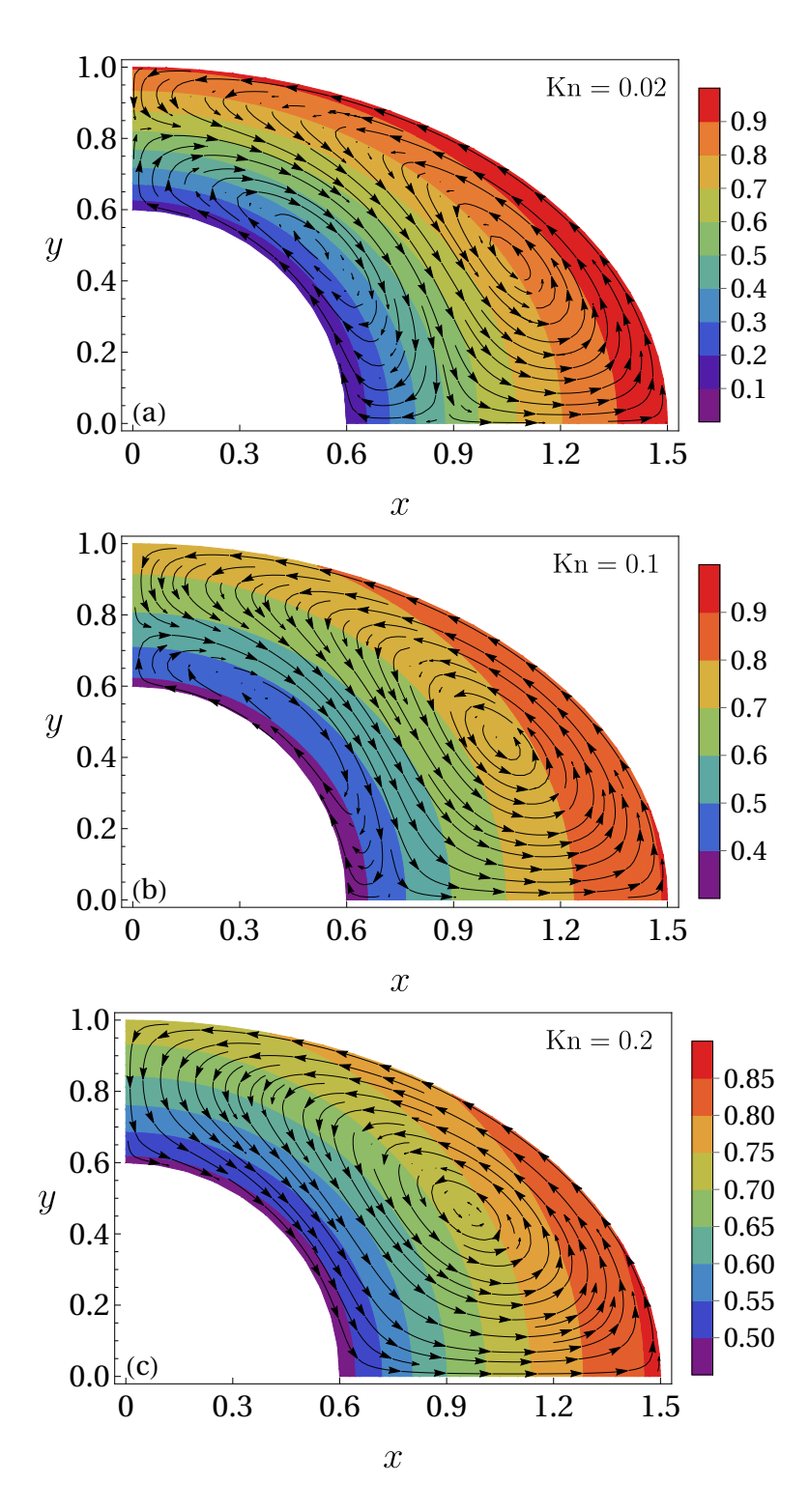


Figure 4.22: Same as Fig. 4.21 but for  $\beta = 0.3197$ .

The streamlines predicted by the MFS applied to the CCR model in the case of  $\beta = 1/5$  align with those obtained in Refs. [4] and [82] using the DSMC method for Kn = 0.5 and Kn = 0.02, respectively.

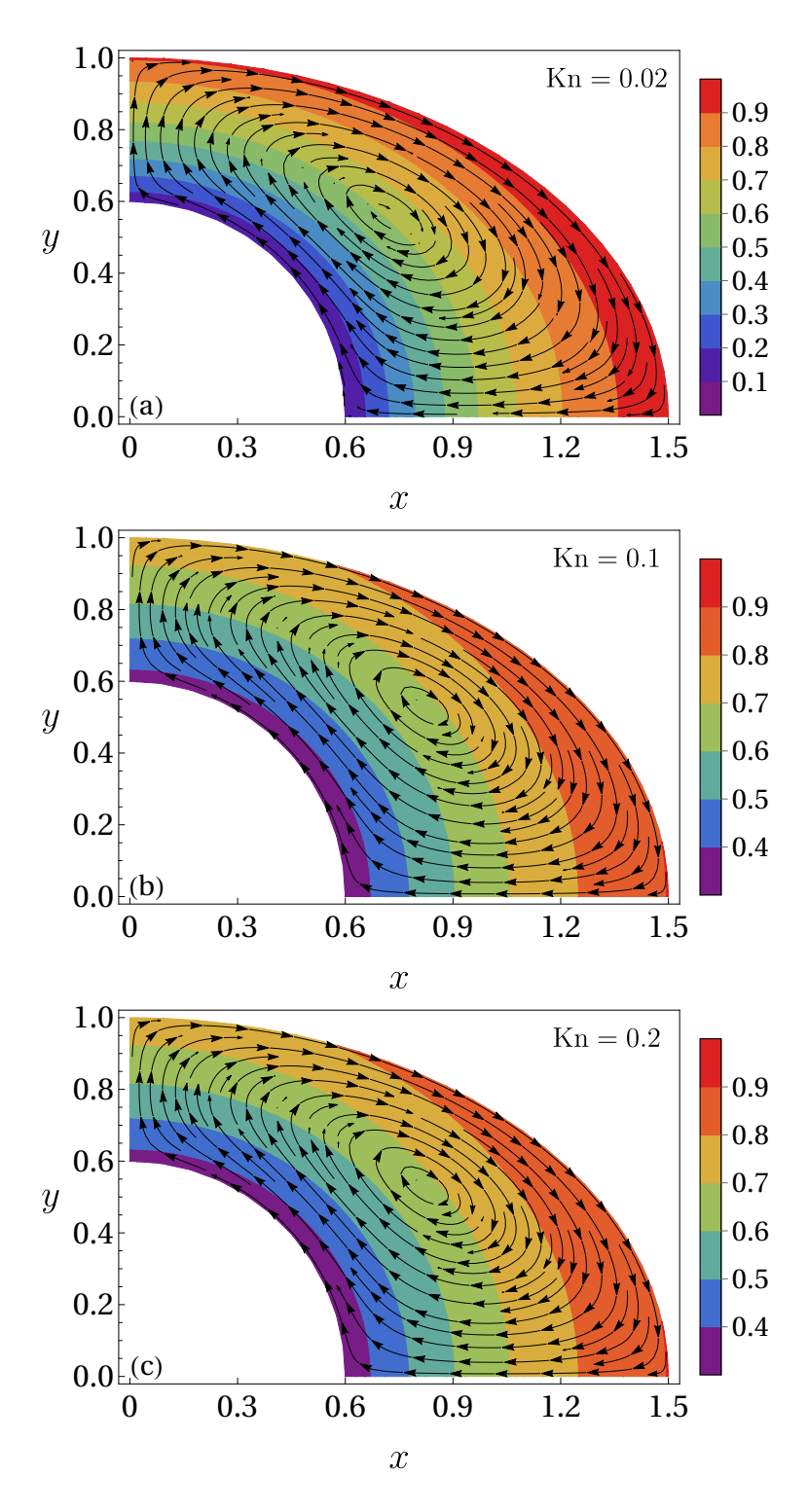


Figure 4.23: Same as Fig. 4.21 but with the MFS applied on the NSF model.

The thermal-slip coefficient  $\beta$  plays a significant role in anticipating the interplay between thermal-creep and thermal-stress effects. To illustrate this, the streamlines in

the case of  $\beta = \alpha_0 = 0.3197$  are plotted along with temperature contours for Kn = 0.02, 0.1 and 0.2 in Fig. 4.22. For very small values of the Knudsen number (Kn = 0.02), two counter-rotating flows are generated—one rotating counterclockwise originates along the outer cylinder while the other rotating clockwise along the inner cylinder; see Fig. 4.22. The former is due to the flow driven by thermal stress, causing the gas to move from the outer (hotter) cylinder toward the inner (colder) cylinder at  $\theta = \pi/2$ . The latter, on the other hand, is attributed to thermal creep causing the gas molecules to move from the colder (inner) cylinder to the hotter (outer) cylinder at  $\theta = \pi/2$ . Evidently from Fig. 4.22, as the Knudsen number increases, the flow along the outer cylinder intensifies whereas the flow along the inner cylinder diminishes. At sufficiently high Knudsen numbers (Kn = 0.2), the flow along the inner cylinder ceases entirely, and the counterclockwise flow along the outer cylinder extends across the entire quadrant (see the bottom panel of Fig. 4.22). As mentioned above, the appearance of a secondary circulating flow near the inner cylinder is due to the interplay between thermal-creep and thermal-stress effects, which is attributed to the coefficient  $\beta$ . In the case of a small value of the coefficient  $\beta$  (e.g.,  $\beta = 1/5$  which is smaller that  $\beta = 0.3197$ ), the thermal stresses still dominate the flow and a flow rendered by the thermal-creep is invisible for a small value of  $\beta$  (as in Fig. 4.21). For large values of  $\beta$ , the thermal creep effects become more pronounced. Even  $\beta = 0.3197$  is not large enough to show the thermal creep effects for large Knudsen numbers (bottom panel of Fig. 4.22). Nevertheless, the correct value of the thermal-slip coefficient  $\beta$  is intricately tied to the gas-surface interaction that could be better explored through molecular dynamics simulations, a task currently beyond the scope of this work.

Another crucial remark in this study pertains to the limitations of the NSF equations in accurately predicting thermal-stress slip flows, even with the second-order slip and jump boundary conditions. To demonstrate the limitations of the NSF equations, we have also employed the MFS to solve the linearized NSF equations (obtained by setting  $\alpha_0 = 0$  in Eqs.  $(2.20)_1$  and  $(2.20)_2$ ) along with the second-order slip and jump boundary conditions (obtained by setting  $\alpha_0 = 1/4$  and  $\beta = 1/5$  in boundary conditions (4.19) and (4.20)). Fig. 4.23 illustrates the streamlines plotted over the temperature contours obtained from the NSF equations with the second-order slip and jump boundary conditions for Kn = 0.02, 0.1 and 0.2. It is evident from the figure that the streamlines from the NSF equations

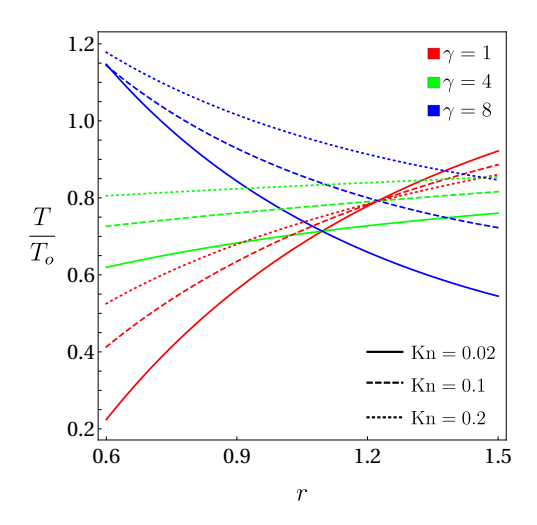


Figure 4.24: Variation of the (scaled) temperature of the vapor with the radial distance r between the two cylinders at  $\theta = 0$ —for three different values of the parameter  $\gamma$ , namely  $\gamma = 1$  (red color),  $\gamma = 4$  (green color)  $\gamma = 8$  (blue color), and for three different values of the Knudsen number, namely Kn = 0.02 (solid lines), Kn = 0.1 (dashed lines) and Kn = 0.2 (dotted lines). The other parameters are a = 1.5, b = 1,  $r_s = 0.3$ ,  $a_s = 3$ ,  $b_s = 2$ ,  $n_b = n_s = 70$ ,  $T_i = 0$ .

are directed in completely reverse direction in contrast to those from the CCR model in Figs. 4.21. Since the stream directions obtained from the CCR model are consistent with those obtained from the DSMC method in Refs. [4] and [82], it is apparent that the streamlines predicted by the NSF equations are incorrect even for Kn = 0.02. Thus, the NSF equations are in general unsuitable for describing thermal-stress and thermal-creep flows. A similar problem of thermally-induced flow between coaxial elliptic and circular cylinders is investigated in Appendix C to further demonstrate the interplay between thermal stress and thermal creep.

4.3.3.2 Problem 2: Evaporation/condensation between the condensed phases of a vapor confined between coaxial circular and elliptic cylinders

For the problem of phase-transition flow, we have fixed  $T_o$  to  $T_o = 4$ , and we vary  $p_o$  to change the parameter  $\gamma = p_o/T_o$ , where  $\gamma$  represents the characterization parameter for phase change. Figure 4.24 displays the variation of the (scaled) temperature of the vapor in the radial direction along  $\theta = 0$  for different values of the parameters  $\gamma$  and Kn. The red, green and blue colored lines represent the temperature variation for  $\gamma = 1$ , 4 and

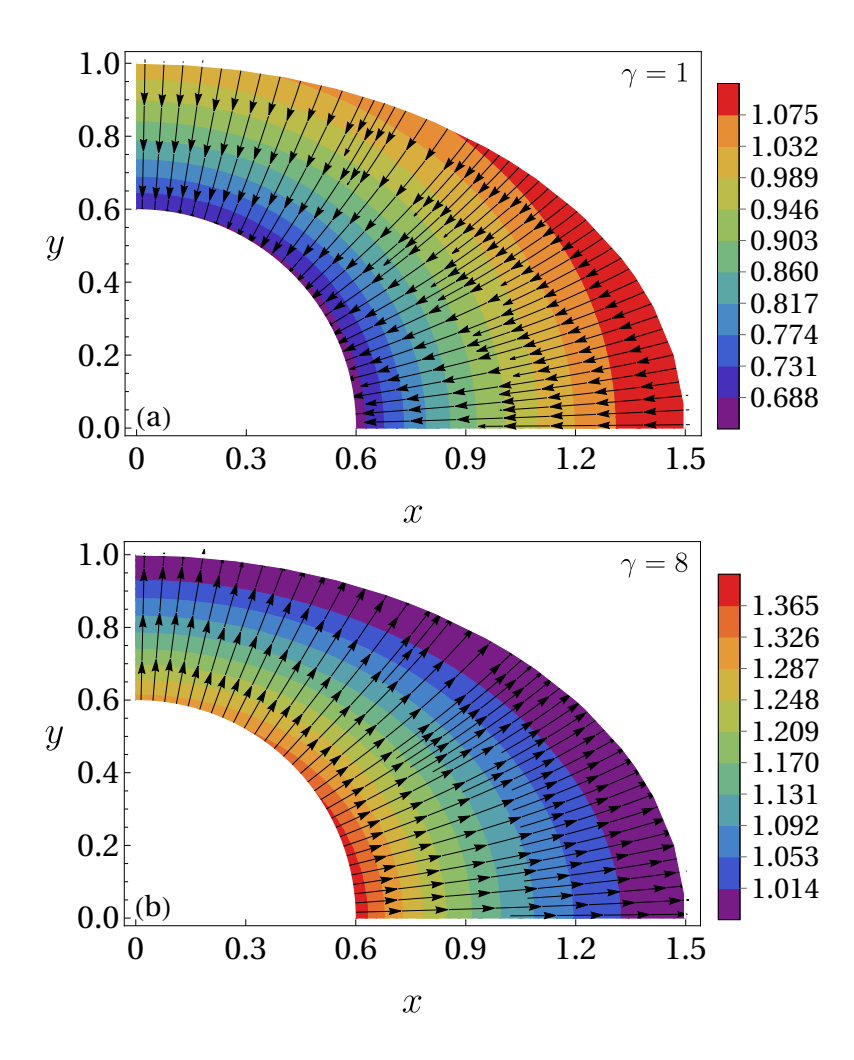


Figure 4.25: Heat flow lines plotted over (scaled) temperature contours for (a)  $\gamma = 1$  and (b)  $\gamma = 8$  and Kn = 0.1. The other parameters are the same as those in Fig. 4.24.

8, respectively. Solid, dashed and dotted lines represent the temperature variation in the cases when Kn = 0.02, 0.1 and 0.2, respectively. The figure shows that the temperature of the vapor increases on moving away from the inner cylinder toward the outer cylinder for smaller values of  $\gamma$  (for  $\gamma = 1$  and 4 in the figure), and that it decreases on moving away from the inner cylinder toward the outer cylinder for larger values of  $\gamma$  ( $\gamma = 8$  in the figure). This connotes the existence of a reverse temperature gradient after some critical value of the parameter  $\gamma$ . The figure also suggests that the critical value of the parameter  $\gamma$  at which the temperature gradient reverses should be slightly larger than 4. This critical value is actually that value of  $\gamma$  at which there is no temperature variation between the two cylinders. Before further discussion on the critical value of

 $\gamma$ , let us demonstrate the phenomenon of temperature gradient reversal with the help of temperature contours and heat flux lines. Figure 4.25 illustrates the heat flux lines plotted over the temperature contours for Kn = 0.1 and for (a)  $\gamma = 1$  (top panel) and (b)  $\gamma = 8$  (bottom panel). As depicted by the temperature contours in the case of  $\gamma = 1$  (top panel), the temperature of the vapor increases on moving from the inner cylinder toward the outer cylinder and correspondingly, the heat flows from the outer cylinder toward the inner cylinder. However, beyond the critical stage of  $\gamma$  is surpassed, the situation reverses, as can be seen for  $\gamma = 8$  (bottom panel). This phenomenon of temperature gradient reversal can be explained using the boundary condition (2.51). The normal component of the heat flux in boundary condition (2.51) consists of two parts which determine the evaporation or condensation rate: first, the difference between the pressure and saturation pressure and second, the difference between the temperatures of the vapor and interface. The temperature gradient gets reversed when one dominates the other. For large values of  $\gamma$ , the former dominates whereas for small values of  $\gamma$ , the latter dominates. Although not shown here for brevity, the phenomenon of reversal of temperature gradient happens analogously for Kn = 0.02 and 0.2 as well.

Owing to the asymmetry associated with the elliptic cylinder, the critical value of  $\gamma$  also varies with  $\theta$ . Therefore, for further investigation of the critical value of the parameter  $\gamma$  (that determines the reversal of temperature gradient), we plot  $\gamma$  against the angle  $\theta$ 

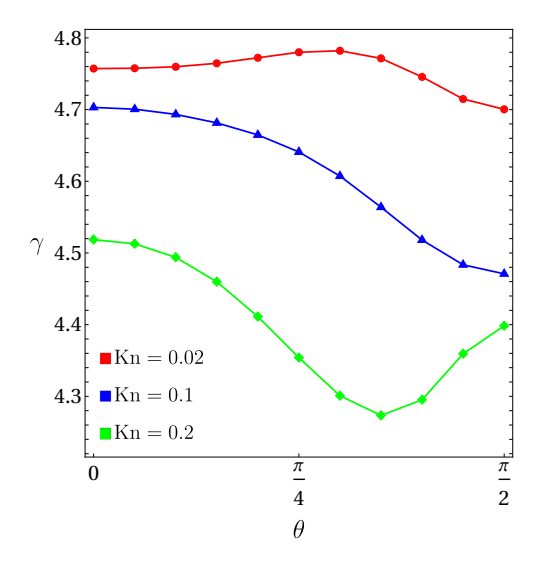


Figure 4.26: Variation of the parameter  $\gamma$  with the angle  $\theta$  for Kn = 0.02, 0.1 and 0.2. The other parameters are the same as those in Fig. 4.24.

for the Knudsen numbers Kn = 0.02, 0.1 and 0.2 in Fig. 4.26. The figure reveals that for a fixed  $\theta$  the critical value of  $\gamma$  in general decreases with the increasing Knudsen number, which was not so obvious in Fig. 4.24. In the similar problem of rarefied vapor flow between the condensed phases of two coaxial circular cylinders studied in Sec. 4.1 and also in Ref. [77], an explicit expression for the critical value of  $\gamma$  depending on Knudsen number was given. The critical value of  $\gamma$  for the present problem, however, not only depends on the Knudsen number but also on the angle due to the asymmetry associated with the elliptic cylinder. This is why we are unable to proffer an explicit expression for the critical value of  $\gamma$  for the present problem.

# 4.4 Rarefied gas flow inside a lid-driven square cavity

#### 4.4.1 Problem statement

A monatomic rarefied gas is considered to be contained inside an isothermal square cavity having dimensionless length of the side as L=1. Apart from the classical single lid-driven cavity problem, we also consider two other problems of two-sided lid-driven square cavities with top and bottom walls moving in the same and opposite directions. The considered flow scenarios are as follows.

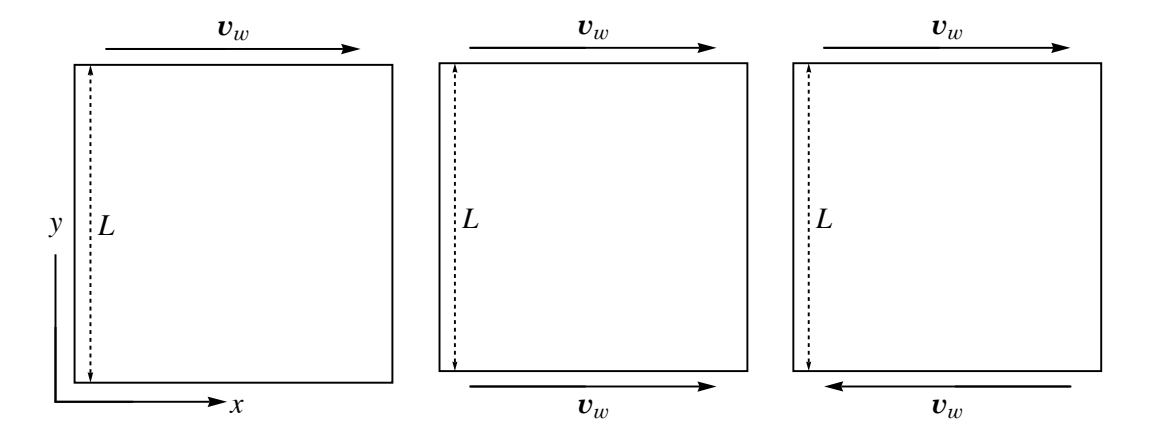


Figure 4.27: Schematics of (a) single-sided lid-driven cavity, and two-sided lid-driven cavities with top and bottom walls moving in the (b) same and (c) opposite directions.

1. In the first scenario, the upper boundary (referred to as the lid) of the square cavity is considered to be moving with a constant (dimensionless) velocity  $v_w$  in

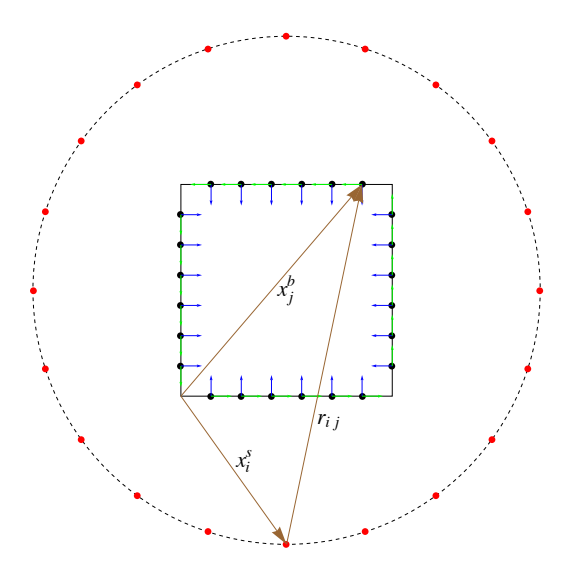


Figure 4.28: Schematic of the distribution of collocation points (or boundary nodes) on the boundaries and source points outside the flow region for the problem described in Sec. 4.4.1. The magenta and blue arrows demonstrate the tangential and normal directions at each boundary node, respectively.

the positive x-direction as shown in Fig. 4.27 (a). The other three boundaries are considered to be stationary.

- 2. The second scenario consists of the movement of the top and bottom walls of the square cavity. Both walls are considered to be moving in the positive x-direction with the same velocity  $v_w$  as shown in Fig. 4.27 (b). The left and right walls of the cavity are assumed to be stationary.
- 3. In the third scenario, the top and bottom walls of the square cavity are considered to be moving in opposite directions with the same speed as shown in Fig. 4.27 (c).

The boundary conditions (2.51)–(2.53) associated with the CCR model [(2.19)–(2.20)] in this problem reduce to

$$\boldsymbol{v} \cdot \boldsymbol{n} - \boldsymbol{v}_w \cdot \boldsymbol{n} = 0, \tag{4.21}$$

$$\boldsymbol{q} \cdot \boldsymbol{n} = -2\tau_0 (T + \alpha_0 \boldsymbol{n} \cdot \boldsymbol{\sigma} \cdot \boldsymbol{n}), \tag{4.22}$$

$$\boldsymbol{n} \cdot \boldsymbol{\sigma} \cdot \boldsymbol{t} = -\varsigma (\boldsymbol{v} \cdot \boldsymbol{t} - \boldsymbol{v}_w \cdot \boldsymbol{t} + \alpha_0 \boldsymbol{q} \cdot \boldsymbol{t}), \tag{4.23}$$

where  $v_w$  is the wall velocity, n and t are the unit normal and tangent vectors at the boundary, respectively. Throughout this section, the values of coupling coefficient and Prandtl number are fixed as  $\alpha_0 = 2/5$  and Pr = 2/3, respectively, which correspond to

the Maxwell molecules [88]. Implementation of the MFS for current problem involves the placement of source points outside the flow domain on a circular fictitious boundary, a schematic of which is illustrated in Fig. 4.28. The results have been obtained by fixing an equal number of boundary nodes and source points, i.e.,  $N_b = N_s = 200$  and the cavity region  $\{(x,y): 0 \le x \le 1, 0 \le y \le 1\}$ . The fictitious circular boundary on which the singularities or source points are placed is centered at (0.5, 0.5) with (dimensionless) radius  $R_s = 2$ .

# 4.4.2 Results for a single-sided lid-driven cavity

The dimensionless velocity of the lid is fixed to  $(v_x, v_y) = (1,0)$ . To validate the results obtained from the MFS applied to the CCR model, we illustrate the comparison with the data taken from Ref. [85] for the results obtained from DSMC method and the R13 equations. The left panel of Fig. 4.29 illustrates the variation of the (dimensionless)

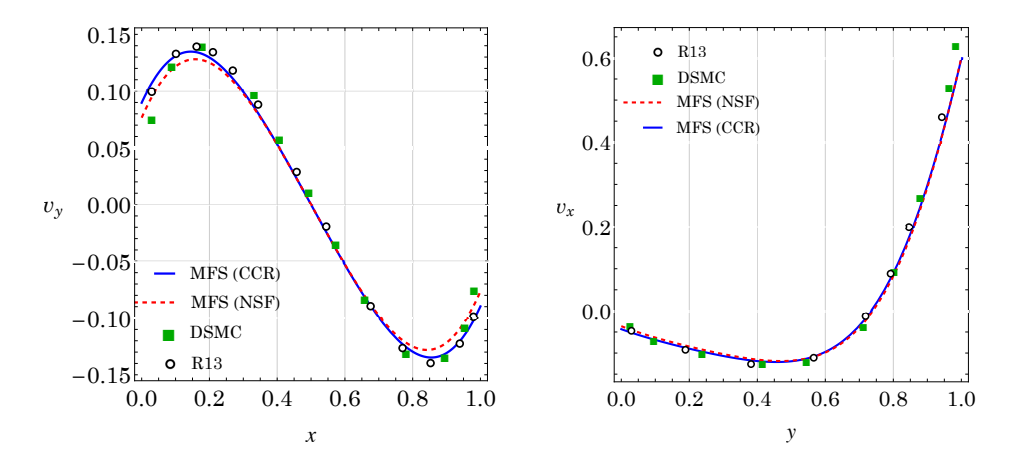


Figure 4.29: Variation of  $v_y$  along the horizontal centerline (i.e., for y=0.5) of the cavity (left panel) and variation of  $v_x$  along the vertical centerline (i.e., for x=0.5) of the cavity (right panel) for Kn = 0.08. The solid blue curve represents the results for the MFS applied to the CCR model, the dashed red curve represents the results for the MFS applied to the NSF model, the green (square) and black (circle) symbols denote the data from the DSMC method and R13 model, respectively, taken from Ref. [85].

vertical velocity along the x-direction at fixed y = 0.5, i.e., the variation of  $v_y(x, 0.5)$  along the horizontal centerline of the cavity for Kn = 0.08. Analogously, the right panel of Fig. 4.29 depicts the variation of the (dimensionless) horizontal velocity  $v_x(0.5, y)$  along

the vertical centerline of the cavity for Kn = 0.08. The solid blue curve represents the results for the CCR model solved via the MFS whereas the green (square) and black (circle) symbols denote the data from the DSMC method and the R13 model, respectively taken from [85]. Furthermore, we investigate the results obtained from the MFS applied to the NSF equations with second-order slip and jump boundary conditions [obtained by setting  $\alpha_0 = 1/4$  in Eq. (4.22) and  $\alpha_0 = 1/5$  in Eq. (4.23)]. The dashed red curve in Fig. 4.29 represents the results obtained from the MFS applied to the NSF model. It is evident that there is a good agreement among the results from the NSF model, CCR model, DSMC method and R13 model in both panels. The small inaccuracies near corners, especially with the DSMC results are due to the incapability of the NSF and CCR models to capture Knudsen layers, which are more pronounced near the boundaries.

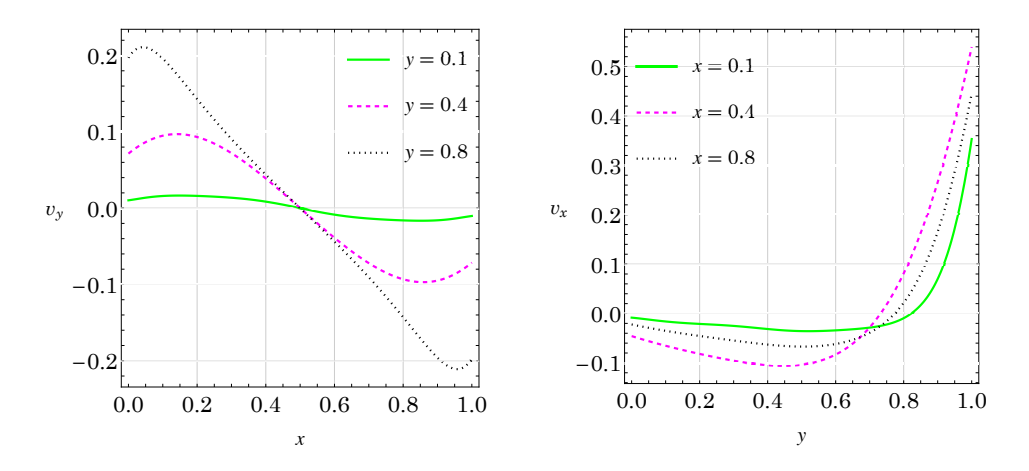


Figure 4.30: Variation in  $v_y$  along different horizontal lines y = 0.1, 0.4 and 0.8 inside the cavity (left panel) and the variation of  $v_x$  along different vertical lines x = 0.1, 0.4 and 0.8 inside the cavity (right panel) obtained by the MFS applied to the CCR model.

We also demonstrate the variation of  $v_y$  and  $v_x$  obtained from the MFS applied to the CCR model along different lines inside the cavity. Fig. 4.30 illustrates the variation in the vertical velocity  $v_y$  along different horizontal lines y = 0.1, 0.4 and 0.8 inside the cavity (left panel) and also the variation of the horizontal velocity  $v_x$  along different vertical lines x = 0.1, 0.4 and 0.8 inside the cavity (right panel). The increasing tendency of horizontal velocity component  $v_x$  with increase in y is due to the maximum horizontal velocity at lid, whereas the wave-like nature of the vertical velocity component  $v_y$  with

variation in x is due to the formation of vortices which could be depicted via velocity streamlines, which have been exhibited in Fig. 4.31. The left panel of Fig. 4.31 shows

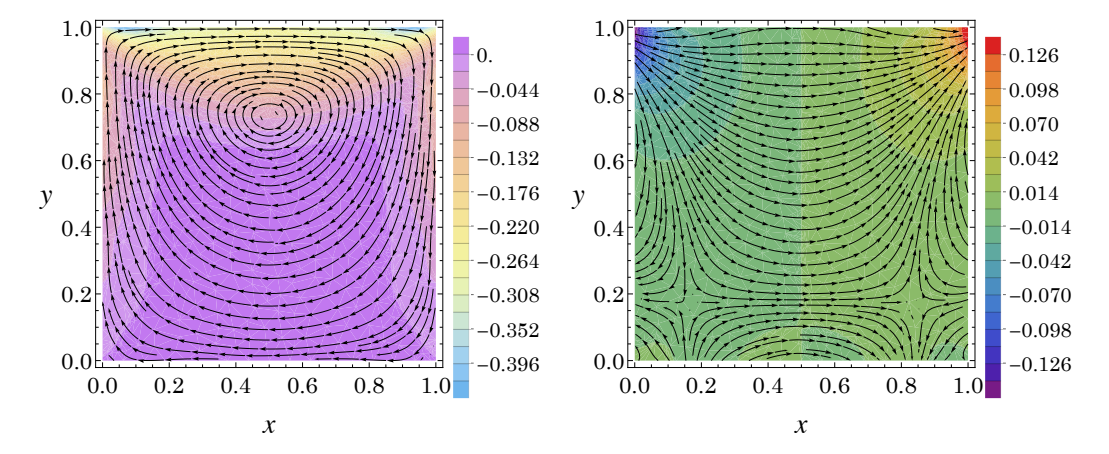


Figure 4.31: Velocity streamlines plotted over shear stress contours (left panel) and heat flux lines plotted over temperature contours (right panel) for the case when top wall is moving in the positive x-direction.

velocity streamlines over shear stress  $\sigma_{xy}$  contours for Kn = 0.08, indicating the clockwise vortex structure driven by the moving lid. The contours represent the distribution of shear stress  $\sigma_{xy}$  within the cavity induced due to velocity gradient. The right panel in Fig. 4.31 depicts the heat flux lines plotted over the temperature contours for Kn = 0.08. The second-order temperature-jump condition (4.22) causes cold and hot regions at the left and right corners near the moving lid, respectively, as wall temperature is influenced by stress. Moreover, the coupling between stress and heat flux (substituting Eq. (2.19)<sub>2</sub> into Eq. (2.20)<sub>2</sub>), gives

$$\boldsymbol{q} = -\frac{5\mathrm{Kn}}{2\mathrm{Pr}}(\boldsymbol{\nabla}T - \alpha_0 \boldsymbol{\nabla}p),\tag{4.24}$$

highlighting that heat flux depends on both temperature and pressure gradients. This relation introduces a competition between these gradients in determining the heat flow direction. In the present scenario, the pressure gradient dominates over the temperature gradient, leading to an anti-Fourier heat flow, as evidenced by the heat flux lines in the right panel Fig. 4.31. This non-classical phenomenon, observed in microscale and rarefied gas flows, occurs when heat flows from cooler to warmer regions, opposite to the conventional Fourier law of heat conduction [2]. This phenomenon can be predicted well by the CCR model due to the relation (4.24). However, as illustrated in the right panel

of Fig. 4.32, a clear limitation of the NSF model emerges when examining the heat flux lines. Although the NSF model with second-order slip and jump boundary conditions is able to reproduce the overall velocity field and streamlines reasonably well in the bulk region, it fails to capture the anti-Fourier heat transfer phenomena observed in both the CCR-MFS and DSMC simulations.

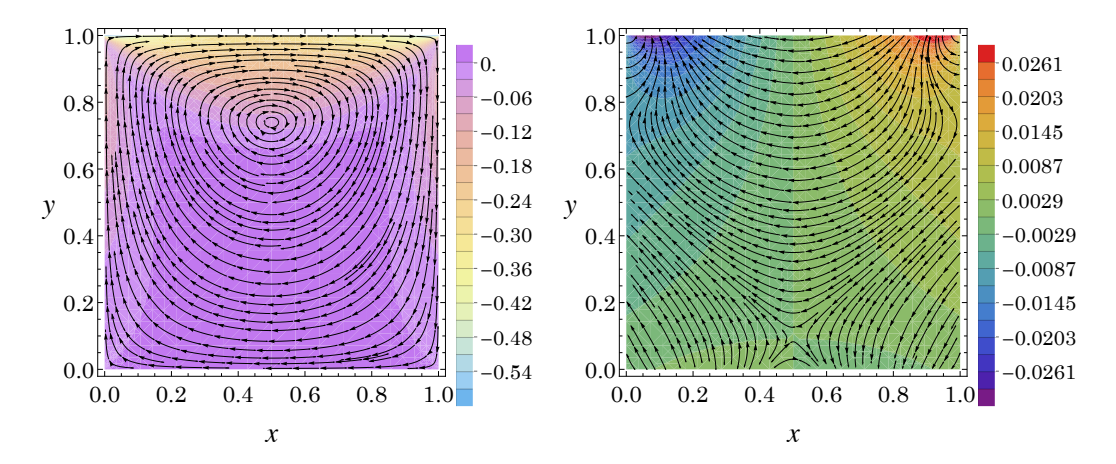


Figure 4.32: Velocity streamlines plotted over shear stress contours (left panel) and heat flux lines plotted over temperature contours (right panel) for Kn = 0.08 obtained from the MFS applied to the NSF model.

We also note that although the bulk flow and centerline velocity profiles agree closely with those in Ref. [85], significant differences appear in the temperature and heat-flux contours. The tilting and asymmetry reported in Ref. [85] arises due to fully non-linear equations, whereas the MFS framework employs the linearized CCR equations. The omission of non-linear convective terms enforces strictly symmetric fields. Such symmetric profiles are also seen in lid-driven cavity simulations for gas mixtures using linearized equations [39].

## 4.4.3 Results for the two-sided lid-driven cavity with top and bottom walls moving in the same direction

In this subsection, we showcase the flow characteristics when the top and bottom walls are moving in the same direction with the same horizontal speed  $v_x$  which is fixed as  $v_x = 1$  for computational purpose. The left panel in Fig. 4.33 shows the velocity streamlines overlaid on the shear stress  $\sigma_{xy}$  contours for Kn = 0.1. The streamlines indicate the flow pattern within the cavity, driven by the motion of the top and bottom walls. The flow

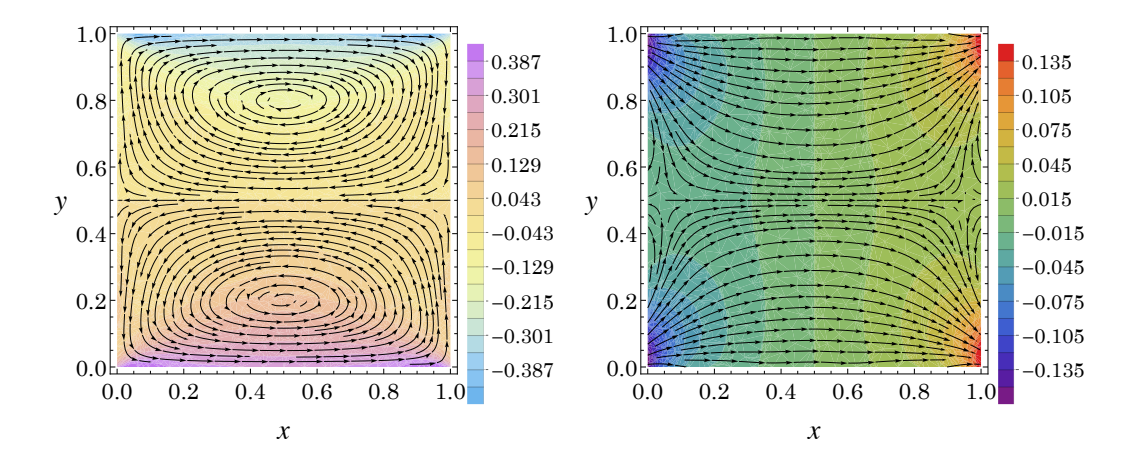


Figure 4.33: Velocity streamlines plotted over shear stress contours (left panel) and heat flux lines plotted over temperature contours (right panel) for the case when top and bottom walls are moving in same directions with the same speeds.

pattern reveals two primary vortices, each occupying the upper and lower halves of the cavity, rotating in the same direction as the moving walls. The contours show that the absolute shear stress is highest along the top and bottom walls. The negative/positive scales of shear stress are due to positive/negative velocity gradients inside the cavity. The heat flux lines plotted over the temperature contours for Kn = 0.1 are illustrated in the right panel of Fig. 4.33. The temperature contours depict hot and cold regions near the corners associated with both top and bottom walls. As evident from the right panel of the figure, the heat flows from colder to hotter regions again depicting the anti-Fourier effect produced due to pressure gradients inside the cavity.

## 4.4.4 Results for the two-sided lid-driven cavity with top and bottom walls moving in opposite directions

In this case, the horizontal velocity is fixed at  $v_x = 1$  and  $v_x = -1$  for the top and bottom walls, respectively, and the movement of walls leads to formation of a large vortex covering the entire cavity. As evident from the left panel of Fig. 4.34, the absolute value of shear stress is greatest near the corners of both top and bottom walls. In this scenario, the hot and cold regions along the bottom walls are opposite as compared to the previous case (Sec. 4.4.3). However, the heat flux lines again depict the anti-Fourier effect.

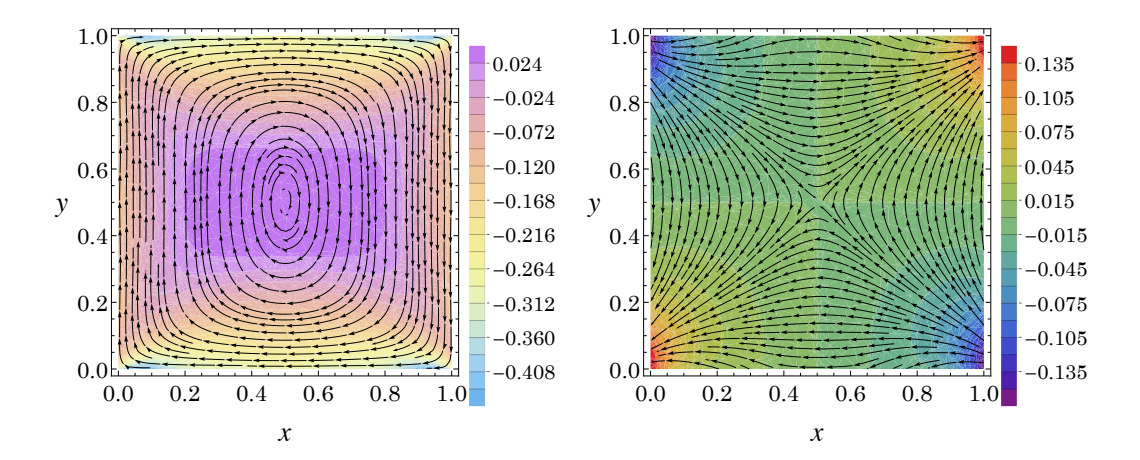


Figure 4.34: Velocity streamlines plotted over shear stress contours (left panel) and heat flux lines plotted over temperature contours (right panel) for the case when top and bottom walls are moving in opposite directions with the same speeds.

#### 4.5 Summary

In this chapter, the CCR-MFS framework has been applied to a few internal rarefied gas flow problems to assess its accuracy and demonstrate its potential. The framework has been tested for flow between coaxial circular cylinders, non-coaxial circular cylinders, coaxial circular and elliptic cylinders, and lid-driven square cavities. For coaxial circular cylinders, the results obtained from the CCR-MFS framework have shown excellent agreement with analytic solutions based on the linearized BGK model from the literature, particularly for low Knudsen numbers. The framework has successfully captured key flow features like reversal of temperature gradient. In the non-coaxial configuration involving thermally-induced flow, the CCR-MFS framework accurately captured the primary flow characteristics and key global quantities, including circulation patterns and drag, while minor discrepancies observed at higher Knudsen numbers are attributed to Knudsen layer effects not captured with the CCR model.

The framework has also been used to investigate flows between coaxial circular and elliptic cylinders, under both temperature-driven and evaporation/condensation conditions. It has accurately captured circulation patterns and demonstrated the effect of geometry on thermal-stress-slip flows. For lid-driven cavity flows, the results obtained from the CCR-MFS framework have matched well with DSMC and R13 data in the bulk

region, with noticeable differences near walls due to the limitations of the CCR model in capturing Knudsen layers. Importantly, the framework has captured non-classical effects such as anti-Fourier heat transfer. A sensitivity analysis on the location of source points has also been carried out to ensure numerical stability and accuracy.

### Chapter 5

# Application of the CCR-MFS framework for external flow problems

While the Stokes equations (a simplified version of the Navier–Stokes–Fourier equations) are effective in modeling slow and steady liquid flow past a sphere, they fail to yield a non-trivial solution to the problem of slow and steady liquid flow past an infinitely long cylinder (a two-dimensional problem essentially); this is referred to as Stokes' paradox. The paradox also arises when studying these problems for gases. In this chapter, we present a way to obtain meaningful solutions for two-dimensional flows of rarefied gases around objects by circumventing Stokes' paradox. To this end, we adopt the CCR model and determine its analytic solution for the problem and compare it with a numerical solution based on the MFS. Apart from addressing the problem of flow past a circular cylinder, we aim to showcase the capabilities of the MFS to predict the flow past other objects in two dimensions for which analytic solutions either do not exist or are difficult to determine. For that, we investigate the problem of rarefied gas flow past an infinitely long semicircular cylinder.

#### 5.1 Stokes' paradox

Fluid flow around stationary objects, especially spheres and cylinders, is a classic problem in fluid dynamics. Early research on low-speed viscous flows (often, referred to as low-Reynolds-number flows) of incompressible fluids was pioneered by Sir George Gabriel Stokes in the 19th century. He postulated that at low velocities, the inertial forces become negligible with the pressure forces predominantly balanced by the viscous forces alone and, for such flows, the Navier–Stokes equations in turn boil down to the celebrated Stokes equations. In the honor of Sir Stokes, such a flow is referred to as a Stokes flow

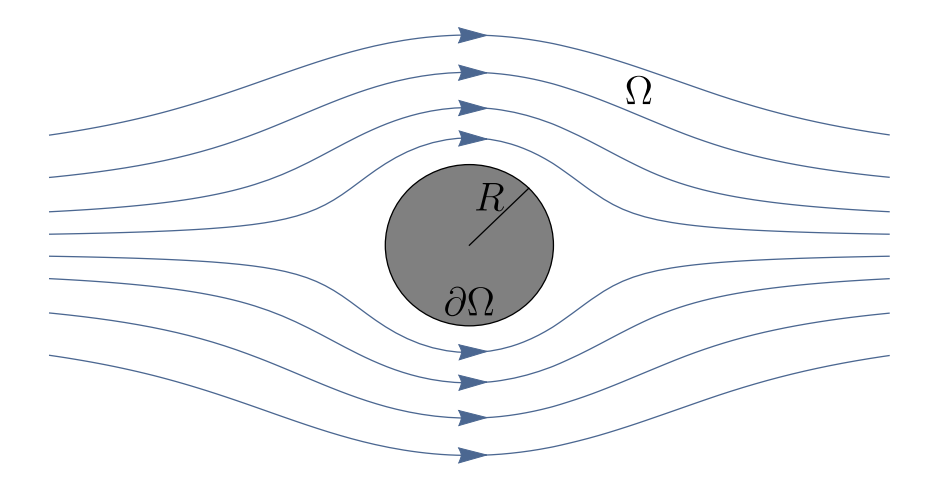


Figure 5.1: Schematic of Stokes flow past an infinite circular cylinder of radius R, where the fluid is moving transversely to the axis of the cylinder.

(or creeping flow). Stokes flows are often encountered in nature, e.g., in swimming of microorganisms and sperms, and also in industries dealing with paints, polymers, etc.

Stokes was successful in describing slow and steady flow of a viscous fluid past a sphere mathematically through the Stokes equations. However, when attempting to describe a slow and steady flow of a viscous fluid past an infinite cylinder (which is essentially a quasi-two-dimensional flow) using the Stokes equations [103], he encountered difficulties in satisfying the boundary conditions at the cylinder surface and in the fluid at infinity simultaneously. That led him to suggest the potential absence of a solution for the steady-state fluid flow past an infinite cylinder—a notion later coined as Stokes' paradox.

To explain the paradox mathematically, we consider a viscous fluid moving slowly and steadily past an infinitely long right-circular cylinder of radius R in the direction transverse to the axis of the cylinder as shown in Fig. 5.1. Let the flow domain be denoted by  $\Omega$  and the boundary of the disk by  $\partial\Omega$  and let the far-field velocity of the fluid be  $(v_0, 0, 0)$  in the Cartesian coordinate system. Owing to the symmetry around the axis of the cylinder, the problem essentially reduces to a (quasi-)two-dimensional problem or, equivalently, to the problem of fluid flow past a circular disk of radius R. The Stokes equations for the problem read

$$\nabla \cdot \mathbf{v} = 0 \quad \text{and} \quad \nabla p - \mu \Delta \mathbf{v} = \mathbf{0} \quad \text{in} \quad \Omega,$$
 (5.1)

where  $\boldsymbol{v}$ , p and  $\mu$  are the velocity, pressure and viscosity, respectively, of the fluid. The no-slip boundary condition on the surface of the cylinder reads

$$\mathbf{v} = \mathbf{0} \quad \text{on} \quad \partial \Omega$$
 (5.2)

and the far-field boundary condition reads

$$\lim_{|x| \to \infty} v_x = v_0. \tag{5.3}$$

Eliminating the pressure p from the Stokes equations (5.1) and introducing the stream function  $\psi(x,y)$ —which is related to the components of the velocity via the relations

$$v_x = \frac{\partial \psi}{\partial y}$$
 and  $v_y = -\frac{\partial \psi}{\partial x}$ , (5.4)

the Stokes equations (5.1) reduce to the biharmonic equation

$$\Delta^2 \psi = 0 \quad \text{in} \quad \Omega, \tag{5.5}$$

and the no-slip boundary condition (5.2) reduces to

$$\frac{\partial \psi}{\partial x} = \frac{\partial \psi}{\partial y} = 0 \quad \text{on} \quad \partial \Omega.$$
 (5.6)

For determining  $\psi$ , it is convenient to transform the equations from the Cartesian coordinate system (x, y) to the polar coordinate system  $(r, \theta)$  so that  $x = r \cos \theta$ ,  $y = r \sin \theta$ ,  $\psi(x, y) \equiv \psi(r, \theta)$ , which is related to the components of the velocity in the polar coordinates via the relations

$$v_r = r^{-1} \frac{\partial \psi}{\partial \theta}$$
 and  $v_\theta = -\frac{\partial \psi}{\partial r}$ . (5.7)

In the polar coordinates, the no-slip boundary condition (5.6) changes to

$$\frac{\partial \psi}{\partial r} = \frac{\partial \psi}{\partial \theta} = 0 \quad \text{at} \quad r = R \quad \text{and} \quad \forall \quad \theta \in [0, 2\pi)$$
 (5.8)

and the far-field condition (5.3) changes to

$$\lim_{r \to \infty} \frac{1}{r} \frac{\partial \psi}{\partial \theta} = v_0 \cos \theta \quad \text{and} \quad \lim_{r \to \infty} \frac{\partial \psi}{\partial r} = v_0 \sin \theta. \tag{5.9}$$

The far-field conditions (5.9) require that the stream function be of the form  $\psi = f(r) \sin \theta$  [58, 112, 121]. Inserting this form of  $\psi$  in (the polar form of) the biharmonic equation (5.5), its solution reads [67, 112]

$$\psi(r,\theta) = \left(Ar + \frac{B}{r} + Cr^3 + Dr\ln r\right)\sin\theta,\tag{5.10}$$

where A, B, C, D are constants that need to be determined using boundary conditions (5.8) and (5.9). Both conditions in boundary condition (5.9) imply that C = D = 0 and  $A = v_0$ . Consequently, there remains only one constant B with which two conditions in boundary conditions (5.8) are to be fulfilled, a scenario that is impossible unless  $v_0 = 0$ . This shows the nonexistence of solution to the Stokes equations for a steady flow past an infinite circular cylinder whereas such flows do exist physically—this is the essence of Stokes' paradox. The paradox arises not only in the case of flow past a circular cylinder, but also for an unbounded flow past any two-dimensional object of any shape [97].

Another important consequence of Stokes' paradox is that the drag force on the cylinder in the aforementioned problem turns out to be infinite [70], which is unreasonable physically. Numerous endeavors have been dedicated to addressing Stokes' paradox and to determine the correct drag force on an infinitely long cylinder immersed in a viscous fluid moving transversely to the axis of the cylinder [51, 53, 54, 57, 78, 81, 115]. Oseen [78], in 1910, propounded an improvement to the Stokes equations by considering inertia effects at large distances and proposed the Oseen equations by adding convective acceleration terms to the Stokes equations. Oseen equations not only resolved Stokes' paradox but also led to an improved approximation of the drag force on a sphere immersed in a slow viscous flow. Subsequent contributions by Lamb [57], Bairstow et al. [6] and Tomotika and Aoi [115], refined the drag coefficient approximations for the cylinder using the Oseen equations. Further attempts to advance Oseen's ideas sparked the birth of a novel domain in applied mathematics known as the method of matched asymptotic expansions. Originally, Kaplun [50] and Kaplun and Lagerstrom [51] executed the method of matched asymptotic expansions to obtain a new drag coefficient for flow past a circular cylinder. Further, Proudman and Pearson [81] used the method of matched asymptotic expansions for flows past cylinder and sphere, and they came up with a novel drag result for sphere. Later, Kida and Take [54], through asymptotic expansions, provided expressions for the drag coefficient at different orders of approximation for low-Reynolds-number flow past a cylinder. Their results on the drag coefficient agreed well with experimental measurements at low Reynolds numbers. Recently, Khalili and Liu [53] studied the problem of flow past a cylinder with the lattice-Boltzmann method and their simulation results on the drag coefficient led them to propose a slight correction to the expression for the drag coefficient obtained at the first order of approximation by Kida & Take [54].

In this chapter, we revisit the problem of fluid flow past a cylinder but with fluid being a rarefied gas instead of a viscous liquid. The reason for taking this problem is threefold: (i) the classic fluid dynamics models, e.g. the Navier–Stokes–Fourier (NSF) equations (or Stokes equations for that matter), are incapable of capturing many intriguing rarefaction effects pertinent to rarefied gases, and hence better models (typically more involved than the Stokes equations, which are somewhat easy to handle) are needed for modeling rarefied gas flows, (ii) the occurrence of Stokes' paradox in rarefied gases too poses mathematical challenges, and (iii) the problem leads to a method whose usefulness is noteworthy especially for problems for which an analytic solution either does not exist or is very difficult to obtain. Despite the presence of sufficient literature on two-dimensional unbounded flows in continuum fluid dynamics, there has been comparatively less attention towards rarefied gas flows past objects, particularly in two dimensions. To the best of the authors' knowledge, the first study on Stokes' paradox in rarefied gas flows was presented by Cercignani [17], wherein he showed that, despite the fact that the Boltzmann equation is the most accurate model for investigating rarefied gases, the linearized Boltzmann equation—similarly to the Stokes equations—does not give bounded solutions for the flow past an axisymmetric body. To circumvent Stokes' paradox, he proposed an inner-outer expansion of the Boltzmann equation. Yamamoto & Sera [128] investigated rarefied gas flow past a circular cylinder at low Mach numbers by dividing the flow into two regions: (i) the kinetic region (flow domain near the cylinder) modeling and (ii) near continuum region (flow domain outside the kinetic region). They handled the kinetic region with the simultaneous integral equations derived from the linearized Bhatnagar-Gross-Krook model and the continuum region with the Oseen-Stokes equation. Their result on the drag on the cylinder matched reasonably well with those available in previous studies for a wide range of the Knudsen number. Utilizing the advancements of moment methods in kinetic theory, Gu et al. [37] recently investigated non-equilibrium effects on flow past a circular cylinder. In this chapter, we investigate and validate slow flow of a monatomic rarefied gas past an infinitely long right-circular cylinder using the CCR model solved with the MFS.

#### 5.2 Flow past a circular cylinder

#### 5.2.1 Problem description

We consider a steady low-speed flow of a rarefied monatomic gas past an infinitely long right-circular cylinder having radius  $\tilde{R}_1$ . We assume that the cylinder is isothermal (having uniform temperature  $\tilde{T}_0$ , which is the same as the far-field ambient temperature of the gas) with a large solid-to-gas thermal conductivity ratio. Let the circular cross section of the cylinder be in the  $\tilde{x}\tilde{y}$ -plane, the axis of the cylinder be coinciding with the  $\tilde{z}$ -axis and the flow be approaching the cylinder from the negative  $\tilde{x}$ -direction toward the positive  $\tilde{x}$ -direction. As aforementioned, owing to the axial symmetry of the cylinder, the problem is quasi-two-dimensional, i.e. it is sufficient to study the problem for a circular disk of the same radius instead of studying the problem for the infinitely long cylinder. A two-dimensional cross-sectional view of the problem is depicted in Fig. 5.2 wherein the center of the disk is assumed to be fixed at the origin of the coordinate system. The radius of the disk is taken as the characteristic length scale  $\tilde{L}$  for non-dimensionalization so that

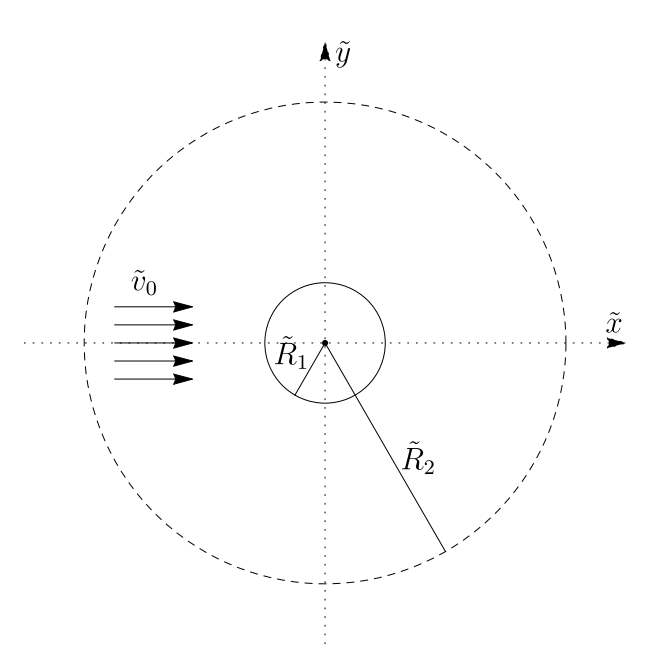


Figure 5.2: Cross-sectional view of the problem of a rarefied gas flow past an infinitely long cylinder. The solid circle represents the periphery of the cylinder while the dashed circle represents an artificial boundary far away from the cylinder.

the dimensionless radius of the disk is  $R_1 = \tilde{R}_1/\tilde{L} = 1$ . To circumvent Stokes' paradox and hence the non-existence of a solution to the problem, we assume an artificial circular boundary of radius  $\tilde{R}_2$  (where  $\tilde{R}_2 \gg \tilde{R}_1$ ) outside the disk. The radius of the artificial boundary is taken to be sufficiently large in comparison to the radius of the disk so that the artificial boundary has insignificant effects on the problem under consideration.

#### 5.2.2 Boundary conditions

From Sec. 2.2.3.1, the boundary conditions complementing the linear CCR model in two dimensions are

$$(\boldsymbol{v} - \boldsymbol{v}_w) \cdot \boldsymbol{n} = 0, \tag{5.11}$$

$$\boldsymbol{q} \cdot \boldsymbol{n} = -2\tau_0 (T - T_w + \alpha_0 \, \boldsymbol{n} \cdot \boldsymbol{\sigma} \cdot \boldsymbol{n}), \tag{5.12}$$

$$\boldsymbol{t} \cdot \boldsymbol{\sigma} \cdot \boldsymbol{n} = -\varsigma (\boldsymbol{v} - \boldsymbol{v}_w + \alpha_0 \, \boldsymbol{q}) \cdot \boldsymbol{t}, \tag{5.13}$$

where n and t are the unit normal and tangent vectors, respectively; and  $v_w$  and  $T_w$  are dimensionless perturbations in the velocity and temperature of the boundary wall.

To circumvent Stokes' paradox, an artificial boundary in the flow domain has been introduced. To ensure that there is no disturbance to the flow due to this artificial boundary, the boundary conditions at the artificial boundary are taken as

$$v_x = v_0, \quad v_y = 0 \quad \text{and} \quad T = 0.$$
 (5.14)

#### 5.2.3 Analytic solution

As mentioned above, flow past an infinitely long right circular cylinder is indeed a quasi-two-dimensional problem when the fluid flow is in the normal direction of the axis of the cylinder. In this case, there is no change in the flow variables in the axial direction of the cylinder. To tackle the problem, it is convenient to work in a cylindrical coordinate system  $(r, \vartheta, z)$ , wherein the z-axis coincides with the axis of the cylinder. Owing to the axial symmetry, the flow variables do not change along the z-direction.

In this cylindrical coordinate system, the linear steady-state CCR model (Eqs. (2.19) and (2.20)) can be written as follows. The mass, momentum and energy balance equations (2.19) in the cylindrical coordinate system read

$$\frac{\partial v_r}{\partial r} + \frac{1}{r} \frac{\partial v_{\vartheta}}{\partial \vartheta} + \frac{v_r}{r} = 0, \tag{5.15}$$

$$\frac{\partial p}{\partial r} + \frac{\partial \sigma_{rr}}{\partial r} + \frac{1}{r} \frac{\partial \sigma_{r\vartheta}}{\partial \vartheta} + \frac{\sigma_{rr} - \sigma_{\vartheta\vartheta}}{r} = 0, \tag{5.16a}$$

$$\frac{1}{r}\frac{\partial p}{\partial \vartheta} + \frac{\partial \sigma_{r\vartheta}}{\partial r} + \frac{1}{r}\frac{\partial \sigma_{\vartheta\vartheta}}{\partial \vartheta} + \frac{2\sigma_{r\vartheta}}{r} = 0, \tag{5.16b}$$

$$\frac{\partial q_r}{\partial r} + \frac{1}{r} \frac{\partial q_{\vartheta}}{\partial \vartheta} + \frac{q_r}{r} = 0, \tag{5.17}$$

where Eq. (5.15) is the mass balance equation  $(2.19)_1$ , Eqs. (5.16a) and (5.16b) are the momentum balance equation  $(2.19)_2$  in the r- and  $\vartheta$ -directions, respectively, and Eq. (5.17) is the energy balance equation  $(2.19)_3$ . It may be noted that the momentum balance equation in the z-direction is trivially satisfied, owing to the fact that there is no change in flow variables with respect to the z-coordinate. The closure relations (2.20) in the cylindrical coordinate system read

$$\sigma_{rr} = -2\operatorname{Kn}\frac{\partial v_r}{\partial r} - 2\operatorname{Kn}\alpha_0 \frac{\partial q_r}{\partial r},\tag{5.18a}$$

$$\sigma_{r\vartheta} = -\operatorname{Kn}\left(\frac{\partial v_{\vartheta}}{\partial r} + \frac{1}{r}\frac{\partial v_{r}}{\partial \vartheta} - \frac{v_{\vartheta}}{r}\right) - \alpha_{0}\operatorname{Kn}\left(\frac{\partial q_{\vartheta}}{\partial r} + \frac{1}{r}\frac{\partial q_{r}}{\partial \vartheta} - \frac{q_{\vartheta}}{r}\right),\tag{5.18b}$$

$$\sigma_{\vartheta\vartheta} = -2\operatorname{Kn}\left(\frac{1}{r}\frac{\partial v_{\vartheta}}{\partial\vartheta} + \frac{v_r}{r}\right) - 2\alpha_0\operatorname{Kn}\left(\frac{1}{r}\frac{\partial q_{\vartheta}}{\partial\vartheta} + \frac{q_r}{r}\right),\tag{5.18c}$$

$$q_r = -\frac{c_p \operatorname{Kn}}{\operatorname{Pr}} \left[ \frac{\partial T}{\partial r} + \alpha_0 \left( \frac{\partial \sigma_{rr}}{\partial r} + \frac{1}{r} \frac{\partial \sigma_{r\vartheta}}{\partial \vartheta} + \frac{\sigma_{rr} - \sigma_{\vartheta\vartheta}}{r} \right) \right], \tag{5.19a}$$

$$q_{\vartheta} = -\frac{c_p \operatorname{Kn}}{\operatorname{Pr}} \left[ \frac{1}{r} \frac{\partial T}{\partial \vartheta} + \alpha_0 \left( \frac{\partial \sigma_{r\vartheta}}{\partial r} + \frac{1}{r} \frac{\partial \sigma_{\vartheta\vartheta}}{\partial \vartheta} + \frac{2\sigma_{r\vartheta}}{r} \right) \right]. \tag{5.19b}$$

To determine an analytic solution of the CCR model (5.15)–(5.19b) (in quasi-two dimensions), we convert the partial differential equations (5.15)–(5.19b) into ordinary differential equations using symmetry ansatz, which is inspired by the solution of the Stokes equations. This approach has also been utilized in determining analytic solutions of the regularized 13-moment (R13) and regularized 26-moment (R26) equations in the linearized state for the problems of flow past a sphere and a cylinder [87, 116, 124]. In symmetry ansatz, the radial dependency of the variables is separated and the angular dependency of the variables is expressed using the sine and cosine functions. For this purpose, the vector and tensor components having an odd number of indices in  $\vartheta$  are selected to be proportional to  $\sin \vartheta$  whereas the scalars and tensor components with an even number of indices in  $\vartheta$  are made proportional to  $\cos \vartheta$  [116]. Furthermore, since the problem is quasi-two-dimensional, the dependency in z-coordinate of the variables is automatically eliminated. With these symmetry ansatz, the solutions for the vectors  $\mathbf{v}$  and  $\mathbf{q}$  are of the

form

$$\mathbf{v}(r,\vartheta) = \begin{bmatrix} a(r) \cos \vartheta \\ b(r) \sin \vartheta \\ 0 \end{bmatrix} \quad \text{and} \quad \mathbf{q}(r,\vartheta) = \begin{bmatrix} \alpha(r) \cos \vartheta \\ \beta(r) \sin \vartheta \\ 0 \end{bmatrix}, \tag{5.20}$$

the solutions for the scalars p and T are of the form

$$p(r, \vartheta) = c(r)\cos\vartheta$$
 and  $T(r, \vartheta) = d(r)\cos\vartheta$ , (5.21)

and the solution for  $\sigma$  is of the form

$$\boldsymbol{\sigma}(r,\vartheta) = \begin{bmatrix} \gamma(r)\cos\vartheta & \kappa(r)\sin\vartheta & 0\\ \kappa(r)\sin\vartheta & \omega(r)\cos\vartheta & 0\\ 0 & 0 & \sigma_{zz} \end{bmatrix}, \tag{5.22}$$

where a(r), b(r),  $\alpha(r)$ ,  $\beta(r)$ , c(r), d(r),  $\gamma(r)$ ,  $\kappa(r)$  and  $\omega(r)$  are the unknown functions that need to be determined, and  $\sigma_{zz} = -\left[\gamma(r) + \omega(r)\right] \cos \vartheta$  as  $\boldsymbol{\sigma}$  is a symmetric and tracefree tensor of rank 2. Insertion of ansatz (5.20)–(5.22) in Eqs. (5.15)–(5.19b) leads to a system of ordinary differential equations in the unknowns a(r), b(r),  $\alpha(r)$ ,  $\beta(r)$ , c(r), d(r),  $\gamma(r)$ ,  $\kappa(r)$  and  $\omega(r)$  that is solved to determine these unknowns. Substituting the obtained values of the unknowns in ansatz (5.20)–(5.22), we get the following solution for the field variables.

$$v_r(r,\theta) = \left(c_3 - \frac{c_4}{r^2} + c_5 r^2 + c_6 \ln r\right) \cos \theta, \tag{5.23}$$

$$v_{\vartheta}(r,\vartheta) = \left(-c_3 - \frac{c_4}{r^2} - 3c_5r^2 - c_6 - c_6 \ln r\right) \sin \vartheta, \tag{5.24}$$

$$q_r(r,\vartheta) = \left(\frac{c_1}{r^2} + c_2\right)\cos\vartheta,\tag{5.25}$$

$$q_{\vartheta}(r,\vartheta) = \left(\frac{c_1}{r^2} - c_2\right)\sin\vartheta,\tag{5.26}$$

$$p(r,\vartheta) = \operatorname{Kn}\left(8rc_5 - \frac{2c_6}{r}\right)\cos\vartheta,\tag{5.27}$$

$$\sigma_{rr}(r,\vartheta) = \operatorname{Kn}\left(\frac{4\alpha_0 c_1}{r^3} - \frac{4c_4}{r^3} - 4rc_5 - \frac{2c_6}{r}\right)\cos\vartheta,\tag{5.28}$$

$$\sigma_{r\vartheta}(r,\vartheta) = \operatorname{Kn}\left(\frac{4\alpha_0 c_1}{r^3} - \frac{4c_4}{r^3} + 4rc_5\right) \sin\vartheta, \tag{5.29}$$

$$\sigma_{\vartheta\vartheta}(r,\vartheta) = \operatorname{Kn}\left(\frac{-4\alpha_0 c_1}{r^3} + \frac{4c_4}{r^3} + 4rc_5 + \frac{2c_6}{r}\right)\cos\vartheta,\tag{5.30}$$

$$T(r,\vartheta) = \left[ \frac{\Pr}{c_p \operatorname{Kn}} \left( \frac{c_1}{r} - rc_2 \right) + \operatorname{Kn}\alpha_0 \left( 8rc_5 - \frac{2c_6}{r} \right) \right] \cos \vartheta.$$
 (5.31)

The constants  $c_1$ ,  $c_2$ ,  $c_3$ ,  $c_4$ ,  $c_5$  and  $c_6$  in the above solution are determined using boundary conditions (5.11)–(5.14). However, it is crucial to acknowledge that without the presence of the outer artificial wall or, in other words, without imposing the specified boundary conditions (5.14), determining the six constants  $c_1$ ,  $c_2$ ,  $c_3$ ,  $c_4$ ,  $c_5$  and  $c_6$  uniquely through three boundary conditions (5.11)–(5.13) is impracticable. Moreover, for solutions to converge in the far-field (as  $r \to \infty$ ), it becomes necessary that  $c_2 = c_5 = c_6 = 0$ . Additionally, if the boundary conditions (5.11)–(5.13) are imposed, it follows that the remaining constants  $c_1$ ,  $c_3$ , and  $c_4$  also become zero, resulting in an overall zero solution. This scenario illustrates the occurrence of Stokes' paradox with the CCR model as well, and thereby affirms the necessity of employing an artificial boundary to circumvent this paradox. Therefore, the constants  $c_1$ ,  $c_2$ , ...,  $c_6$  are determined using boundary conditions (5.11)–(5.14). The obtained flow variables—when required—can be converted back into the Cartesian coordinate system using the transformation

$$\begin{bmatrix} \hat{x} \\ \hat{y} \\ \hat{z} \end{bmatrix} = \begin{bmatrix} \cos \vartheta & -\sin \vartheta & 0 \\ \sin \vartheta & \cos \vartheta & 0 \\ 0 & 0 & 1 \end{bmatrix} \begin{bmatrix} \hat{r} \\ \hat{\vartheta} \\ \hat{z} \end{bmatrix}, \tag{5.32}$$

where  $\hat{x}, \hat{y}, \hat{z}$  denote the unit vectors in the Cartesian coordinate system and  $\hat{r}, \hat{\vartheta}, \hat{z}$  are the unit vectors in the polar coordinate system. For instance, the velocity is given by

$$\mathbf{v} = \begin{bmatrix} v_x & v_y & 0 \end{bmatrix}^\mathsf{T} = \begin{bmatrix} v_r \cos \vartheta - v_\vartheta \sin \vartheta & v_r \sin \vartheta + v_\vartheta \cos \vartheta & 0 \end{bmatrix}^\mathsf{T}. \tag{5.33}$$

#### 5.2.4 Implementing the MFS

In the present problem, we do not deal with evaporation/condensation problems, so it is not necessary to include a sourcing term in the mass balance equation and hence the fundamental solutions with point force heat source are utilized from Sec. 3.3. The fundamental solutions of the CCR model in 2D read

$$\boldsymbol{v}(\boldsymbol{r}) = \frac{1}{8\pi \mathrm{Kn}} \boldsymbol{f} \cdot \left[ \frac{2\boldsymbol{r}\boldsymbol{r}}{r^2} - (2\ln r - 1)\boldsymbol{I} \right] + \frac{c_p \mathrm{Kn}}{2\pi \mathrm{Pr}} \alpha_0^2 \boldsymbol{f} \cdot \left( \frac{2\boldsymbol{r}\boldsymbol{r}}{r^4} - \frac{\boldsymbol{I}}{r^2} \right), \tag{5.34}$$

$$p(\mathbf{r}) = \frac{\mathbf{f} \cdot \mathbf{r}}{2\pi r^2},\tag{5.35}$$

$$\boldsymbol{\sigma}(\boldsymbol{r}) = \frac{2\operatorname{Kn} g \,\alpha_0 + \boldsymbol{f} \cdot \boldsymbol{r}}{2\pi} \left( \frac{2\boldsymbol{r}\boldsymbol{r}}{r^4} - \frac{\boldsymbol{I}}{r^2} \right),\tag{5.36}$$

$$T(\mathbf{r}) = -\frac{\Pr g}{2\pi \operatorname{Kn} c_n} \ln r, \tag{5.37}$$

$$\boldsymbol{q}(\boldsymbol{r}) = \frac{g}{2\pi} \frac{\boldsymbol{r}}{r^2} - \frac{c_p \operatorname{Kn}}{2\pi \operatorname{Pr}} \alpha_0 \boldsymbol{f} \cdot \left( \frac{2\boldsymbol{r}\boldsymbol{r}}{r^4} - \frac{\boldsymbol{I}}{r^2} \right), \tag{5.38}$$

where  $r = |\mathbf{r}|$ .

As discussed in Sec. 5.1, the mathematical origin of Stokes' paradox lies in the logarithmic dependence of the solution of the Stokes equations. This logarithmic dependence is also seen in the fundamental solutions of the CCR model (see Eqs. (5.34) and (5.37)), due to which the solution diverges in the far field. To circumvent this difficulty, we employ the MFS on a bounded domain by introducing an artificial outer boundary which is far enough from the original circular disk. To place the singularity points outside the computational domain, we assume that the source points are located on two circles—one inside the actual periphery of the disk and the other outside of the artificial boundary. The circles on which the singularity points are placed will henceforth be referred to as the fictitious boundaries. An illustration depicting the boundary nodes on the periphery of the disk and on the artificial boundary, and the location of source points on the fictitious boundaries is presented in Fig. 5.3. We consider a total of  $N_s$  source points, out of which  $N_{s_1}$  points lie on the inner fictitious boundary having dimensionless radius  $R'_1$ 

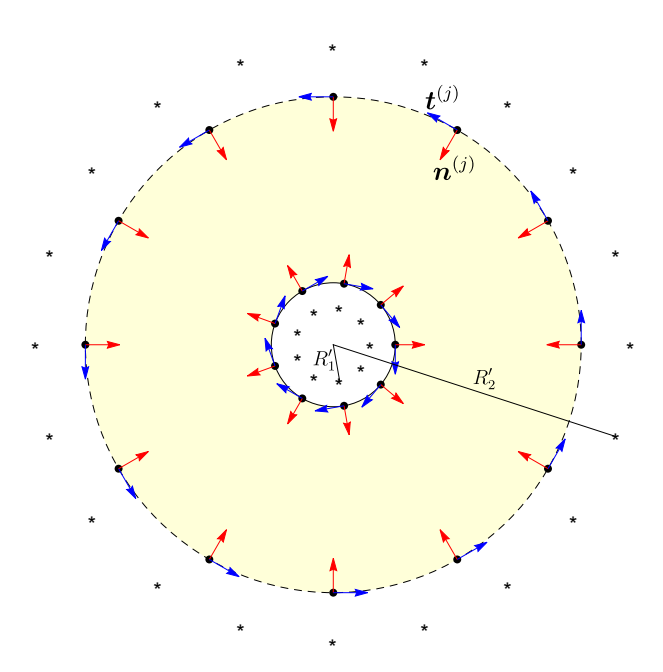


Figure 5.3: Placement of the collocation points (black dots) on the actual and artificial boundaries and singularities (black stars) outside of these boundaries. The blue and red arrows at each boundary node denote the unit tangent and normal vectors, respectively.

and  $N_{s_2}$  points on the outer fictitious boundary having dimensionless radius  $R'_2$  (where  $R'_1 < R_1$  and  $R'_2 > R_2$ ). Furthermore, we place  $N_{b_1}$  boundary nodes on the actual periphery of the disk and  $N_{b_2}$  boundary nodes on the artificial boundary accounting for a total of  $N_b$  boundary points. Corresponding to the  $i^{\text{th}}$  singularity  $(i = 1, 2, 3, \dots, N_s)$ , there are three unknowns, namely  $f_{1_i}$ ,  $f_{2_i}$  and  $g_i$ , where  $f_{1_i}$  and  $f_{2_i}$  are the components of the point force  $f_i$  applied on the  $i^{th}$  singularity, i.e.  $f_i = \begin{bmatrix} f_{1_i} & f_{2_i} \end{bmatrix}^{\mathsf{I}}$ , and  $g_i$  is the point heat source applied on the  $i^{\text{th}}$  singularity. Thus, there are a total of  $3 \times N_s$  unknowns, which are to be computed using the boundary conditions at both the actual and artificial boundaries. This means that three boundary conditions need to be applied at each boundary node, which leads to a set of  $3 \times N_b$  linear algebraic equations that are to be solved for  $3 \times N_s$  unknowns. The boundary conditions (5.11)–(5.13) are evaluated for the  $j^{\text{th}}$  boundary node on the actual periphery of the disk (for  $j = 1, 2, ..., N_{b_1}$ ), while the boundary conditions (5.14) are evaluated for the  $j^{th}$  boundary node on the artificial boundary (for  $j = 1, 2, ..., N_{b_2}$ ). Using the boundary conditions, we obtain a system of  $3N_{b_1}+3N_{b_2}=3N_b$  linear equations in  $3N_s$  unknowns, namely  $f_{1_1},\,f_{2_1},\,g_1,\,f_{1_2},\,f_{2_2},\,g_2,\ldots,$  $f_{1_{N_s}}, f_{2_{N_s}}, g_{N_s}$ . This system can be written in a matrix form as

$$\mathcal{M}U = b, \tag{5.39}$$

where U is the column vector containing all the unknowns, i.e.  $U = \begin{bmatrix} f_{1_1} & f_{2_1} & g_1 & f_{1_2} & f_{2_2} \\ g_2 & \dots & f_{1_{N_s}} & f_{2_{N_s}} & g_{N_s} \end{bmatrix}^\mathsf{T}$ ;  $\mathcal{M}$  is the corresponding collocation matrix and  $\mathbf{b}$  is the column vector containing only the wall properties, e.g.,  $v_0$ . We have solved the system using the method of least squares in Mathematica. Since the MFS may lead to a bad-conditioned collocation matrix, it is favorable to use the method of least squares even if the collocation matrix is square [26].

#### 5.2.5 Results and discussion

For numerical computations, we fix the dimensionless radius of the artificial boundary to  $R_2 = 10$  and the dimensionless radii of the inner and outer fictitious boundaries to  $R'_1 = 0.5$  and  $R'_2 = 20$ , respectively, the number of boundary nodes on the actual periphery of the disk to  $N_{b_1} = 50$  and the number of boundary nodes on the artificial boundary to  $N_{b_2} = 100$ . For simplicity, we fix the number of singularity points on the inner fictitious boundary to be equal to the number of inner boundary nodes, i.e.  $N_{s_1} = N_{b_1} = 50$ , and the number of singularity points on the outer fictitious boundary to be equal to the

number of boundary nodes on the outer artificial boundary, i.e.  $N_{s_2} = N_{b_2} = 100$  so as to make the collocation matrix (having dimensions  $3N_b \times 3N_s$ ) square. Notwithstanding, the results obtained with a rectangular collocation matrix do not differ significantly from those obtained with a square collocation matrix in the present work since we have used the method of least squares for solving the formed system of equations numerically. Furthermore, the (dimensionless) approaching velocity (in the x-direction) of the gas far away from the cylinder has been fixed to  $v_0 = 1$ .

In order to validate our code, we first plot the (dimensionless) speed of the gas against the radial position (as one moves away from the cylinder) for the angles  $\vartheta = 0$ ,  $\pi/4$  and  $\pi/2$  in Fig. 5.4.

From left to right, the panels in the figure depict the speed of the gas for Kn = 0.1, 0.5 and 1. The solid lines in the figure delineate the results obtained from the MFS applied on the CCR model while the symbols display the results obtained from the analytic solution of the CCR model obtained in Sec. 5.2.3. An excellent agreement of the results from the MFS with the analytic results—evident in the figure—validates our numerical code. The figure reveals that the speed of the gas starts increasing for all values of  $\vartheta$  as one moves away from the disk. For  $\vartheta = 0$ , the speed keeps on increasing with r all the way till the artificial boundary. On the other hand, for  $|\vartheta| > 0$  (blue and red colors in the figure), the speed of the gas starts increasing as one moves away from the disk; the speed

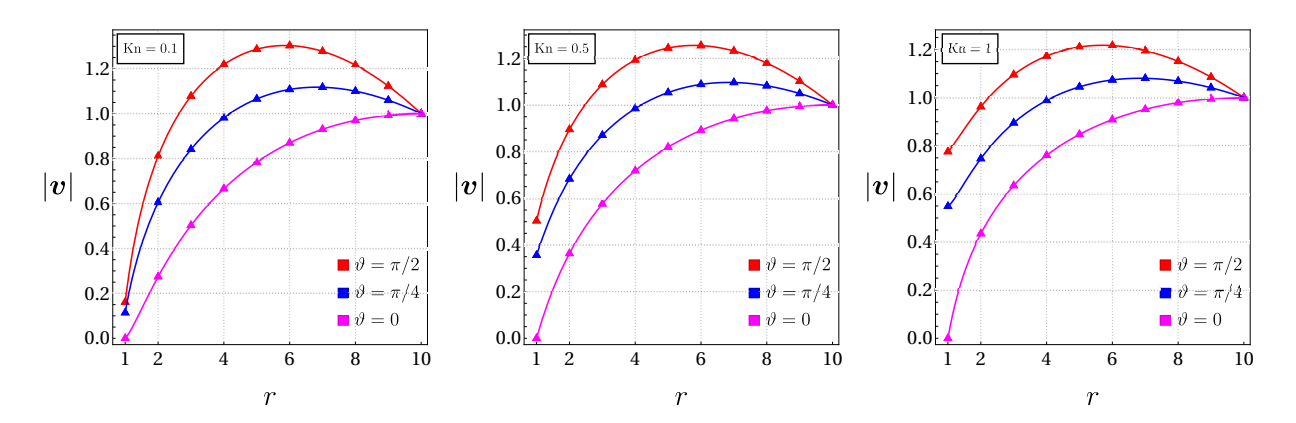


Figure 5.4: Speed of the gas varying with the radial position in different directions for Kn = 0.1, 0.5 and 1. The solid lines represent the results obtained from the MFS applied to the CCR model and the symbols represent the analytic solutions. The other parameters are  $N_{b_1} = N_{s_1} = 50$ ,  $N_{b_2} = N_{s_2} = 100$ ,  $R_1 = 1$ ,  $R_2 = 10$ ,  $R'_1 = 0.5$  and  $R'_2 = 20$ .

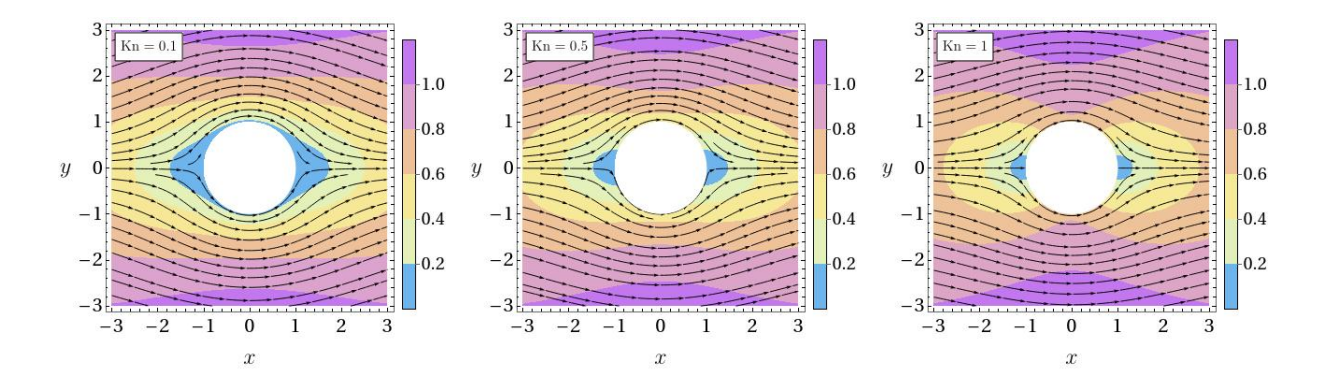


Figure 5.5: Velocity streamlines over speed contours obtained from the MFS applied on the CCR model for the Knudsen numbers Kn = 0.1, 0.5 and 1. The other parameters are the same as those for Fig. 5.4.

even surpasses its inlet value due to the accelerated flow occurring due to the production of pressure gradient around the disk; after attaining a maximum at a point somewhere in between the periphery of the disk and the artificial boundary the speed slows down on moving further away from the disk to match the fixed speed (through the boundary condition) on the artificial boundary. The figure also shows that for  $|\vartheta| > 0$  (blue and red colors in the figure), the speed of the gas on the disk increases with the Knudsen number due to increasing slip velocity with the Knudsen number.

In order to have a better idea about the speed and velocity profiles around the disk, the streamlines and speed contours obtained from the MFS for Kn = 0.1, 0.5 and 1 are exhibited in Fig. 5.5. While the streamlines in Fig. 5.5 are qualitatively alike, the speed contours reveal the quantitative differences for different Knudsen numbers. The speed contours in Fig. 5.5, similarly to Fig. 5.4, also show that the speed of the gas at any point in the domain increases with increasing the Knudsen number in general. Particularly, it is clearly visible from the speed contours in a close proximity of the disk. Moreover, for  $|\vartheta| = \pi/2$ , Fig. 5.5—similarly to that shown by red lines in Fig. 5.4—shows that the point at which the speed surpasses its inlet value of  $v_0 = 1$  becomes closer and closer to the disk with increasing the Knudsen number.

It is well established theoretically as well as experimentally that rarefied gases, when flowing around an object, manifest temperature polarization near the boundary of the object, even in the absence of any external temperature difference [7, 85, 111, 116, 124]. Temperature polarization in rarefied gas flows past solid objects is a phenomenon where a

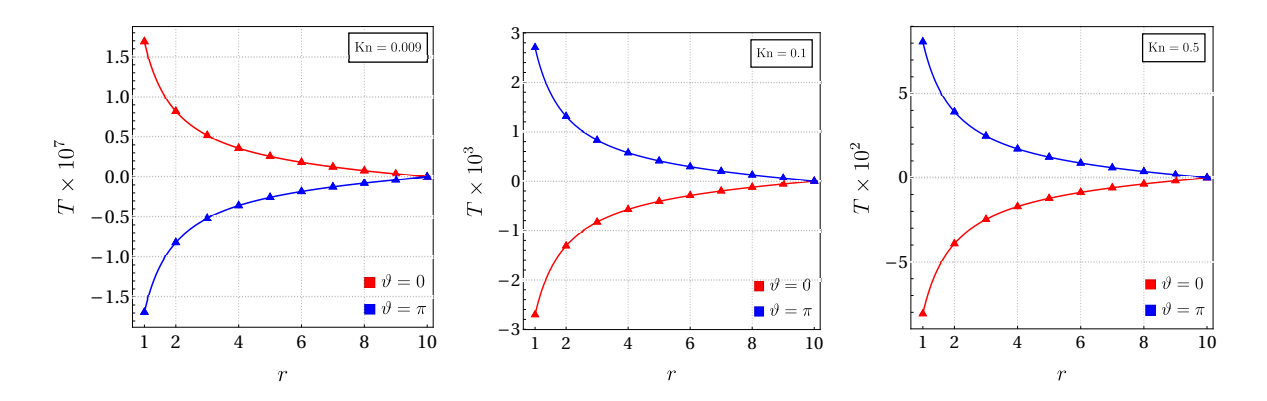


Figure 5.6: Temperature along the left and right sides of the disk for Kn = 0.009, 0.1 and 0.5. Solid lines represent the results obtained from the MFS applied to the CCR model and the triangles represent the analytic solutions. The other parameters are the same as those for Fig. 5.4.

solid object—such as a cylinder or sphere—develops a non-uniform temperature distribution on its surface, even if the object itself is maintained at a constant temperature, when it is placed in a steady flow of rarefied gas. In other words, because of rarefaction effects, some regions of the object may become slightly warmer or cooler compared to other regions, despite the entire surface being isothermal in terms of boundary conditions. The underlying reason for temperature polarization is the non-equilibrium nature of molecular interactions at the gas-surface interface when the gas is rarefied. The incoming and reflected molecules transfer energy differently at various points on the surface depending on the flow direction and rarefaction level. To check for the temperature polarization effect in the problem under consideration, we plot the (dimensionless) temperature of the gas at different points along the x-axis in Fig. 5.6, which illustrates the temperature on the left and right sides of the disk (i.e. along  $\theta = \pi$  and  $\theta = 0$ , respectively) for different values of the Knudsen number Kn = 0.009, 0.1 and 0.5. Since the induced temperature is very small, the temperature has been scaled up by its order while depicting it in Fig. 5.6. The solid lines and symbols again denote the results obtained from the MFS applied on the CCR model and from the analytic solution, respectively, and they again turn out to be in an admirable agreement. The figure shows the presence of temperature polarization. Nonetheless, for small Knudsen number Kn = 0.009 that corresponds to the hydrodynamic regime (the left most panel in the figure), the magnitude of temperature polarization is very small (of the order of  $10^{-7}$ ) with minute cold and hot regions near the disk boundary at  $\theta = \pi$  and  $\theta = 0$ , respectively. However, as the Knudsen number increases (see the middle and right panels of the figure), the magnitude of temperature polarization increases and, moreover, temperature reversal can also be seen from the middle and right panels of the figure for Kn = 0.1 and Kn = 0.5. The temperature reversal for higher Knudsen numbers has also been seen in rarefied gas flows around spheres [116]. To get deeper insights of temperature polarization and temperature reversal, we plot the temperature contours and heat-flux lines in Fig. 5.7. The figure shows that the heat-flux lines in all panels are starting from the right side of the disk and going toward the left side of the disk for all Knudsen numbers. However, the temperature on the right side of the disk is higher than that on the left side only for very small Knudsen numbers (e.g. for Kn = 0.009 in the left most panel of Fig. 5.7), i.e. when the flow is in the hydrodynamic regime. In this regime, Fourier's law remains valid and hence the heat flows from hot to cold regions. For large Knudsen numbers (e.g., for Kn = 0.1 and 0.5 in the middle and right panels of Fig. 5.7), the temperature on the left side of the disk is higher than that on the right side due to temperature reversal and heat interestingly seems to be flowing from cold to hot regions, which is an anti-Fourier effect and is common to stress-driven rarefied gas flows; see, e.g., Refs. [39, 85, 87, 88, 116]. As no temperature difference is applied externally in such problems, minuscule temperature differences are rendered by stress gradients. In other words, stress gradients in such problems dominate the temperature gradients and since Fourier's law depends only on the temperature gradient, anti-Fourier effect cannot be described by the NSF equations. On the other hand, the inherent coupling of the heat flux with stress gradient in the constitutive relations for the CCR model enables it to capture the anti-Fourier effect. To corroborate the inability of the NSF model in capturing the above findings, we have also applied the MFS to the NSF model (by setting  $\alpha_0 = 0$  in the CCR model) and displayed the temperature contours and heat-flux lines obtained from the MFS applied to the NSF model in Fig. 5.8. It turns out that the NSF model with the first-order temperature-jump boundary condition does not show temperature polarization at all (not shown here explicitly). With the second-order temperature jump boundary condition, the NSF model does show temperature polarization, yet reversal of temperature does not appear in order to respect imposed Fourier's law adherent to the NSF equations, which is clearly discernible in Fig. 5.8 that has been made using the second-order velocity-slip and temperature-jump boundary conditions.

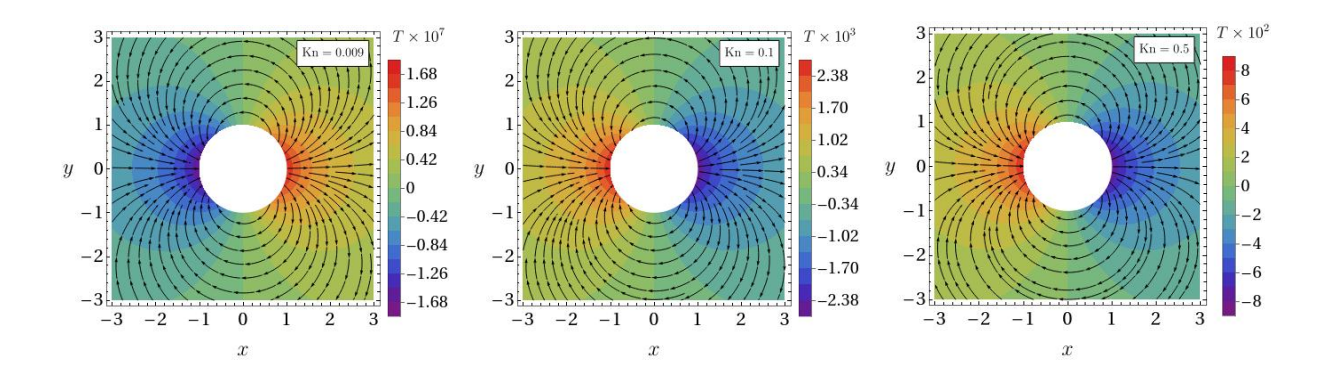


Figure 5.7: Heat-flux lines over temperature contours obtained from the MFS applied to the CCR model for Knudsen numbers Kn = 0.009, 0.1 and 0.5. The other parameters are the same as those for Fig. 5.4.

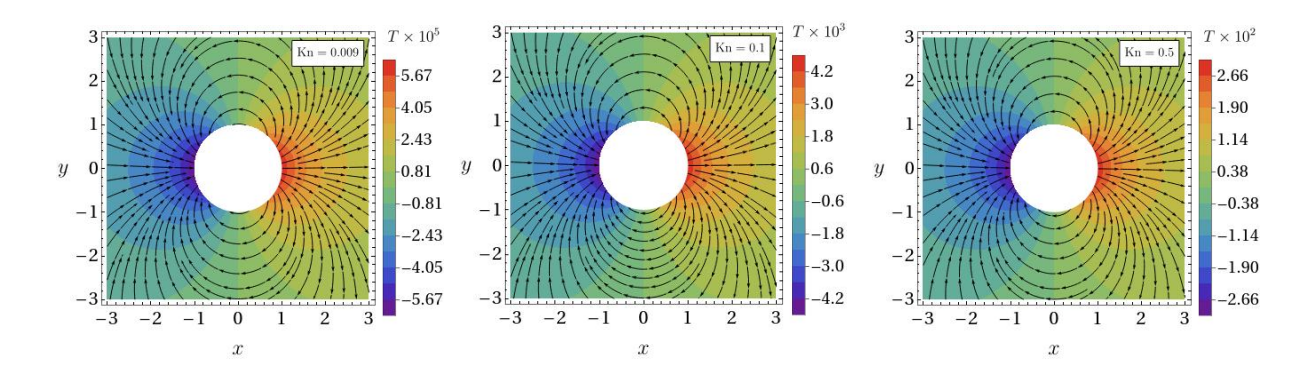


Figure 5.8: Heat-flux lines over temperature contours obtained from the MFS applied to the NSF model for Knudsen numbers Kn = 0.009, 0.1 and 0.5. The other parameters are the same as those for Fig. 5.4.

Furthermore, by comparing Figs. 5.7 and 5.8, it is evident that the NSF model does not show the temperature reversal.

As also mentioned above, Fig. 5.6 and the color bars in Figs. 5.7 and 5.8 show that the magnitude of the temperature generated near the left and right sides of the disk increases with the increasing the Knudsen number. Indeed, the temperature polarization and temperature reversal are second-order effects with respect to the Knudsen number. Hence, the generated temperature is actually of  $\mathcal{O}(\mathrm{Kn^2})$ . In order to illustrate this, we plot the temperature of the gas at r=1 and  $\vartheta=0$  scaled with  $\mathrm{Kn^2}$  against the Knudsen number for different locations of the artificial boundary in Fig. 5.9. The left panel of the figure displays the results obtained with the CCR model and the right panel exhibits the results obtained with the NSF equations and the second-order accurate boundary

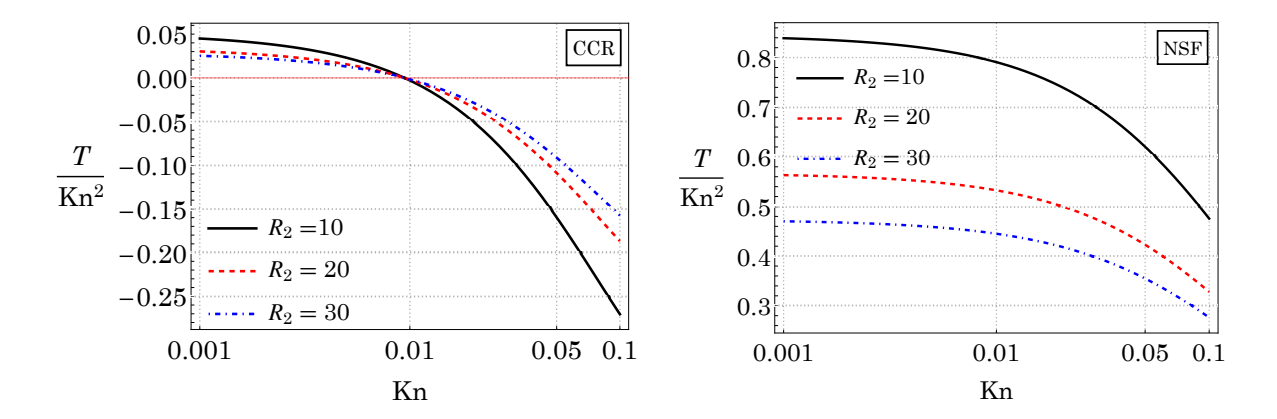


Figure 5.9: Temperature of the gas at r = 1 and  $\vartheta = 0$  scaled with Kn<sup>2</sup> plotted against the Knudsen number for different locations of the artificial boundary. The left panel shows the results obtained with the CCR model and the right panel shows the results obtained with the NSF equations and the second-order accurate boundary conditions.

conditions. The figure shows that  $T/\mathrm{Kn^2}$  indeed has a common scale for all Knudsen numbers. The left panel of Fig. 5.9 again reveals the presence of a critical Knudsen number at which  $T/\mathrm{Kn^2}$  changes its sign. This critical Knudsen number, which is  $\mathrm{Kn} \approx 0.0094115$ , in the left panel of the figure demarcates the point of temperature reversal. Evidently from the right panel, the NSF equations even with the second-order boundary conditions do not show the temperature reversal. Fig. 5.9 further shows that while the temperature profiles are qualitatively similar for all locations of the artificial boundary, quantitative differences are conspicuously present. Indeed, the figure exhibits decreasing magnitudes of the temperature with increasing values of  $R_2$ . It is interesting, however, to note that irrespective of the location of the artificial boundary, the critical Knudsen number for the temperature reversal remains fixed as evident from the left panel of Fig. 5.9.

In order to check the dependence of other flow variables on the location of the artificial boundary, we also plot the maximum speed of the gas  $v_{\text{max}} = \max\{|\boldsymbol{v}|\}$  on the disk (i.e. the speed of the gas at r=1 and  $\vartheta=\pi/2$  or  $\vartheta=3\pi/2$ ) for different locations of the artificial boundary in Fig. 5.10. Similarly to Fig. 5.9, Fig. 5.10 shows that the maximum speed (i.e. the speed at r=1 and  $\vartheta=\pi/2$  or  $\vartheta=3\pi/2$ ) of the gas is also reduced as the distance between the artificial boundary and the actual boundary increases. It turns out (although not shown here) that the magnitudes of the other flow variables also decrease with the increasing gap between the artificial and actual boundaries in

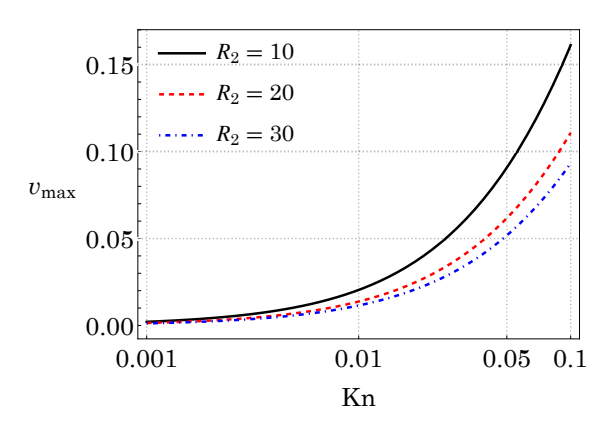


Figure 5.10: Maximum speed of the gas on the disk plotted against the Knudsen number for different locations of the artificial boundary.

general. Thus, the location of the artificial boundary or the distance at which the farfield conditions are applied does influence the results quantitatively. But, as we could not find any theoretical/numerical/experimental data on the flow variables for this problem in the literature, it is difficult to say which location of the artificial boundary gives the best results. Nevertheless, data on the drag force on the cylinder are available in the literature, which gives us a chance to compute the drag force on the cylinder with the demonstrated method and to compare it with the existing results in order to decide for an appropriate location of the artificial boundary. Therefore, we compute the drag force acting on the disk analytically as well as numerically through the MFS.

The analytic expression for the net force  $\mathbf{F}^{(A)}$  acting on disk is given by the integration of the normal component of the pressure tensor  $\mathbf{P}(=\boldsymbol{\sigma}+p\mathbf{I})$  over the periphery of the disk, i.e.

$$\mathbf{F}^{(A)} = \int \mathbf{P} \cdot \mathbf{n} \, ds = R_1 \int_0^{2\pi} (\mathbf{P} \cdot \mathbf{n}) \, d\vartheta, \qquad (5.40)$$

where n is the normal vector to the boundary and ds is the length of the arc that subtends angle  $d\vartheta$  on the center of the disk. The drag force on the disk is given by the projection of the net force in the upstream direction, i.e. by

$$F_d^{(A)} = -\mathbf{F}^{(A)} \cdot \hat{\mathbf{x}},\tag{5.41}$$

where  $\hat{x}$  denotes the unit vector in the downstream direction. On simplification the (analytic) drag force turns out to be

$$F_d^{(A)} = 4\pi \mathrm{Kn}c_6, \tag{5.42}$$

where the value of the  $c_6$  is evaluated from the boundary conditions and hence changes with the values of the parameters Kn and  $\alpha_0$ . In order to calculate the net force acting on the disk through the MFS, all the point force vectors acting on the singularity points lying on the inner fictitious boundary inside the disk are superimposed, i.e.

$$\mathbf{F}^{(MFS)} = \sum_{i=1}^{N_{s_1}} \mathbf{f}^{(i)}.$$
 (5.43)

The drag force on the disk is again given by the projection of the net force in the upstream direction, i.e. by

$$F_d^{(MFS)} = -\sum_{i=1}^{N_{s_1}} \mathbf{f}^{(i)} \cdot \hat{\mathbf{x}} = -\sum_{i=1}^{N_{s_1}} f_1^{(i)}.$$
 (5.44)

For illustrative purpose, it is convenient to compare the normalized drag, defined by the drag force normalized with the Stokes drag (drag force in the limit  $Kn \to 0$ ). In the following, we shall investigate the effect of the location of the artificial boundary on the normalized drag. But, prior to this, Ref. [37] must be acknowledged wherein the authors performed a thorough study of the drag coefficient for the problem of flow past a circular cylinder and gave analytic expressions for the drag coefficient valid in the continuum, slip and transition regime.

In addition, they also computed the drag coefficient for the problem through the nonlinear R26 equations. The drag coefficient on dividing by its value in the limit  $Kn \to 0$  is exactly the same as the normalized drag. This gives us an opportunity to compare the normalized drag obtained in the present work with that obtained using the results presented in Ref. [37]. Figure 5.11 illustrates the variation in the normalized drag with the Knudsen number on changing the location of the artificial boundary. The dashed red, blue and magenta lines in the figure depict the analytic solution of the CCR model for  $R_2 = 10$ , 20 and 30, respectively, while the square (red), disk (blue) and diamond (magenta) symbols denote the solution obtained from the MFS applied on the CCR model for  $R_2 = 10$ , 20 and 30, respectively. The solid orange, black and gray lines in the figure delineate the normalized drag obtained with the analytic expressions given in Refs. [79], [128] and [37] at the Reynolds number Reformalized and Reformalized drag computed directly from the data on the drag coefficient that have been obtained with the nonlinear R26 equation in Ref. [37]. The figure shows that the normalized drag obtained numerically with the MFS applied on the CCR model

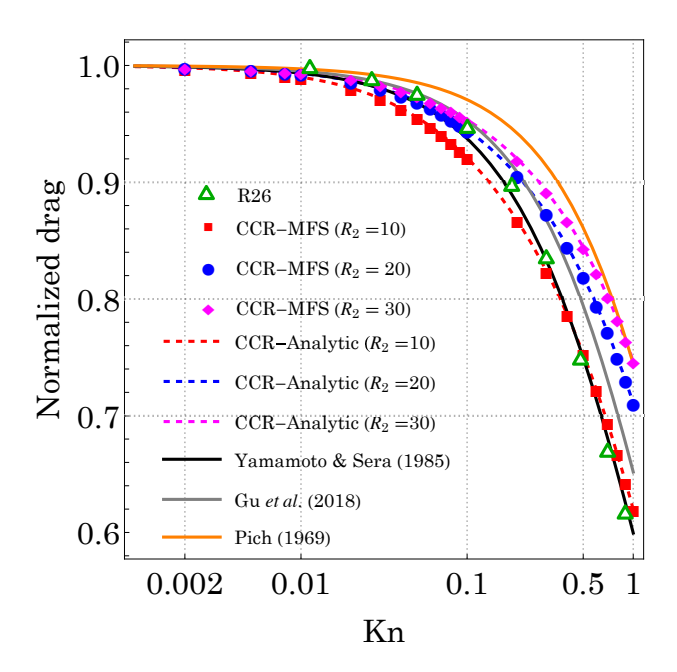


Figure 5.11: Normalized drag on the cylinder plotted against the Knudsen number for different locations of the artificial boundary. The dashed red, blue and magenta lines represent the analytic solution of the CCR model for  $R_2 = 10$ , 20 and 30, respectively. The square (red), disk (blue) and diamond (magenta) symbols represent the numerical solution of the CCR model obtained with the MFS for  $R_2 = 10$ , 20 and 30, respectively. The solid orange, black and gray lines depict the normalized drag obtained with the analytic expressions given in Refs. [79], [128] and [37]. The green triangle symbol shows the normalized drag computed with the nonlinear R26 equations in Ref. [37]. The other parameters are the same as those for Fig. 5.4.

is in an excellent agreement with that obtained with the analytic solution of the CCR model, irrespective of the location of the artificial boundary, which is no surprise as both (analytic and numerical) methods use a common location of the artificial boundary. Notwithstanding, these results do validate the correctness of our MFS-based numerical framework one more time in spite of the fact that the location of the artificial boundary does affect the results. The figure also reveals that while the normalized drag obtained from the CCR model in the present work is in qualitatively good agreement with the normalized drag obtained from other methods existing in the literature, quantitative differences are certainly there. Consequently, it is hard to tell a universal location of the

artificial boundary (or, in other words, a fixed value of  $R_2$ ) that can lead to the best results for all quantities. However, as the normalized drag predicted by the CCR model for  $R_2 = 10$  is generally close to that predicted by [128] and to the R26 data taken from Ref. [37], we take  $R_2 = 10$  throughout the chapter.

Although we have presented the results for somewhat large Knudsen numbers and the normalized drag—being a global quantity—also turned out to be agreeing well with that obtained with other models, it is important to note that the flow profiles predicted by the CCR model are accurate only in the bulk and only for relatively small Knudsen numbers ( $\text{Kn} \lesssim 0.2$ ) and that the flow profiles predicted by the CCR model near the boundary of the cylinder may differ from the actual kinetic data, especially for large Knudsen numbers. The reason for this is that Knudsen layers become more and more prominent near the boundary of the disk with the increasing the Knudsen number and the CCR model cannot describe them. This is a limitation of the CCR model and better continuum models, e.g. the R13 or R26 equations, are needed to obtain an accurate flow description near the boundary of the disk. The R13 and R26 equations can be expected to give correct flow profiles for the Knudsen number up to 0.5 and 1, respectively. Notwithstanding, the fundamental solutions of the R13 equations in two dimensions will be explored in chapter 7 and the fundamental solutions of the R26 equations are not available in any dimensions at present, and exploring them is beyond the scope of the present work.

#### 5.2.6 Sensitivity of the results towards the location of singularities

We investigate the relationship between the effective condition number and absolute error in the speed for the case of flow past circular cylinder—aiming to get an appropriate location for the placement of singularity points.

We define the absolute error  $\epsilon$  in the speed of the flow by  $\epsilon = |\text{speed}_{\text{MFS}} - \text{speed}_{\text{analytic}}|$  and introduce a dilation parameter  $\alpha > 1$ , which relates the radii of the inner and outer fictitious boundaries (containing singularities) to the radii of the inner and outer actual boundaries via the relations  $R'_1 = R_1/\alpha$  and  $R'_2 = \alpha R_2$ . In what follows, we examine the changes in the effective condition number  $\kappa_{\text{eff}}$  and in the absolute error  $\epsilon$  on changing the dilation parameter for different numbers of the boundary and source points in the cases when the total number of boundary points are the same as the total number of singularity

points (i.e.  $N_b = N_s$ ) and when the total number of boundary points are different from the total number of singularity points (i.e.  $N_b \neq N_s$ ).

Figure 5.12 illustrates the effective condition number (left panel) and absolute error in the speed (right panel) both plotted against the dilation parameter in the first case when the total number of boundary points is the same as the total number of the singularity points (i.e.  $N_b = N_s$ ) for different values of the number of boundary nodes (or singularity points)—specifically, for  $N_b = N_s = 120$ , 150 and 180. The left panel of the figure shows that, for small  $\alpha$  (close to 1), the effective condition number is relatively small (of  $\mathcal{O}(10^5)$ ), and it increases rapidly with increasing the dilation parameter but peaks for  $\alpha$  values somewhere in between  $\alpha \approx 1.5$  and  $\alpha \approx 2$  for all the considered numbers of boundary (or singularity) points, attaining maximum values of  $\mathcal{O}(10^{12})$ . For  $\alpha \gtrsim 2$ , the effective condition number tends to stabilize a bit and starts to decrease slightly with increasing the dilation parameter. The right panel of Fig. 5.12 shows that, for small  $\alpha$ (close to 1), the absolute error in the speed is relatively large (of  $\mathcal{O}(10^{-3})$ ), and it decreases sharply with increasing the dilation parameter but bottoms out for  $\alpha$  values somewhere in between  $\alpha \approx 1.9$  and  $\alpha \approx 2.7$  for all the considered numbers of boundary (or singularity) points, attaining values of  $\mathcal{O}(10^{-15})$ . For even larger values of the dilation parameter, the error remains at  $\mathcal{O}(10^{-15})$  and no significant improvement in the accuracy is achieved on increasing the dilation parameter further.

Figure 5.13 also displays the effective condition number (left panel) and absolute error in the speed (right panel) both plotted against the dilation parameter but in the second case when the total number of boundary points is different from the total number of singularity points (i.e.  $N_b \neq N_s$ ). We have considered three combinations of the numbers of boundary nodes and singularity points, namely (i)  $N_b = 120$  and  $N_s = 90$ , (ii)  $N_b = 150$  and  $N_s = 120$ , and (iii)  $N_b = 180$  and  $N_s = 150$ . Similarly to the left panel in Fig. 5.12, the effective condition number is relatively small (of  $\mathcal{O}(10^3)-\mathcal{O}(10^6)$ ) for the dilation parameter close to 1, and increases sharply with increasing  $\alpha$  but peaks for  $\alpha$  values somewhere in between  $\alpha \approx 1.7$  and  $\alpha \approx 2.2$  for all the considered numbers of boundary and singularity points, attaining maximum values of  $\mathcal{O}(10^{12})$ . Similarly to the right panel in Fig. 5.12, the absolute error in the speed is relatively large (of  $\mathcal{O}(10^{-3})$ ) for the dilation parameter close to 1, and it decreases sharply with increasing the dilation parameter but bottoms out for  $\alpha$  values somewhere in between  $\alpha \approx 2.1$  and  $\alpha \approx 3$  for all the

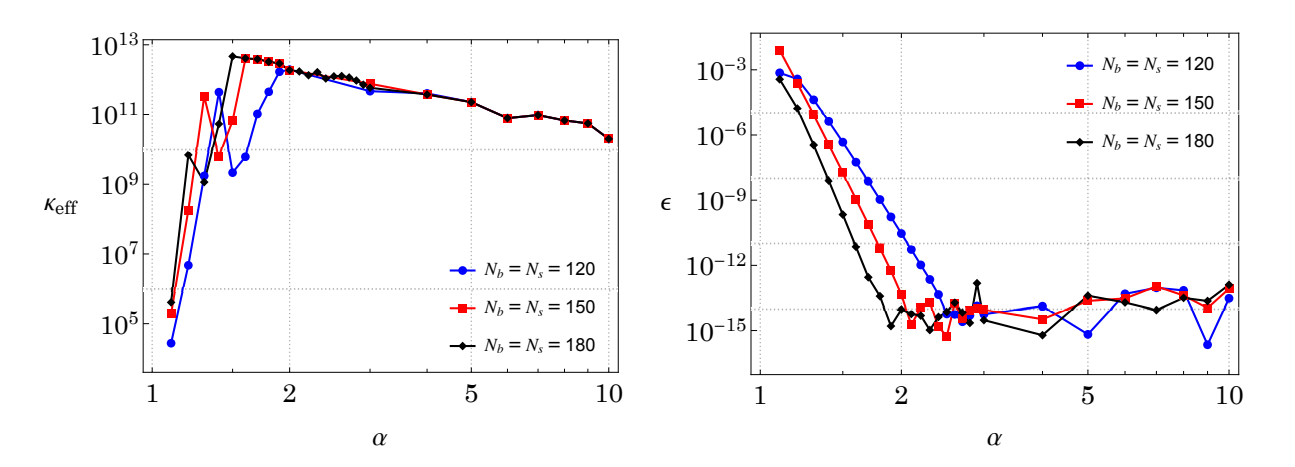


Figure 5.12: Effective condition number  $\kappa_{\text{eff}}$  (left panel) and absolute error  $\epsilon$  in speed (right panel) both plotted against the dilation parameter  $\alpha$  in the case when the total number of boundary nodes  $N_b$  is equal to the total number of singularity points  $N_s$  (the case of square collocation matrix) for Kn = 0.1.

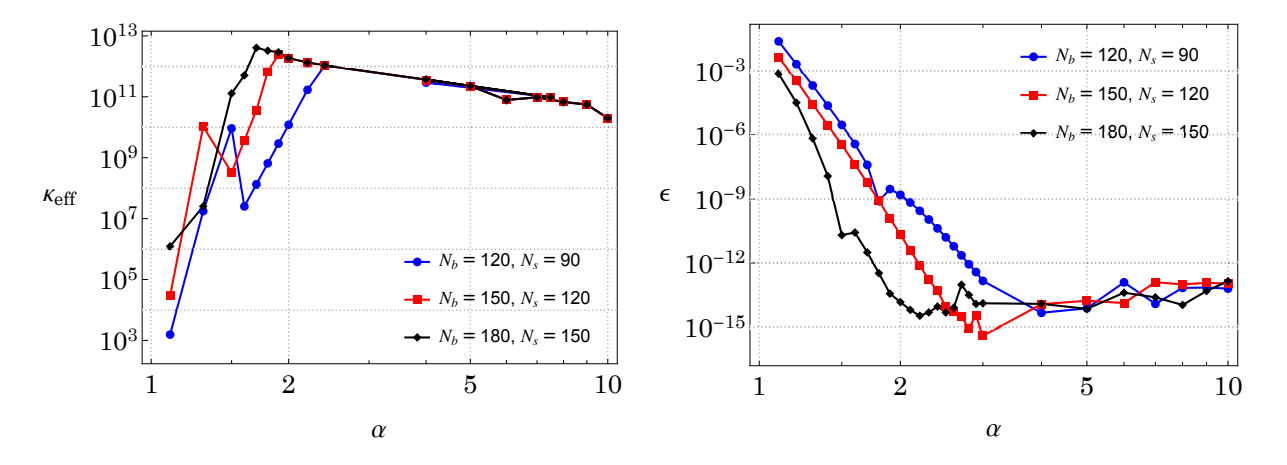


Figure 5.13: Effective condition number  $\kappa_{\text{eff}}$  (left panel) and absolute error  $\epsilon$  in speed (right panel) both plotted against the dilation parameter  $\alpha$  in the case when the total number of boundary nodes  $N_b$  is different from the total number of singularity points  $N_s$  (the case of non-square collocation matrix) for Kn = 0.1.

considered combinations of the numbers of boundary and singularity points, attaining values of  $\mathcal{O}(10^{-15})$ . For even larger values of the dilation parameter, the error remains at  $\mathcal{O}(10^{-15})$  with a slightly increasing trend and hence no significant improvement in the accuracy is achieved on increasing the dilation parameter further.

Both Figs. 5.12 and 5.13 exhibit an inverse relationship between the effective condition number and absolute error, which is concurrent with the findings of Refs. [22, 125]. Noticing the trends in the effective condition number and absolute error, we choose  $N_b = N_s = 150$  as it ensures a sufficiently high number of boundary nodes and singularities in order to achieve a high effective condition number and better accuracy along with computational efficiency. Additionally, the choice of  $\alpha = 2$  balances the trade-off between achieving a high condition number and minimizing the error.

#### 5.3 Flow past semi-circular cylinder

The numerical framework developed in the present work can be employed to investigate other quasi-two-dimensional flow problems as well. In particular, the expediency of the method is notable for problems wherein either an analytic solution cannot be found or is arduous to find.

To showcase the capabilities of the method, we now consider a problem, where the radial symmetry is absent. We consider the problem of rarefied gas flow past an infinitely long semicircular cylinder in its transverse direction. The problem is still quasi-two-dimensional but flow behavior changes according to the orientation of the cylinder. To setup the orientation of the cylinder and the flow direction, let an infinitely long semicircular cylinder of radius  $\tilde{R}_1$  be placed in such a way that its axis is along the  $\tilde{z}$ -direction

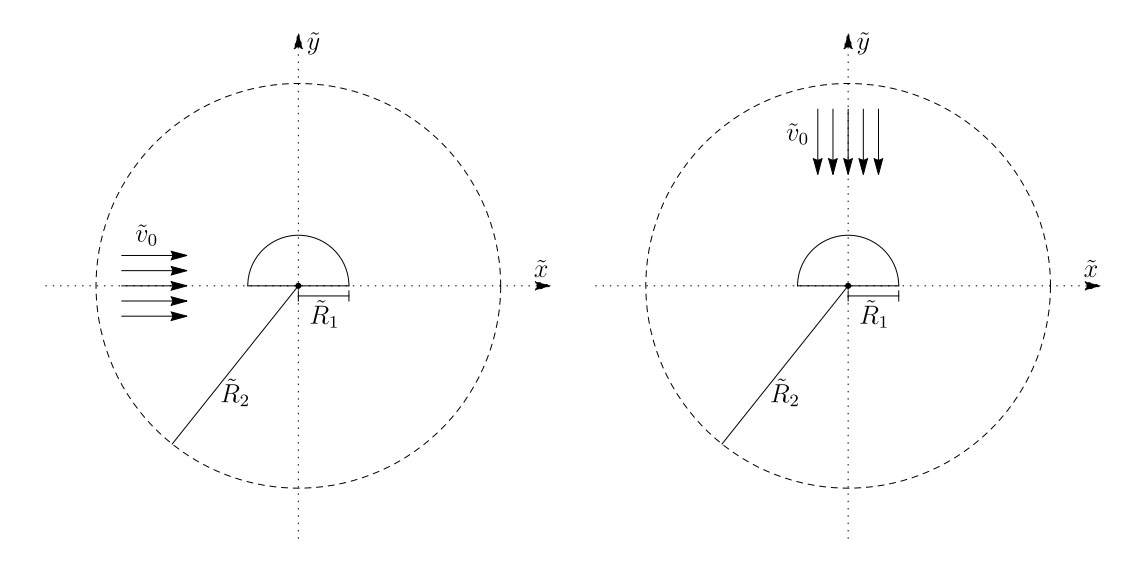


Figure 5.14: Cross-sectional view of the horizontal and vertical flows past a semicircular cylinder.

and its semicircular base is in the upper half of the  $\tilde{x}\tilde{y}$ -plane with the midpoint of the diameter of the semicircular base being fixed at the origin of the Cartesian coordinate system  $(\tilde{x}, \tilde{y}, \tilde{z})$  as shown in Fig. 5.14. Two cases are considered: (i) a rarefied monatomic gas approaching the cylinder from the negative  $\tilde{x}$ -direction; we refer to this case as the case of horizontal flow or simply the horizontal case, and (ii) a rarefied monatomic gas approaching the cylinder from the positive  $\tilde{y}$ -direction; we refer to this case as the case of vertical flow or simply the vertical case analogously. A schematic exhibiting the crosssectional view of both cases has also been shown in Fig. 5.14. Furthermore, it is assumed that the temperature at the surface of the cylinder is the same as the far-field ambient temperature of the gas  $T_0$ . Needless to say, we shall solve the problem in the  $\tilde{x}\tilde{y}$ -plane or equivalently in the  $\tilde{r}\vartheta$ -plane, where  $\tilde{x} = \tilde{r}\cos\vartheta$  and  $\tilde{y} = \tilde{r}\sin\vartheta$ , for the semi-circular disk. The radius of the disk  $R_1$  is taken as the characteristic length scale L for nondimensionalization so that  $x = \tilde{x}/\tilde{R}_1$ ,  $y = \tilde{y}/\tilde{R}_1$ ,  $r = \tilde{r}/\tilde{R}_1$ , and the dimensionless radius of the disk  $R_1 = \tilde{R}_1/\tilde{L} = 1$ . To circumvent Stokes' paradox, we—similarly to the problem in Sec. 5.2—place an artificial circular boundary of radius  $\tilde{R}_2$  centered at (0,0) sufficiently far from the semicircular disk. The dimensionless radius of the artificial boundary

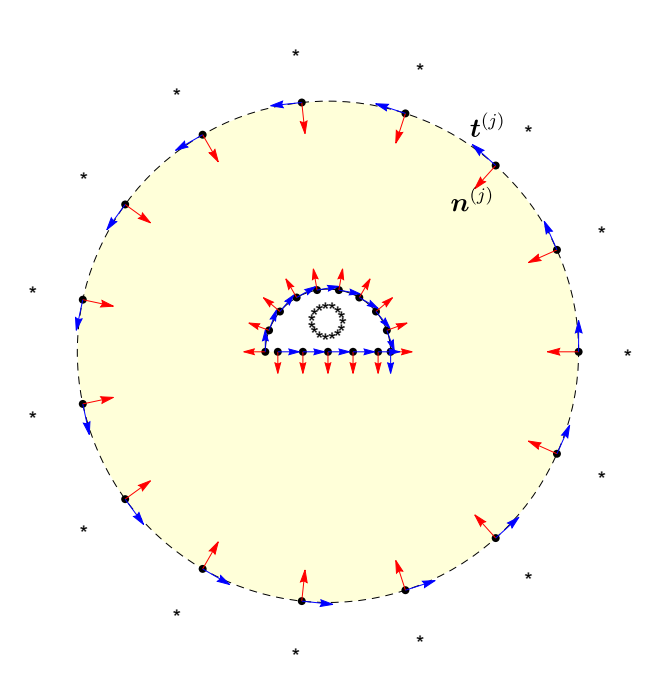


Figure 5.15: Schematic representation for an arrangement of singularities (stars) and boundary nodes (dots). The red and blue arrows represent the normal and tangent vectors at each boundary node.

is  $R_2 = \tilde{R}_2/\tilde{L}$ , where  $R_2 > R_1$ . Furthermore, for implementation of the MFS, we also introduce two fictitious boundaries, one inside the semicircular disk and other outside the artificial circular boundary, on which the source points are to be placed. Let the inner fictitious boundary be a circle of radius  $\tilde{R}'_1$  centered at (0,0.5) and the outer fictitious boundary be a circle of radius  $\tilde{R}'_2$  centered at (0,0). The dimensionless radii of the inner and outer fictitious boundaries are  $R'_1 = \tilde{R}'_1/\tilde{L}$  and  $R'_2 = \tilde{R}'_2/\tilde{L}$ . An illustration exhibiting the boundary nodes on the semicircular disk and on the artificial boundary, and the location of source points on the fictitious boundaries is shown in Fig. 5.15. Once the singularities are placed, the rest of the procedure of implementing the MFS remains the same as explained in previous chapters.

The horizontal and vertical flow cases are covered by changing the boundary conditions on the artificial boundary. For the horizontal case, the boundary conditions on the artificial boundary are

$$v_x = v_0, \quad v_y = 0 \quad \text{and} \quad T = 0,$$
 (5.45)

while for the vertical case, the boundary conditions on the artificial boundary are

$$v_x = 0, \quad v_y = -v_0 \quad \text{and} \quad T = 0.$$
 (5.46)

The boundary conditions on the actual periphery of the disk remain the same as boundary conditions (5.11)–(5.13).

In numerical computations,  $v_0$  is taken as unity, the number of boundary nodes on the actual periphery of the disk is taken as  $N_{b_1} = 200$  and that on the artificial boundary is taken as  $N_{b_2} = 400$ , and the number of singularity points on the inner and outer fictitious boundaries are taken as  $N_{s_1} = 200$  and  $N_{s_2} = 400$ , respectively. The dimensionless radius of the semicircular disk is  $R_1 = 1$  and the dimensionless radius of the artificial boundary is taken as  $R_2 = 10$ . Although the dependence of the results on the location of the artificial boundary cannot be neglected, the validation of the results done using  $R_2 = 10$  in Sec. 5.2.5 suggests the sufficiency for fixing  $R_2$  to 10 to get adequate qualitative results for the current problem as well. The dimensionless radii of the inner and outer fictitious boundaries are taken as  $R'_1 = 0.1$  and  $R'_2 = 50$ , respectively. In the case of a circular cylinder, we had the advantage of having an analytic solution, allowing us to validate our results even with relatively lesser number of boundary nodes and singularity points ( $N_{b_1} = 10.00$ ).

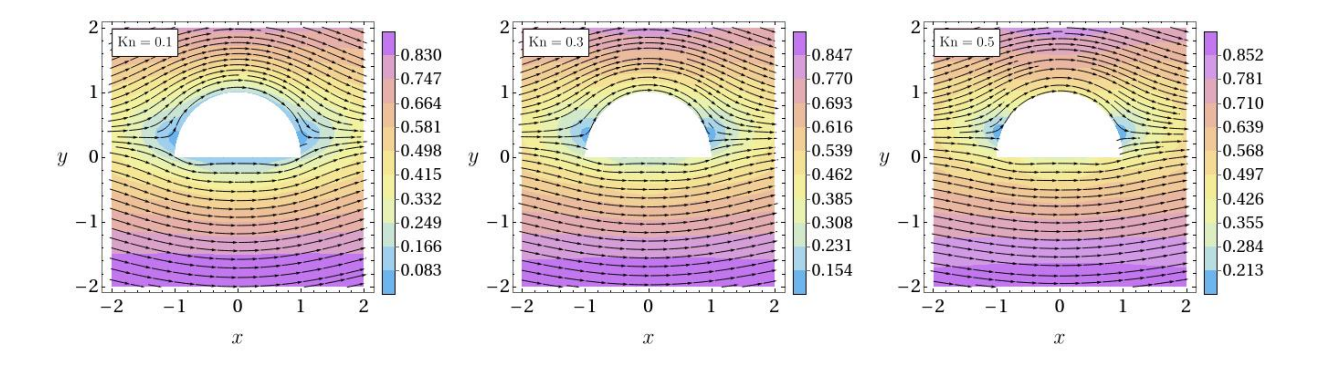


Figure 5.16: Velocity streamlines along with contour plots of the speed in the background obtained with the MFS applied on the CCR model for Kn = 0.1, 0.3 and 0.5. The other parameters are  $R_1 = 1$ ,  $R_2 = 10$ ,  $R'_1 = 0.1$ ,  $R'_2 = 50$ ,  $N_{b_1} = N_{s_1} = 200$  and  $N_{b_2} = N_{s_2} = 400$ .

 $N_{s_1} = 50$  and  $N_{b_2} = N_{s_2} = 100$ ). However, when dealing with the case of semicircular cylinder, we have taken a relatively larger number of boundary nodes and singularities. This decision is based on the studies from the existing literature [26, 32], which suggest that more boundary nodes and singularity points in the method of fundamental solution lead to improved accuracy. Furthermore, as neither it is easy to obtain an analytic solution for the present problem nor we could find any experimental or theoretical study in the existing literature, our focus in these problems remains only on the qualitative analysis of the results.

#### 5.3.1 Results in the case of horizontal flow

Figure 5.16 illustrates the velocity streamlines around the semicircular disk along with contour plots of the speed in the background for  $Kn=0.1,\,0.3$  and 0.5 in the case of horizontal flow, i.e. when the flow is along the x-direction. Analogously to problem of flow past a circular cylinder demonstrated in Sec. 5.2.5, the streamlines in Fig. 5.16 are qualitatively alike for the considered Knudsen numbers. Nonetheless, contour plots of the speed do depict quantitative differences in the speed of the gas for different Knudsen numbers that are prominently discernible in the close proximity of the disk. It is evident from the colors of the contour plots near the disk that the speed of the gas on the disk increases with the Knudsen number due to increase in the slip velocity with the increasing Knudsen number. Apparently, it is true even for any point in the domain that the speed of the gas at this point increases with increasing the Knudsen number.

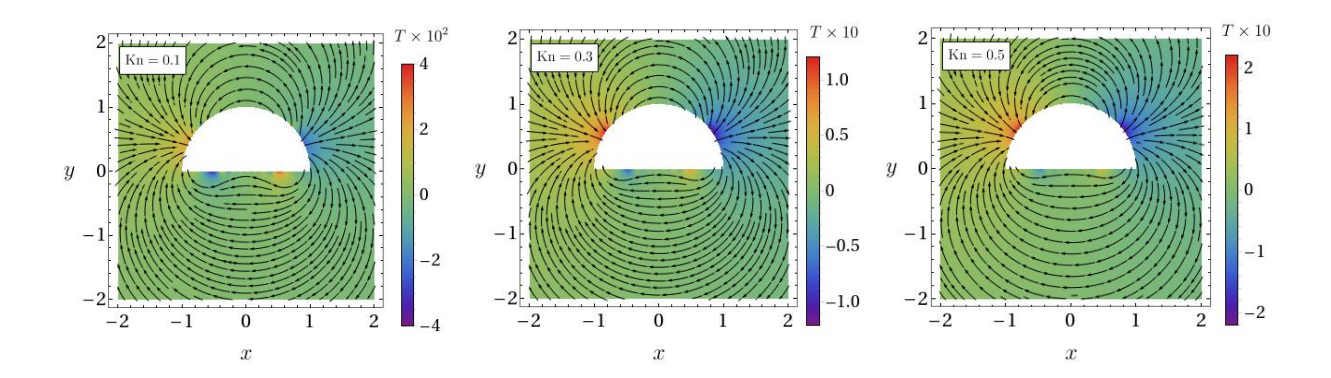


Figure 5.17: Heat-flux lines along with density plots of the temperature in the background obtained with the MFS applied on the CCR model for Kn = 0.1, 0.3 and 0.5. The other parameters are the same as those for Fig. 5.16.

Interestingly, the effects of asymmetry in the shape of the object are revealed when the variation of temperature of the gas is explored. In order to explore the asymmetry effects, we plot in Fig. 5.17 the heat-flux lines superposed on density plots of the temperature for Kn = 0.1, 0.3 and 0.5. The figure reveals the existence of temperature polarization near the disk for all Knudsen numbers—with hot region (denoted by red color) on the left side of the curved portion of the disk and cold region (denoted by blue color) on the right side due to compression (expansion) of the gas on the left (right) side. In addition, a minute (but opposite in sign) temperature polarization also occurs below the flat portion of the disk and is conspicuous for small Knudsen numbers (for Kn = 0.1 in the figure) but diminishes as the Knudsen number increases. This double polarization could be attributed to the presence of corners in the geometry or to the asymmetry present in the geometry. As the Knudsen number increases, the strength of temperature polarization on the curved portion of the disk increases and hence it takes over the minute temperature polarization below the flat portion of the disk, and the latter fades away gradually as the Knudsen number increases. The heat-flux lines in Fig. 5.17 indicate the flow of heat from cold to hot regions, depicting anti-Fourier effect that again cannot be captured with the classical models of fluid dynamics.

#### 5.3.2 Results in the case of the vertical flow

Figure 5.18 exhibits the velocity streamlines around the semicircular disk along with contour plots of the speed in the background for Kn = 0.1, 0.3 and 0.5 in the case of

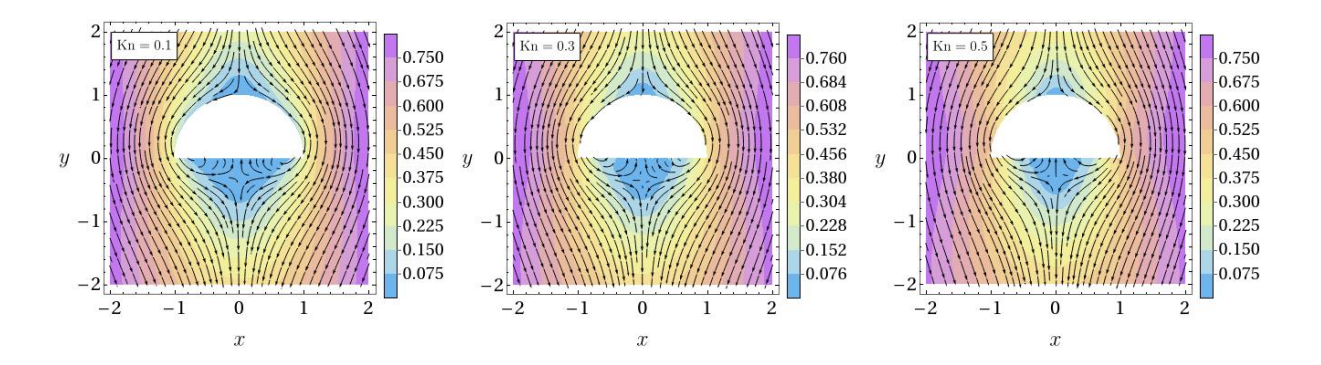


Figure 5.18: Velocity streamlines along with contour plots of the speed in the background obtained with the MFS applied on the CCR model for Kn = 0.1, 0.3 and 0.5. The other parameters are the same as those for Fig. 5.16.

vertical flow, i.e. when the flow is along the negative y-direction. The figure presents flow separation and formation of circulation zones after the flow crosses the disk. The figure shows that the flow separation starts reducing slightly with increasing the Knudsen number. Flow separation and an analogous outcome—reduction in the size of circulation zone with decreasing Reynolds number—have also been reported by [74] for a creeping (or low-Reynolds-number) flow past a semicircular cylinder. Thus, owing to the inverse relationship between the Reynolds and the Knudsen numbers, the qualitative nature of the flow predicted by the CCR model in the present work is justified. Contour plots of the speed in Fig. 5.18 again depict that the speed of the gas around the disk increases with increase in the Knudsen number.

Figure 5.19 illustrates the heat-flux lines superposed over density plots of the temperature for Kn = 0.1, 0.3 and 0.5 in the case of vertical flow. Temperature polarization again occurs in this case but it is symmetric about the y-axis in this case, creating hot and cold regions on the top and bottom of the disk, respectively. The strength of temperature polarization increases with increase in the Knudsen number. The heat-flux lines are also symmetric about the y-axis for all Knudsen numbers and show the heat flowing from cold to hot regions, illustrating the anti-Fourier effect in the present case as well.

#### 5.3.3 Drag force in the horizontal and vertical cases

To the best of our knowledge, an analytic expression or any experimental result for the drag force exerted on the semicircular disk in this problem does not exist in the

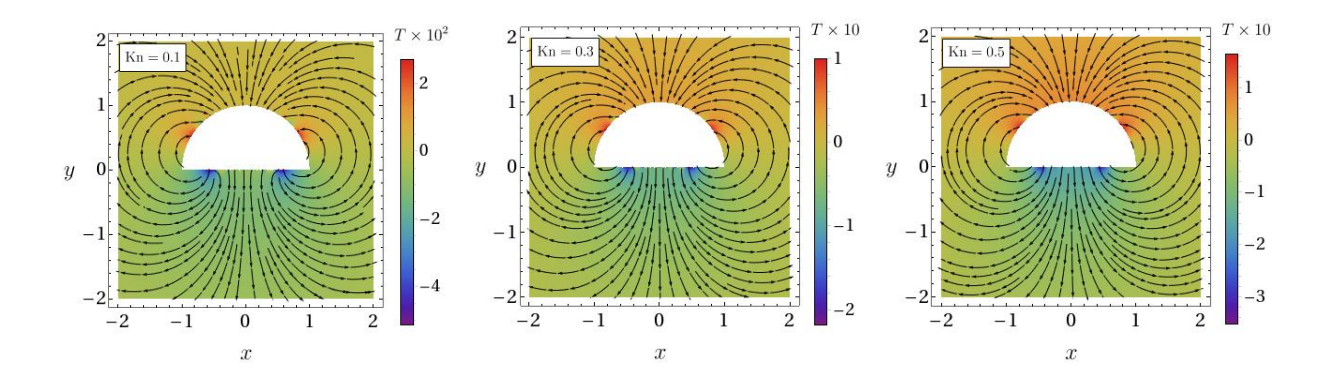


Figure 5.19: Heat-flux lines along with density plots of the temperature in the background obtained with the MFS applied on the CCR model for Kn = 0.1, 0.3 and 0.5. The other parameters are the same as those for Fig. 5.16.

literature. Therefore, we directly present the drag force predicted by the CCR model through the MFS in Fig. 5.20 for the horizontal and vertical cases. The drag force in the horizontal case has been obtained by taking the projection of the net force in the negative x-direction (similarly to that in the problem of flow past a circular cylinder in Sec. 5.2.5). The variation of the drag force with the Knudsen number in horizontal case is illustrated in Fig. 5.20 by the solid (black) line. For the vertical case, the drag force is determined by projecting the net force in the positive y-direction and its variation with Knudsen number is shown in Fig. 5.20 by the dashed (blue) line. Similarly to the drag force on the

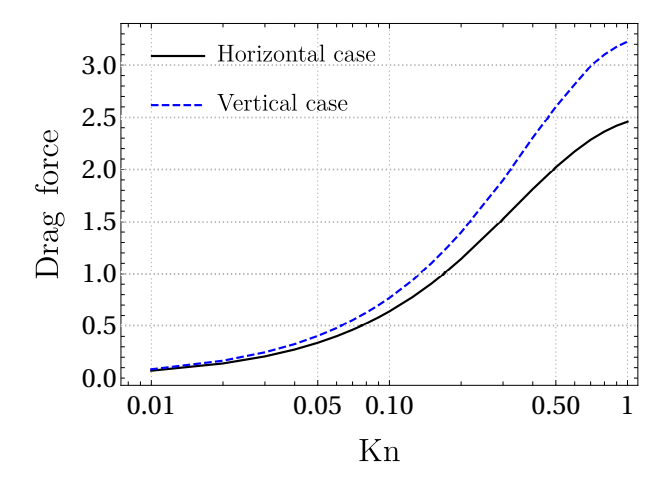


Figure 5.20: Drag force on the semicircular disk plotted against the Knudsen number in the horizontal and vertical cases. The other parameters are the same as those for Fig. 5.16.

circular cylinder obtained in Sec. 5.2.5, Fig. 5.20 shows that the drag force increases with increasing the Knudsen number in both horizontal and vertical cases. However, unlike the case of a circular cylinder where the dependence of the drag force on the Knudsen number was apparent through Eq. (5.42), an expression revealing dependence of the drag force on the Knudsen number in the case of a semicircular cylinder is lacking at present.

#### 5.4 Summary

In this chapter, the slow transverse-directional flows of a rarefied monatomic gas past both circular and semicircular cylinders have been investigated using the CCR-MFS framework. To overcome the challenges imposed by Stokes' paradox in two-dimensional external flows, the computational domain has been restricted artificially by introducing an external boundary sufficiently far from the disk. Appropriate boundary conditions have been imposed on the artificial boundary to preserve the physical character of the flow, which has allowed us to derive a meaningful analytic solution for the flow past a circular cylinder. It is however important to note that the solutions obtained—both numerical and analytic—are dependent on the location of the artificial boundary. Eliminating this dependency entirely would require removing the artificial boundary and addressing Stokes' paradox by alternate means, such as incorporating convective terms (e.g., via an Oseen-type correction) in the CCR model. Nevertheless, deriving and implementing the corresponding fundamental solutions for such an approach remains a subject for future work. The numerical results for physical quantities, including velocity, temperature, and drag force, obtained from the MFS applied to the CCR model, have shown excellent agreement with the analytic solutions of the CCR model. Moreover, the values of the normalized drag compare favorably well with those reported in existing literature.

The CCR-MFS framework has successfully captured rarefaction effects such as temperature polarization and anti-Fourier heat transfer that classical continuum models fail to resolve. To further demonstrate the capabilities of the developed framework, the flow past a semicircular disk has also been investigated to showcase the capability of the framework for describing flow past non-simple geometries. A sensitivity analysis based on the effective condition number has also been conducted to determine the sufficient number of boundary and source points required for achieving high accuracy.

# Chapter 6

# Phase transition around liquid jets

Previous studies based on the extended hydrodynamic models (the R13, R26 and CCR models) have examined complete evaporation or condensation in spherical droplets and planar geometries [12, 87, 89, 90, 107]. However, they do not address partial phase-change scenarios. In this chapter, we present the thermodynamically admissible evaporation/condensation boundary conditions for the CCR model in both partial and complete evaporation scenarios. We employ the MFS on the CCR model to study phase transition processes in evaporating liquid jets. Here, we refer to the jet as a long stream whose one axis is significantly larger than the other two. We consider liquid jets with circular and non-circular cross sections. The numerical results for a circular cross-section are validated with analytical solutions, and the framework is extended to deformed shapes using spherical harmonic perturbations. An error analysis is included to demonstrate the accuracy and convergence of the method.

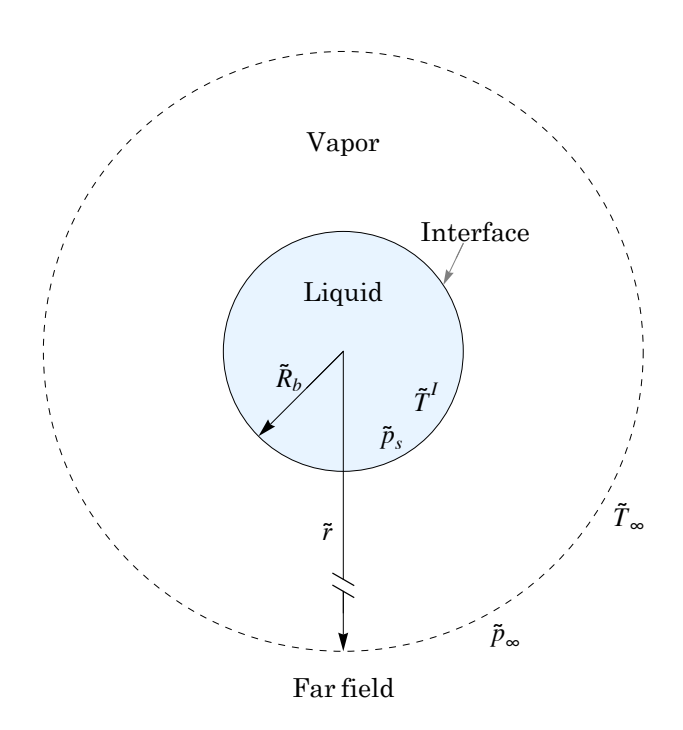


Figure 6.1: Schematic representation of 2D cross-section of an evaporating liquid jet immersed in its vapor.

## 6.1 Problem description

We consider the 2D cross-section of a circular cylindrical liquid jet having radius of interface boundary  $\tilde{R}_b$ . The jet is assumed to be evaporating and immersed in its vapor. The schematic of the problem is illustrated in Fig. 6.1. An analytic solution of this problem can be obtained from the CCR model. The liquid-vapor interface in the problem has been assumed to be infinitely thin to avoid coexisting phases of significant width. It has also been assumed that far away from the jet (i.e., for  $\tilde{r} \to \infty$ ), the vapor reaches the equilibrium. Consequently, the far-field temperature  $\tilde{T}_{\infty}$  and the far-field pressure  $\tilde{p}_{e}$ , respectively.

#### 6.1.1 Boundary conditions

Recall the thermodynamically admissible boundary conditions (2.51)–(2.53) discussed in Chapter 2

$$(\boldsymbol{v} - \boldsymbol{v}^{I}) \cdot \boldsymbol{n} = -\eta_{11}(p - p_{s} + \boldsymbol{n} \cdot \boldsymbol{\sigma} \cdot \boldsymbol{n}) + \eta_{12} (T - T^{I} + \alpha_{0} \boldsymbol{n} \cdot \boldsymbol{\sigma} \cdot \boldsymbol{n}), \qquad (6.1)$$

$$\boldsymbol{q} \cdot \boldsymbol{n} = \eta_{12}(p - p_s + \boldsymbol{n} \cdot \boldsymbol{\sigma} \cdot \boldsymbol{n}) - (\eta_{22} + 2\tau_0) \left( T - T^I + \alpha_0 \boldsymbol{n} \cdot \boldsymbol{\sigma} \cdot \boldsymbol{n} \right), \quad (6.2)$$

$$\boldsymbol{t} \cdot \boldsymbol{\sigma} \cdot \boldsymbol{n} = -\varsigma \left( \boldsymbol{v} - \boldsymbol{v}^{I} + \alpha_{0} \boldsymbol{q} \right) \cdot \boldsymbol{t}, \tag{6.3}$$

where  $p_s$  denotes the saturation pressure and  $T^I$  denotes the temperature at the interface. For the problem under consideration, the interface is assumed to be stationary, i.e.,  $\mathbf{v}^I = \mathbf{0}$ . Further, the general form of Onsager reciprocity coefficients  $\eta_{ij}$ 's mentioned in (2.54), under the assumption of full accommodation (i.e.  $\chi = 1$ ), turns out to be

$$\eta_{11} = \omega_1 \sqrt{\frac{2}{\pi}} \frac{\Theta}{2 - \Theta}, \quad \eta_{12} = \omega_2 \sqrt{\frac{2}{\pi}} \frac{\Theta}{2 - \Theta} \quad \text{and} \quad \eta_{22} = \omega_3 \sqrt{\frac{2}{\pi}} \frac{\Theta}{2 - \Theta}, \tag{6.4}$$

with  $\Theta$  being the evaporation/condensation coefficient. The values of coefficients  $\omega_1, \omega_2$  and  $\omega_3$  vary with the values of evaporation/condensation coefficient  $\Theta$ . In Ref. [90], as well as in Chapter 4,  $\Theta = 1$  was fixed for full evaporation/condensation case, corresponding to which  $\omega_1 = 0.9134, \omega_2 = 0.3915$  and  $\omega_3 = 0.1678$ . However, the values of coefficients  $\omega_1, \omega_2$  and  $\omega_3$  in the thermodynamically-admissible boundary conditions of the CCR model corresponding to partial evaporation/condensation cases are lacking in the literature. In Ref. [49], the temperature- and pressure-jump coefficients have been computed using the Skinetic model for the linearized Boltzmann equation. Therefore, we utilize the coefficients

given in Ref. [49] to obtain the values of  $\omega_1, \omega_2$  and  $\omega_3$  in the boundary condition of the CCR model. Boundary conditions (6.1) and (6.2) can be expressed as a linear system

$$\begin{bmatrix} p - p_s + \boldsymbol{n} \cdot \boldsymbol{\sigma} \cdot \boldsymbol{n} \\ T - T^I + \alpha_0 \boldsymbol{n} \cdot \boldsymbol{\sigma} \cdot \boldsymbol{n} \end{bmatrix} = \begin{bmatrix} -\eta_{11} & \eta_{12} \\ \eta_{12} & -\eta_{22} - 2\tau_0 \end{bmatrix}^{-1} \begin{bmatrix} \boldsymbol{v} \cdot \boldsymbol{n} \\ \boldsymbol{q} \cdot \boldsymbol{n} \end{bmatrix}.$$
(6.5)

The comparison with Eqs. (75) and (76) of Ref. [49] is performed by selecting the values of  $\epsilon_p^{(u)}, \epsilon_p^{(T)}$ , and  $\epsilon_T^{(T)}$  from Table II in Ref. [49], which allows us to determine  $\omega_1, \omega_2$ , and  $\omega_3$ . It is important to note that in Ref. [49], the term corresponding to  $\mathbf{n} \cdot \boldsymbol{\sigma} \cdot \mathbf{n}$  is absent because they consider an infinite condensed surface, whereas in our case, this term appears on the left-hand side of Eq. (6.5). The obtained values of  $\omega_1, \omega_2$ , and  $\omega_3$  are presented in Table 6.1 for different values of  $\Theta$ . These values are also consistent with the values from Ref. [90] in the special case of full evaporation/condensation ( $\Theta = 1$ ), showing a fair comparison.

Θ	$\omega_1$	$\omega_2$	$\omega_3$
0.1	0.9977	0.4291	0.1882
0.2	0.9897	0.4249	0.1842
0.4	0.9769	0.4190	0.1805
0.6	0.9610	0.4120	0.1771
0.8	0.9406	0.4032	0.1732
1	0.9134	0.3915	0.1678

Table 6.1: The values of the coefficients  $\omega_i$  appearing in the Onsager reciprocity coefficients  $\eta_{ij}$  in the boundary conditions (6.1) and (6.2) for different values of  $\Theta$ .

#### 6.1.2 Numerical implementation

In the present problem, we depict the placement of  $N_b$  equispaced boundary nodes on the circular boundary (having dimensionless radius  $R_b$ ) and  $N_s$  equispaced source points placed on a concentric circle of dimensionless radius  $R_s$  lying inside the liquid, a schematic of which is displayed in Fig. 6.2. There are  $4 \times N_s$  number of unknowns associated with the  $i^{\text{th}}$  singularity point, namely  $h_i$ ,  $f_{1_i}$ ,  $f_{2_i}$  and  $g_i$  which are calculated by satisfying boundary conditions (6.1)–(6.3) at every  $j^{\text{th}}$  boundary node.

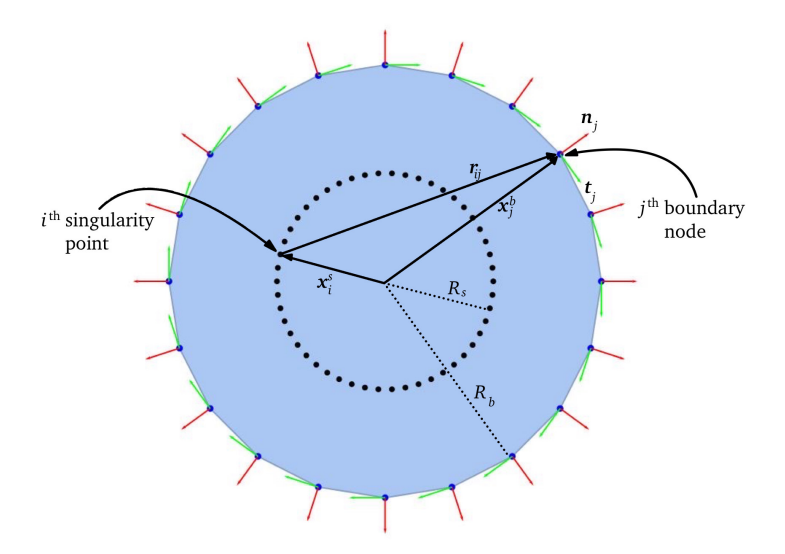


Figure 6.2: Boundary discretization depicting the boundary nodes and singularity points placed outside of the domain along with the normal and tangent vectors shown at each boundary node.

## 6.2 Analytic solution

In this section, the analytic solution for the problem of evaporation from a 2D crosssection of a cylindrical evaporating jet, as detailed in Sec. 6.1, is presented. Owing to the symmetry, it is indeed easy to solve the CCR equations for the problem analytically by transforming the equations to the polar coordinates (as done in Eqs. (5.15)–(5.19b) in Sec. 5.2.3). As a result of symmetry there is no variation along the azimuthal angle  $\vartheta$ and hence  $v_{\vartheta} = \sigma_{r\vartheta} = q_{\vartheta} = 0$ . The mass, momentum and energy balance equations thus reduce to

$$\frac{\partial v_r}{\partial r} + \frac{v_r}{r} = 0, (6.6)$$

$$\frac{\partial p}{\partial r} + \frac{\partial \sigma_{rr}}{\partial r} + \frac{2\sigma_{rr}}{r} = 0, \tag{6.7a}$$

$$\frac{\partial q_r}{\partial r} + \frac{q_r}{r} = 0, (6.8)$$

and the closure relations reduce to

$$\sigma_{rr} = -2\operatorname{Kn}\frac{\partial v_r}{\partial r} - 2\operatorname{Kn}\alpha_0 \frac{\partial q_r}{\partial r},\tag{6.9}$$

$$q_r = -\frac{c_p \operatorname{Kn}}{\operatorname{Pr}} \left[ \frac{\partial T}{\partial r} + \alpha_0 \left( \frac{\partial \sigma_{rr}}{\partial r} + \frac{2\sigma_{rr}}{r} \right) \right]. \tag{6.10}$$

It is now straightforward to obtain the analytic solution of the Eqs. (6.6)–(6.10) This analytic solution will serve as the reference solution for analyzing errors in the solution obtained through the MFS. The analytic solutions of the CCR equations for the problem under consideration are as follows

$$v_r = \frac{c_1}{r}, \quad \sigma_{rr} = \frac{2\text{Kn}}{r^2}(c_1 + \alpha_0 c_2), \quad T = -\frac{2c_2\text{Pr}}{5\text{Kn}}\log r, \quad q_r = \frac{c_2}{r},$$
 (6.11)

$$p = v_{\vartheta} = \sigma_{r\vartheta} = q_{\vartheta} = 0, \tag{6.12}$$

where the subscripts 'r' and ' $\vartheta$ ' on the field variables denote their radial and angular components, respectively, and the integration constants  $c_1$  and  $c_2$  are to be calculated using boundary conditions (6.1) and (6.2). Note that boundary condition (6.3) is identically satisfied with solution (6.11). Moreover, two additional integration constants appear in the analytic expressions for pressure and temperature. Those constants are set to zero based on the far-field equilibrium conditions. However, due to the logarithmic behavior of temperature, enforcing an exact  $T_{\infty} = 0$  condition—as done for three dimensions in Ref. [89]—is not feasible in the present formulation in 2D.

It is customary to determine the integration constants  $c_1$  and  $c_2$  for the problem in two different cases: (i) the pressure-driven case wherein there is no difference in the liquid temperature and the far-field temperature, and the evaporation is entirely due to the pressure difference between the saturation and far-field pressures (i.e.,  $p_s = 1$ and  $T^I = 0$ ) and (ii) the temperature-driven case wherein there is no difference in the saturation and far-field pressures, and the evaporation is solely driven by the difference in the liquid temperature and the far-field temperature (i.e.,  $p_s = 0$  and  $T^I = 1$ ); see, e.g., Refs. [87, 89, 90]. Applying boundary conditions (6.1) and (6.2) at  $r = R_b$ , the integration constants  $c_1$  and  $c_2$  in the pressure-driven case turn out to be

$$c_{1}^{p} = -\frac{2\sqrt{2}\pi R_{b} \Theta\left(A_{3}(15 \alpha_{0}^{2} \operatorname{Kn}^{2} - 2R_{b}^{2} \log R_{b}) + \sqrt{\pi}\omega_{1}(\Theta - 2)\left(A_{4} - 8R_{b}^{2} \tau_{0} \log R_{b}\right)\right)}{4R_{b} \log R_{b} \left(4\operatorname{Kn} \Theta A_{2} + R_{b}(\Theta - 2)\left(\sqrt{2\pi}\omega_{3}\Theta - 2\pi\tau_{0}(\Theta - 2)\right)\right) + 15A_{1}\operatorname{Kn}(\Theta - 2)},$$
(6.13)

$$c_2^p = \frac{30\pi \operatorname{Kn} R_b \Theta \left( 4A_2 \alpha_0 \operatorname{Kn} + \sqrt{2\pi} R_b \omega_2(\Theta - 2) \right)}{4R_b \log R_b \left( 4\operatorname{Kn} \Theta A_2 + R_b(\Theta - 2) (\sqrt{2\pi} \omega_3 \Theta - 2\pi \tau_0(\Theta - 2)) \right) + 15A_1 \operatorname{Kn}(\Theta - 2)},$$
(6.14)

while in the temperature-driven case, they turn out to be

$$c_1^T = c_2^p, (6.15)$$

$$c_2^T = -\frac{30\pi \operatorname{Kn} R_b \left( 4\operatorname{Kn} \Theta A_2 + R_b(\Theta - 2) \left( \sqrt{2\pi} \omega_3 \Theta - 2\pi \tau_0(\Theta - 2) \right) \right)}{4R_b \log R_b \left( 4A_2\operatorname{Kn} \Theta + R_b(\Theta - 2) \left( \sqrt{2\pi} \omega_3 \Theta - 2\pi \tau_0(\Theta - 2) \right) \right) + 15A_1\operatorname{Kn}(\Theta - 2)},$$
(6.16)

where

$$A_1 = \pi(\Theta - 2) \left( 4\alpha_0^2 \operatorname{Kn} \tau_0 + R_b \right) - 2\sqrt{2\pi} \operatorname{Kn} \Theta \left( \alpha_0 \left( \alpha_0 \omega_3 - 2\omega_2 \right) + \omega_1 \right), \tag{6.17}$$

$$A_2 = \sqrt{2\pi}\tau_0 \,\omega_1(\Theta - 2) + \left(\omega_2^2 - \omega_1 \omega_3\right)\Theta,\tag{6.18}$$

$$A_3 = 2\sqrt{2} \left(\omega_2^2 - \omega_1 \omega_3\right) \Theta, \quad A_4 = 15 \text{Kn} \left(4\alpha_0^2 \text{Kn} \tau_0 + R_b\right),$$
 (6.19)

and the superscripts 'p' and 'T' on the integration constants  $c_1$  and  $c_2$  have been used for denoting their values in the pressure- and temperature-driven cases, respectively. It is evident from (6.15) that the Onsager reciprocity relations hold true due to the microscopic reversibility of the evaporation and condensation processes. Physically, these integration constants  $c_1$  and  $c_2$  represent the mass-flux and heat-flux coefficients, respectively. The mass-flux and heat-flux coefficients can also be obtained by the MFS utilizing the unknowns corresponding to point mass and point heat sources corresponding to the all the singularity points. These coefficients are related to the unknown point mass and heat sources included as Dirac-delta sourcing terms in the mass balance and energy balance equations  $(2.19)_1$  and  $(2.19)_3$ , respectively. Therefore, the combined effects of all mass and heat sources determine the mass and heat fluxes in different scenarios using the MFS. These coefficients have also been obtained for the spherical droplet case using the three-dimensional CCR model in Ref. [90]. The mass-and heat-flux coefficients obtained from the MFS read

$$c_1^{\text{MFS}} = \frac{1}{2\pi} \int_0^{2\pi} \mathbf{v} \cdot \mathbf{n} \, d\vartheta = \frac{1}{2\pi} \sum_{i=1}^{N_s} h_i,$$
 (6.20)

$$c_2^{\text{MFS}} = \frac{1}{2\pi} \int_0^{2\pi} \mathbf{q} \cdot \mathbf{n} \, d\vartheta = \frac{1}{2\pi} \sum_{i=1}^{N_s} g_i.$$
 (6.21)

## 6.3 Validation and discussion

The numerical results are obtained with the MFS parameters as  $N_s = 60$ ,  $R_b = 0.5$  and  $R_s = 0.4R_b$ . The choice for  $N_s$  and  $R_s$  will be justified later in Sec. 6.5. Throughout this section, the solid lines represent the results obtained from the analytic solution whereas the symbols (disks) denote the results obtained using the MFS. In order to validate the results obtained from the MFS with those from the analytic solution, we first compare the mass-and heat-flux coefficients.

Figure 6.3 shows the mass-flux and heat-flux coefficients ( $c_1$  and  $c_2$ , respectively) plotted against the Knudsen number (Kn) for the pressure- and temperature-driven cases. The variations are depicted for different values of the evaporation/condensation coefficient  $\Theta$ . An excellent agreement is evident between the results obtained from the MFS and analytic solution in all the scenarios. The mass-flux coefficient for the pressure-driven case is presented in the left panel of Fig. 6.3. For very small values of the Knudsen number Kn  $\lesssim 0.001$ , the values of the mass-flux coefficient  $c_1^p$  remain constant for all values of

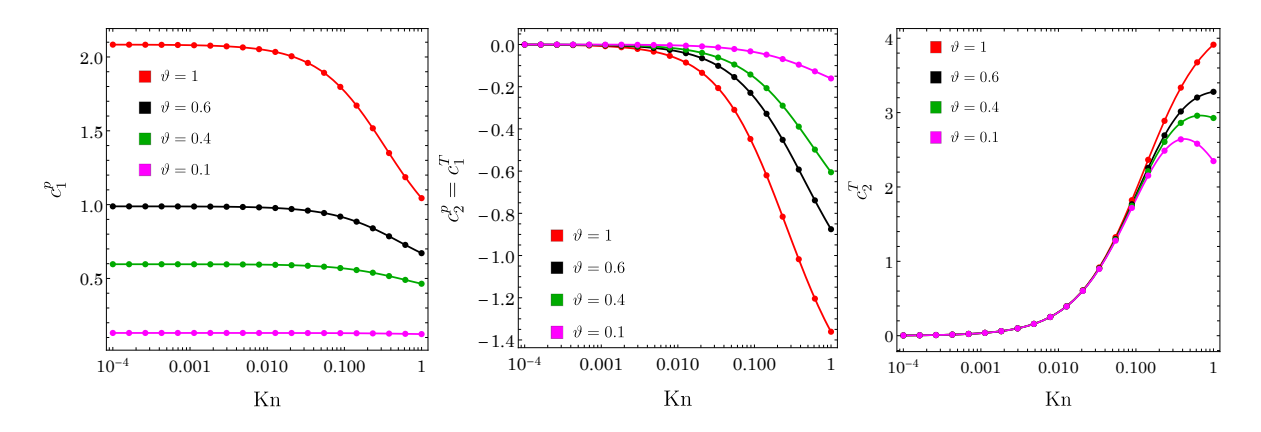


Figure 6.3: The mass-flux coefficient  $c_1$  in the pressure-driven ( $T^I=0$ ,  $p_s=1$ ) case (left) and in temperature-driven ( $T^I=1$ ,  $p_s=0$ ) case (middle); and the heat-flux coefficient  $c_2$  for the temperature-driven ( $T^I=1$ ,  $p_s=0$ ) case (right) as a function of Knudsen number with different values of  $\Theta$ . The middle panel also represents the heat-flux coefficient  $c_2$  in the pressure-driven ( $T^I=0$ ,  $p_s=1$ ) case. The numerical results obtained from the MFS using expressions (6.20) and (6.21) are represented by symbols while the analytical results calculated using (6.13) and (6.15) are shown with solid lines.

 $\Theta$ . However, beyond Kn  $\gtrsim 0.01$ , the values of  $c_1^p$  decrease as Kn increases for all larger of evaporation/condensation coefficient ( $\Theta = 1, 0.6, 0.4$ ). Middle panel of Fig. 6.3 shows the heat-flux coefficient in the pressure-driven case  $c_2^p$  (or the mass-flux coefficient in the temperature-driven case  $c_1^T$ ) and Right panel of Fig. 6.3 shows the variation in heat-flux coefficient  $c_2^T$  in the temperature-driven case. It is evident from the pressure-driven scenario (left and middle panels) that  $c_1^p > 0$  and  $c_2^p < 0$  indicating the evaporation at the interface as mass flows from liquid to vapor and heat flows from vapor to liquid. On the other hand, from the temperature-driven scenario (middle and right panels),  $c_1^T < 0$  and  $c_2^T > 0$  which indicate the condensation at the interface as the mass flows from vapor to liquid and heat flows from liquid to vapor. To further understand this phenomenon of evaporation/condensation at the interface, we plot the radial velocity and temperature varying around the liquid jet in the Figs. 6.4 and 6.5, for the pressure- and temperature-driven cases, respectively.

The left and right panels of Fig. 6.4 depict the variation of the radial velocity  $v_r$  and temperature T, respectively, with the radial distance in the pressure-driven case for Kn = 0.1. As depicted in the left panel of the figure, the radial velocity decreases with the increase in radial distance, due to the relation  $v_r = c_1/r$  [in (6.11))]and  $c_1^p > 0$ . Moreover

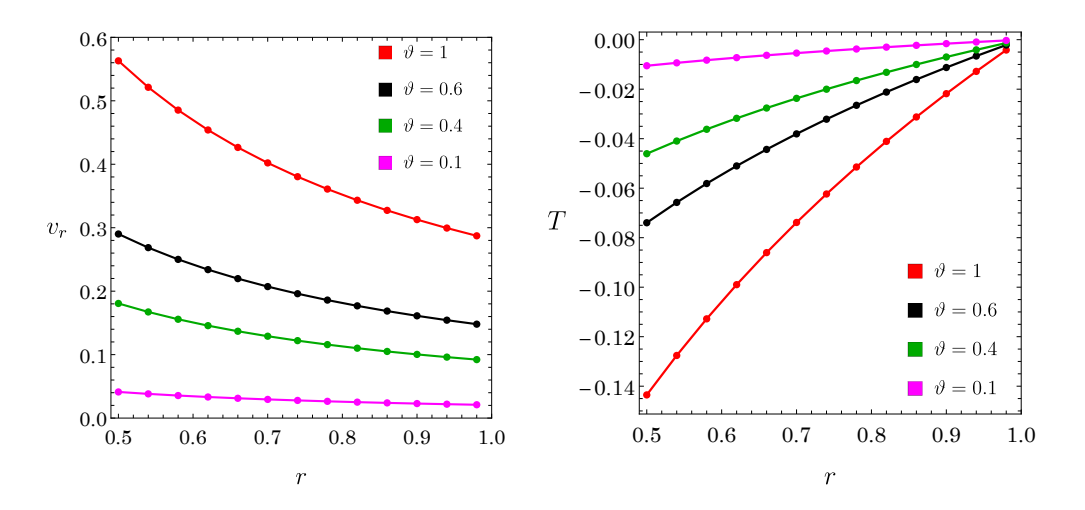


Figure 6.4: Variation in the radial velocity (left panel) and temperature (right panel) with the radial distance for the pressure-driven case ( $p_s = 1$  and  $T^I = 0$ ) at Kn = 0.1 for different values of  $\Theta$ . Numerical results obtained using the CCR-MFS framework are illustrated using symbols (disks) and analytical solutions are represented by solid lines.

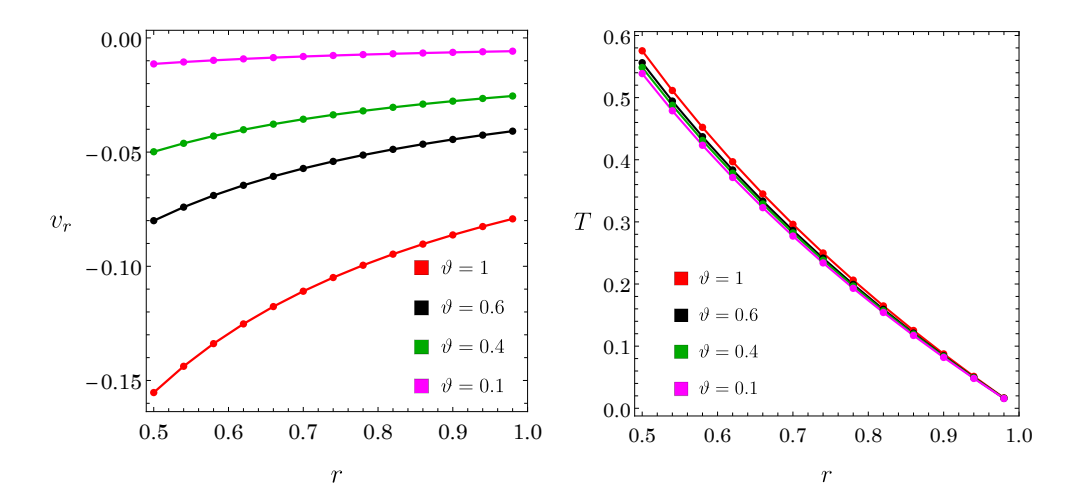


Figure 6.5: Same as Fig. 6.4 but for the temperature-driven case  $(T^I = 1$  and  $p_s = 0)$ .

the right panel of the figure indicates the temperature at the interface (r=0.5) is lower in comparison to the temperature of the surrounding vapor. This leads the heat to flow from vapor toward the liquid (as also indicated by  $c_2^p < 0$  in Fig. 6.3) and in turn causing evaporation at the interface. The left and right panels of Fig. 6.5 depict the variation of the radial velocity  $v_r$  and temperature T, respectively, with radial distance in the temperature-driven case for  $\mathrm{Kn} = 0.1$ . In this case, the left panel of the figure indicates a negative radial velocity, which is due to  $c_1^T < 0$  from Fig. 6.3. As evident from the right panel of the figure, the temperature on the interface is higher than the surrounding vapor leading the heat to flow from liquid toward the vapor (as also indicated by  $c_2^T > 0$  in Fig. 6.3) and in turn causing condensation at the interface. In both pressure- and temperature-driven scenarios, the magnitudes of the flow variables  $v_r$  and T are higher for larger values of the evaporation/condensation coefficient  $\Theta$ . However, the temperature in the temperature-driven case is not significantly sensitive toward  $\Theta$ .

## 6.4 Evaporation/condensation on noncircular cross-sections

In the present section, we utilize spherical harmonics to generate jets with non-circular cross-sections. Spherical harmonics are mathematical functions defined on the surface of a sphere [45] which describe smooth deformations of spherical surfaces, useful for modeling deformed droplets.. To study the effects of evaporation and condensation at an interface with complex geometry, spherical harmonics offer a practical framework for introducing

controlled perturbations or deformations to a circular cross-section. Spherical harmonics are defined as  $Y_{\ell}^{m}(\theta,\varphi)$  [71]:

$$Y_{\ell}^{m}(\theta,\varphi) = \sqrt{\frac{(2\ell+1)}{4\pi} \frac{(\ell-m)!}{(\ell+m)!}} P_{\ell}^{m}(\cos\theta) e^{im\varphi}, \tag{6.22}$$

where  $P_{\ell}^m(x)$  are the associated Legendre polynomials of degree  $\ell$  and order m,  $\theta \in [0, \pi]$  is the polar angle, and  $\varphi \in [0, 2\pi]$  is the azimuthal angle.

Any surface coordinate that is a function of  $\theta$  and  $\varphi$  is defined as

$$r(\theta,\varphi) = \sum_{\ell=0}^{L} \sum_{m=-\ell}^{\ell} a_{\ell}^{m} Y_{\ell}^{m}(\theta,\varphi), \tag{6.23}$$

where  $a_{\ell}^{m}$  are the harmonic coefficients that determine the contribution of each spherical harmonic mode. For modeling the surface of a droplet, the radial distance r is defined as a perturbation of a perfect sphere with radius  $r_0$ 

$$r(\theta, \varphi) = r_0 \left( 1 + \sum_{\ell=0}^{L} \sum_{m=-\ell}^{\ell} a_{\ell}^m \operatorname{Re}(Y_{\ell}^m(\theta, \varphi)) \right). \tag{6.24}$$

For a cylindrical geometry,  $Y_{\ell}^{m}(\theta, \varphi)$  depends only on  $\theta$  and becomes independent of  $\varphi$  as m = 0. This makes the spherical harmonics axisymmetric and reduces them to Legendre polynomials

$$Y_{\ell}^{0}(\theta) = \sqrt{\frac{(2\ell+1)}{4\pi}} P_{\ell}^{0}(\cos\theta). \tag{6.25}$$

With this, Eq. (6.24) reduces to

$$r(\theta) = r_0 \left( 1 + \sum_{\ell=0}^{L} a_{\ell}^0 Y_{\ell}^0(\theta) \right). \tag{6.26}$$

In the present work, we use harmonics up to L=4 ( $\ell=0,1,2,3,4$ ) and for the sake of simplicity, we drop the superscript "0" and adopt the notation  $a_{\ell}$  instead of  $a_{\ell}^0$  to describe the parameters in the considered examples. We consider two set of parameters (a)  $a_0=0$ ,  $a_1=0.01$ ,  $a_2=0.8$ ,  $a_3=0.01$ ,  $a_4=0.01$  for shape 1 and (b)  $a_0=0$ ,  $a_1=0.05$ ,  $a_2=0.05$ ,  $a_3=0$ ,  $a_4=0.1$  for shape 2. A two-dimensional cross-section for the corresponding deformed non-circular jet is illustrated in Fig. 6.6. Both jets are considered to be surrounded by their own vapors with an infinitely thin separating liquid-vapor interface. The rest far-field equilibrium assumptions are analogous to those in the circular case. For the sake of MFS implementation, the boundary nodes are discretized at equispaced angular distances. A fictitious boundary containing singularity points is

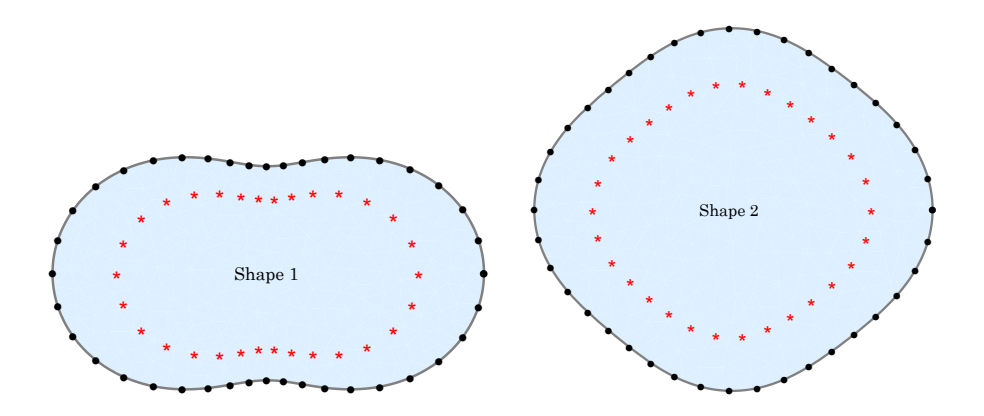


Figure 6.6: Shapes generated using equation (6.26) for set of parameters  $a_0 = 0$ ,  $a_1 = 0.01$ ,  $a_2 = 0.8$ ,  $a_3 = 0.01$ ,  $a_4 = 0.01$  (left) and  $a_0 = 0$ ,  $a_1 = 0.05$ ,  $a_2 = 0.05$ ,  $a_3 = 0$ ,  $a_4 = 0.1$  (right) with  $r_0 = 0.5$ . The black (disk) symbols denote the boundary nodes discretized over the interfacial boundary whereas the red (star) symbols denote the chosen singularity points in both the shapes.

chosen to be in the same shape as the cross section, shrunk inside the actual boundary of both jets. A dilation parameter  $\alpha$  is used to decide the location of fictitious boundary inside the original boundary, such that  $a_{s0} = a_0/\alpha$ ,  $a_{s1} = a_1/\alpha$ ,  $a_{s2} = a_2/\alpha$ ,  $a_{s3} = a_3/\alpha$ ,  $a_{s4} = a_4/\alpha$  are the shape parameters.

The left and middle panels of Fig. 6.7 illustrate the variation in the mass-and heat-flux coefficients in the pressure-driven case for the circular and non-circular cross sections. The (solid) red, (dot-dashed) black and (dashed) blue curves represent the results for the circle, shape 1 and shape 2, respectivey. The results are presented as a function of Kn for complete evaporation by taking  $\Theta = 1$ . In shape 2, which retains symmetry in both x- and y-directions, the mass-flux and heat-flux coefficients  $c_1^p$  and  $c_2^p$  in the pressure-driven case show slight deviations from those of the circular shape. However, in shape 1, the asymmetric deformation leads to significant deviation, especially in the mass-flux coefficient. Since the heat-flux coefficient for the pressure-driven case is equal to the the mass-flux coefficient in the temperature-driven case, the right panel of Fig. 6.7 demonstrates the variation in heat-flux coefficient for the temperature-driven case. In this case also, the deformity in shape 1 leads to significant deviation in comparison to shape 2 and circular case.

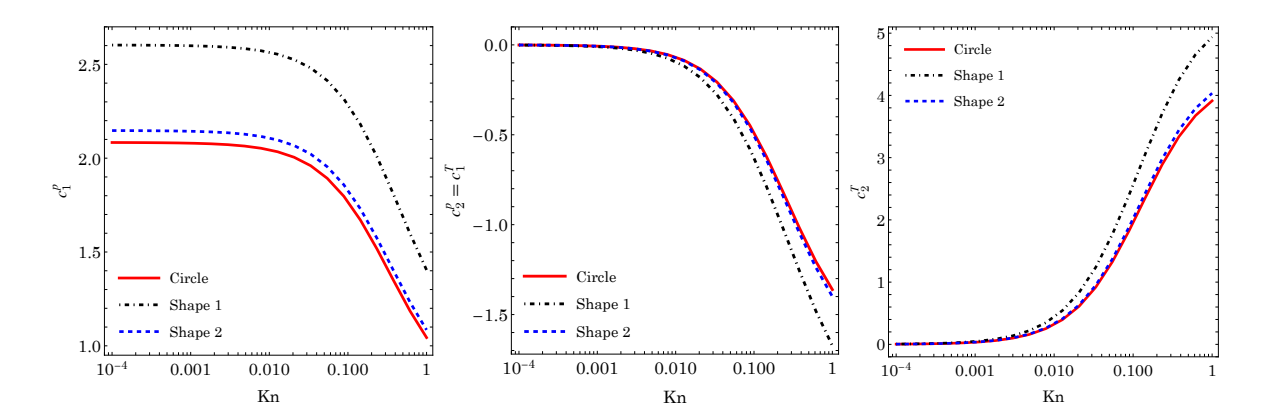


Figure 6.7: The mass-flux coefficient  $c_1$  in the pressure-driven  $(T^I = 0, p_s = 1)$  case (left) and in temperature-driven  $(T^I = 1, p_s = 0)$  case (middle); and the heat-flux coefficient  $c_2$  for the temperature-driven  $(T^I = 1, p_s = 0)$  case (right) as a function of Knudsen number for  $\Theta = 1$ . The middle panel also represents the heat-flux coefficient  $c_2$  in the pressure-driven  $(T^I = 0, p_s = 1)$  case. Results correspond to the circle and two deformed shapes presented in Fig. 6.6.

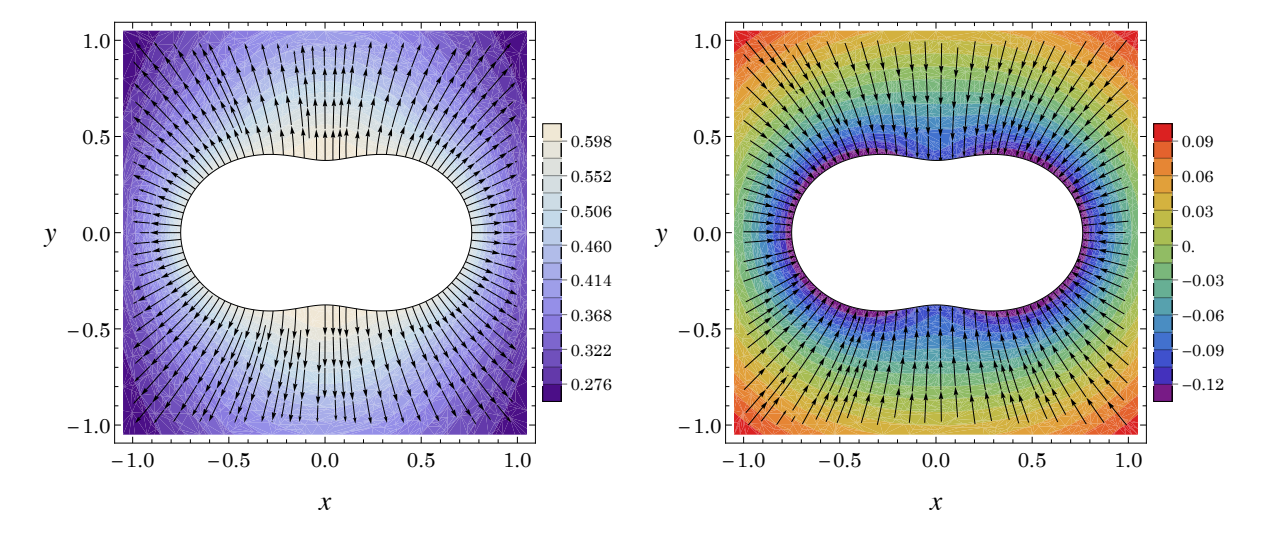


Figure 6.8: Velocity streamlines over speed contours (left panel) and heatflux lines over temperature contours (right panel) in the pressure-driven case ( $T^I = 0$  and  $p_s = 1$ ) for shape 1 at Kn = 0.1.

Figures 6.8 to 6.11 show the flow and heat profiles around the jets with non-circular cross-sections having shapes depicted in Fig. 6.6. The left panel of Fig. 6.8 illustrates the streamlines plotted over speed contours around the interface with shape 1 (left panel in Fig. 6.6) for the pressure-driven case ( $T^{I} = 0$  and  $p_{s} = 1$ ). The flow pattern exhibits

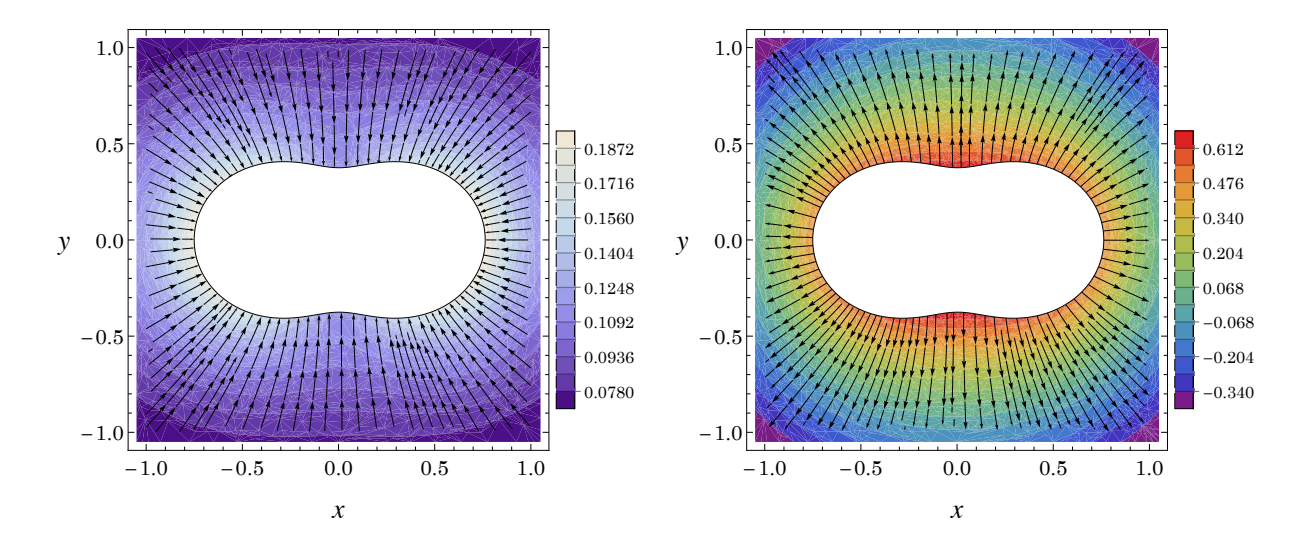


Figure 6.9: Velocity streamlines over speed contours (left panel) and heatflux lines over temperature contours (right panel) in the temperature-driven case ( $T^I = 1$  and  $p_s = 0$ ) for shape 1 at Kn = 0.1.

symmetric behavior around the interface, with higher speeds observed near the interface. The magnitude of velocity decreases as we move away from the interface. The right panel of Fig. 6.8 illustrates the heat-flux lines superimposed over temperature contours for the same shape. Due to the existence of a negative pressure gradient in this case, the heat flows from vapor to the liquid interface as shown by the direction of the heat-flux lines, leading to evaporation at the interface.

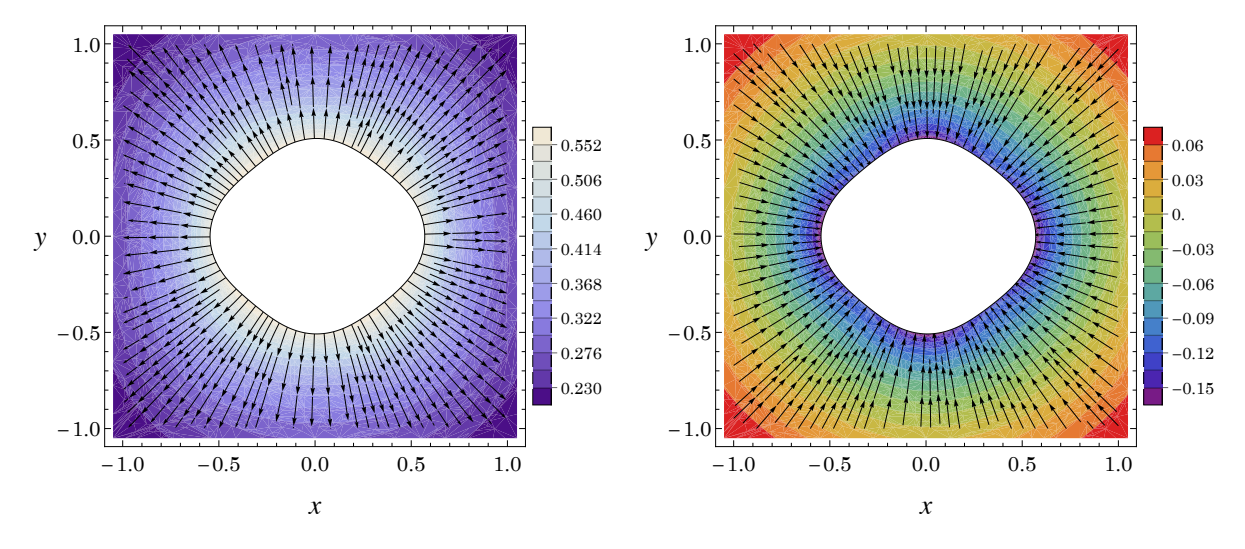


Figure 6.10: Same as Fig. 6.8 but for shape 2.

Figure 6.9 depicts analogous velocity streamlines plotted over speed contours (left panel) and heat-flux lines plotted over temperature contours (right panel) for shape 1, but

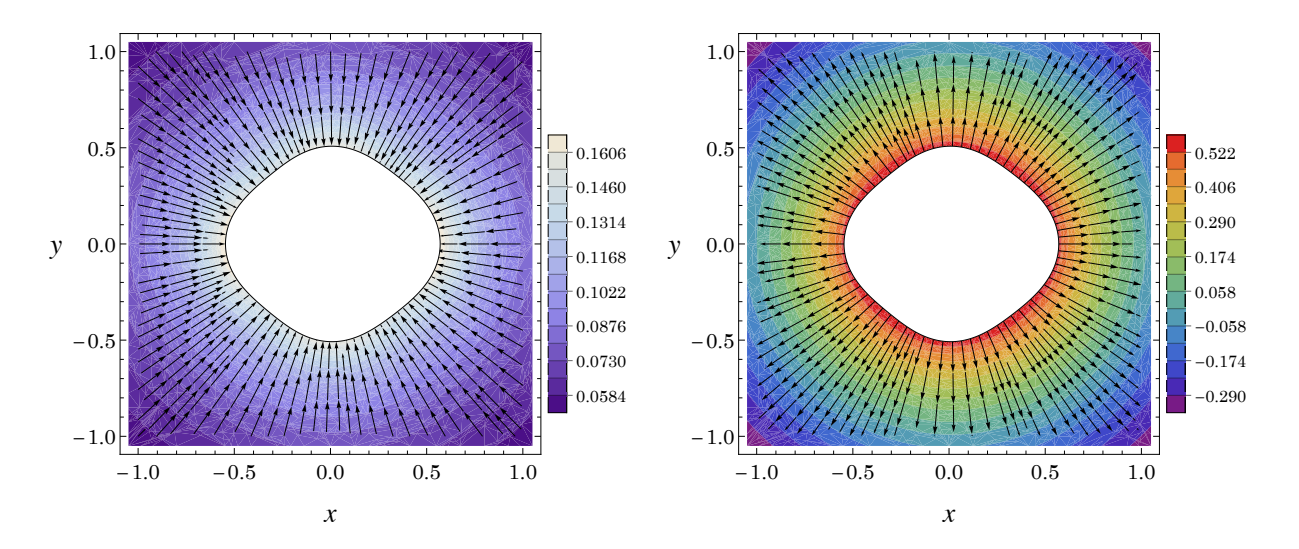


Figure 6.11: Same as Fig. 6.9 but for shape 2.

in the temperature-driven case ( $p_s = 0$  and  $T^I = 1$ ). The streamlines again demonstrate symmetric behavior around the jet with higher speeds observed near the interface but with a direction opposite to the pressure-driven case. In this scenario, the negative temperature gradients around the jet lead the heat to flow outward from hotter to colder regions, which in turn leads to condensation at the interface.

Figures 6.10 and 6.11 illustrate the flow and heat profiles for shape 2 (left panel in Fig. 6.6) in the pressure-driven and temperature-driven cases, respectively. The direction of the streamlines and heat-flux lines in both the pressure-driven and temperature-driven cases are analogous to those obtained for shape 1. The similar behavior again indicates the evaporation(condensation) in the pressure(temperature)-driven case.

## 6.5 Sensitivity analysis

The error analysis is aimed to study the effects of the positioning of the fictitious boundary, the numbers of the singularity and boundary points, the effective condition number and the shape of the collocation matrix on the error. For numerical tests, we have computed the absolute error in the radial velocity and the radial heat flux obtained with the MFS from its corresponding analytic solution (in Sec. 6.2) at the interface. We shall analyze the error in two specific cases for the circular interface, namely the pressure-and temperature-driven cases, for which the analytic solution (including the values of the integration constants) is entirely known. For the shape of the collocation matrix,

there can only be two possibilities—it can either be square or rectangular depending on what the numbers  $N_b$  and  $N_s$  are. The collocation matrix is of size  $3N_b \times 4N_s$  because there are four unknowns corresponding to each singularity point, but only three boundary conditions to use at a boundary node. The collocation matrix can still be made square in two ways: (i) by choosing  $N_b$  and  $N_s$  appropriately so that  $3N_b = 4N_s$  and (ii) by splitting one (or more) boundary condition(s) properly so that the number of boundary conditions equals the number of unknowns for a singularity point. To have an additional boundary condition in the latter case, the sourcelet part of the velocity boundary condition (6.1) in the present work can be extracted. We split the velocity at the  $j^{\text{th}}$  node as

$$v_j = v_j^{(1)} + v_j^{(2)},$$
 (6.27)

where

$$\boldsymbol{v}_{j}^{(1)} = \sum_{i=1}^{N_{s}} \left( \frac{1}{8\pi \operatorname{Kn}} \boldsymbol{f}_{i} \cdot \boldsymbol{J}(\boldsymbol{r}_{ij}) + \frac{1}{4\pi} \frac{5\operatorname{Kn}}{\operatorname{Pr}} \alpha_{0}^{2} \boldsymbol{f}_{i} \cdot \boldsymbol{K}(\boldsymbol{r}_{ij}) \right)$$
(6.28)

$$\mathbf{v}_{j}^{(2)} = \sum_{i=1}^{N_s} \frac{h_i \mathbf{r}_{ij}}{2\pi r_{ij}^2},\tag{6.29}$$

and the source let part of velocity  $\boldsymbol{v}_{j}^{(2)}$  is responsible for evaporation/condensation effects, owing to which we can use two boundary conditions

$$\boldsymbol{v}_j^{(1)} \cdot \boldsymbol{n}_j = 0, \tag{6.30}$$

$$\boldsymbol{v}_{j}^{(2)} \cdot \boldsymbol{n}_{j} = -\eta_{11}(p_{j} - p_{s} + \boldsymbol{n}_{j} \cdot \boldsymbol{\sigma}_{j} \cdot \boldsymbol{n}_{j}) + \eta_{12} \left( T_{j} - T^{I} + \alpha_{0} \boldsymbol{n}_{j} \cdot \boldsymbol{\sigma}_{j} \cdot \boldsymbol{n}_{j} \right). \tag{6.31}$$

in order to have four boundary conditions at each boundary node. Now, on taking  $N_b = N_s$ , the collocation matrix is a square matrix of size  $4N_s \times 4N_s$ . In summary, we have considered the following three cases throughout our analysis.

- Case 1: The collocation matrix is made square by choosing the values of  $N_b$  and  $N_s$  in such a way that  $3N_b = 4N_s$ .
- Case 2: The collocation matrix is made square by splitting boundary condition (6.1) into two new boundary conditions [which at the  $j^{\text{th}}$  boundary node are (6.30) and (6.31)], and taking  $N_b = N_s$ .
- Case 3: The values of  $N_b$  and  $N_s$  are such that the collocation matrix is rectangular and we do not try to make it square. In this case, the numerical solution is obtained using the method of least squares.

In cases 1 and 2,  $N_b$  varies with  $N_s$ , meaning that once one is chosen, the other is determined by the constraints  $3N_b = 4N_s$  (for Case 1) or  $N_b = N_s$  (for Case 2). In case 3, where the collocation matrix remains rectangular,  $N_b$  and  $N_s$  can be chosen more flexibly, provided that  $3N_b > 4N_s$  to ensure an overdetermined system. We exclude cases where  $3N_b < 4N_s$ , as this would lead to an underdetermined system with more unknowns than equations. For case 3, we have taken  $N_b = 65$  in all our computations. For determining the location of singularities, we use a parameter  $\alpha$  which relates the radius of the boundary to that of the fictitious boundary via  $R_s = \alpha R_b$ . A smaller value of the parameter  $\alpha$  implies a greater distance between the actual and fictitious boundaries.

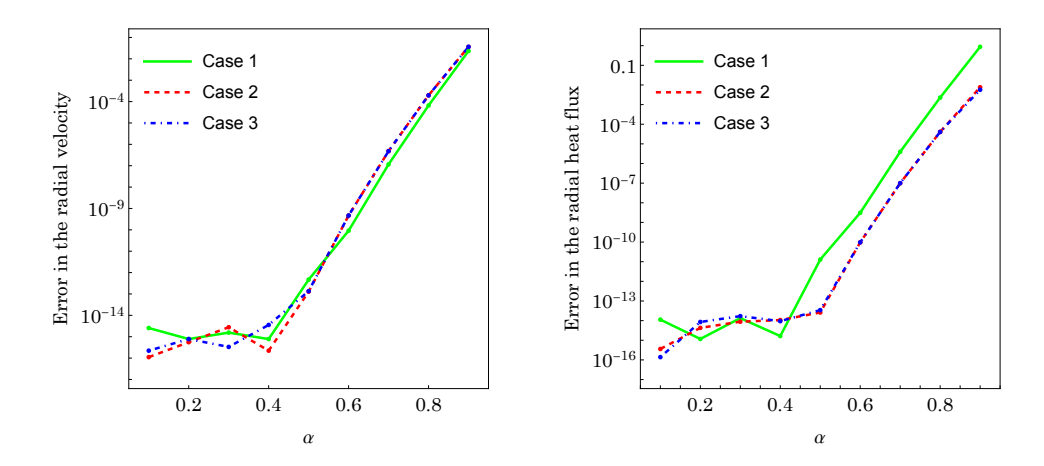


Figure 6.12: Absolute errors in the radial velocity and radial heat flux plotted against the dilation parameter in the pressure-driven case for Kn = 0.1 and  $N_s = 45$ .

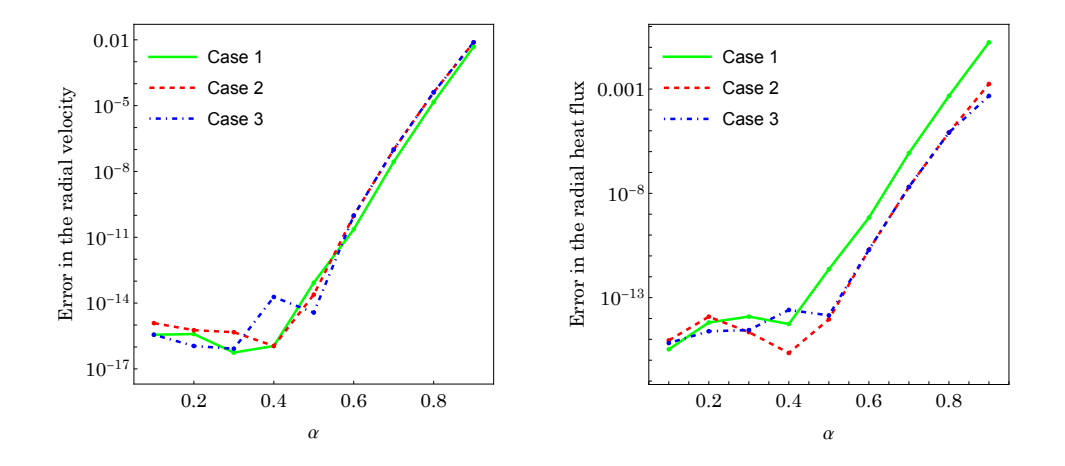


Figure 6.13: Same as Fig. 6.12 but in the temperature-driven case.

Figures 6.12–6.14 illustrate the absolute errors in the radial velocity radial heat flux in different cases. Figures 6.12 and 6.13 exhibit the change in the error on varying the dilation parameter in the pressure- and temperature-driven cases, respectively for the evaporation/condensation coefficient  $\Theta = 1$ . It is evident from Figs. 6.12 and 6.13 that the error in both the quantities remains negligible for  $\alpha \lesssim 0.5$ . However, the error starts increasing with increasing  $\alpha$  beyond this. This means that, beyond a certain position of the fictitious boundary, the error in the solution becomes larger and larger as the fictitious boundary is placed closer and closer to the actual boundary. This feature remains the same even for different Knudsen numbers (we have checked it for different values of the Knudsen number ranging from 0.1 to 1).

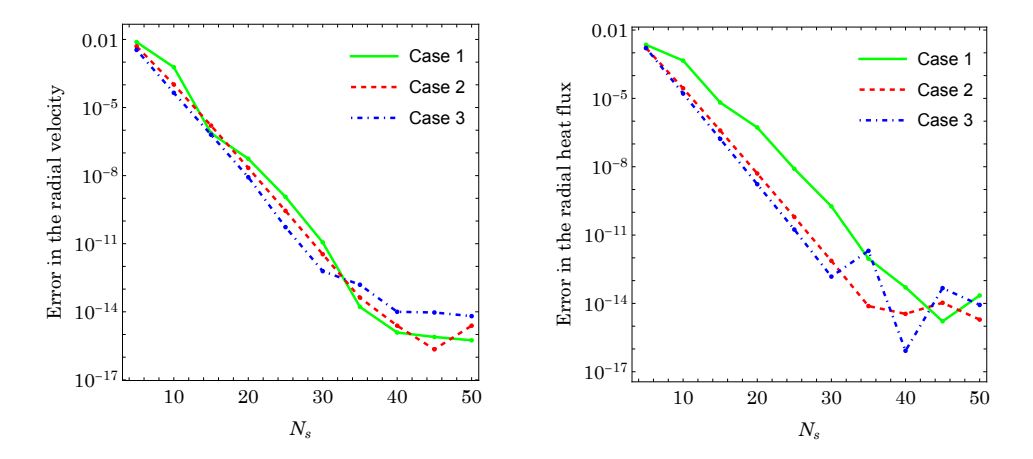


Figure 6.14: Absolute errors in the radial velocity and radial heat flux plotted over the number of singularity points in the pressure-driven case for Kn = 0.1 and  $\alpha = 0.4$ .

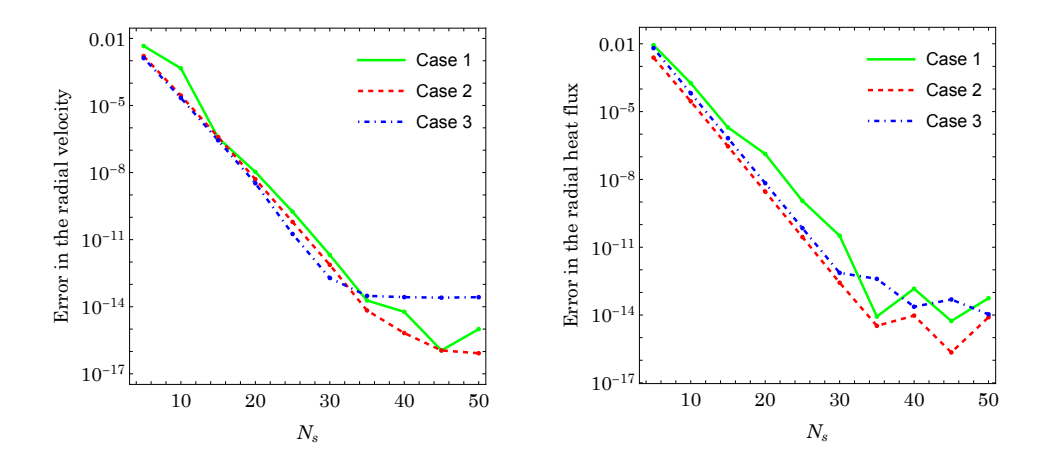


Figure 6.15: Same as Fig. 6.14 but in the temperature-driven case.

Figures 6.14 and 6.15 display the change in the error on varying the number of the singularity points placed on a circle of radius  $R_s = 0.2$ , i.e. for  $\alpha = 0.4$  in the pressure- and temperature-driven cases, respectively. As expected, Figs. 6.14 and 6.15 also confirm that an increase in the number of singularity points leads to more accuracy. From Figs. 6.12–6.15, it is evident that the overall behavior in the errors remains analogous for all three considered cases. The computational time of our simulations depends primarily on the number of singularity points  $N_s$  used in the MFS. However, it remains independent of the dilation parameter  $\alpha$ , which determines the location of singularities, as well as the choice of a square or rectangular collocation matrix. Each of the calculations presented was computed in less than or around 1–2 seconds on a single 2.10 GHz Intel Core i7 processor using Mathematica<sup>®</sup>.

Another important parameter that indicates the right choice of the location of singularities is the effective condition number for a linear system. Figure 6.16 demonstrates the

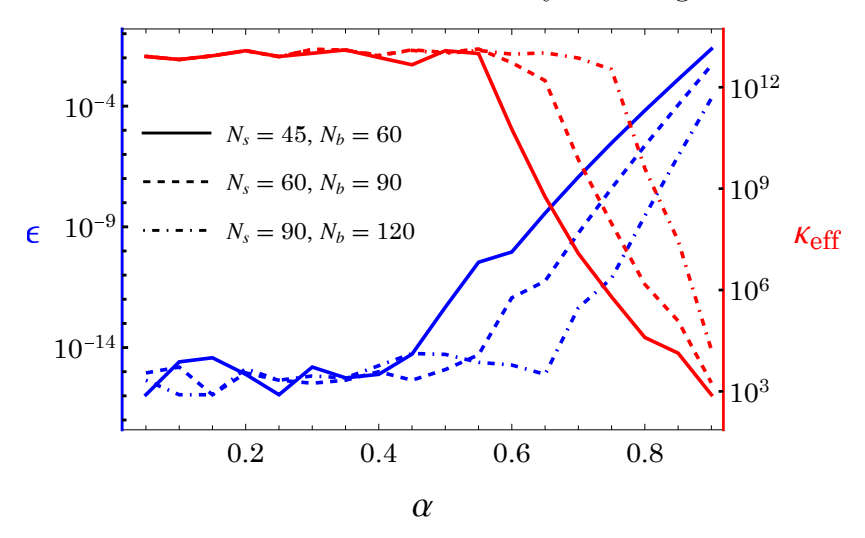


Figure 6.16: Absolute error  $\epsilon$  in the radial velocity at the interface (represented by the blue axis and curves) and the effective condition number  $\kappa_{\rm eff}$  (represented by the red axis and curves) varying with the dilation parameter  $\alpha$  for different number of boundary nodes and singularity points. The solid, dashed and dot-dashed curves represent the cases with  $N_s=45, N_b=60;$   $N_s=60, N_b=80;$  and  $N_s=90, N_b=120,$  respectively.

error in radial velocity (denoted by  $\epsilon$ ) in the pressure-driven case and effective condition number  $\kappa_{\rm eff}$ , plotted simultaneously against the dilation parameter  $\alpha$  for Kn = 0.1. The collocation matrix has been constructed as described in case 1 with square  $3N_b \times 4N_s$ 

system. The blue solid, dashed and dot-dashed lines represent the variation in error with respect to  $\alpha$  for  $N_s=45, N_b=60; N_s=60, N_b=80;$  and  $N_s=90, N_b=120;$  respectively whereas the red solid, dashed and dot-dashed lines represent the variation in effective condition number for  $N_s = 45, N_b = 60; N_s = 60, N_b = 80; \text{ and } N_s = 90, N_b = 120, \text{ re-}$ spectively. The link between  $\alpha$  and  $N_s$  becomes clear from the figure as fictitious boundary can be shifted towards the actual boundary while maintaining roughly the same accuracy by increasing the numbers of the collocation and singularity points. In other words, it is feasible to use less numbers of boundary nodes and source points when choosing a smaller value of  $\alpha$  for computational efficiency in the case of a circular interface. This link between the number of source and boundary points as depicted in Fig. 6.16 is not universally true for all problems. Nevertheless, the interesting aspect is to note the inverse relation of effective condition number with accuracy as it helps determine an optimal location for singularities for the problems where the analytic solution is not known. To discuss the choice of location of singularities for deformed interfaces (shape 1 and shape 2), we plot the effective condition number  $\kappa_{\rm eff}$  varying with the dilation parameter  $\alpha$  for shape 1 (left panel) and shape 2 (right panel) in Fig. 6.17. It is evident from the figure that the highest value of effective condition number is achieved somewhere in between  $0.6 \lesssim \alpha \lesssim 0.8$  for all the considered values of  $N_s, N_b$  for both the shapes. Moreover, considering a greater number of boundary and singularity points yields higher values of  $\kappa_{\rm eff}$ . The computational time for both considered shapes with  $N_s = 180$ ,  $N_b = 240$  is approximately 20 seconds, which is higher than that for  $N_s = 120$ ,  $N_b = 180$  ( $\sim 9$  seconds) and  $N_s = 90$ ,  $N_b = 120$ 

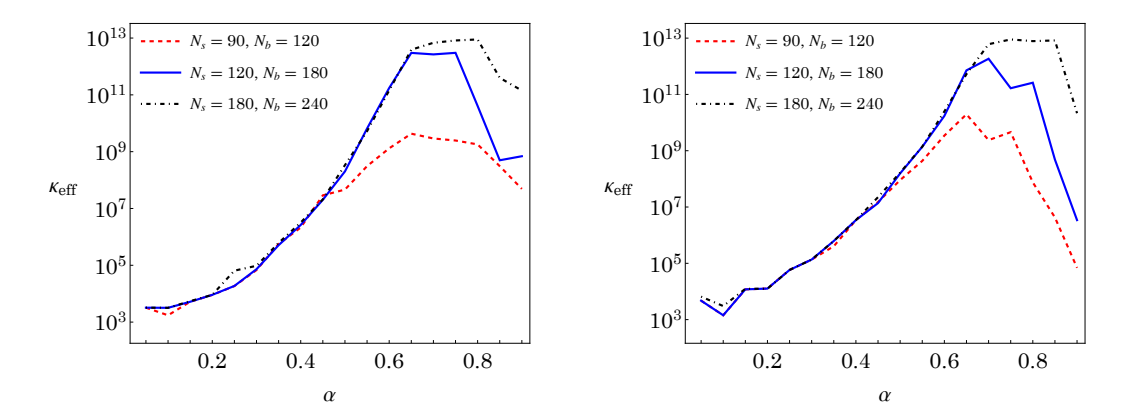


Figure 6.17: Variation in the effective condition number  $\kappa_{\text{eff}}$  with respect to the dilation parameter  $\alpha$  for different numbers of boundary and source points in case of shape 1 (left panel) and shape 2 (right panel).

( $\sim 5$  seconds). Nevertheless, we fix  $N_s = 180$ ,  $N_b = 240$  with  $\alpha = 0.7$  to ensure accurate results for the problems with deformed interface (shape 1 and shape 2).

## 6.6 Summary

In this chapter, the evaporation and condensation phenomena have been investigated around liquid jets with both circular and non-circular cross-sections. The thermodynamically admissible boundary conditions for the CCR model in both complete and partial evaporation/condensation scenarios have been presented and implemented. By exploiting the symmetry inherent in the circular configuration, analytic solutions have been obtained for the circular case, and the results from the MFS have been validated against these solutions. Across the cases—including both pressure-driven and temperature-driven evaporation/condensation cases—an excellent agreement has been observed between the analytic and numerical results.

The numerical framework has been further extended to non-circular jets for investigating the effect of the shape of the interface by introducing controlled deformations via spherical harmonics. The results have shown that for nearly symmetric, mildly deformed-circular jets, mass and energy fluxes remain comparable to those of corresponding to the circular jet. However, significant asymmetry in the interface shape has been observed to cause notable deviations in the mass-flux and heat-flux coefficients. The velocity streamlines and heat-flux lines have further clarified how these deformations influence local flow and transport fields. A comprehensive sensitivity analysis has also been conducted to assess the influence of the placement of source points, the number of source and boundary points, and the matrix structure on numerical accuracy and computational cost.

## Chapter 7

# Generalizing the MFS to higher-order moment systems

As mentioned in Sec. 1.2, all previous works on the MFS for rarefied gas flows [27, 64, 90], and also Chapters 3 to 6 of this thesis required deriving fundamental solutions for specific models by prescribing Dirac-delta source terms in selected governing equations within the system and/or in the closure relations. While effective, this methodology typically makes it challenging to extend the MFS for new or more complex models, where the fundamental solutions are unknown and the choice of source terms is not straightforward. To address the limitations posed by fixing the source terms manually, we propose a generic approach that allows for the computation of fundamental solutions for any large system of equations without the need to predefine specific Dirac-delta source terms. The generic MFS approach relies on two steps. The first step involves identifying the fundamental solutions of the system. This process is similar to Hörmander's method [8, 47] and employs Fourier transformation in combination with partial fraction decomposition to derive expressions for the fundamental solutions. The second step is determining the source strengths using the boundary conditions for the problem under consideration.

## 7.1 The technique

This section introduces a general technique to determine and implement the fundamental solutions for any linear first-order system of partial differential equations. We consider a linearized system of  $N \in \mathbb{N}$  partial differential equations in (two-dimensional) Cartesian coordinates, expressed as

$$\mathbf{A}^{(x)}\partial_x \mathbf{U} + \mathbf{A}^{(y)}\partial_y \mathbf{U} + \mathbf{P}\mathbf{U} = \mathbf{S}\delta(\mathbf{r}), \tag{7.1}$$

where  $U: \Omega \to \mathbb{R}^N$  is the variable vector field,  $A^{(x)}, A^{(y)} \in \mathbb{R}^{N \times N}$  are constant advection matrices and  $P \in \mathbb{R}^{N \times N}$  is the constant reaction matrix,  $S \in \mathbb{R}^N$  is a constant forcing vector (including source terms) and  $\delta(\mathbf{r})$  is the Dirac delta. To determine the fundamental

solution of the system, we define the Fourier transform  $\hat{F}(\mathbf{k})$  of a function  $F(\mathbf{r})$  as

$$\mathcal{F}(F(\mathbf{r})) = \hat{F}(\mathbf{k}) := \int_{\mathbb{R}^2} F(\mathbf{r}) e^{-i \mathbf{k} \cdot \mathbf{r}} d\mathbf{r}, \qquad (7.2)$$

where i is the imaginary unit,  $\mathbf{k} = (k_x, k_y) \in \mathbb{R}^2$  is the wave vector in the spatial-frequency domain. The corresponding inverse Fourier transformed counterpart is defined as

$$\mathcal{F}^{-1}(\hat{F}(\boldsymbol{k})) = F(\boldsymbol{r}) := \frac{1}{(2\pi)^2} \int_{\mathbb{R}^2} \hat{F}(\boldsymbol{k}) \, e^{i \boldsymbol{k} \cdot \boldsymbol{r}} \, d\boldsymbol{k}. \tag{7.3}$$

Applying Fourier transformation on Eq. (7.1) we obtain

$$\mathbf{A}(\mathbf{k})\hat{\mathbf{U}} := (ik_x \mathbf{A}^{(x)} + ik_y \mathbf{A}^{(y)} + \mathbf{P})\hat{\mathbf{U}} = \mathbf{S}\hat{\delta}, \tag{7.4}$$

wherein the inverse of the matrix  $\boldsymbol{A} \in \mathbb{R}^{N \times N}$  can be written as

$$\mathbf{A}(\mathbf{k})^{-1} = \frac{1}{\det(\mathbf{A}(\mathbf{k}))} \mathbf{A}(\mathbf{k}) = \frac{1}{s(\mathbf{k})} \mathbf{A}(\mathbf{k}). \tag{7.5}$$

Here, the determinant  $\det(\mathbf{A}(\mathbf{k})) = s(\mathbf{k})$  is identified as the *symbol* [35] of the partial differential operator and the matrix  $\mathbf{A}$  is the adjugate matrix, which contains the cofactor expansions of the original matrix. Since both adjugate matrix and symbol contain polynomial terms in  $k_x$  and  $k_y$ , they can be easily inverted using the Fourier inverse transformation. Using the fact that

$$\mathbf{A}(\nabla)\mathbf{A}(\nabla) = s(\nabla)I_N,\tag{7.6}$$

where  $I_N$  is the  $N \times N$  identity matrix, one can conclude

$$s(\mathbf{k})\hat{\mathbf{U}} = \mathbf{A}(\mathbf{k})\mathbf{S}\hat{\delta} \iff s(\mathbf{\nabla})[\mathbf{U}] = \mathbf{A}[\delta]\mathbf{S}.$$
 (7.7)

This crucial step makes this approach commendable. Finding the fundamental solution corresponding to only the symbol operator leads us to the fundamental solution for the complete system. The fundamental solution for the full system is given by

$$U(r) = \mathcal{A}(\nabla)[\Phi](r)S, \tag{7.8}$$

where  $\Phi$  is the two-dimensional fundamental solution associated with the symbol  $s(\nabla)$  of the PDE, i.e.

$$s(\mathbf{\nabla})[\Phi] = \delta. \tag{7.9}$$

It is straightforward to calculate  $\Phi$  if the symbol turns out to be a differential operator with a known fundamental solution. Furthermore, if the symbol can be factorized into

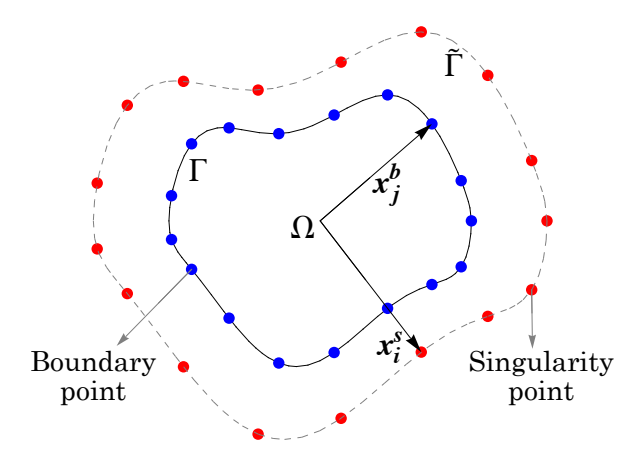


Figure 7.1: Schematic representation for discretization of boundary points (blue disks) on the domain boundary and singularity points (red disks) outside the problem domain.

Laplace, polyharmonic and Helmholtz operators, the fundamental solution  $\Phi$  can be calculated using partial fraction decomposition along with inverse Fourier transforms of the known factor operators. It is important to note that a fundamental solution  $\Phi$  is not unique. Different solutions can be obtained by adding the homogeneous solutions, which correspond to the null space of the operator. This non-uniqueness plays a crucial role in constructing tailored solutions for specific boundary conditions and physical scenarios.

After finding the fundamental solution for the complete system, the MFS involves the discretization of the domain boundary into boundary nodes and placement of the singularity or source points on some fictitious boundary outside the problem domain. We demonstrate this by considering an arbitrary domain  $\Omega$  having boundary  $\Gamma$  as shown in Fig. 7.1. The boundary  $\Gamma$  is discretized into  $N_b$  equispaced boundary points having position vectors  $\mathbf{x}_j^b$ ;  $j = 1, \ldots, N_b$ . Outside the domain  $\Omega$ , a fictitious boundary  $\tilde{\Gamma}$  is considered with source points  $\mathbf{x}_i^s$ ;  $j = 1, \ldots, N_s$ . The relative position of the *i*th source point with respect to  $j^{\text{th}}$  boundary node is denoted by  $\mathbf{r}_{ij} = \mathbf{x}_j^b - \mathbf{x}_i^s$ . The boundary conditions for the problem are written in the form

$$\boldsymbol{B}(\boldsymbol{x}^b)\boldsymbol{U}(\boldsymbol{x}^b) = \boldsymbol{g}(\boldsymbol{x}^b), \tag{7.10}$$

where  $\boldsymbol{B}(\boldsymbol{x}^b) \in \mathbb{R}^{p \times N}$  is a matrix depending on the normal and tangent vectors  $\boldsymbol{n}$  and  $\boldsymbol{t}$  associated with any point  $\boldsymbol{x}^b$  lying on the boundary  $\Gamma$  and  $\boldsymbol{g}(\boldsymbol{x}^b) \in \mathbb{R}^p$  is the corresponding right-hand-side vector. The numerical solution obtained by the MFS is the superposition

of the obtained fundamental solutions, i.e.

$$U_{\text{MFS}}(\boldsymbol{x}) = \sum_{i=1}^{N_s} \mathfrak{A}(\boldsymbol{x} - \boldsymbol{x}_i^s) \boldsymbol{S}_i, \qquad (7.11)$$

where  $U_{MFS}(\boldsymbol{x})$  denotes the solution at any point  $\boldsymbol{x} \in \Omega$ ,  $\mathfrak{A}(\boldsymbol{r}) \equiv \mathcal{A}(\boldsymbol{\nabla})[\Phi](\boldsymbol{r})$  and  $\boldsymbol{S}_i \in \mathbb{R}^N$  contains the unknown source strengths corresponding to  $i^{\text{th}}$  source point  $\boldsymbol{x}_i^s$ . The unknown strengths are then calculated by solving a linear system formed on applying the boundary conditions at each boundary node. The linear system reads

$$B(x_j^b)U(x_j^b) = B(x_j^b) \sum_{i=1}^{N_s} \mathfrak{A}(x_j^b - x_i^s) S_i = g(x_j^b), \quad j = 1, 2, \dots, N_b.$$
 (7.12)

The overall linear system is  $\mathcal{M}X = \mathcal{G}$ , where  $\mathcal{M}$  is the  $pN_b \times NN_s$  collocation matrix,  $X \in \mathbb{R}^{NN_s}$  is the vector containing the unknown source strengths  $S_i$  corresponding to  $i = 1, 2, ..., N_s$  singularities and  $\mathcal{G} \in \mathbb{R}^{pN_b}$  contains the right-hand-side vectors  $g(x_j^b)$  for  $j = 1, 2, ..., N_b$ . Since the matrix  $\mathcal{M}$  is generally non-square, it is possible to have many equations (N) with comparatively fewer boundary conditions (p). The choice of the number of boundary and singularity points  $(N_b$  and  $N_s$ , respectively) significantly influences the structure and solvability of the system. To facilitate a square system, we introduce a decomposition  $S = M\mu$ , and choose  $N_b = N_s$ , so that the number of boundary conditions imposed at each boundary node matches the number of unknown source strengths associated with each singularity point. This shall be discussed further in detail in the subsequent sections.

## 7.2 Implementing generic MFS for Stokes' equations

We show the implementation of generic MFS via an example of the Stokes equations (in two dimensions) which read

$$\nabla \cdot \boldsymbol{v} = 0, \tag{7.13}$$

$$\nabla p + \nabla \cdot \boldsymbol{\sigma} = \mathbf{0},\tag{7.14}$$

$$\sigma = -\overline{\nabla v}.\tag{7.15}$$

#### 7.2.1 Fundamental solutions

Rewriting these equations as in the form of Eq. (7.1), the unknowns are  $\boldsymbol{U} = \begin{bmatrix} p & v_x & v_y \\ \sigma_{xx} & \sigma_{xy} & \sigma_{yy} \end{bmatrix}^\mathsf{T}$ , and the matrices are

$$\boldsymbol{A}^{(x)} = \begin{bmatrix} 0 & 1 & 0 & 0 & 0 & 0 \\ 1 & 0 & 0 & 1 & 0 & 0 \\ 0 & 0 & 0 & 0 & 1 & 0 \\ 0 & \frac{2}{3} & 0 & 0 & 0 & 0 \\ 0 & 0 & \frac{1}{2} & 0 & 0 & 0 \\ 0 & -\frac{1}{3} & 0 & 0 & 0 & 0 \end{bmatrix}, \quad \boldsymbol{A}^{(y)} = \begin{bmatrix} 0 & 0 & 1 & 0 & 0 & 0 \\ 0 & 0 & 0 & 0 & 1 & 0 \\ 1 & 0 & 0 & 0 & 0 & 1 \\ 0 & 0 & -\frac{1}{3} & 0 & 0 & 0 \\ 0 & 0 & \frac{2}{3} & 0 & 0 & 0 \end{bmatrix}, \quad (7.16)$$

and  $\mathbf{P} = \text{diag}(0,0,0,1,1,1)$ . On taking the Fourier transformation of the rewritten system, we obtain the matrix

$$\mathbf{A}(\mathbf{k}) = \begin{bmatrix} 0 & ik_x & ik_y & 0 & 0 & 0\\ ik_x & 0 & 0 & ik_x & ik_y & 0\\ ik_y & 0 & 0 & 0 & ik_x & ik_y\\ 0 & \frac{2ik_x}{3} & -\frac{1}{3}(ik_y) & 1 & 0 & 0\\ 0 & \frac{ik_y}{2} & \frac{ik_x}{2} & 0 & 1 & 0\\ 0 & -\frac{1}{3}(ik_x) & \frac{2ik_y}{3} & 0 & 0 & 1 \end{bmatrix},$$
(7.17)

for which the symbol turns out to be

$$s(\mathbf{k}) = \frac{1}{2}(k_x^2 + k_y^2)^2 = \frac{1}{2}k^4, \tag{7.18}$$

where  $k = \sqrt{k_x^2 + k_y^2}$ . In order to find the fundamental solution  $\phi$  associated with the above symbol (such that  $s(\nabla)[\phi] = \delta$ ), we utilize the definition (7.2) and (7.3) for the Biharmonic equation  $\Delta^2 \phi = \delta$  whose fundamental solution in two dimensions is given by [25]

$$\phi = \frac{r^2 (\ln r - 1)}{8\pi},\tag{7.19}$$

where  $r = \sqrt{x^2 + y^2}$ . This fundamental solution  $\phi$  corresponds to the fundamental solution associated with the symbol for Stokes' equations and  $\mathcal{F}^{-1}(1/k^4) = \phi$ . Applying the Fourier transformation [defined by Eq. (7.2)] to the Biharmonic equation  $\Delta^2 \phi = \delta$ , we

obtain

$$(-k_x^2 - k_y^2)^2 \hat{\phi} = k^4 \hat{\phi} = 1 \implies \hat{\phi} = \frac{1}{k^4}.$$
 (7.20)

Taking inverse Fourier transformation,

$$\mathcal{F}^{-1}\left(\frac{1}{k^4}\right) = \phi = \frac{r^2 (\ln r - 1)}{8\pi}.$$
 (7.21)

Utilizing the above inverse Fourier transformation and the fundamental solution  $\phi$ , we thus obtain the complete fundamental solution for U

$$\hat{\boldsymbol{U}} = \frac{\mathcal{A}(\boldsymbol{k})}{s(\boldsymbol{k})} \boldsymbol{S} = \frac{2}{k^4} \mathcal{A}(\boldsymbol{k}) \boldsymbol{S} \implies \boldsymbol{U} = 2\mathcal{A}(\boldsymbol{\nabla})[\phi] \boldsymbol{S}, \tag{7.22}$$

where the adjugate matrix in operator form reads

$$\mathcal{A}(\nabla) = \begin{bmatrix}
\frac{\Delta^2}{3} & \frac{\Delta\partial_x}{2} & \frac{\Delta\partial_y}{2} & -\frac{1}{2}\partial_x^2\Delta & -\partial_x\partial_y\Delta & -\frac{1}{2}\partial_y^2\Delta \\
\frac{\Delta\partial_x}{2} & -\partial_y^2 & \partial_x\partial_y & \partial_x\partial_y^2 & \partial_y^3 - \partial_x^2\partial_y & -\partial_x\partial_y^2 \\
\frac{\Delta\partial_y}{2} & \partial_x\partial_y & -\partial_x^2 & -\partial_x^2\partial_y & \partial_x(\partial_x^2 - \partial_y^2) & \partial_x^2\partial_y \\
-\frac{1}{6}\Delta\left(2\partial_x^2 - \partial_y^2\right) & \partial_x\partial_y^2 & -\partial_x^2\partial_y & \frac{1}{2}\left(\partial_x^4 + \partial_y^4\right) & \partial_x\partial_y(\partial_x^2 - \partial_y^2) & \partial_x^2\partial_y^2 \\
-\frac{1}{2}\Delta\partial_x\partial_y & -\frac{1}{2}\partial_y(\partial_x^2 - \partial_y^2) & \frac{1}{2}\partial_x(\partial_x^2 - \partial_y^2) & \frac{1}{2}\partial_x\partial_y(\partial_x^2 - \partial_y^2) & 2\partial_x^2\partial_y^2 & -\frac{1}{2}\partial_x\partial_y(\partial_x^2 - \partial_y^2) \\
\frac{1}{6}\Delta\left(\partial_x^2 - 2\partial_y^2\right) & -\partial_x\partial_y^2 & \partial_x^2\partial_y & \partial_x^2\partial_y & \partial_x\partial_y^3 - \partial_x^3\partial_y & \frac{1}{2}\left(\partial_x^4 + \partial_y^4\right)
\end{bmatrix} (7.23)$$

where  $\Delta \equiv \partial_x^2 + \partial_y^2$  represents the Laplacian operator. Applying the adjugate matrix (7.23) to the fundamental solution  $\phi$ , we obtain the matrix containing basis functions used to approximate the overall solution via superposition, i.e.

$$\mathbf{\mathfrak{A}}_{\text{Stokes}}(\boldsymbol{r}) = \begin{bmatrix} 0 & \frac{x}{2\pi r^2} & \frac{y}{2\pi r^2} & \frac{x^2 - y^2}{2\pi r^4} & \frac{2xy}{\pi r^4} & \frac{y^2 - x^2}{2\pi r^4} \\ \frac{x}{2\pi r^2} & -\frac{r^2 \log(r^2) - r^2}{4\pi r^2} & \frac{xy}{2\pi r^2} & \frac{x(x^2 - y^2)}{2\pi r^4} & \frac{2x^2y}{\pi r^4} & -\frac{x(x^2 - y^2)}{2\pi r^4} \\ \frac{y}{2\pi r^2} & \frac{xy}{2\pi r^2} & -\frac{r^2 \log(r^2) + x^2 - y^2}{4\pi r^2} & \frac{y(x^2 - y^2)}{2\pi r^4} & \frac{2xy^2}{\pi r^4} & \frac{y(y^2 - x^2)}{2\pi r^4} \\ \frac{x^2 - y^2}{2\pi r^4} & \frac{x(x^2 - y^2)}{2\pi r^4} & \frac{y(x^2 - y^2)}{2\pi r^4} & \frac{x^4 - 6x^2y^2 + y^4}{2\pi r^6} & \frac{4xy(x^2 - y^2)}{\pi r^6} & -\frac{x^4 - 6x^2y^2 + y^4}{2\pi r^6} \\ \frac{xy}{\pi r^4} & \frac{x^2y}{\pi r^4} & \frac{xy^2}{\pi r^4} & \frac{2xy(x^2 - y^2)}{\pi r^6} & -\frac{x^4 - 6x^2y^2 + y^4}{\pi r^6} & -\frac{2xy(x^2 - y^2)}{\pi r^6} \\ \frac{y^2 - x^2}{2\pi r^4} & -\frac{x(x^2 - y^2)}{2\pi r^4} & \frac{y(y^2 - x^2)}{2\pi r^4} & -\frac{x^4 - 6x^2y^2 + y^4}{2\pi r^6} & -\frac{4xy(x^2 - y^2)}{\pi r^6} & \frac{x^4 - 6x^2y^2 + y^4}{2\pi r^6} \end{bmatrix},$$

$$(7.24)$$

where  $\mathfrak{A}_{\text{Stokes}}(\mathbf{r}) \equiv 2\mathcal{A}(\nabla)[\phi]$ . Now it remains to decide the entries of the vector S which decides the Dirac-delta sourcing terms. This choice will be discussed with an example setup in the following subsection.

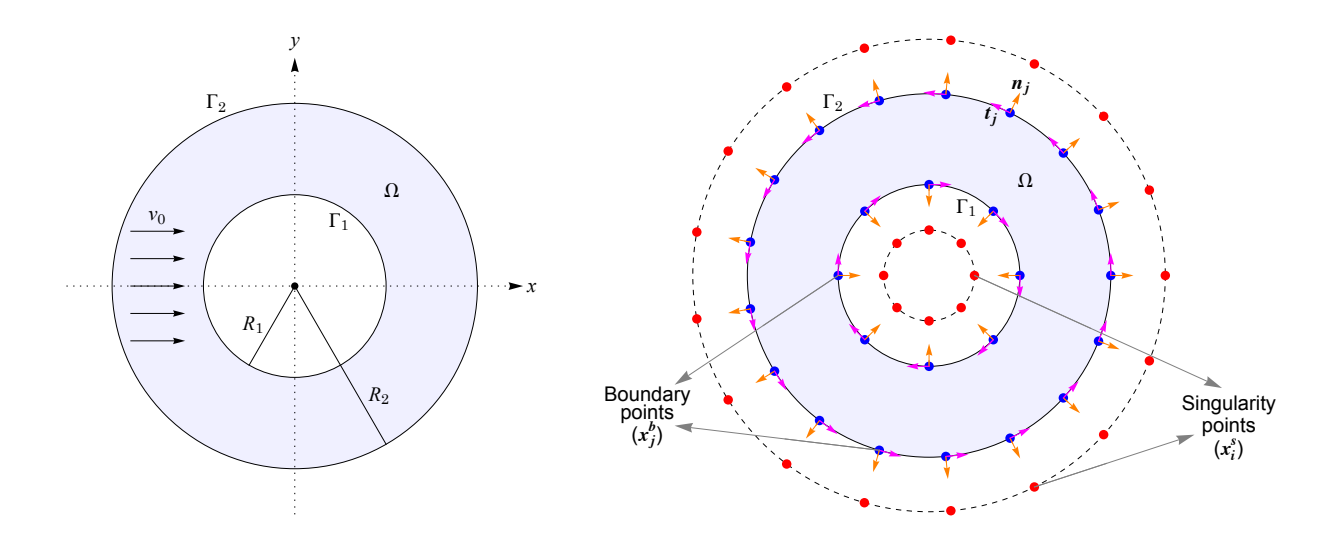


Figure 7.2: Stokes' flow between two cylinders (left) and the placement of boundary nodes and singularities in the MFS (right).

## 7.2.2 An example setup

Let us consider the flow of a monatomic gas past an infinitely long circular cylinder with radius  $R_1$ . To make the computational domain bounded, an outer cylinder with a larger radius  $R_2$  ( $R_2 > R_1$ ) is considered, serving as an artificial inflow/outflow boundary. Owing to the axial symmetry, the problem can be investigated in two dimensions. A cross-sectional view of problem is depicted in the left panel of Fig. 7.2, where the flow domain is given by

$$\Omega = \{ (x, y) \in \mathbb{R}^2 \mid R_1^2 \le x^2 + y^2 \le R_2^2 \}, \tag{7.25}$$

with  $\Gamma_1 = \{(x,y) \in \mathbb{R}^2 \mid x^2 + y^2 = R_1^2\}$  and  $\Gamma_2 = \{(x,y) \in \mathbb{R}^2 \mid x^2 + y^2 = R_2^2\}$  denoting the inner and outer boundaries, respectively. The inner cylinder is assumed to be impermeable with standard slip condition given by

$$|\boldsymbol{v}\cdot\boldsymbol{n}|_{\Gamma_1} = 0 \text{ and } \boldsymbol{n}\cdot\boldsymbol{\sigma}\cdot\boldsymbol{t}|_{\Gamma_1} = -\zeta\boldsymbol{v}\cdot\boldsymbol{t}|_{\Gamma_1},$$
 (7.26)

where  $\mathbf{n} = (n_x, n_y)$  and  $\mathbf{t} = (t_x, t_y)$  are the unit normal and tangent vectors on the inner boundary  $\Gamma_1$  and  $\zeta \in \mathbb{R}$  is the velocity-slip coefficient. The outer cylinder enforces in- and out-flow boundary conditions, leading to

$$\boldsymbol{v} \cdot \boldsymbol{n}\big|_{\Gamma_2} = v_0 \, n_x \big|_{\Gamma_2} \quad \text{and} \quad \boldsymbol{v} \cdot \boldsymbol{t}\big|_{\Gamma_2} = -v_0 \, n_y \big|_{\Gamma_2},$$
 (7.27)

where  $v_0 \in \mathbb{R}$  is the horizontal velocity. The boundary condition matrix constructed using (7.26) and (7.27) for the unknown solution vector  $\boldsymbol{U} = \begin{bmatrix} p & v_x & v_y & \sigma_{xx} & \sigma_{xy} & \sigma_{yy} \end{bmatrix}^\mathsf{T}$  is given by

$$\boldsymbol{B}(\boldsymbol{x}^{b}) = \begin{cases} \begin{bmatrix} 0 & n_{x} & n_{y} & 0 & 0 & 0 \\ 0 & \zeta t_{x} & \zeta t_{y} & n_{x} t_{x} & n_{x} t_{y} + n_{y} t_{x} & n_{y} t_{y} \end{bmatrix}, & \text{if } \boldsymbol{x}^{b} \in \Gamma_{1}, \\ \begin{bmatrix} 0 & n_{x} & n_{y} & 0 & 0 & 0 \\ 0 & t_{x} & t_{y} & 0 & 0 & 0 \end{bmatrix}, & & \text{if } \boldsymbol{x}^{b} \in \Gamma_{2}. \end{cases}$$
(7.28)

The right-hand-side vector is given by

$$\mathbf{g}(\mathbf{x}^b) = \begin{cases} \begin{bmatrix} 0 \\ 0 \end{bmatrix}, & \text{if } \mathbf{x}^b \in \Gamma_1, \\ \begin{bmatrix} v_0 n_x \\ -v_0 n_y \end{bmatrix}, & \text{if } \mathbf{x}^b \in \Gamma_2, \end{cases}$$

$$(7.29)$$

where  $\boldsymbol{x}^b$  represents the position of a point on the boundary of the cylinders. In order to implement the MFS for the current setup, a total of  $N_b$  boundary nodes are chosen on the boundaries  $\Gamma_1$  and  $\Gamma_2$ . Two concentric circular fictitious boundaries  $\tilde{\Gamma}_1$  (inside  $\Gamma_1$ ) and  $\tilde{\Gamma}_2$  (outside  $\Gamma_2$ ) are considered on which  $N_s$  singularity points are placed as shown in the right panel of Fig. 7.2. The overall solution obtained from the MFS is then given by

$$U(x) = \sum_{i=1}^{N_s} \mathfrak{A}_{\text{Stokes}}(x - x_i^s) S_i.$$
 (7.30)

To find the unknown source strengths in  $S_i$ , we split  $S = M\mu$ , where M is a fixed matrix and  $\mu$  contains the deciding source strengths parameters.

## 7.2.3 Choice of the matrix M

The main task in the MFS is to calculate the unknown source strengths using the boundary conditions. For the classical Stokeslet approach, where a point force vector is included in the momentum balance equation, the corresponding matrix M is given by

$$\mathbf{M} = \begin{bmatrix} 0 & 1 & 0 & 0 & 0 & 0 \\ 0 & 0 & 1 & 0 & 0 & 0 \end{bmatrix}^{\mathsf{T}},\tag{7.31}$$

and  $\boldsymbol{\mu} = \begin{bmatrix} \mu_1 & \mu_2 \end{bmatrix}^\mathsf{T}$  represents the point force associated with the singularity. Alternatively, one may introduce source terms into any of the Eqs. (7.13)–(7.15), for instance, setting  $\boldsymbol{M} = I_6$ , where  $I_6$  is the  $6 \times 6$  identity matrix, corresponds to Dirac delta source terms in all governing equations. Nevertheless, while working with large and complex system of linear partial differential equation, it is not trivial to choose the non-zero entries in the vector  $\boldsymbol{S}$  as the choice significantly affects the results. We propose the choice of the matrix  $\boldsymbol{M}$  to be dependent of the boundary conditions by fixing  $\boldsymbol{M}(\boldsymbol{x}^b) = \boldsymbol{B}(\boldsymbol{x}^b)^\mathsf{T}$ , which yields the boundary condition

$$B(x^b)\mathfrak{A}_{\text{Stokes}}B(x^b)^{\mathsf{T}}\mu = g(x^b), \tag{7.32}$$

for any boundary point  $x^b$ . This choice of M is advantageous as it gives a symmetric structure to the overall system and keeps the number of source parameters in  $\mu$  equal to the number of boundary conditions at each node and yields a square system when the number of boundary nodes and source points are the same  $(N_b = N_s)$ . The system (7.32) is evaluated at each boundary node for determining the source parameters in  $\mu$  corresponding to each singularity point. This results in a large linear system

$$\boldsymbol{B}(\boldsymbol{x}_{j}^{b}) \sum_{i=1}^{N_{s}} \mathfrak{A}_{\text{Stokes}}(\boldsymbol{r}_{ij}) \boldsymbol{B}(\boldsymbol{x}_{i}^{b})^{\mathsf{T}} \boldsymbol{\mu}_{i} = \boldsymbol{g}(\boldsymbol{x}_{j}^{b}), \quad j = 1, 2, \dots, N_{b} (= N_{s}),$$
 (7.33)

where  $\mathbf{r}_{ij} = \mathbf{x}_j^b - \mathbf{x}_i^s$  is the relative distance and  $\boldsymbol{\mu}_i$  denotes the vector containing unknown source parameters corresponding to  $i^{\text{th}}$  singularity point. The complete linear system can be denoted by  $\mathcal{L}\Lambda = \mathcal{G}$ , where  $\mathcal{L}$  is the  $2N_b \times 2N_s$  collocation matrix and the unknown source strength vector is  $\boldsymbol{\Lambda} = \begin{bmatrix} \mu_{1_1} & \mu_{1_2} & \mu_{2_1} & \mu_{2_2} & \dots & \mu_{N_{s_1}} & \mu_{N_{s_2}} \end{bmatrix}^\mathsf{T}$ . After calculating the unknown parameters in  $\boldsymbol{\mu}$ , one can approximate any flow variable by using the superposition  $\boldsymbol{U}(\boldsymbol{x}) = \sum_{i=1}^{N_s} \mathfrak{A}_{\text{Stokes}}(\boldsymbol{r}_i) \boldsymbol{B}(\boldsymbol{x}_i)^\mathsf{T} \boldsymbol{\mu}^i$ , where  $\boldsymbol{r}_i = \boldsymbol{x} - \boldsymbol{x}_i^s$  for any vector  $\boldsymbol{x}$  in the computational flow domain. For instance, the  $\boldsymbol{x}$ -component of velocity  $v_x$  can be calculated—using the second row of  $\mathfrak{A}_{\text{Stokes}}$  given in (7.24)—as

$$v_{x} = \sum_{i=1}^{N_{s}} \left[ \frac{x_{i}}{2\pi r_{i}^{2}} - \frac{r_{i}^{2}(2\log r_{i}-1)}{4\pi r_{i}^{2}} \frac{x_{i}y_{i}}{2\pi r_{i}^{2}} \frac{x_{i}(x_{i}^{2}-y_{i}^{2})}{2\pi r_{i}^{4}} \frac{2x_{i}^{2}y_{i}}{\pi r_{i}^{4}} - \frac{x_{i}(x_{i}^{2}-y_{i}^{2})}{2\pi r_{i}^{4}} \right] \boldsymbol{B}(\boldsymbol{x}_{i}^{b})^{\mathsf{T}} \begin{bmatrix} \mu_{1}^{i} \\ \mu_{2}^{i} \end{bmatrix}. \quad (7.34)$$

## 7.3 Generic MFS for R13 equations

Expressing the R13 equations (2.43)–(2.49) in the form (7.1), the unknown vector is  $U = \begin{bmatrix} p & v_x & v_y & \sigma_{xx} & \sigma_{xy} & \sigma_{yy} & \theta & q_x & q_y & m_{xxx} & m_{xxy} & m_{yyx} & m_{yyy} & R_{xx} & R_{xy} & R_{yy} \end{bmatrix}^\mathsf{T}$ . Applying Fourier transformation on the resulting system (7.1) as done in Sec. 7.2.1, the symbol for R13 system turns out to be

$$s(\mathbf{k}) = \gamma(k^2)^3 (k^2 + \lambda_1)(k^2 + \lambda_2)(k^2 + \lambda_3), \tag{7.35}$$

where

$$\gamma = \frac{3087 \text{Kn}^8}{160}, \quad \lambda_1 = \frac{3}{2 \text{Kn}^2}, \quad \lambda_2 = \frac{5}{9 \text{Kn}^2}, \quad \lambda_3 = \frac{5}{6 \text{Kn}^2}.$$
(7.36)

These three constants  $\lambda_1, \lambda_2$  and  $\lambda_3$  represent the three Knudsen layers\*. This symbol in the operator form reads

$$s(\Delta) = \gamma(\Delta)^3 (\Delta - \lambda_1)(\Delta - \lambda_2)(\Delta - \lambda_3), \tag{7.37}$$

where  $\Delta \equiv \partial_x^2 + \partial_y^2$ . Utilizing Eqs. (7.4) and (7.5) gives an idea to compute the main fundamental solution  $\Phi$  corresponding to the symbol. In Fourier transformed coordinates,

$$\hat{U} = \frac{1}{\gamma(k^2)^3(k^2 + \lambda_1)(k^2 + \lambda_2)(k^2 + \lambda_3)} \mathcal{A}(k) S.$$
 (7.38)

It is convenient to get the inverse Fourier transform of  $\hat{U}$  if 1/s(k) is expressed in its partial fraction form:

$$\frac{1}{s(\mathbf{k})} = \frac{1}{\gamma} \left[ \frac{\alpha_1}{(k^2)^3} + \frac{\alpha_2}{(k^2)^2} + \frac{\alpha_3}{k^2} + \frac{\alpha_4}{k^2 + \lambda_1} + \frac{\alpha_5}{k^2 + \lambda_2} + \frac{\alpha_6}{k^2 + \lambda_3} \right]. \tag{7.39}$$

The constants  $\alpha_i$ s can be computed in a straightforward way, and hence Eq. (7.38) becomes

$$\hat{\mathbf{U}} = \frac{1}{\gamma} \left[ \frac{36 \,\mathrm{Kn}^6}{25(k^2)^3} - \frac{132 \,\mathrm{Kn}^8}{25(k^2)^2} + \frac{8356 \,\mathrm{Kn}^{10}}{625k^2} - \frac{8 \,\mathrm{Kn}^{10}}{17 \left(k^2 + \frac{3}{2\mathrm{Kn}^2}\right)} + \frac{5832 \,\mathrm{Kn}^{10}}{625 \left(k^2 + \frac{5}{6\mathrm{Kn}^2}\right)} - \frac{236196 \,\mathrm{Kn}^{10}}{10625 \left(k^2 + \frac{5}{9\mathrm{Kn}^2}\right)} \right] \mathcal{A}(\mathbf{k}) \mathbf{S}. \tag{7.40}$$

<sup>\*</sup> Knudsen layers are thin boundary regions in rarefied gas flows where non-equilibrium effects dominate due to gas-surface interactions. The constants  $\sqrt{5/6}$ ,  $\sqrt{3/2}$ , and  $\sqrt{5}/3$  correspond to eigenvalues governing exponential decay rates of Knudsen layer modes in the R13 equations. Three eigenvalues align with the prediction of three Knudsen layers by the R13 model [85, 105, 117]

In order to compute the complete fundamental solution  $\Phi$ , it is easier to use the inverse Fourier transforms of the partial fraction terms using the preknown fundamental solutions of polyharmonic or Helmholtz operators [25]. For any polyharmonic equation having the fundamental solution  $\phi_n$  which satisfies  $\Delta^n \phi_n = \delta$ , its Fourier transformation is obtained by using the property  $\mathcal{F}(\partial F/\partial x_i) = ik_i$ , which yields

$$(-1)^n k^{2n} \hat{\phi}_n = \hat{\delta} = 1 \implies \hat{\phi}_n = \frac{(-1)^n}{k^{2n}}.$$
 (7.41)

Analogously, for a Helmholtz equation having the fundamental solution  $\psi_{\lambda}$  which satisfies  $(\Delta - \lambda)\psi_{\lambda} = \delta$ , the Fourier transformation yields

$$(-k^2 - \lambda)\hat{\psi}_{\lambda} = \hat{\delta} = 1 \implies \hat{\psi}_{\lambda} = -\frac{1}{k^2 + \lambda}.$$
 (7.42)

Utilizing Eq. (7.41) and the preknown fundamental solutions for polyharmonic operators [25], one can obtain

$$\mathcal{F}^{-1}\left(\frac{1}{k^2}\right) = -\phi_1 = -\frac{\log r}{2\pi},\tag{7.43}$$

$$\mathcal{F}^{-1}\left(\frac{1}{k^4}\right) = \phi_2 = \frac{r^2(\log r - 1)}{8\pi},\tag{7.44}$$

$$\mathcal{F}^{-1}\left(\frac{1}{k^6}\right) = -\phi_3 = -\frac{r^4(\log r - 3/2)}{128\pi}.\tag{7.45}$$

Using fundamental solution  $\psi_{\lambda}$  for Helmholtz equation, and Eq. (7.42), we get

$$\mathcal{F}^{-1}\left(\frac{1}{k^2 + \lambda}\right) = -\psi_{\lambda} = -\frac{K_0(\sqrt{\lambda}r)}{2\pi}.$$
 (7.46)

Here,  $K_0$  denotes the modified Bessel function of the second kind of order zero. Since inverse Fourier transformation is linear, the fundamental solution  $\Phi$  is

$$\Phi(r) = -\frac{4178 \operatorname{Kn}^{10} \log r}{625\pi} - \frac{33 \operatorname{Kn}^{8} r^{2} (\log r - 1)}{50\pi} - \frac{9 \operatorname{Kn}^{6} r^{4} (\log r - 3/2)}{800\pi} + \frac{2916 \operatorname{Kn}^{10} K_{0} \left(\sqrt{\frac{5}{6} \frac{r}{\operatorname{Kn}}}\right)}{625\pi} - \frac{4 \operatorname{Kn}^{10} K_{0} \left(\sqrt{\frac{3}{2} \frac{r}{\operatorname{Kn}}}\right)}{17\pi} - \frac{118098 \operatorname{Kn}^{10} K_{0} \left(\sqrt{\frac{5}{3} \frac{r}{\operatorname{Kn}}}\right)}{10625\pi}.$$
(7.47)

Taking the inverse Fourier transform in Eq. (7.38), we obtain the fundamental solution for the R13 equations as

$$U(r) = \frac{1}{\gamma} \mathcal{A}(\nabla)[\Phi] S = \mathfrak{A}_{R13}(r) M \mu. \tag{7.48}$$

The matrix  $\mathfrak{A}_{R13}$  incorporates all fundamental solutions that contribute to approximating the complete numerical solution of any given problem. In the R13 system, different

choices of the matrix M allow for varying degrees of freedom. The choice can be made independent of the specific problem by setting  $M(x^b) = B(x^b)^{\mathsf{T}}$ . Here  $B(x^b) \in \mathbb{R}^{6 \times 16}$  boundary conditions matrix is constructed using boundary conditions (2.56)–(2.61). With this choice (as also discussed in Sec. 7.2.3), the unknown source strengths corresponding to the  $i^{\text{th}}$  singularity  $\mu_i \in \mathbb{R}^6$  is calculated by solving the linear system

$$\boldsymbol{B}(\boldsymbol{x}_{j}^{b}) \sum_{i=1}^{N_{s}} \mathfrak{A}_{R13}(\boldsymbol{r}_{ij}) \boldsymbol{B}(\boldsymbol{x}_{i}^{b})^{\mathsf{T}} \boldsymbol{\mu}_{i} = \boldsymbol{g}(\boldsymbol{x}_{j}^{b}), \quad j = 1, 2, \dots, N_{b} (= N_{s}).$$
 (7.49)

This linear system can be expressed as  $\mathcal{L}\Lambda = \mathcal{G}$ , where  $\mathcal{L}$  is the  $6N_b \times 6N_b$  collocation matrix (due to 6 boundary conditions associated with each boundary node and 6 source strengths associated with each singularity). Further,  $\Lambda \in \mathbb{R}^{6N_b}$  is the unknown vector (containing source strengths  $\mu_i$ ) and  $\mathcal{G} \in \mathbb{R}^{6N_b}$  is the right-hand-side vector containing boundary properties  $g(x_j^b)$ . The numerical solution approximated by the MFS at any point x in the domain is determined by

$$U(\boldsymbol{x}) = \sum_{i=1}^{N_s} \mathfrak{A}_{R13}(\boldsymbol{x} - \boldsymbol{x}_i^s) \boldsymbol{B}(\boldsymbol{x}_i^b)^\mathsf{T} \boldsymbol{\mu}_i. \tag{7.50}$$

## 7.4 Results and discussion

To validate our code for the generic MFS for the R13 equations, we compare the results obtained from the MFS with an analytical solution for a rarefied gas flow confined between two coaxial cylinders. Additionally, we examine the influence of various parameters on the accuracy of the numerical method.

#### 7.4.1 Problem description

We consider the flow of a rarefied monatomic gas around a rotating, infinitely long circular cylinder, with the flow domain bounded by a coaxial outer circular cylinder. The dimensionless radii of the inner and outer cylinders are  $R_1 = 1$  and  $R_2 = 2$ , respectively, with the inner and outer boundaries denoted by  $\Gamma_1$  and  $\Gamma_2$ , respectively, as depicted in Fig 7.3. The outer cylinder serves as an inflow and outflow boundary, with normal component of velocity  $\mathbf{v}^{\mathbf{w}} \cdot \mathbf{n}|_{\Gamma_2} = v_0 n_x|_{\Gamma_2}$  and tangential component  $\mathbf{v}^{\mathbf{w}} \cdot \mathbf{t}|_{\Gamma_2} = -v_0 n_y|_{\Gamma_2}$  in the boundary conditions (2.56)–(2.61). To introduce additional complexity, the inner cylinder is assumed to be rotating with a tangential velocity, given by  $\mathbf{v}^{\mathbf{w}} \cdot \mathbf{t}|_{\Gamma_1} = -v_1$ . The temperatures of the inner and outer cylinders are fixed at  $\theta^{\mathbf{w}}|_{\Gamma_1} = \theta_1 = 1$  and

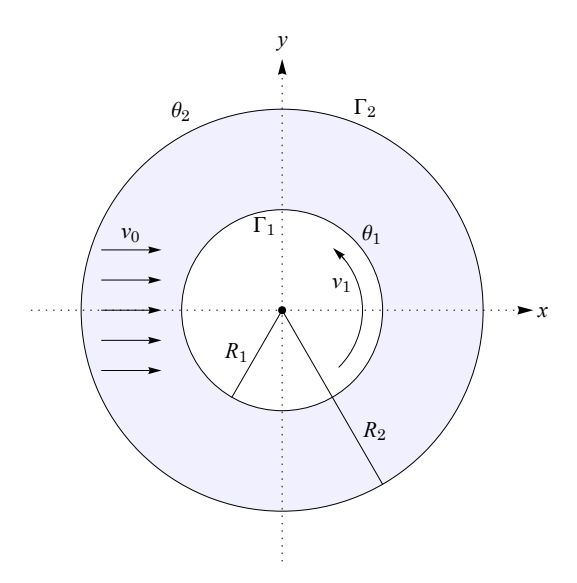


Figure 7.3: Schematic of the cross-section of rarefied gas confined between two coaxial cylinders where the inner cylinder is rotating anticlockwise.

 $\theta^{\rm w}\big|_{\Gamma_2}=\theta_2=2$ , respectively. The velocity prescription coefficient at inner cylinder is  $\epsilon^{\rm w}\big|_{\Gamma_1}=10^{-5}$ , while that on outer cylinder is  $\epsilon^{\rm w}\big|_{\Gamma_2}=1$ . Furthermore, we fix  $v_0=v_1=1$  and  $p^{\rm w}\big|_{\Gamma_1}=p^{\rm w}\big|_{\Gamma_2}=0$ .

#### 7.4.2 Validation with analytic solution

The details for obtaining the analytic solution to this problem are provided in Appendix D. To validate the code, we plot the speed of gas varying with radial gap between the two cylinders along different directions in the left panel of Fig. 7.4. The solid blue, red and black lines indicate the results obtained from the analytic solution of the R13 model for the azimuthal angles  $\vartheta = 0, \pi/4$  and  $\pi/2$ , respectively, whereas the symbols (triangles) represent the corresponding results obtained from the MFS for Kn = 0.5. The right panel of Fig. 7.4 illustrates the variation in temperature with respect to the radial gap along different angles. We observe an excellent agreement between the results obtained from the MFS and those from the analytic solution for both speed and temperature. The complete source code for the generic MFS and the analytical solution for the R13 equations has been made publicly accessible<sup>†</sup> [44]. For a better analysis, we measure the accuracy of the generic MFS in the following subsection using the standard relative error in the  $L^2$  norm

$$\epsilon_{L^2} = \frac{\|f_{\text{MFS}} - f_{\text{exact}}\|_{L^2(\Omega)}}{\|f_{\text{exact}}\|_{L^2(\Omega)}},\tag{7.51}$$

<sup>†</sup> https://github.com/himanshikhungar/R13\_MFS

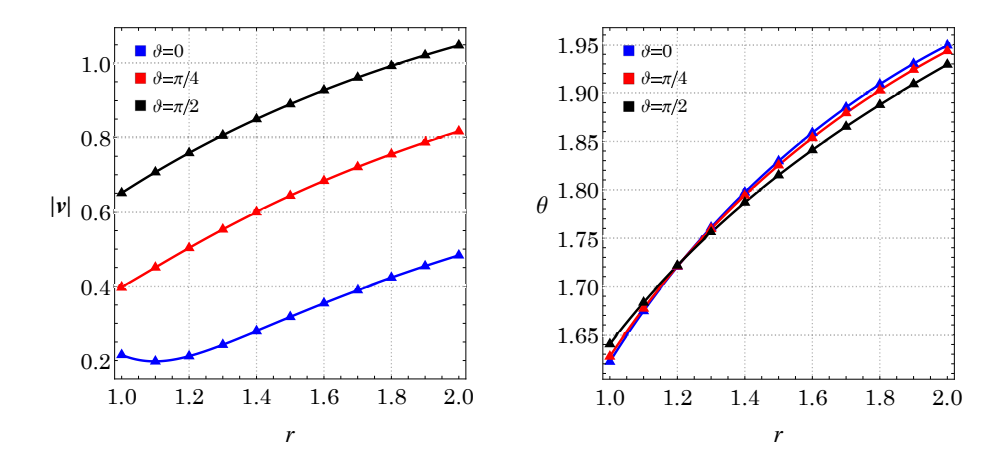


Figure 7.4: Variation of the speed (left panel) and temperature (right panel) in the gap between the two cylinders. The solid blue, red and black lines denote the analytic results of the R13 model along  $\vartheta = 0, \pi/4$  and  $\pi/2$ , respectively. The corresponding blue, red and black (triangle) symbols denote the results obtained from the MFS for Kn = 0.5.

where  $f_{\text{MFS}}$  denotes the numerical solution obtained with the MFS and  $f_{\text{exact}}$  denotes the corresponding analytic solution.

## 7.4.3 Choice of parameters

The accuracy of the MFS solution is highly dependent on key parameters, namely the numbers of boundary and source points, and the location of source points outside the computational domain. To systematically analyze the error and justify the choice of these parameters, we define a grid spacing parameter d, which determines the distance between two consecutive boundary points. A smaller d results in a higher number of boundary points and vice versa. Given the grid spacing parameter d, the number of boundary points placed on the circumference of a circle of radius R is computed as  $N_b = \lfloor 2\pi R/d \rfloor$ , where  $\lfloor \cdot \rfloor$  denotes the floor function. As previously mentioned, we set the number of boundary points equal to the number of source points to construct a square linear system using the relation  $\mathbf{M} = \mathbf{B}(\mathbf{x})^{\mathsf{T}}$ .

To determine an appropriate placement of source points, we introduce the dilation parameter  $\alpha = R_1/R_{s_1} = R_{s_2}/R_2$  where  $R_{s_1}$  and  $R_{s_2}$  denote the radii of the inner and outer fictitious boundaries on which source points are placed. A larger  $\alpha$  corresponds to source points being positioned farther from the boundary and vice versa. To evaluate the accuracy of the MFS, we compute the  $L^2$  error in velocity  $\epsilon_{L^2}$  for different values

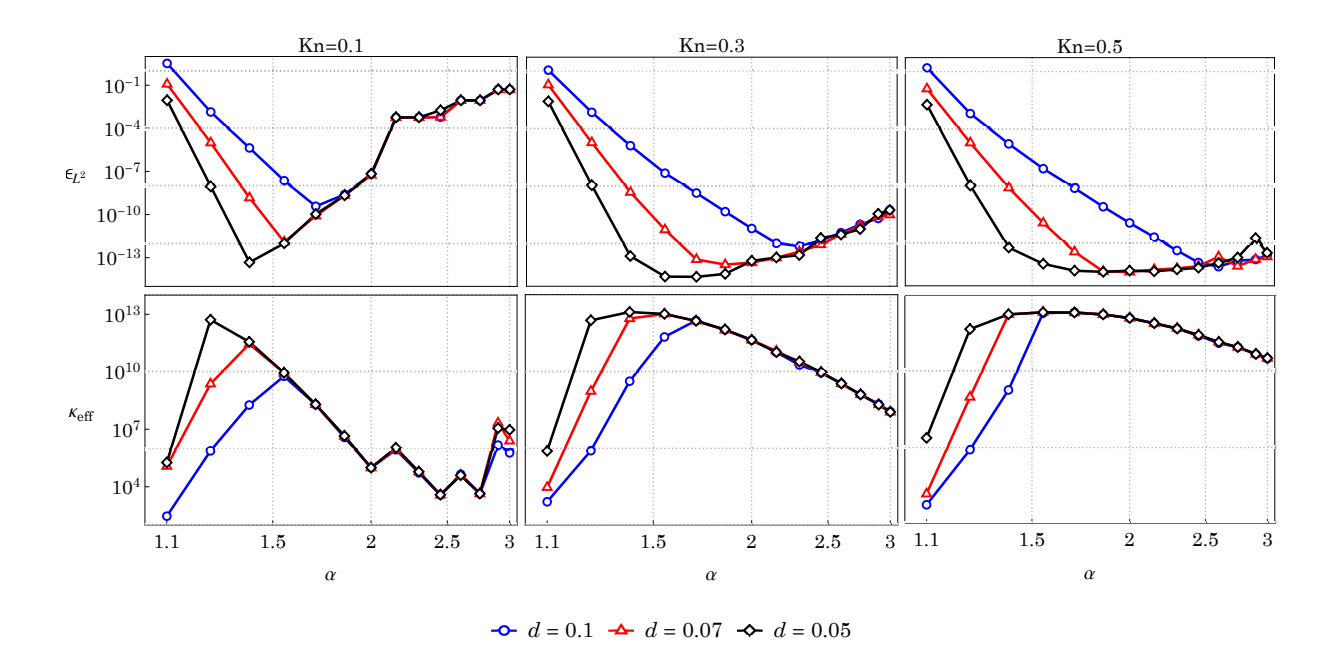


Figure 7.5: Variation in  $L^2$  error in velocity  $\epsilon_{L^2}$  and effective condition number  $\kappa_{\text{eff}}$  with respect to the dilation parameter  $\alpha$  for different values of grid spacing d and  $\mathbf{M} = \mathbf{B}(\mathbf{x})^{\mathsf{T}}$ .

of d and  $\alpha$ . The top panels in Fig. 7.5 illustrate the variation in  $\epsilon_{L^2}$  with respect to  $\alpha$  for grid spacings  $d \in \{0.1, 0.07, 0.05\}$  and Knudsen numbers  $\mathrm{Kn} \in \{0.1, 0.3, 0.5\}$ . For a higher Knudsen number  $\mathrm{Kn} = 0.5$  (rightmost top panel), fewer boundary points (d = 0.1) provide good accuracy when  $\alpha$  is sufficiently large, meaning the source points are placed sufficiently far from the boundary. In contrast, for d = 0.07 and d = 0.05, accurate results are achieved for  $\alpha \gtrsim 1.7$  and  $\alpha \gtrsim 1.5$ , respectively. This suggests that for computational efficiency, a smaller number of boundary points with more distant source points can be a viable choice. However, for lower Knudsen numbers ( $\mathrm{Kn} = 0.1$  and 0.3, leftmost and middle top panels), the accuracy depends more sensitively on the choice of boundary and source points. The error is minimized only within a narrow range of  $\alpha$ , particularly for  $\mathrm{Kn} = 0.1$ , indicating that source points should neither be too close nor too far from the boundary for an optimum accuracy.

The accuracy of the numerical solution depends strongly on the Knudsen number, which makes it challenging to determine where the source points should be placed, especially in the absence of an analytic solution. The effective condition number provides a reliable indicator of the accuracy of the solution. The bottom panel in Fig. 7.5 shows

how the effective condition number  $\kappa_{\text{eff}}$  varies with the dilation parameter  $\alpha$  for three values of the grid spacing  $d \in \{0.1, 0.07, 0.05\}$  and Knudsen numbers  $\text{Kn} \in \{0.1, 0.3, 0.5\}$ . A comparison with the corresponding top panel, which displays the error  $\epsilon_{L^2}$ , reveals an approximate inverse proportionality between  $\kappa_{\text{eff}}$  and the error: in general, lower errors are associated with higher values of  $\kappa_{\text{eff}}$ . However, the value of  $\alpha$  corresponding to the minimum error does not always align precisely with the peak in  $\kappa_{\text{eff}}$ , indicating that the relationship is not strictly proportional. This observation suggests that the source point placement should be chosen to strike a balance—achieving sufficiently high  $\kappa_{\text{eff}}$  while also minimizing the numerical error. Based on this reasoning, we select  $\alpha = 1.5$  and d = 0.05 for our computations.

#### 7.4.4 Choice of the matrix M

Previous studies on the MFS for rarefied gas flows formulated the fundamental solutions by imposing only a few degrees of freedom as Dirac-delta source terms in some governing equations and/or in some closure relations. Ref. [27] derived the fundamental solutions for the R13 equations by including sourcing terms in the momentum, energy and stress balance equations in three dimensions. This choice ensured that the number of boundary conditions matched the number of unknown sources associated with each singularity. The corresponding 2D fundamental solutions for the R13 equations, including similar source terms, can be obtained from the general matrix  $\mathfrak{A}_{R13}$  containing the full set of fundamental solutions. Setting  $\mathbf{M} = \begin{bmatrix} \mathbf{0}_{1\times 6} & I_6 & \mathbf{0}_{9\times 6} \end{bmatrix}^\mathsf{T}$ , leads to the parameter  $\boldsymbol{\mu} = \begin{bmatrix} \mu_1 & \mu_2 & \mu_3 & \mu_4 & \mu_5 & \mu_6 \end{bmatrix}^\mathsf{T}$  with six degrees of freedom. In this scenario, the linear system formed by implementing boundary conditions at each boundary node reads

$$B(x_j^b) \sum_{i=1}^{N_s} \mathfrak{A}_{R13}(r_{ij}) M \mu_i = g(x_j^b), \quad j = 1, 2, \dots, N_b.$$
 (7.52)

While this approach was effective for the specific problem considered in [27], this particular choice may not always yield accurate results. To illustrate this, Fig. 7.6 shows the variation in the  $L^2$  error in velocity (left panel) and the effective condition number  $\kappa_{\rm eff}$  (right panel) as functions of the dilation parameter  $\alpha$  for Kn = 0.5. As evident from the left panel of Fig. 7.6, the error remains large at all the locations of the source points, and the effective condition number does not exhibit any structured behavior. Although not shown here, the errors remain high for all the considered Knudsen number values as well. This suggests

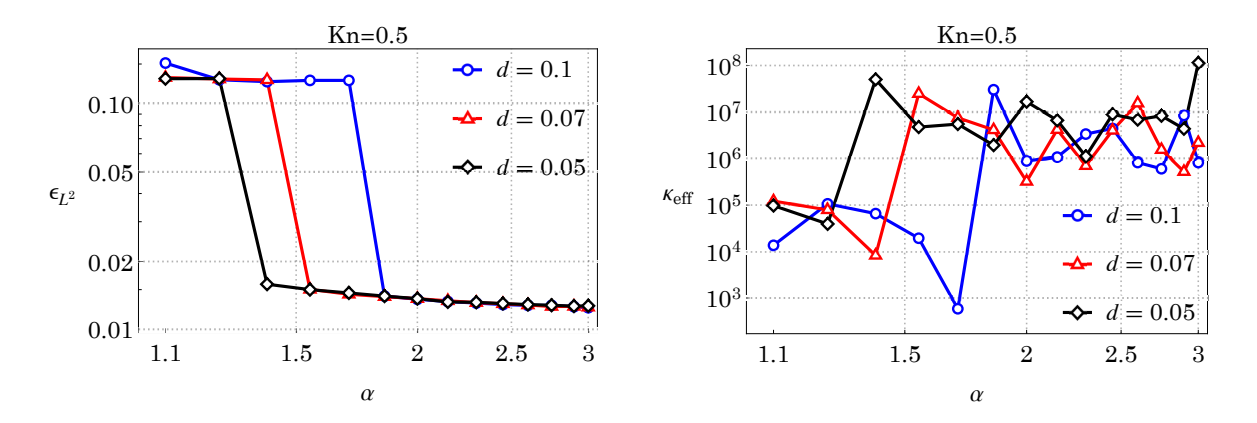


Figure 7.6: Variation in  $L^2$  error in velocity  $\epsilon_{L^2}$  (left panel) and effective condition number  $\kappa_{\rm eff}$  (right panel) with respect to dilation parameter  $\alpha$  for  $\mathbf{M} = \begin{bmatrix} \mathbf{0}_{1\times 6} & I_6 & \mathbf{0}_{9\times 6} \end{bmatrix}^\mathsf{T}$  for Kn = 0.5.

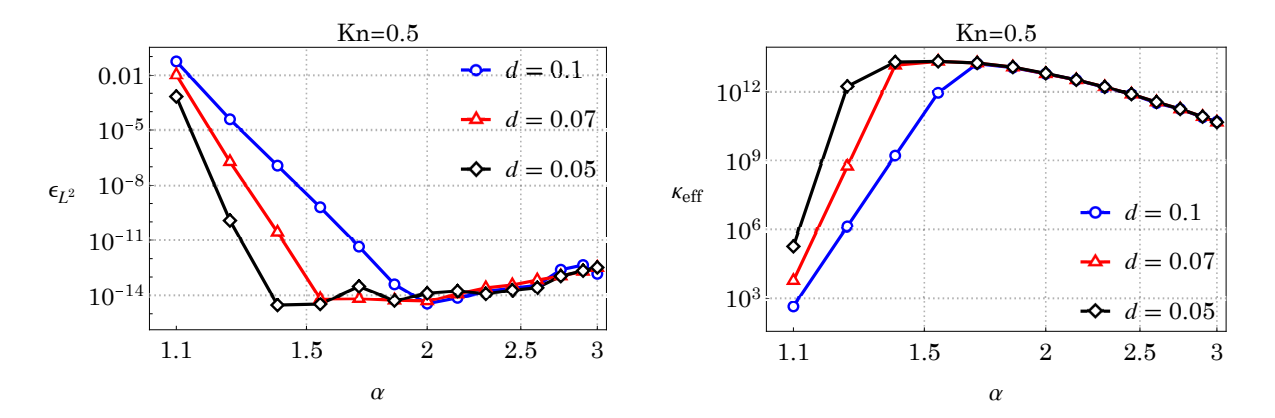


Figure 7.7: Variation in  $L^2$  error in velocity  $\epsilon_{L^2}$  (left panel) and effective condition number  $\kappa_{\rm eff}$  (right panel) with respect to dilation parameter  $\alpha$  for  $\mathbf{M} = \begin{bmatrix} I_9 & \mathbf{0}_{7\times 9} \end{bmatrix}^{\mathsf{T}}$  for Kn = 0.5.

that the choice with six degrees of freedom does not perform well for the present problem. A more suitable choice for the current study is to set  $\boldsymbol{M} = \begin{bmatrix} I_9 & \mathbf{0}_{7\times 9} \end{bmatrix}^\mathsf{T}$ , which introduces nine degrees of freedom corresponding to mass, momentum, energy, stress, and heat balance equations. In this case, the collocation matrix  $\boldsymbol{\mathcal{L}}$  has dimensions  $6N_b \times 9N_s$  and the corresponding linear system can be solved using the method of least squares. Figure 7.7 illustrates the variation in  $L^2$  error in velocity (left panel) and effective condition number (right panel) with the dilation parameter  $\alpha$  for  $\mathrm{Kn} = 0.5$ . The behavior of both  $\epsilon_{L^2}$  and  $\kappa_{\mathrm{eff}}$  closely resemble with those observed for  $\boldsymbol{M} = \boldsymbol{B}(\boldsymbol{x})^\mathsf{T}$  in Fig. 7.5. Although not shown here, the resemblance exists for  $\mathrm{Kn} = 0.1$  and 0.3 as well. The comparison indicates that this choice of  $\boldsymbol{M} = \begin{bmatrix} I_9 & \mathbf{0}_{7\times 9} \end{bmatrix}^\mathsf{T}$  is more appropriate than  $\boldsymbol{M} = \begin{bmatrix} \mathbf{0}_{1\times 6} & I_6 & \mathbf{0}_{9\times 6} \end{bmatrix}^\mathsf{T}$  for the

present problem. However, this choice of M cannot be guaranteed to work well for other problems.

#### 7.5 Comparison with the FEM

After validating the generic MFS framework for the R13 equations with an analytic solution, we now consider a problem for which an analytic solution is unknown. The results are therefore compared to the results obtained from the FEM. Furthermore, we observe the key differences and advantages of the MFS over FEM.

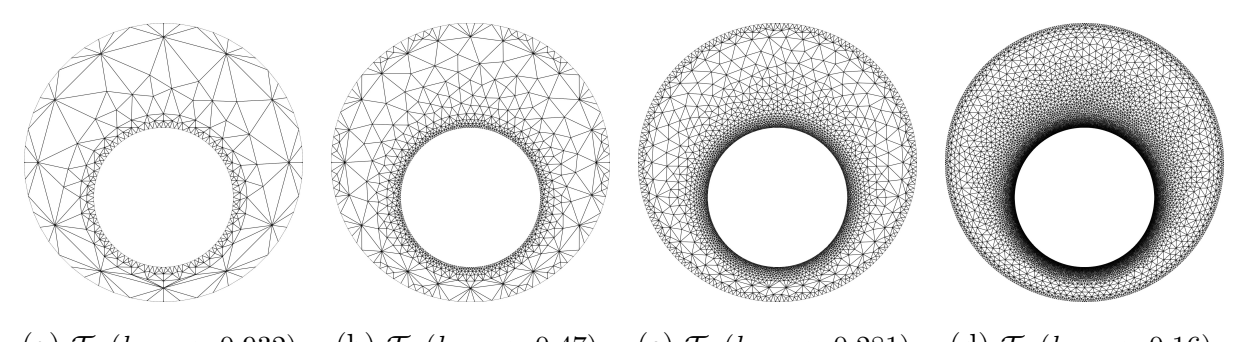
The FEM simulations presented in this chapter have been performed Dr. Lambert Theisen as part of our collaborative research effort [43]. These results are included with permission to ensure completeness in the comparison of the proposed meshless framework.

#### 7.5.1 Problem description

In this scenario, a monatomic rarefied gas is considered to be confined between two noncoaxial infinitely long cylinders. The circular cross-sections of the inner and outer cylinders have radii  $R_1 = 1$  and  $R_2 = 2$ , respectively and centers at (0, -0.25) and (0,0), respectively. The boundaries are again denoted by  $\Gamma_1$  and  $\Gamma_2$ , respectively. The (dimensionless) temperatures on the inner and outer cylinders are fixed at  $\theta^w|_{\Gamma_1} = \theta_1 = 1$  and  $\theta^w|_{\Gamma_2} = \theta_2 = 2$ , respectively. Both the cylinders are assumed to be stationary  $(\boldsymbol{v}^w|_{\Gamma_1} = \boldsymbol{v}^w|_{\Gamma_2} = 0)$  with the velocity prescription coefficient  $\epsilon^w|_{\Gamma_1} = \epsilon^w|_{\Gamma_2} = 0$  in the boundary conditions (2.56)–(2.61). The flow is induced purely by the temperature difference.

#### 7.5.2 FEM for the R13 model

In the FEM (see, e.g., [29] for an introduction focusing on flow equations), the equations are not solved pointwise for all  $\boldsymbol{x} \in \Omega$ , but in an integral sense (weakly) on a triangulation  $\mathcal{T}_h$  of  $\Omega$  into finite elements  $\tau \in \mathcal{T}_h$  (triangles in our case). Here,  $h \in \mathbb{R}$  denotes the maximum diameter of the elements. In contrast to the first-order system (7.1), we do not solve for all moments but restrict ourselves to the three balance laws (2.43), (2.44), and (2.45), complemented by the two additional Eqs. (2.46) and (2.47). The higher-order moments (2.48), (2.49), and (2.50) are directly inserted into these five equations, resulting in a field vector  $\boldsymbol{V} = \begin{bmatrix} p & v_x & v_y & \sigma_{xx} & \sigma_{xy} & \sigma_{yy} & \theta & q_x & q_y \end{bmatrix}^\mathsf{T}$ .



(a)  $\mathcal{T}_1$  ( $h_{\text{max}} \approx 0.932$ ). (b)  $\mathcal{T}_2$  ( $h_{\text{max}} \approx 0.47$ ). (c)  $\mathcal{T}_3$  ( $h_{\text{max}} \approx 0.281$ ). (d)  $\mathcal{T}_4$  ( $h_{\text{max}} \approx 0.16$ ).

Figure 7.8: Series of finite element meshes  $\mathcal{T}_i$  with decreasing mesh size  $h_{\text{max}}$  for increasing i.

To obtain the weak formulation, we multiply each equation by corresponding test functions  $W = (\varphi_p, \dots)$ , integrate over  $\Omega$ , and apply integration by parts. This procedure lowers the order of differentiation and allows incorporating the boundary conditions (2.56)–(2.61). In the Galerkin approach, the test functions are chosen from the same finite element space as the solution. An example is the weak formulation of the mass balance (2.43), where testing with  $\varphi_p : \Omega \to \mathbb{R}$  and integrating by parts yields

$$\int_{\Omega} (\boldsymbol{\nabla} \cdot \boldsymbol{v}) \, \varphi_{p} \, d\boldsymbol{x} = -\int_{\Omega} \boldsymbol{v} \cdot \boldsymbol{\nabla} \varphi_{p} \, d\boldsymbol{x} + \int_{\Gamma} v_{n} \varphi_{p} \, dl$$

$$= -\int_{\Omega} \boldsymbol{v} \cdot \boldsymbol{\nabla} \varphi_{p} \, d\boldsymbol{x} + \int_{\Gamma} (\epsilon^{w} \tilde{\chi} ((p - p^{w}) + \sigma_{nn}) + v_{n}^{w}) \, \varphi_{p} \, dl, \qquad (7.53)$$

A reordering of terms for the unknowns and test functions leads to

$$\int_{\Omega} \boldsymbol{v} \cdot \boldsymbol{\nabla} \varphi_p \, \mathrm{d}\boldsymbol{x} + \int_{\Gamma} \epsilon^{\mathrm{w}} \tilde{\chi} \left( p + \sigma_{nn} \right) \varphi_p \, \mathrm{d}l = -\int_{\Gamma} \left( v_n^{\mathrm{w}} - \epsilon^{\mathrm{w}} p^{\mathrm{w}} \right) \varphi_p \, \mathrm{d}l, \tag{7.54}$$

which has to hold for all  $\varphi_p \in W$ . Repeating these steps for all equations leads to a well-posed system [60, 113]. Finally, we discretize all functions in V and W by approximating them in the finite element space, i.e. as a linear combination of basis functions  $\phi_{\star,i}$  with coefficients  $c_i$ , such that, for example,

$$p(\boldsymbol{x}) = \sum_{i=1}^{N_p} c_{p,i} \phi_{p,i}(\boldsymbol{x}). \tag{7.55}$$

We use stabilized first-order Lagrange elements, which are piecewise linear and globally continuous on the mesh. Inserting the ansatz (7.55) into the weak equations and evaluating the integrals via numerical quadrature, we obtain a linear system of equations:

$$\boldsymbol{A}_{h}\boldsymbol{x}_{h} = \boldsymbol{b}_{h}, \tag{7.56}$$

where  $\mathbf{A}_h \in \mathbb{R}^{N \times N}$  is a sparse system matrix,  $\mathbf{x}_h \in \mathbb{R}^N$  contains the degrees of freedom of the solution (i.e. the vectors of coefficients  $\{c_{\star,i}\}_{i=1}^{N_{\star}}$ ), and  $\mathbf{b}_h \in \mathbb{R}^N$  is the right-hand side vector. The sparsity of  $\mathbf{A}_h$  results from the local support of the basis functions, i.e.  $\phi_{\star,i}$  is non-zero only on a small subset of elements  $\tau$ .

However, particularly for thermally induced flows as discussed in Sec. 7.5.1, a fine and locally refined mesh is required to accurately capture the characteristic flow features. For the test case, we generated a sequence of meshes  $\{\mathcal{T}_1, \ldots, \mathcal{T}_7\}$  with decreasing maximal radii  $h_{\text{max}}$ . The first four of these meshes are shown schematically in Fig. 7.8 and illustrate the essential requirement of local refinement near the boundaries. For full reproducibility, the FEM source code along with all metadata is publicly available at [114].

#### 7.5.3 Results and discussion

In this problem, the gas flow is entirely driven by the temperature difference between the two cylinders without any external effect or gravity under consideration. To gain insight into the velocity and temperature profiles, we visualize the velocity streamlines superimposed on temperature contours for different Knudsen numbers Kn = 0.05, 0.1, 0.2and 0.4 in Fig. 7.9, as predicted by the MFS. The parameters for the MFS are fixed at  $\alpha = 1.5$  and d = 0.07 for these computations. These streamline plots reveal the intricate interplay between thermal stress and thermal transpiration effects, which arise due to the stress and heat flux evolution equations in the R13 model. For small Kn = 0.05, two counter-rotating circulation zones emerge: one in the left half and the other in the right half of the annular region. As Kn increases to 0.1, two additional vortices begin to form near the outer cylinder which indicate a shift in the flow structure. With a further increase in the Knudsen number to Kn = 0.2, the newly formed vortices near the outer cylinder intensify, while the inner vortices diminishes in strength. For even larger Kn = 0.4, the small inner vortices disappear completely, restoring a two-vortex system similar to that at Kn = 0.05, but with the flow directions reversed. This transformation in flow behavior highlights the competition between thermal stress and thermal transpiration effects, which govern rarefied gas flows under temperature gradients.

To compare the results from MFS with those from FEM, we use three finest FEM meshes: Mesh 1 ( $\mathcal{T}_5$ , coarsest), Mesh 2 ( $\mathcal{T}_6$ , finer than Mesh 1), and Mesh 3 ( $\mathcal{T}_7$ , finest). Figure 7.10 illustrates the speed of gas  $|\mathbf{v}|$  along the line y = x in the first quadrant

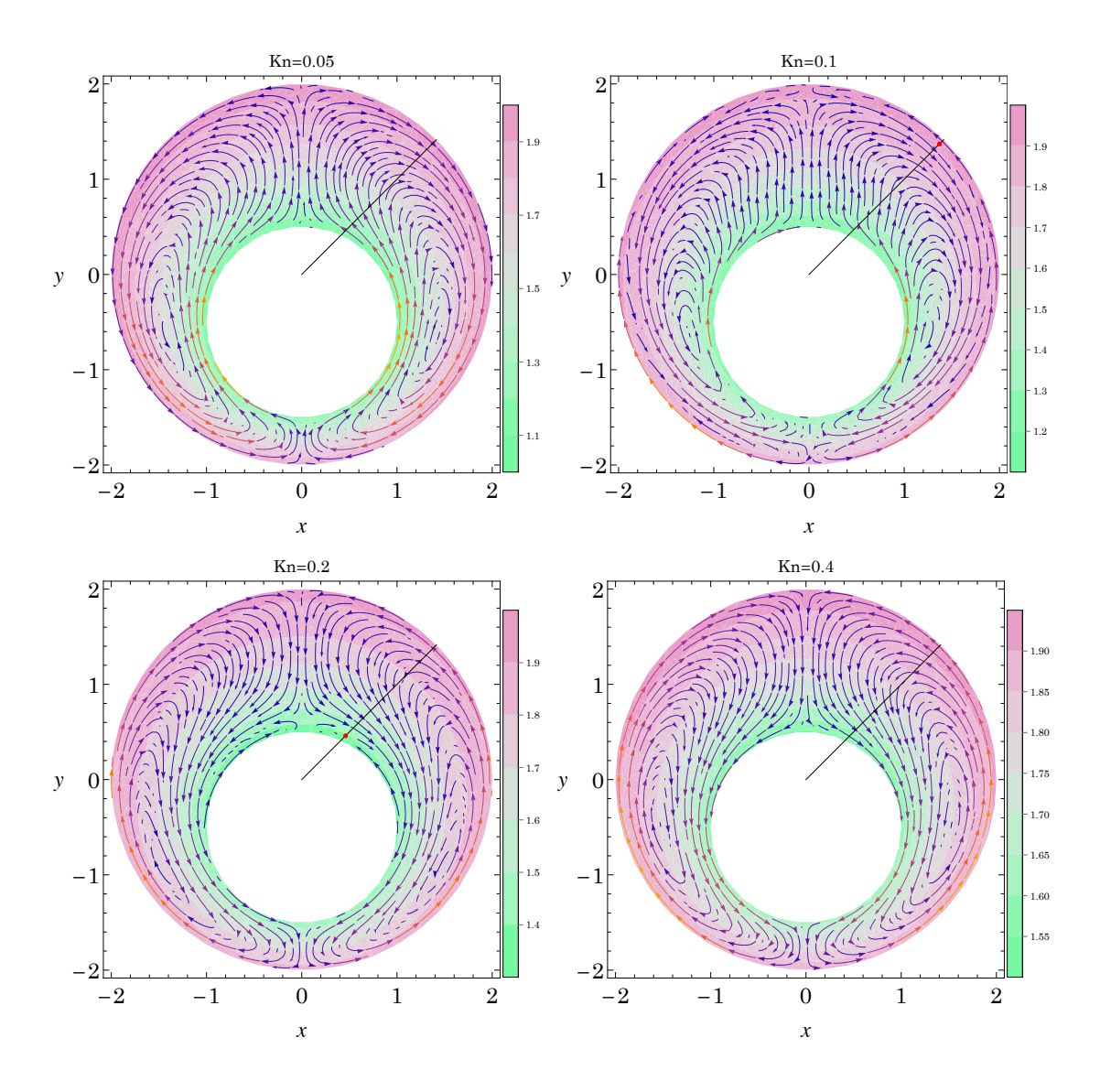


Figure 7.9: Velocity streamlines overlaid on temperature contours for different Knudsen numbers Kn = 0.05, 0.1, 0.2, 0.4 as predicted by the MFS.

(or equivalently along  $\vartheta = \pi/4$ , as shown over Fig. 7.9) measured from the center of the outer cylinder for different Knudsen numbers Kn = 0.05, 0.1, 0.2 and 0.4. For small Knudsen numbers (Kn = 0.05 and 0.1), the choice of FEM mesh significantly affects the results. Meshes 1 and 2 are not refined enough to capture the gas speed accurately due to the small scale ( $\mathcal{O}(10^{-5})$ ), as shown by the green dashed (Mesh 1) and cyan dot-dashed (Mesh 2) lines in the top panels of Fig. 7.10. For larger Knudsen numbers (Kn = 0.2 and 0.4), the discrepancy between the three FEM meshes is significantly reduced and for Kn = 0.4, the results are nearly identical. A reason for this behavior is that the magnitude of the velocity gets smaller with decreasing Knudsen number, which requires a finer mesh

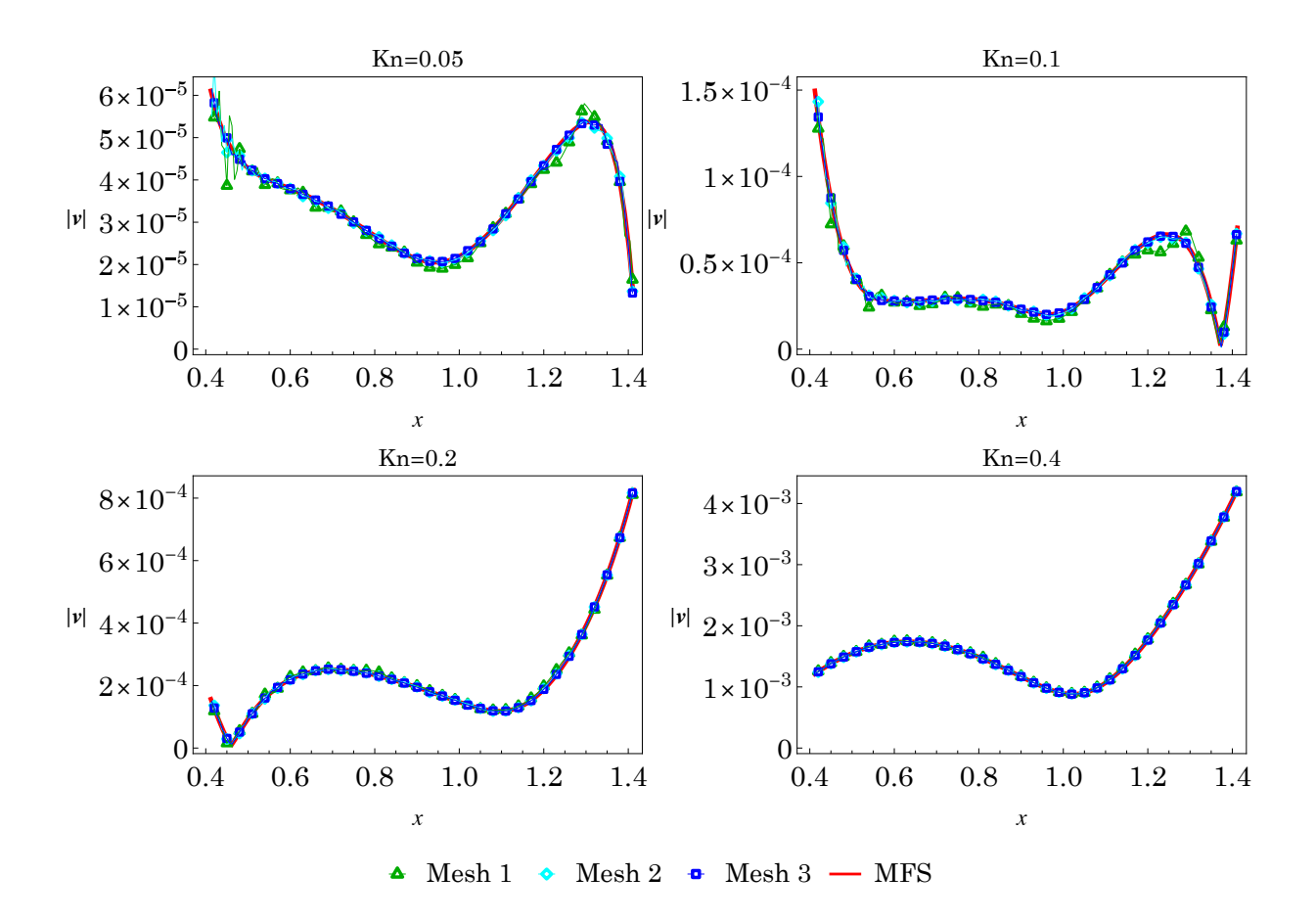


Figure 7.10: Speed of the gas between the two cylinders along y = x in the first quadrant for different Knudsen numbers.

to resolve the flow features in the FEM. In contrast, the MFS (solid red lines) exhibits stable convergence regardless of the Knudsen number or the grid spacing parameter. The speed of the gas for Kn = 0.1 and 0.2 is zero at x = 1.37 and x = 0.46, respectively. These points correspond to the highlighted red dots in the streamline plot Fig. 7.9, at which the transition between the vortices along the inner and outer cylinder takes place for Kn = 0.1 and 0.2.

Additionally, we calculate the heat flow rate through the inner cylinder defined as

$$Q_{\Gamma_1} = \int_{\Gamma_1} \boldsymbol{q} \cdot \boldsymbol{n} \, \mathrm{d}l. \tag{7.57}$$

Table 7.1 depicts the values of  $Q_{\Gamma_1}$  obtained by considering different meshes for the FEM and different grid spacing (or number of boundary and singularity points) for different Knudsen numbers Kn = 0.05, 0.1, 0.2, 0.4. We also calculate the time taken by the FEM and MFS to calculate  $Q_{\Gamma_1}$  using different FEM meshes and grid spacing d for the MFS

Table 7.1: Comparison of the heat flow rate through the inner cylinder  $Q_{\Gamma_1}$  and computation time for FEM (top) and MFS (bottom) for different mesh refinements and source distances d using 8 CPU cores.

	$\mathbf{FEM}$						
Kn	Mesh 1		Mesh 2		Mesh 3		
	$Q_{\Gamma_1}$	Time	$Q_{\Gamma_1}$	Time	$Q_{\Gamma_1}$	Time	
0.05	1.5276481	5s	1.5276241	29s	1.5276212	185s	
0.1	2.4815209	5s	2.4815120	30s	2.4815119	185s	
0.2	3.5116585	5s	3.5116914	29s	3.5117014	187s	
0.4	4.1411597	5s	4.1412806	30s	4.1413130	191s	

MFS						
Kn	$d = 0.15 (N_b = 124)$		$d = 0.1 (N_b = 187)$		$d = 0.07 (N_b = 268)$	
	$Q_{\Gamma_1}$	Time	$Q_{\Gamma_1}$	Time	$Q_{\Gamma_1}$	Time
0.05	1.5276979	17s	1.5276204	28s	1.5276204	49s
0.1	2.4815252	16s	2.4815121	27s	2.4815121	50s
0.2	3.5117115	16s	3.5117048	28s	3.5117048	51s
0.4	4.1413392	16s	4.1413240	30s	4.1413240	52s

using 8 CPU cores. As the FEM mesh is refined from Mesh 1 to Mesh 3, the values of  $Q_{\Gamma_1}$  converge, albeit with significantly increased computational time—reaching up to 191 seconds for Mesh 3. However, the MFS achieves the accuracy up to 7 significant digits with significantly lower computational cost. For instance, in the finest FEM mesh (Mesh 3), the computation time reaches up to 191 seconds, while the most refined MFS case with d = 0.07 having  $N_b = N_s = 268$  achieves a higher precision in less than a third of the time (approximately 52 seconds). Additionally, even the coarser MFS configurations (e.g., with d = 0.15) yield accurate results with computation times as low as 16–17 seconds.

It has also been noticed that, when the grid spacing is reduced to d = 0.07, the MFS attains convergence in  $Q_{\Gamma_1}$  values up to 10 decimal digits. This highlights the MFS as not only a computationally efficient alternative to mesh-based solvers like FEM, but also a powerful method for achieving rapid convergence with high numerical accuracy in rarefied flow simulations.

### 7.6 Summary

In this chapter, a generic methodology has been developed for computing fundamental solutions of any linear moment system without prescribing Dirac-delta source terms in specific governing or closure equations. This approach had been designed to overcome the limitations of previous implementations of the MFS, which relied on problem-specific formulations and varying choices of Dirac-delta sources. The proposed methodology utilizes the Fourier transformation combined with partial-fraction decomposition to obtain the fundamental solutions corresponding to given linear system. This strategy has been firstly demonstrated for the Stokes equations in two dimensions and subsequently extended to the more complex R13 equations. Validation against an analytic solution for the R13 model in the case of rarefied gas flow between coaxial cylinders has confirmed the accuracy of the proposed framework. The influence of numerical parameters—including grid spacing and dilation parameter—has been systematically analyzed through error estimates and effective condition number. Furthermore, the framework has been applied to a thermally induced flow between two noncoaxial circular cylinders, a problem for which no analytic solution exists. To assess the accuracy of our method, we compare the results with those obtained using the FEM, a widely trusted numerical approach known for its ability to handle complex geometries with high precision. Results obtained using the MFS have shown excellent agreement with those from the FEM. The MFS achieves comparable or higher accuracy while being significantly more computationally efficient. The mesh-free nature of the MFS has proven particularly beneficial for capturing complex flow features in thermally-driven configurations and for enabling rapid convergence even in simulations involving intricate geometries.

# Chapter 8

# Summary and future directions

### 8.1 Summary and conclusions

A meshless numerical framework based on the MFS has been developed to study rarefied gas flows—especially in quasi-two-dimensional scenarios. The work relies upon determining the fundamental solutions of the linearized CCR and R13 models in 2D and the implementation of the determined fundamental solutions in the MFS. To gauge the accuracy of the numerical framework, different internal and external flow problems have been investigated. The long-standing Stokes' paradox in the context of external flows has been addressed using the CCR-MFS framework. To extend the applicability of the MFS beyond problem-specific fundamental solutions, a generic approach has been proposed to systematically compute fundamental solutions for any linear moment system. The main findings and contributions of the thesis are summarized below.

- The fundamental solutions of the CCR model in 2D have been determined by exploiting the fundamental solutions of some well-known partial differential equations, e.g., the Laplace and biharmonic equations. It has turned out that the fundamental solutions of the linearized NSF and G13 equations in 2D can also be recovered from the derived fundamental solutions of the CCR model.
- The capability of the developed CCR-MFS framework has been assessed by comparing its results with analytic and benchmark solutions for some internal flow problems. One of these problems involves evaporating (or condensing) vapor flow between two coaxial cylinders, where our results show strong agreement with those obtained from the linearized BGK model in Ref. [77], particularly at small Knudsen numbers. Additionally, two temperature-driven rarefied gas flow problems have been studied: one between two non-coaxial circular cylinders and another between a circular cylinder and an elliptical cylinder, having different temperatures. The results for these problems have been compared with those reported in Refs. [4, 5, 82].

The CCR-MFS results show good agreement with the linearized BGK model for local flow fields at small Knudsen numbers, but differences become noticeable as the Knudsen number increases, despite similar overall trends. However, global quantities like drag force are captured accurately even at large Knudsen numbers. The thermal-slip coefficient is also found to significantly influence velocity profiles due to interplay between thermal creep and thermal stress. Furthermore, the lid-driven cavity problem in the context of rarefied gases has also been investigated for both single- and two-sided lid-driven configurations.

- The CCR-MFS framework has also been utilized to obtain solutions for external rarefied gas flows around circular and semi-circular cylinders by circumventing Stokes' paradox. To address the limitations imposed by Stokes' paradox in studying flow past two-dimensional objects, the domain has been made "bounded" artificially by introducing an artificial boundary in the flow domain far from the disk. This has allowed us to obtain a meaningful analytic solution for the flow past a circular disk and to use it to validate our numerical framework. The normalized drag over the circular disk obtained from the CCR-MFS framework has agreed quite well with the analytic solution and reasonably well even with the results on the normalized drag available in the literature [37, 79, 128]. It is, however, worth mentioning that the results depend on the placement of the artificial boundary, which poses a limitation and points to the need for including convective terms in the CCR model (like Oseen's correction to the Stokes equations).
- The MFS has been utilized to study evaporation/condensation from/on liquid jets using the CCR model. Both circular and non-circular jet interfaces have been considered to evaluate the mass-and heat-flux coefficients under pressure- and temperature-driven conditions for partial and complete phase change. The influence of shape deformation from circular to non-circular interface has been examined using spherical harmonics.
- A general framework has been developed for deriving the fundamental solutions of linear moment systems and for their implementation in the MFS. This approach eliminates the need for predefined Dirac-delta source terms in the governing equations and/or in the constitutive relations. The proposed approach has first been demonstrated for the Stokes equations and then been extended to the R13 equations

in two dimensions. The derived fundamental solutions of the R13 equations have been implemented successfully in the MFS solver and validated against analytic solutions to confirm their accuracy. To further assess its performance, we have applied the generic MFS for R13 equations to the problem of thermally-induced flow between two noncoaxial cylinders and compared the results with those obtained from the FEM. We have found that the MFS has not only captured rarefaction effects accurately but also demonstrated computational efficiency.

- Numerical performance of the MFS is significantly influenced by the location of source points, grid spacing and the effective condition number. Sensitivity and error analysis has been illustrated for some of the considered problems to identify optimal choices for the location of singularities in achieving high accuracy.
- Rarefaction effects, such as thermal creep, temperature polarization, and anti-Fourier heat transfer have been accurately captured for the considered problems.

### 8.2 Future scopes

The present work opens up several promising avenues for future exploration:

- The developed MFS framework, currently formulated for monatomic gases, can be extended to polyatomic gases and gas mixtures to enhance its applicability to more realistic scenarios.
- For external flows, the current reliance on artificial boundaries to bypass Stokes' paradox may be avoided by incorporating convective terms into the CCR model, similarly to Oseen's correction [78] to the Stokes equations. This would result in physically more accurate modeling, although it necessitates deriving and implementing the fundamental solutions for the CCR model with convective terms included.
- An important direction for future work is the extension of the MFS to unsteady
  problems involving moving interfaces. This would allow the modeling of dynamic
  interface phenomenon such as time-dependent evaporation/condensation using the
  unsteady CCR model.
- Flow around evaporating jets studied in this thesis can be generalized to multiphase flow problems by coupling gas and liquid phases. The internal motion within the

- liquid jet can be modeled using the Stokes equations, while the surrounding gas can be treated using either the CCR or R13 model.
- The generic MFS framework developed here can be extended to three-dimensional configurations in a straightforward way. Moreover, it can be utilized to determine and implement the fundamental solutions for better but involved models—such as the R26 equations—in both 2D and 3D.
- The general methodology developed for constructing fundamental solutions of large linear systems can be applied to other meshless numerical methods such as the boundary element method.
- The MFS approach needs to be enhanced to handle inhomogeneous and nonlinear systems in rarefied gas flows, possibly using iterative schemes, like Picard iteration.
   The approach also has potential to extend it for more complex moment models and kinetic models.

Table 8.1: Summary of problems studied, models used, and validation or model limitations.

Problem description	Framework Used	Validation / Comparison	Notes
Phase-transition flow between coaxial cylinders	CCR-MFS	Validated against BGK solution	CCR outperforms NSF in accuracy
Thermally-induced flow between non-coaxial circular cylinders	CCR-MFS	Compared with BGK model	CCR-MFS overpredicts local fields but accurately captures global quantities
Thermally-induced flow between coaxial elliptic and circular cylinders	CCR-MFS		CCR-MFS correctly predicts flow profile; NSF fails
Lid-driven cavity (single and dual wall motion)	CCR-MFS	Compared with DSMC and R13	CCR-MFS captures anti- Fourier heat flux effects
Flow past a circular cylinder	CCR-MFS	Validated against analytic solution	Artificial boundary used to handle Stokes' paradox
Flow past a semicircular cylinder	CCR-MFS		CCR-MFS predicts temperature polarization and anti- Fourier effects
Evaporation/condensation from circular jet	CCR-MFS	Validated against analytic solution	Both partial and complete evaporation/condensation boundary conditions imple- mented
Evaporation/condensation from deformed jet	CCR-MFS		Geometry effects on flux studied using spherical har- monics
Phase-transition flow between coaxial cylinders with inner rotating cylinder	Generic MFS for R13	Validated against analytic R13 solution	Source strengths obtained by system matrix using boundary conditions
Thermally-induced flow between non-coaxial circular cylinders	Generic MFS for R13	Compared with FEM results	MFS shown to be more efficient than FEM

# Appendix A

## **Inverse Fourier transforms**

We use the fundamental solutions of some well-known equations, such as the Laplace and biharmonic equations, from the literature [22, 80, 98] to find the inverse Fourier transforms of the terms on the right-hand sides of Eqs. (3.70), (3.71) and (3.73)–(3.75). Note that the Einstein summation holds over the repeated indices in this appendix and the indices can take values 1 and 2 only. The fundamental solution of the Laplace equation (with a point source of unit strength)

$$\nabla^2 \phi \equiv \frac{\partial^2 \phi}{\partial x_i^2} = \delta(\mathbf{r}) \tag{A.1}$$

in 2D is given by

$$\phi = \frac{\ln r}{2\pi} \tag{A.2}$$

where  $r = |x_i|$ .

Applying the Fourier transformation [defined by Eq. (3.37)] to the Laplace equation (A.1), we obtain

$$(-i)^2 k^2 \hat{\phi} = 1 \quad \Longrightarrow \quad \hat{\phi} = -\frac{1}{k^2}. \tag{A.3}$$

Hence, the inverse Fourier transform of  $1/k^2$  is

$$\mathcal{F}^{-1}\left(\frac{1}{k^2}\right) = \mathcal{F}^{-1}(\hat{\phi}) = -\frac{\ln r}{2\pi}.\tag{A.4}$$

Also, by definition (3.38), the inverse Fourier transform of  $1/k^2$  is given by

$$\mathcal{F}^{-1}\left(\frac{1}{k^2}\right) = \frac{1}{(2\pi)^2} \int_{\mathbb{R}^2} \frac{1}{k^2} e^{-i \mathbf{k} \cdot \mathbf{r}} d\mathbf{k}. \tag{A.5}$$

Therefore, from Eqs. (A.4) and (A.5), we have

$$\frac{1}{(2\pi)^2} \int_{\mathbb{R}^2} \frac{1}{k^2} e^{-i \mathbf{k} \cdot \mathbf{r}} d\mathbf{k} = -\frac{\ln r}{2\pi}.$$
 (A.6)

Now, taking the partial derivative with respect to  $x_i$  on both sides in (A.6), we obtain

$$-\frac{\mathrm{i}}{(2\pi)^2} \int_{\mathbb{R}^2} \frac{k_i}{k^2} \mathrm{e}^{-\mathrm{i}\,\boldsymbol{k}\cdot\boldsymbol{r}} \,\mathrm{d}\boldsymbol{k} = -\frac{1}{2\pi} \frac{x_i}{r^2} \tag{A.7}$$

which, in turn, gives

$$\mathcal{F}^{-1}\left(\frac{k_i}{k^2}\right) = -\frac{i x_i}{2\pi r^2}.$$
 (A.8)

Moreover, taking the partial derivative with respect to  $x_i$  on both sides in (A.7), we obtain

$$\frac{-1}{(2\pi)^2} \int_{\mathbb{R}^2} \frac{k_i k_j}{k^2} e^{-i \mathbf{k} \cdot \mathbf{r}} d\mathbf{k} = -\frac{1}{2\pi} \left( \frac{\delta_{ij}}{r^2} - \frac{2x_i x_j}{r^4} \right), \tag{A.9}$$

which, in turn, gives

$$\mathcal{F}^{-1}\left(\frac{k_i k_j}{k^2}\right) = -\frac{1}{\pi} \frac{x_i x_j}{r^4} + \frac{1}{2\pi} \frac{\delta_{ij}}{r^2}.$$
 (A.10)

The fundamental solution of the biharmonic equation (with a point source of unit strength)

$$\frac{\partial^4 \phi}{\partial^2 x_i \, \partial^2 x_j} = \delta(\mathbf{r}) \tag{A.11}$$

in 2D is given by

$$\phi = \frac{r^2 \ln r}{8\pi}.\tag{A.12}$$

Following similar steps as for the Laplace equation above, we obtain

$$\mathcal{F}^{-1}\left(\frac{1}{k^4}\right) = \frac{r^2 \ln r}{8\pi},\tag{A.13}$$

$$\mathcal{F}^{-1}\left(\frac{k_i}{k^4}\right) = i\frac{x_i(2\ln r + 1)}{8\pi},\tag{A.14}$$

$$\mathcal{F}^{-1}\left(\frac{k_i k_j}{k^4}\right) = -\frac{(2\ln r + 1)}{8\pi} \delta_{ij} - \frac{x_i x_j}{4\pi r^2}.$$
 (A.15)

# Appendix B

# Fundamental solutions of the CCR model

Now, we derive the fundamental solutions (previously derived in Sec. 3.3) via alternate approach of considering three different cases by incorporating the sourcing terms separately in the mass balance, momentum balance and the energy balance equation. In the first case, a sourcing term is considered in the momentum balance equation, which is a point force vector  $f_i$ . The balance equations (2.19) in indicial notations read

$$\frac{\partial v_i}{\partial x_i} = 0, \tag{B.1}$$

$$\frac{\partial p}{\partial x_i} + \frac{\partial \sigma_{ij}}{\partial x_j} = f_i \, \delta(\mathbf{r}), \tag{B.2}$$

$$\frac{\partial q_i}{\partial x_i} = 0, (B.3)$$

where  $\mathbf{r} = (x_1, x_2)^{\mathsf{T}}$ . The constitutive relations (2.20) read

$$\sigma_{ij} = -2\operatorname{Kn}\left[\frac{1}{2}\left(\frac{\partial v_i}{\partial x_j} + \frac{\partial v_j}{\partial x_i}\right) - \frac{1}{3}\delta_{ij}\frac{\partial v_\ell}{\partial x_\ell}\right] - 2\alpha_0\operatorname{Kn}\left[\frac{1}{2}\left(\frac{\partial q_i}{\partial x_j} + \frac{\partial q_j}{\partial x_i}\right) - \frac{1}{3}\delta_{ij}\frac{\partial q_\ell}{\partial x_\ell}\right].$$
(B.4)

$$q_i = -\frac{c_p \operatorname{Kn}}{\operatorname{Pr}} \left( \frac{\partial T}{\partial x_i} + \alpha_0 \frac{\partial \sigma_{ij}}{\partial x_j} \right). \tag{B.5}$$

Applying the Fourier transformation in Eqs. (B.1)–(B.3), (B.4) and (B.5) and using the fact that  $\mathcal{F}[\delta(\mathbf{r})] = 1$ , we obtain  $(i, j, \ell \in \{1, 2\})$ 

$$k_i \hat{v}_i = 0, \tag{B.6}$$

$$k_i \hat{p} + k_j \hat{\sigma}_{ij} = i f_i, \tag{B.7}$$

$$k_i \hat{q}_i = 0, \tag{B.8}$$

$$\hat{\sigma}_{ij} = i \operatorname{Kn} \left[ k_j (\hat{v}_i + \alpha_0 \hat{q}_i) + k_i (\hat{v}_j + \alpha_0 \hat{q}_j) - \frac{2}{3} \delta_{ij} k_\ell (\hat{v}_\ell + \alpha_0 \hat{q}_\ell) \right], \tag{B.9}$$

$$\hat{q}_i = i \frac{c_p Kn}{Pr} \left( k_i \hat{T} + \alpha_0 k_j \hat{\sigma}_{ij} \right), \tag{B.10}$$

where the variables with hat are the Fourier transforms of the corresponding field variables. Using Eqs. (B.6) and (B.8), Eq. (B.9) simplifies to

$$\hat{\sigma}_{ij} = i \operatorname{Kn} \left[ k_j (\hat{v}_i + \alpha_0 \hat{q}_i) + k_i (\hat{v}_j + \alpha_0 \hat{q}_j) \right]. \tag{B.11}$$

Multiplying the above equation with  $k_j$  and  $k_i k_j$ , we obtain

$$k_j \hat{\sigma}_{ij} = i \operatorname{Kn} k^2 (\hat{v}_i + \alpha_0 \hat{q}_i), \tag{B.12}$$

$$k_i k_j \hat{\sigma}_{ij} = 0, \tag{B.13}$$

respectively, where  $k_i k_i = |k_i|^2 = k^2$  has been used. Multiplying Eq. (B.10) with  $k_i$  utilizing Eqs. (B.8) and (B.13), we obtain

$$\hat{T} = 0. (B.14)$$

Again, multiplying Eq. (B.7) with  $k_i$  and utilizing Eq. (B.13), we obtain

$$\hat{p} = i\frac{k_i f_i}{k^2}.\tag{B.15}$$

Now, from Eqs. (B.7) and (B.15), one can easily write

$$k_j \hat{\sigma}_{ij} = i f_i - i \frac{k_i k_j f_j}{k^2}. \tag{B.16}$$

Substituting the value of  $\hat{T}$  from Eq. (B.14) and the value of  $k_j \hat{\sigma}_{ij}$  from Eq. (B.16) into Eq. (B.10), we obtain

$$\hat{q}_i = -\frac{c_p \text{Kn}}{\text{Pr}} \alpha_0 f_j \left( \delta_{ij} - \frac{k_i k_j}{k^2} \right). \tag{B.17}$$

Now, from Eqs. (B.12), (B.16) and (B.17),

$$\hat{v}_i = \frac{f_j}{\operatorname{Kn}} \left( \frac{\delta_{ij}}{k^2} - \frac{k_i k_j}{k^4} \right) + \frac{c_p \operatorname{Kn}}{\operatorname{Pr}} \alpha_0^2 f_j \left( \delta_{ij} - \frac{k_i k_j}{k^2} \right).$$
 (B.18)

Finally, using Eqs. (B.17) and (B.18) in Eq. (B.9), we obtain

$$\hat{\sigma}_{ij} = i f_{\ell} \left( \frac{k_j \delta_{i\ell} + k_i \delta_{j\ell}}{k^2} - 2 \frac{k_i k_j k_{\ell}}{k^4} \right). \tag{B.19}$$

Applying the inverse Fourier transformation in Eqs. (B.14), (B.15) and (B.17)–(B.19) with the help of the formulae derived in [42], the field variables turn out to be

$$v_{i} = \frac{f_{j}}{\operatorname{Kn}} \left( \frac{x_{i}x_{j}}{4\pi r^{2}} - \frac{2\ln r - 1}{8\pi} \delta_{ij} \right) + \frac{c_{p}\operatorname{Kn}}{\operatorname{Pr}} \alpha_{0}^{2} \frac{f_{j}}{2\pi} \left( \frac{2x_{i}x_{j}}{r^{4}} - \frac{\delta_{ij}}{r^{2}} \right),$$

$$q_{i} = -\frac{c_{p}\operatorname{Kn}}{\operatorname{Pr}} \alpha_{0} \frac{f_{j}}{2\pi} \left( \frac{2x_{i}x_{j}}{r^{4}} - \frac{\delta_{ij}}{r^{2}} \right),$$

$$p = \frac{f_{i}x_{i}}{2\pi r^{2}},$$

$$T = 0,$$

$$\sigma_{ij} = \frac{f_{\ell}x_{\ell}}{2\pi} \left( \frac{2x_{i}x_{j}}{r^{4}} - \frac{\delta_{ij}}{r^{2}} \right),$$

$$\left\{ \text{Case I} \right\}$$

$$(B.20)$$

where  $r = |x_i|$  and  $i, j, \ell \in \{1, 2\}$ . In the second case, a sourcing term is considered in the energy balance equation i.e. balance equations read

$$\frac{\partial v_i}{\partial x_i} = 0, (B.21)$$

$$\frac{\partial p}{\partial x_i} + \frac{\partial \sigma_{ij}}{\partial x_j} = 0, \tag{B.22}$$

$$\frac{\partial q_i}{\partial x_i} = g \,\delta(\mathbf{r}). \tag{B.23}$$

Applying the Fourier transformation in Eqs. (B.21)–(B.23), (B.4) and (B.5) in this case, we obtain

$$k_i \hat{v}_i = 0, \tag{B.24}$$

$$k_i \hat{p} + k_j \hat{\sigma}_{ij} = 0, \tag{B.25}$$

$$k_i \hat{q}_i = i g. \tag{B.26}$$

Using Eqs. (B.24) and (B.26), Eq. (B.9) simplifies to

$$\hat{\sigma}_{ij} = i \operatorname{Kn} \left[ k_j (\hat{v}_i + \alpha_0 \hat{q}_i) + k_i (\hat{v}_j + \alpha_0 \hat{q}_j) \right] + \frac{2}{3} \delta_{ij} \operatorname{Kn} \alpha_0 g.$$
 (B.27)

Multiplying the above equation with  $k_j$  and  $k_i k_j$ , we obtain

$$k_j \hat{\sigma}_{ij} = i \operatorname{Kn} k^2 (\hat{v}_i + \alpha_0 \hat{q}_i) - \frac{1}{3} \operatorname{Kn} k_i \alpha_0 g,$$
 (B.28)

$$k_i k_j \hat{\sigma}_{ij} = -\frac{4}{3} \operatorname{Kn} k^2 \alpha_0 g. \tag{B.29}$$

Multiplying Eq. (B.10) with  $k_i$  and exploiting Eqs. (B.26) and (B.29), we obtain

$$\hat{T} = \frac{\Pr}{c_p \operatorname{Kn}} \frac{g}{k^2} + \frac{4}{3} \operatorname{Kn} \alpha_0^2 g.$$
 (B.30)

Again, multiplying Eq. (B.7) with  $k_i$  and exploiting Eq. (B.29), we obtain

$$\hat{p} = \frac{4}{3} \text{Kn} \alpha_0 g. \tag{B.31}$$

Now, from Eqs. (B.7) and (B.31), one can easily write

$$k_j \hat{\sigma}_{ij} = -\frac{4}{3} k_i \text{Kn} \alpha_0 g. \tag{B.32}$$

Substituting the value of  $\hat{T}$  from Eq. (B.30) and the value of  $k_j \hat{\sigma}_{ij}$  from Eq. (B.32) into Eq. (B.10), we obtain

$$\hat{q}_i = i \frac{k_i g}{k^2}. \tag{B.33}$$

Now, from Eqs. (B.28), (B.32) and (B.33),

$$\hat{v}_i = 0. \tag{B.34}$$

Finally, using Eqs. (B.33) and (B.34) in Eq. (B.9), we obtain

$$\hat{\sigma}_{ij} = -2\operatorname{Kn}\left(\frac{k_i k_j}{k^2} - \frac{\delta_{ij}}{3}\right) \alpha_0 g. \tag{B.35}$$

Applying the inverse Fourier transformation in Eqs. (B.30), (B.31) and (B.33)–(B.35) with the help of the formulae derived in Appendix A, the field variables turn out to be

$$v_{i} = 0,$$

$$q_{i} = \frac{g}{2\pi} \frac{x_{i}}{r^{2}},$$

$$p = 0,$$

$$T = -\frac{\Pr}{c_{p}\operatorname{Kn}} \frac{g \ln r}{2\pi},$$

$$\sigma_{ij} = \frac{2\operatorname{Kn}\alpha_{0}g}{2\pi} \left(\frac{2x_{i}x_{j}}{r^{4}} - \frac{\delta_{ij}}{r^{2}}\right).$$
(B.36)

In the third case, a sourcing term is considered in the mass balance equation i.e. balance equations read

$$\frac{\partial v_i}{\partial x_i} = h \,\delta(\mathbf{r}),\tag{B.37}$$

$$\frac{\partial p}{\partial x_i} + \frac{\partial \sigma_{ij}}{\partial x_j} = 0, \tag{B.38}$$

$$\frac{\partial q_i}{\partial x_i} = 0. {(B.39)}$$

Applying the Fourier transformation in Eqs. (B.37)–(B.39), (B.4) and (B.5) in this case, we obtain

$$k_i \hat{v}_i = i h, \tag{B.40}$$

$$k_i \hat{p} + k_j \hat{\sigma}_{ij} = 0, \tag{B.41}$$

$$k_i \hat{q}_i = 0. ag{B.42}$$

Using Eqs. (B.40) and (B.42), Eq. (3.65) simplifies to

$$\hat{\sigma}_{ij} = i \operatorname{Kn} \left[ k_j (\hat{v}_i + \alpha_0 \hat{q}_i) + k_i (\hat{v}_j + \alpha_0 \hat{q}_j) \right] + \frac{2}{3} \delta_{ij} \operatorname{Kn} h.$$
 (B.43)

Multiplying the above equation with  $k_j$  and  $k_i k_j$ , we obtain

$$k_j \hat{\sigma}_{ij} = i \operatorname{Kn} k^2 (\hat{v}_i + \alpha_0 \hat{q}_i) - \frac{1}{3} \operatorname{Kn} k_i h,$$
(B.44)

$$k_i k_j \hat{\sigma}_{ij} = -\frac{4}{3} \operatorname{Kn} k^2 h. \tag{B.45}$$

Multiplying Eq. (B.10) with  $k_i$  and exploiting Eqs. (B.42) and (B.45), we obtain

$$\hat{T} = \frac{4}{3}\alpha_0 \text{Kn}h. \tag{B.46}$$

Again, multiplying Eq. (B.7) with  $k_i$  and exploiting Eq. (B.45), we obtain

$$\hat{p} = \frac{4}{3} \text{Kn}h. \tag{B.47}$$

Now, from Eqs. (B.7) and (B.47), one can easily write

$$k_j \hat{\sigma}_{ij} = -\frac{4}{3} k_i \text{Kn} h. \tag{B.48}$$

Substituting the value of  $\hat{T}$  from Eq. (B.46) and the value of  $k_j \hat{\sigma}_{ij}$  from Eq. (B.48) into Eq. (B.10), we obtain

$$\hat{q}_i = 0. ag{B.49}$$

Now, from Eqs. (B.44), (B.48) and (B.49),

$$\hat{v}_i = i\frac{k_i h}{k^2}.\tag{B.50}$$

Finally, using Eqs. (B.49) and (B.50) in Eq. (B.9), we obtain

$$\hat{\sigma}_{ij} = -2\operatorname{Kn}\left(\frac{k_i k_j}{k^2} - \frac{\delta_{ij}}{3}\right) h. \tag{B.51}$$

Applying the inverse Fourier transformation in Eqs. (B.46), (B.47) and (B.49)–(B.51) with the help of the formulae derived in Appendix A, the field variables turn out to be

$$v_{i} = \frac{hx_{i}}{2\pi r^{2}},$$

$$q_{i} = 0,$$

$$p = 0,$$

$$T = 0,$$

$$\sigma_{ij} = \frac{2\operatorname{Kn}h}{2\pi} \left(\frac{2x_{i}x_{j}}{r^{4}} - \frac{\delta_{ij}}{r^{2}}\right).$$
(B.52)

Combining the three cases (B.20)–(B.52), we obtain the fundamental solutions (3.81)–(3.85).

# Appendix C

# Interplay between thermal stress and thermal creep

In order to investigate the dynamic interplay observed between thermal stress and thermal creep observed in problem 1 of Sec. 4.3, we consider a similar problem where inner cylinder is elliptic and the outer cylinder is circular.

#### C.1 Problem statement

We consider a rarefied gas confined between a circular cylinder and an elliptical cylinder, both of which are coaxial along the  $\tilde{z}$  axis. Let the outer cylinder be circular with radius  $\tilde{r}$  and the inner cylinder be elliptic with the semi-major and semi-minor axes having lengths  $\tilde{a}$  and  $\tilde{b}$ , respectively where  $\tilde{b} < \tilde{a} < \tilde{r}$ . Figure C.1 exhibits a cross-sectional

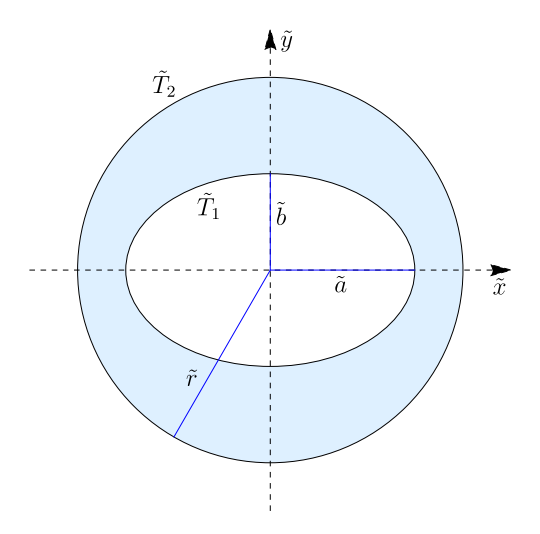


Figure C.1: A cross-sectional view illustrating a rarefied gas contained between two coaxial cylinders, the outer of which is circular and the inner of which is elliptic.

view of the problem. The radius  $\tilde{r}$  of the outer circular cylinder is used as the characteristic length scale  $\tilde{L}$  for non-dimensionalization purposes. Thus, the dimensionless radius of the outer cylinder is  $r = \tilde{r}/\tilde{L} = 1$  and the dimensionless lengths of the semi-major and semi-minor axes are  $a = \tilde{a}/\tilde{r}$  and  $b = \tilde{b}/\tilde{r}$ , respectively. A temperature gradient is induced in the gas by making the wall of outer cylinder to be hotter than that of inner cylinder. Let  $\tilde{T}_1$  and  $\tilde{T}_2$  denote the temperatures of the (inner) elliptic and (outer) circular cylinders, respectively, with  $\tilde{T}_1 < \tilde{T}_2$ . We consider  $\tilde{T}_1$  to be the reference temperature for non-dimesionalization, wherefore the dimensionless perturbations in the temperatures of the outer and inner cylinders are  $T_1 = (\tilde{T}_1 - \tilde{T}_1)/\tilde{T}_1 = 0$  and  $T_2 = (\tilde{T}_2 - \tilde{T}_1)/\tilde{T}_1$ , respectively. Analogous to problem 1 of Sec. 4.3, the boundary conditions for this problem are again (4.18)–(4.20).

# C.2 Results demonstrating thermal creep and thermal stress effects

The dimensionless radius of the outer cylinder is r = 1 and the lengths of the semimajor and semi-minor axes of the outer cylinder are fixed at a = 0.75 and b = 0.5, for computational purpose. The locations of the fictitious boundaries are fixed by fixing parameters  $r_s = 2$ ,  $a_s = 0.375$  and  $b_s = 0.25$ . The number of boundary points on each of the original boundaries is taken as  $n_b = 150$  and the number of source points on each of the fictitious boundaries is fixed as  $n_s = 150$ . The dimensionless temperatures on the elliptic and circular walls are taken as  $T_1 = 0$  and  $T_2 = 1$ , respectively.

In the first case, we set the thermal-slip coefficient to  $\beta=1/5$ , along with parameters  $\alpha_0=0.3197$  and  $\Pr=0.661$ . For Knudsen numbers  $\Pr=0.05,0.1,0.15$ , and 0.2, the velocity streamlines superimposed on the temperature contours are shown in Fig. C.2. Only one form of flow, namely thermal-stress slip flow, is visible at very low values of the Knudsen number ( $\Pr=0.05$ ) (top left panel). The effects of thermal stress arise from temperature gradients within the gas bulk, resulting in thermal-stress slip flow that anticipates the migration of gas from hotter to cooler regions near the wall. Owing to the narrowest gap between the cylinders at  $\theta=0$  (where the angle  $\theta$  is measured from the positive  $\tilde{x}$ -axis anticlockwise around the origin), the normal component of heat flux is highest due to the most substantial temperature gradient between the cylinders.

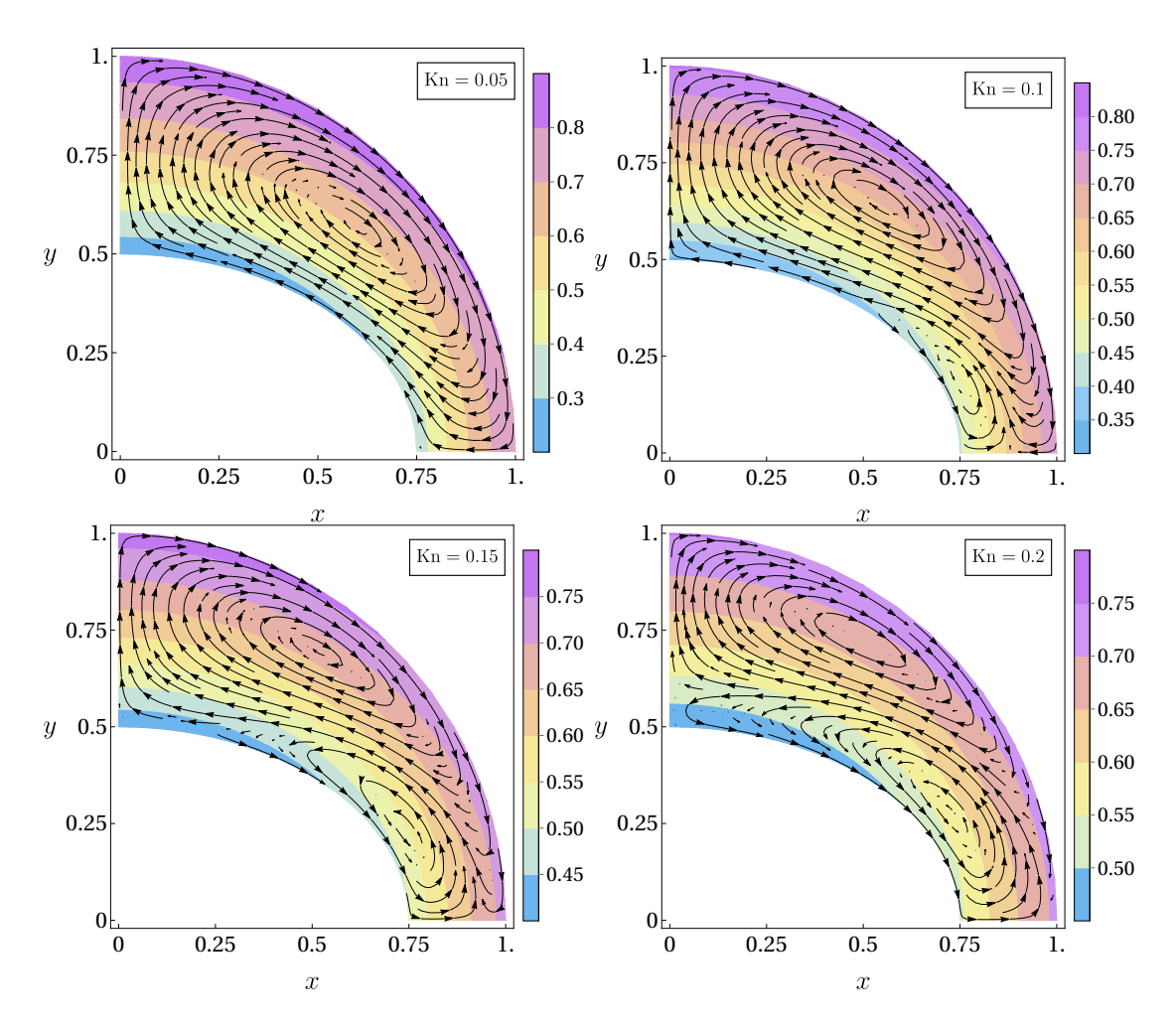


Figure C.2: Temperature contours and velocity streamlines depicted in the first quadrant for different values of the Knudsen number (Kn = 0.05, 0.1, 0.15, and 0.2) for fixed  $\beta = 1/5$ ,  $\alpha_0 = 0.3197$  and Pr = 0.661.

However, at  $\theta = \pi/2$ , the normal component of heat flux is lowest due to the smallest temperature gradient between the cylinders. The gas therefore moves from hotter to colder regions along the boundaries resulting in a clockwise circulating flow in the first quadrant and symmetrically in the other three quadrants. However, with increasing values of the Knudsen number, an additional counterclockwise circulation zone begins to emerge along the inner cylinder which intensifies gradually for Kn = 0.1, 0.15 and 0.2. This phenomenon is attributed to the thermal creep effect which is a boundary effect, causing the gas to flow along the inner cylinder from a comparatively cooler to a hotter location as a result of the tangential temperature gradient. We shall explain the mechanism of the above two types of flows after illustrating the results for other values of  $\beta$ .

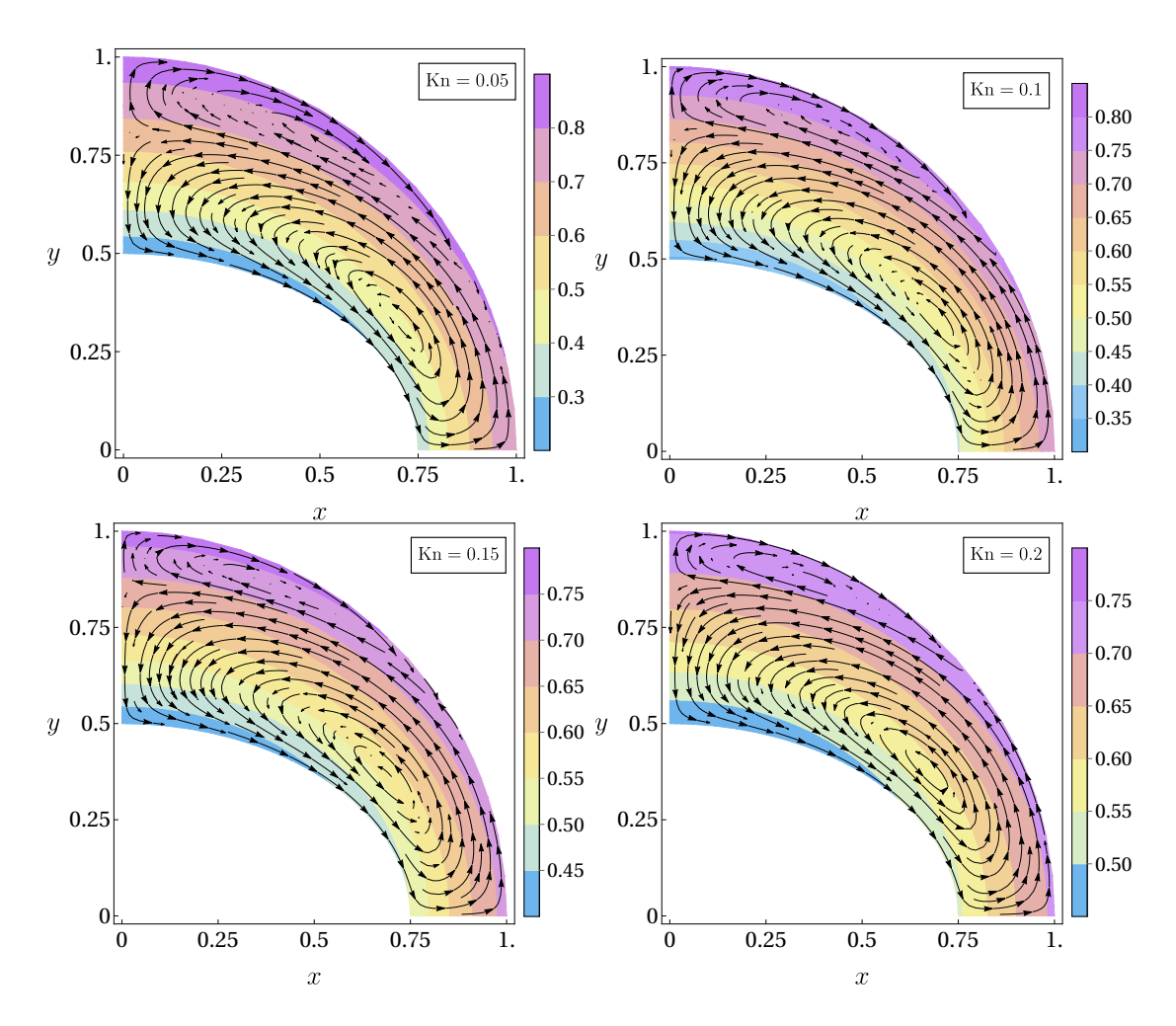


Figure C.3: Temperature comtours and velocity streamlines depicted in the first quadrant for different values of the Knudsen number (Kn = 0.05, 0.1, 0.15 and 0.2) for fixed  $\beta = \alpha_0 = 0.3197$  and Pr = 0.661.

Now, we demonstrate the impact of the thermal-slip coefficient by adopting a larger value of  $\beta$ , specifically  $\beta = \alpha_0 = 0.3197$ , along with Pr = 0.661. The velocity streamlines over the temperature contours are presented in Fig. C.3 for Knudsen numbers Kn = 0.05, 0.1, 0.15 and 0.2. It is apparent that thermal creep flow prevails over thermal-stress slip flow for all values of the Knudsen number that are taken into consideration. Furthermore, the effects of thermal creep get stronger and the effects of thermal stress are diminished as the Knudsen number rises.

To confirm the findings about the competition between thermal stress and thermal creep, we also present results for the case of Maxwell molecules, where  $\alpha_0 = 2/5$  and Pr = 2/3. Assuming a thermal-slip coefficient of  $\beta = \alpha_0 = 2/5$ , we depict the velocity streamlines over the temperature contours in Fig. C.4. As the value of  $\beta$  in this case

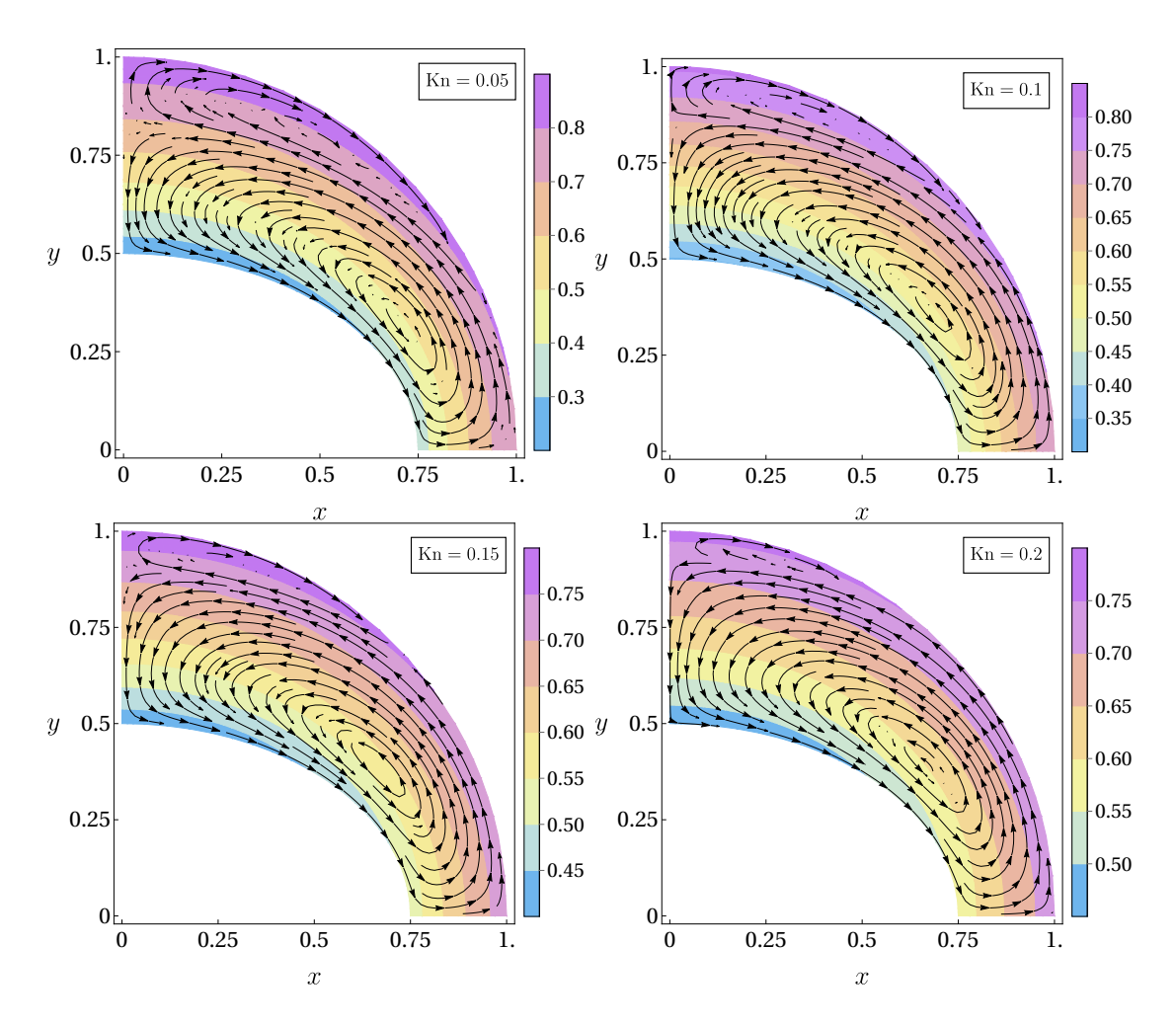


Figure C.4: Temperature contours and velocity streamlines depicted in the first quadrant for different values of the Knudsen number (Kn = 0.05, 0.1, 0.15, and 0.2) for fixed  $\beta = \alpha_0 = 2/5$  and Pr = 2/3.

is greater than the previous value  $\beta = 0.3197$ , a notable prediction is a further increase in thermal creep. Although there is only a slight expansion in the region influenced by thermal creep flow, a close comparison of Fig. C.4 with Fig. C.3 reveals a diminishing trend in thermal-stress slip flow for larger values of  $\beta$ .

We now give a brief description of the two types of slip flows that result from the velocity-slip boundary condition (4.20) and from the coupling between the stress and heat flux in  $(2.20)_1$ . Thermal stress is addressed by the second term on the right-hand side of  $(2.20)_1$ , whereas thermal creep is dealt with by the second term on the right-hand side of (4.20). Thermal-stress slip flow occurs when a tangential gradient is produced in the normal component of heat flux. Figure C.5 presents an illustrative diagram of

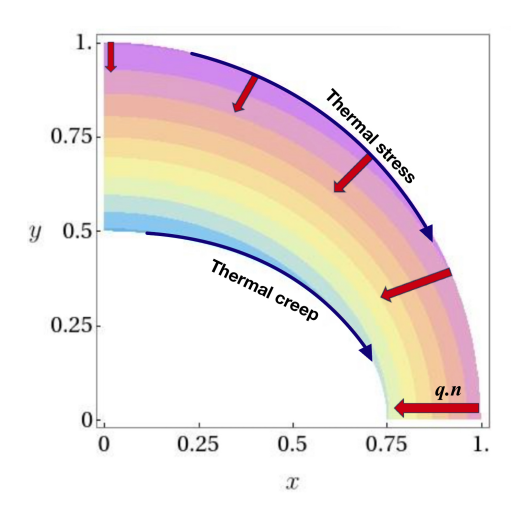


Figure C.5: Schematic for the depiction of the two type of flows induced due to thermal creep and thermal stress effects.

the temperature variation. The pink-colored region represents the region with high temperature while the blue color represents the region with low temperature. The bold red arrows represent the normal heat flux components at the outer cylinder in various directions, with the largest and smallest values at  $\theta = 0$  and  $\theta = \pi/2$ , respectively. For a better idea about the variation of the normal component of the heat flux, we illustrate its variation with  $\theta$  at Kn = 0.1 along with  $\beta = 1/5$ ,  $\alpha_0 = 0.3197$  and Pr = 0.661 in Fig. C.6. The induced tangential gradient is attributed to the thermal-stress slip flows. For a more

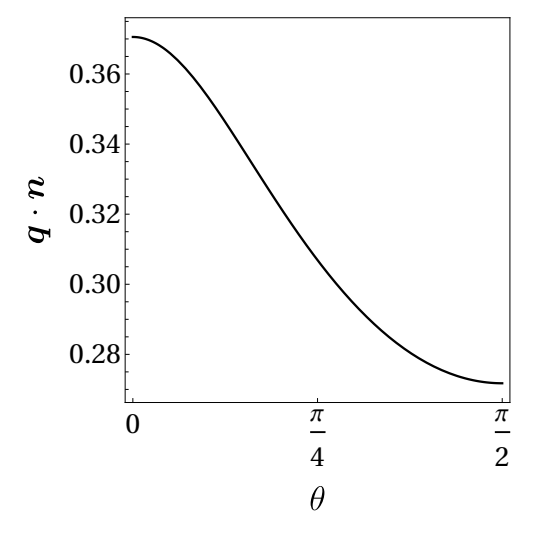


Figure C.6: Variation in the normal component of heat flux on the outer (circular) cylinder with  $\theta$  in the first quadrant for Kn = 0.1. The other parameters are  $\beta = 1/5$ ,  $\alpha_0 = 0.3197$  and Pr = 0.661.

comprehensive understanding of thermal-stress slip flows, additional information can be found in Ref. [101].

The second kind of flow is the thermal creep flow that is a boundary effect initiated by a temperature gradient in the tangential direction across the boundary, prompting the gas to migrate from colder to hotter regions. Although the temperatures on the walls of the cylinders are fixed to be uniform, the temperature-jump condition (2.52) creates a temperature difference close to the wall in the tangential direction. As observed in the temperature contours of Fig. C.5, a tangential temperature gradient is evident along the walls of the inner cylinder. Owing to this, the thermal creep flow induces along the inner cylinder from colder to hotter region.

# Appendix D

# Analytic solution to the R13 equations

To determine an analytic solution of the R13 equations for the problem of flow around a rotating cylinder, we substitute Eqs. (2.48) and (2.49) in Eqs. (2.46) and (2.47), transforming the resulting system of equations (2.43)–(2.47) into the cylindrical coordinates  $(r, \vartheta, z)$ . The choice of the cylindrical coordinates is natural, as the flow variables exhibit axial symmetry, making them invariant along the z-direction. This approach has been previously employed to derive analytic solutions of the regularized 13-moment (R13) and regularized 26-moment (R26) equations in the linearized state for the problems of flow past a stationary cylinder or sphere [87, 116, 124]. The symmetry ansatz used in these studies assumes that the radial and angular dependencies of the variables can be separated, with angular dependencies being expressed using sine and cosine functions. Specifically, the vector and tensor components having an odd number of indices in  $\vartheta$  are selected to be proportional to  $\sin \vartheta$  whereas the scalars and tensor components with an even number of indices in  $\vartheta$  are made proportional to  $\cos \vartheta$  [116]. Furthermore, since the problem is quasi-two-dimensional, the dependency in the z-coordinate of the variables is automatically eliminated. However, in the present problem, the rotation of the inner cylinder introduces an additional radial dependency. To account for this, extra functions dependent only on r are included. Following the symmetry ansatz, the solution for the vectors  $\boldsymbol{v}$  and  $\boldsymbol{q}$  take the forms

$$\boldsymbol{v}(r,\vartheta) = \begin{bmatrix} a_0(r) + a(r)\cos\vartheta \\ b_0(r) - b(r)\sin\vartheta \\ 0 \end{bmatrix}, \text{ and } \boldsymbol{q}(r,\vartheta) = \begin{bmatrix} \alpha_0(r) + \alpha(r)\cos\vartheta \\ \beta_0(r) - \beta(r)\sin\vartheta \\ 0 \end{bmatrix}, \tag{D.1}$$

that for the scalars  $\theta$  and p should take the form

$$\theta(r,\vartheta) = c_0(r) + c(r)\cos\vartheta, \text{ and } p(r,\vartheta) = d_0(r) + d(r)\cos\vartheta,$$
 (D.2)

and that for  $\sigma$  should take the form

$$\boldsymbol{\sigma}(r,\vartheta) = \begin{bmatrix} \gamma_0(r) + \gamma(r) \cos\vartheta & \kappa_0(r) + \kappa(r) \sin\vartheta & 0\\ \kappa_0(r) + \kappa(r) \sin\vartheta & -(\omega_0(r) + \omega(r) \cos\vartheta) & 0\\ 0 & 0 & \sigma_{zz} \end{bmatrix}, \tag{D.3}$$

where  $a_0(r)$ , a(r),  $b_0(r)$ , b(r),  $\alpha_0(r)$ ,  $\alpha_0(r)$ ,  $\alpha_0(r)$ ,  $\beta_0(r)$ ,  $\beta_0(r)$ ,  $c_0(r)$ ,  $c_0(r)$ ,  $d_0(r)$ ,  $d_0(r)$ ,  $d_0(r)$ ,  $\gamma_0(r)$ ,  $\gamma_0(r)$ ,  $\kappa_0(r)$ ,  $\kappa_0(r)$ ,  $\kappa_0(r)$ ,  $\kappa_0(r)$ ,  $\omega_0(r)$  and  $\omega_0(r)$  are the unknown functions that need to be determined, and  $\sigma_{zz} = -\sigma_{rr} - \sigma_{\vartheta\vartheta} = -(\gamma_0(r) - \omega_0(r) + (\gamma(r) - \omega(r)) \cos\vartheta)$  as  $\boldsymbol{\sigma}$  is a symmetric and tracefree tensor. Insertion of ansatz (D.1)–(D.3) in the R13 equations and separation of the radial and angular dependency leads to a system of 18 ordinary differential equations in the 18 unknowns. The analytic solutions obtained using these ODEs consist of a bulk contribution—comprising logarithmic and polynomial terms in r and 1/r—and the Knudsen layer contributions, which involve modified Bessel functions of the first and second kinds. The R13 equations predict three Knudsen layers, characterized by the eigenvalues  $\lambda_1 = \sqrt{5}/(3\mathrm{Kn})$ ,  $\lambda_2 = \sqrt{5}/(\sqrt{6}\mathrm{Kn})$  and  $\lambda_3 = \sqrt{3}/(\sqrt{2}\mathrm{Kn})$ . The bulk solution introduces twelve integration constants  $c_i$   $(i = 1, 2, \ldots, 12)$  while the Knudsen layer part yields another twelve constants:  $C_i^I$   $(i = 1, 2, \ldots, 6)$  for the modified Bessel functions of the second kind. These constants are determined by enforcing boundary conditions at the inner and outer cylinders.

#### REFERENCES

- [1] AGRAWAL, A., KUSHWAHA, H. M. & JADHAV, R. S. 2020 Microscale Flow and Heat Transfer. Springer.
- [2] AKHLAGHI, H., ROOHI, E. & STEFANOV, S. 2018 Ballistic and collisional flow contributions to anti-Fourier heat transfer in rarefied cavity flow. *Sci. Rep.* 8, 13533.
- [3] ALVES, C. J. 2009 On the choice of source points in the method of fundamental solutions. *Eng. Anal. Bound. Elem.* **33**, 1348–1361.
- [4] Aoki, K., Sone, Y. & Waniguchi, Y. 1998 A rarefied gas flow induced by a temperature field: Numerical analysis of the flow between two coaxial elliptic cylinders with different uniform temperatures. *Comput. Math. Appl.* 35, 15–28.
- [5] AOKI, K., SONE, Y. & YANO, T. 1989 Numerical analysis of a flow induced in a rarefied gas between noncoaxial circular cylinders with different temperatures for the entire range of the Knudsen number. *Phys. Fluids* 1, 409–419.
- [6] Bairstow, L., Cave, B. M. & Lang, E. D. 1923 X. The resistance of a cylinder moving in a viscous fluid. *Philos. Trans. Royal Soc. A* 223, 383–432.
- [7] BAKANOV, S. P., VYSOTSKIJ, V. V., DERJAGUIN, B. V. & ROLDUGHIN, V. I. 1983 Thermal polarization of bodies in the rarefied gas flow. J. Non-Equilib. Thermodyn. 8, 75–83.
- [8] Banerjee, P. 1994 The Boundary Element Methods in Engineering. McGraw-Hill.
- [9] Belytschko, T., Lu, Y. Y. & Gu, L. 1994 Element-free Galerkin methods. *Int. J. Numer. Methods Eng.* **37**, 229–256.
- [10] Berger, J. R. & Karageorghis, A. 2001 The method of fundamental solutions for layered elastic materials. *Eng. Anal. Bound. Elem.* **25**, 877–886.
- [11] Bhatnagar, P. L., Gross, E. P. & Krook, M. 1954 A model for collision processes in gases. I. small amplitude processes in charged and neutral one-component systems. *Phys. Rev.* 94, 511–525.
- [12] Bhattacharjee, R., Saini, S., Gupta, V. K. & Rana, A. S. 2024 Rarefied

- gas flow past a liquid droplet: Interplay between internal and external flows. *J. Fluid Mech.* **980**, A4.
- [13] BIRD, G. A. 1994 Molecular Gas Dynamics and the Direct Simulation of Gas Flows.

  Oxford: Clarendon Press.
- [14] Bobylev, A. V. 1982 The Chapman-Enskog and Grad methods for solving the Boltzmann equation. Sov. Phys. Dokl. 27, 29–31.
- [15] Bobylev, A. V. 2006 Instabilities in the Chapman–Enskog expansion and hyperbolic Burnett equations. *J. Stat. Phys.* **124**, 371–399.
- [16] Brebbia, C. A. & Dominguez, J. 1994 Boundary elements: An introductory course. WIT press.
- [17] CERCIGNANI, C. 1968 Stokes paradox in kinetic theory. *Phys. Fluids* 11, 303–308.
- [18] CERCIGNANI, C. 1969 Mathematical Methods in Kinetic Theory. New York: Plenum.
- [19] CERCIGNANI, C. 1975 The Boltzmann equation and its applications. Edinburgh, UK: Scottish Academic Press.
- [20] CERCIGNANI, C. 2000 Rarefied Gas Dynamics: From Basic Concepts to Actual Calculations. Cambridge: Cambridge University Press.
- [21] Chapman, S. & Cowling, T. G. 1970 The Mathematical Theory of Non-Uniform Gases. Cambridge: Cambridge University Press.
- [22] CHEN, C., NOORIZADEGAN, A., YOUNG, D. & CHEN, C.-S. 2023 On the determination of locating the source points of the MFS using effective condition number. J. Comput. Appl. Math. 423, 114955.
- [23] Chen, C. S., Karageorghis, A. & Li, Y. 2016 On choosing the location of the sources in the MFS. *Numer. Algorithms* **72**, 107–130.
- [24] Chen, C. S., Karageorghis, A. & Smyrlis, Y. S. 2008 The method of fundamental solutions: a meshless method. Atlanta: Dynamic Publishers.
- [25] CHENG, A.-D., ANTES, H. & ORTNER, N. 1994 Fundamental solutions of products of Helmholtz and polyharmonic operators. *Eng. Anal. Bound. Elem.* 14, 187– 191.
- [26] CHENG, A. H. & HONG, Y. 2020 An overview of the method of fundamental solutions—Solvability, uniqueness, convergence, and stability. *Eng. Anal. Bound. Elem.* 120, 118–152.

- [27] CLAYDON, R., SHRESTHA, A., RANA, A. S., SPRITTLES, J. E. & LOCKERBY, D. A. 2017 Fundamental solutions to the regularised 13-moment equations: Efficient computation of three-dimensional kinetic effects. J. Fluid Mech. 833, R4.
- [28] Colin, S. 2012 Gas microflows in the slip flow regime: A critical review on convective heat transfer. *J. Heat Transfer* **134**, 020908.
- [29] DONEA, J. & HUERTA, A. 2003 Finite Element Methods for Flow Problems, 1st edn. Wiley.
- [30] Drombosky, T. W., Meyer, A. L. & Ling, L. 2009 Applicability of the method of fundamental solutions. *Eng. Anal. Bound. Elem.* **33**, 637–643.
- [31] Fairweather, G., Karageorghis, A. & Martin, P. 2003 The method of fundamental solutions for scattering and radiation problems. *Eng. Anal. Bound. Elem.* 27, 759–769.
- [32] Fam, G. S. A. & Rashed, Y. F. 2002 A study on the source points locations in the method of fundamental solution. pp. 297–312. WIT Press, Southampton, UK.
- [33] Farkya, A. & Rana, A. S. 2025 Modeling of rarefied gas flows in streamwise periodic channels: Application of coupled constitutive relations and the method of fundamental solutions. *Eng. Anal. Bound. Elem.* 172, 106108.
- [34] Ferziger, J. H. & Kaper, H. G. 1972 Mathematical Theory of Transport Processes in Gases. Amsterdam, London: North-Holland Publishing Company.
- [35] FOLLAND, G. B. 1995 Introduction to Partial Differential Equations, 2nd edn. Princeton University Press.
- [36] GRAD, H. 1949 On the kinetic theory of rarefied gases. Comm. Pure Appl. Math. 2, 331–407.
- [37] Gu, X.-J., Barber, R. W., John, B. & Emerson, D. R. 2019 Non-equilibrium effects on flow past a circular cylinder in the slip and early transition regime. *J. Fluid Mech.* 860, 654–681.
- [38] Gu, X.-J. & Emerson, D. R. 2007 A computational strategy for the regularized 13 moment equations with enhanced wall-boundary conditions. *J. Comput. Phys.* **225**, 263–283.
- [39] Gupta, V. K. 2015 Mathematical modeling of rarefied gas mixtures. PhD thesis, RWTH Aachen University, Germany.

- [40] GUPTA, V. K. 2020 Moment theories for a d-dimensional dilute granular gas of Maxwell molecules. J. Fluid Mech. 888, A12.
- [41] Hancock, G. J. 1953 The self-propulsion of microscopic organisms through liquids. *Proc. R. Soc. Lond. A* 217, 96–121.
- [42] Himanshi, Rana, A. S. & Gupta, V. K. 2023 Fundamental solutions of an extended hydrodynamic model in two dimensions: Derivation, theory, and applications. *Phys. Rev. E* **108**, 015306.
- [43] HIMANSHI, THEISEN, L., RANA, A. S., TORRILHON, M. & GUPTA, V. K. 2025 A generalized fundamental solution technique for the regularized 13-moment system in rarefied gas flows, arXiv: 2504.18261.
- [44] HIMANSHI, THEISEN, L., RANA, A. S., TORRILHON, M. & GUPTA, V. K. 2025 R13\_MFS: A Meshless Solver for the Regularized 13-Moment Equations using the Method of Fundamental Solutions. Zenodo.
- [45] HOBSON, E. W. 1931 The theory of spherical and ellipsoidal harmonics. Cambridge University Press.
- [46] HOLWAY, L. H. 1966 New statistical models for kinetic theory: Methods of construction. *Phys. Fluids* **9**, 1658–1673.
- [47] HÖRMANDER, L. 1955 On the theory of general partial differential operators. *Acta Mathematica* **94**, 161–248.
- [48] Jadhav, R. S., Yadav, U. & Agrawal, A. 2023 OBurnett equations: Thermodynamically consistent continuum theory beyond the Navier-Stokes regime. ASME J. Heat Mass Transf. 145, 060801.
- [49] Kalempa, D. & Graur, I. 2024 Temperature and pressure jump coefficients at a liquid-vapor interface. *Phys. Fluids* **36**, 083622.
- [50] Kaplun, S. 1954 The role of coordinate systems in boundary-layer theory. Z. Angew. Math. Phys. 5, 111–135.
- [51] Kaplun, S. & Lagerstrom, P. A. 1957 Asymptotic expansions of Navier-Stokes solutions for small Reynolds numbers. *Appl. Math. Mech.* **6**, 585–593.
- [52] Karageorghis, A., Lesnic, D. & Marin, L. 2011 A survey of applications of the MFS to inverse problems. *Inverse Probl. Sci. Eng.* **19**, 309–336.
- [53] Khalili, A. & Liu, B. 2017 Stokes' paradox: Creeping flow past a two-dimensional cylinder in an infinite domain. *J. Fluid Mech.* 817, 374–387.

- [54] Kida, T. & Take, T. 1992 Asymptotic expansions for low Reynolds number flow past a cylindrical body. *JSME Int. J. Ser.* 2 35, 144–150.
- [55] Kremer, G. M. 2010 An Introduction to the Boltzmann Equation and Transport Processes in Gases. Berlin: Springer.
- [56] Kupradze, V. D. & Aleksidze, M. A. 1964 The method of functional equations for the approximate solution of certain boundary value problems. *USSR Comput. Math. Math. Phys.* 4, 82–126.
- [57] LAMB, H. 1911 XV. On the uniform motion of a sphere through a viscous fluid. Philos. Mag. 21, 112–121.
- [58] Lamb, H. 1932 Hydrodynamics. Cambridge: Cambridge University Press.
- [59] LEVERMORE, C. D. 1996 Moment closure hierarchies for kinetic theories. J. Stat. Phys. 83, 1021–1065.
- [60] LEWINTAN, P., THEISEN, L. & TORRILHON, M. 2025 Well-Posedness of the R13 Equations Using Tensor-Valued Korn Inequalities, arXiv: 2501.14108.
- [61] LI, M., CHEN, C. & KARAGEORGHIS, A. 2013 The MFS for the solution of harmonic boundary value problems with non-harmonic boundary conditions. *Comput. Math. Appl.* 66, 2400–2424.
- [62] Liu, Q. G., Fan, C. M. & Šarler, B. 2021 Localized method of fundamental solutions for two-dimensional anisotropic elasticity problems. *Eng. Anal. Bound. Elem.* **125**, 59–65.
- [63] LOCKERBY, D., REESE, J., EMERSON, D. & BARBER, R. 2004 Velocity boundary condition at solid walls in rarefied gas calculations. *Phys. Rev. E* **70**, 017303.
- [64] LOCKERBY, D. A. & COLLYER, B. 2016 Fundamental solutions to moment equations for the simulation of microscale gas flows. *J. Fluid Mech.* **806**, 413–436.
- [65] LORENTZ, H. 1897 A general theorem concerning the motion of a viscous fluid and a few consequences derived from it. *Versl. Kon. Acad. Wet. Amst.* 5, 168–175.
- [66] Marin, L. & Lesnic, D. 2005 The method of fundamental solutions for the Cauchy problem associated with two-dimensional Helmholtz-type equations. Comput. Struct. 83, 267–278.
- [67] Marušić-Paloka, E. 2001 On the Stokes paradox for power-law fluids. *Z. Angew. Math. Mech.* 81, 31–36.

- [68] Modi, A. & Rana, A. S. 2022 A finite difference scheme for non-Cartesian mesh: Applications to rarefied gas flows. *Phys. Fluids* **34**, 072002.
- [69] Mohammadzadeh, A., Rana, A. S. & Struchtrup, H. 2015 Thermal stress vs. thermal transpiration: A competition in thermally driven cavity flows. *Phys. Fluids* 27, 112001.
- [70] MORRA, G. 2018 Insights on the physics of Stokes flow. In Pythonic Geodynamics: Implementations for Fast Computing, pp. 93–104. Cham: Springer International Publishing.
- [71] MÜLLER, C. 1966 Spherical harmonics, Lecture Notes in Mathematics, vol. 17. Springer-Verlag, Berlin-New York.
- [72] MÜLLER, I. & RUGGERI, T. 1998 Rational Extended Thermodynamics. New York: Springer.
- [73] NAYROLES, B., TOUZOT, G. & VILLON, P. 1992 Generalizing the finite element method: Diffuse approximation and diffuse elements. *Comput. Mech.* **10**, 307–318.
- [74] Nie, D. & Lin, J. 2019 Numerical study on flow past a confined half cylinder in two bluff arrangements. *Fluid Dyn. Res.* 52, 015506.
- [75] Ohwada, T., Sone, Y. & Aoki, K. 1989 Numerical analysis of the Poiseuille and thermal transpiration flows between two parallel plates on the basis of the Boltzmann equation for hard-sphere molecules. *Phys. Fluids A* 1, 2042–2049.
- [76] OÑATE, E., IDELSOHN, S., ZIENKIEWICZ, O. C. & TAYLOR, R. L. 1996 A finite point method in computational mechanics. applications to convective transport and fluid flow. *Int. J. Numer. Methods Eng.* 39, 3839–3866.
- [77] Onishi, Y. 1977 Kinetic theory of evaporation and condensation of a vapor gas between concentric cylinders and spheres. *J. Phys. Soc. Japan* **42**, 2023–2032.
- [78] OSEEN, C. W. 1910 Uber die Stokes'sche Formel und über eine verwandte Aufgabe in der Hydrodynamik. Arkiv Mat. Astron. Fysk. 6, 1–59.
- [79] PICH, J. 1969 The drag of a cylinder in the transition region. J. Colloid Interface Sci. 29, 91–96.
- [80] POULLIKKAS, A., KARAGEORGHIS, A. & GEORGIOU, G. 1998 Methods of fundamental solutions for harmonic and biharmonic boundary value problems. Comput. Mech. 21, 416–423.

- [81] PROUDMAN, I. & PEARSON, J. R. A. 1957 Expansions at small Reynolds numbers for the flow past a sphere and a circular cylinder. *J. Fluid Mech.* 2, 237–262.
- [82] RAFIEENASAB, S., ROOHI, E. & TEYMOURTASH, A. 2020 Numerical analysis of nonlinear thermal stress flow between concentric elliptical cylinders. *Phys. Fluids* 32, 102007.
- [83] RAHIMI, B. & STRUCHTRUP, H. 2016 Macroscopic and kinetic modelling of rarefied polyatomic gases. *J. Fluid Mech.* **806**, 437–505.
- [84] RANA, A., RAVICHANDRAN, R., PARK, J. H. & MYONG, R. S. 2016 Microscopic molecular dynamics characterization of the second-order non-Navier-Fourier constitutive laws in the Poiseuille gas flow. *Phys. Fluids* 28, 082003.
- [85] RANA, A., TORRILHON, M. & STRUCHTRUP, H. 2013 A robust numerical method for the R13 equations of rarefied gas dynamics: Application to lid driven cavity. J. Comput. Phys. 236, 169–186.
- [86] Rana, A. S. & Barve, S. 2023 A second-order constitutive theory for polyatomic gases: theory and applications. *J. Fluid Mech.* **958**, A23.
- [87] RANA, A. S., GUPTA, V. K., SPRITTLES, J. E. & TORRILHON, M. 2021 Htheorem and boundary conditions for the linear R26 equations: Application to flow past an evaporating droplet. J. Fluid Mech. 924, A16.
- [88] RANA, A. S., GUPTA, V. K. & STRUCHTRUP, H. 2018 Coupled constitutive relations: A second law based higher-order closure for hydrodynamics. *Proc. Roy.* Soc. A 474, 20180323.
- [89] RANA, A. S., LOCKERBY, D. A. & SPRITTLES, J. E. 2018 Evaporation-driven vapour microflows: Analytical solutions from moment methods. *J. Fluid Mech.* **841**, 962–988.
- [90] RANA, A. S., SAINI, S., CHAKRABORTY, S., LOCKERBY, D. A. & SPRITTLES, J. E. 2021 Efficient simulation of non-classical liquid-vapour phase-transition flows: A method of fundamental solutions. J. Fluid Mech. 919, A35.
- [91] Reitebuch, D. & Weiss, W. 1999 Application of high moment theory to the plane Couette flow. *Continuum Mech. Thermodyn.* 11, 217–225.
- [92] SHAKHOV, E. M. 1968 Generalization of the Krook kinetic relaxation equation. Fluid Dyn. 3, 95–96.
- [93] Sharipov, F. 2004 Data on the velocity slip and temperature jump coefficients [gas

- mass, heat and momentum transfer]. In Proceedings of the 5th International Conference on Thermal and Mechanical Simulation and Experiments in Microelectronics and Microsystems, 2004. EuroSimE 2004, pp. 243–249.
- [94] SHIGETA, T., YOUNG, D. & LIU, C.-S. 2012 Adaptive multilayer method of fundamental solutions using a weighted greedy QR decomposition for the Laplace equation. J. Comput. Phys. 231, 7118–7132.
- [95] SINGH, N. & AGRAWAL, A. 2016 Onsager's-principle-consistent 13-moment transport equations. *Phys. Rev. E* **93**, 063111.
- [96] SINGH, N., JADHAV, R. S. & AGRAWAL, A. 2017 Derivation of stable Burnett equations for rarefied gas flows. *Phys. Rev. E* **96**, 013106.
- [97] SMITH, S. H. 1990 Some limitations of two-dimensional unbounded Stokes flow. *Phys. Fluids A* 2, 1724–1730.
- [98] SMYRLIS, Y.-S. 2009 Applicability and applications of the method of fundamental solutions. *Math. Comput.* **78**, 1399–1434.
- [99] Sone, Y. 1972 Flow induced by thermal stress in rarefied gas. *Phys. Fluids* **15**, 1418–1423.
- [100] Sone, Y. 2002 Kinetic Theory and Fluid Dynamics. Boston: Birkhäuser.
- [101] Sone, Y. 2007 Molecular Gas Dynamics: Theory, Techniques and Applications. Boston: Birkhäuser.
- [102] Sone, Y., Ohwada, T. & Aoki, K. 1989 Temperature jump and Knudsen layer in a rarefied gas over a plane wall: Numerical analysis of the linearized Boltzmann equation for hard-sphere molecules. *Phys. Fluids A* 1, 363–370.
- [103] Stokes, G. G. 1851 On the effect of the internal friction of fluids on the motion of pendulums. *Trans. Cambridge Philos. Soc.* 9 (Part II), 8–106.
- [104] STRUCHTRUP, H. 2004 Stable transport equations for rarefied gases at high orders in the Knudsen number. *Phys. Fluids* **16**, 3921–3934.
- [105] STRUCHTRUP, H. 2005 Macroscopic Transport Equations for Rarefied Gas Flows. Berlin: Springer.
- [106] STRUCHTRUP, H. 2008 Linear kinetic heat transfer: Moment equations, boundary conditions, and Knudsen layers. *Physica A* **387**, 1750–1766.
- [107] STRUCHTRUP, H., BECKMANN, A., RANA, A. S. & FREZZOTTI, A. 2017 Evaporation boundary conditions for the R13 equations of rarefied gas dynamics. *Phys.*

- Fluids 29, 092004.
- [108] STRUCHTRUP, H. & TORRILHON, M. 2003 Regularization of Grad's 13 moment equations: Derivation and linear analysis. *Phys. Fluids* **15**, 2668–2680.
- [109] STRUCHTRUP, H. & TORRILHON, M. 2008 Higher-order effects in rarefied channel flows. Phys. Rev. E 78, 046301.
- [110] Taheri, P., Torrilhon, M. & Struchtrup, H. 2009 Couette and Poiseuille microflows: Analytical solutions for regularized 13-moment equations. *Phys. Fluids* 21, 017102.
- [111] TAKATA, S., SONE, Y. & AOKI, K. 1993 Numerical analysis of a uniform flow of a rarefied gas past a sphere on the basis of the Boltzmann equation for hard-sphere molecules. *Phys. Fluids A* 5, 716–737.
- [112] TANNER, R. 1993 Stokes paradox for power-law flow around a cylinder. *J. Non-newton. Fluid Mech.* **50**, 217–224.
- [113] Theisen, L. & Torrilhon, M. 2021 fenicsR13: A tensorial mixed finite element solver for the linear R13 equations using the FEniCS computing platform. *ACM Trans. Math. Softw.* 47.
- [114] Theisen, L. & Torrilhon, M. 2025 fenicsR13: A Tensorial Mixed Finite Element Solver for the Linear R13 Equations Using the FEniCS Computing Platform (v1.5). Zenodo.
- [115] TOMOTIKA, S. & AOI, T. 1950 The steady flow of viscous fluid past a sphere and circular cylinder at small Reynolds numbers. Q. J. Mech. Appl. Math. 3, 141–161.
- [116] TORRILHON, M. 2010 Slow gas microflow past a sphere: Analytical solution based on moment equations. *Phys. Fluids* **22**, 072001.
- [117] TORRILHON, M. 2016 Modeling nonequilibrium gas flow based on moment equations. *Annu. Rev. Fluid Mech.* 48, 429–458.
- [118] TORRILHON, M. & SARNA, N. 2017 Hierarchical Boltzmann simulations and model error estimation. *J. Comput. Phys.* **342**, 66–84.
- [119] TORRILHON, M. & STRUCHTRUP, H. 2008 Boundary conditions for regularized 13-moment equations for micro-channel-flows. *J. Comput. Phys.* **227**, 1982–2011.
- [120] URIBE, F. J., VELASCO, R. M. & GARCIA-COLIN, L. S. 2000 Bobylev's instability. *Phys. Rev. E* **62**, 5835–5838.

- [121] VAN DYKE, M. 1964 Perturbation Methods in Fluid Mechanics. New York: Academic Press.
- [122] Wang, F., Liu, C.-S. & Qu, W. 2018 Optimal sources in the MFS by minimizing a new merit function: Energy gap functional. *Appl. Math. Lett.* **86**, 229–235.
- [123] Weiss, W. 1995 Continuous shock structure in extended thermodynamics. *Phys. Rev. E* **52**, 5760–5763.
- [124] Westerkamp, A. & Torrilhon, M. 2012 Slow rarefied gas flow past a cylinder: Analytical solution in comparison to the sphere. *AIP Conf. Proc.* **1501**, 207–214.
- [125] Wong, K. Y. & Ling, L. 2011 Optimality of the method of fundamental solutions. Eng. Anal. Bound. Elem. 35, 42–46.
- [126] Xu, K., He, X. & Cai, C. 2008 Multiple temperature kinetic model and gaskinetic method for hypersonic non-equilibrium flow computations. J. Comput. Phys. 227, 6779–6794.
- [127] Yadav, U., Jonnalagadda, A. & Agrawal, A. 2024 Derivation of extended-OBurnett and super-OBurnett equations and their analytical solution to plane Poiseuille flow at non-zero Knudsen number. J. Fluid Mech. 983, A29.
- [128] YAMAMOTO, K. & SERA, K. 1985 Flow of a rarefied gas past a circular cylinder. *Phys. Fluids* **28**, 1286–1293.
- [129] YOUNG, D. L., JANE, S. J., FAN, C. M., MURUGESAN, K. & TSAI, C. C. 2006 The method of fundamental solutions for 2D and 3D Stokes problems. *J. Comput. Phys.* 211, 1–8.